Development of methods for measuring optical nonlinearities of third order

Kamil Fedus

To cite this version:

Kamil Fedus. Development of methods for measuring optical nonlinearities of third order. Optics [physics.optics]. Université d'Angers, 2011. English. NNT : . tel-00799815

HAL Id: tel-00799815

https://theses.hal.science/tel-00799815

Submitted on 12 Mar 2013

Année 2011
N° d'ordre : 1120

Développement des méthodes de mesures des non linéarités optiques du troisième ordre.

THÈSE DE DOCTORAT

Spécialité : Physique

ÉCOLE DOCTORALE 3MPL (ED 500)

Matière, Molécules et Matériaux en Pays de Loire

Présentée et soutenue publiquement
Le 13 janvier 2011
à l'Université d'Angers

par **Kamil FEDUS**

Devant le jury ci-dessous:

Dominique BOSC, Rapporteur, *Ingénieur de Recherche (HDR), Université de Rennes 1*
Philippe GRELU, Rapporteur, *Professeur, Université de Bourgogne*
Cid B. de ARAUJO, Examinateur, *Professeur, Universidade Federal de Pernambuco*
Mathieu CHAUVET, Examinateur, *Professeur, Université de Franche-Comté*
Georges BOUDEBS, Directeur de thèse, *Maître de Conférences (HDR), Université d'Angers*

Laboratoire des Photonique d'Angers, EA4464, Université d'Angers, UFR Sciences,
2 Boulevard Lavoisier, 49045 ANGERS Cedex 01

Résumé

Cette étude traite principalement de la sensibilité des techniques expérimentales visant à caractériser la susceptibilité optique non linéaire du troisième ordre. Nous combinons différentes techniques bien connues à l'intérieur d'un système $4f$ d'imagerie en éclairage cohérent. Nous montrons qu'en changeant l'objet à l'entrée et le filtre spatial en sortie de la configuration $4f$ il est possible d'effectuer différentes méthodes de caractérisations non linéaires, telles que le mélange 4 ondes dégénérés (DFWM), Z-scan, EZ-scan, I-scan, imagerie non linéaire avec objet de phase (NIT-PO), etc. En outre, nous introduisons des techniques de mélange multi-ondes en utilisant des objets composés de différents nombres d'ouverture circulaire. Nous montrons que toutes ces méthodes peuvent être considérées comme des cas particuliers d'un même processus d'imagerie non linéaire. Nous étudions les modifications de la distribution d'intensité dans le plan image après filtrage non linéaire des fréquences spatiales relatives à l'objet à travers le matériau placé à proximité du plan de Fourier, pour obtenir des informations sur les non-linéarités induites. Pour procéder à une analyse quantitative, nous définissons le signal à mesurer en généralisant le rendement de diffraction utilisé avec les réseaux au niveau des images acquises par une caméra CCD. A l'aide d'un simple modèle théorique basé sur l'optique de Fourier, nous obtenons, dans le cas de faibles non linéarités, les relations entre le rendement de diffraction et le déphasage non linéaire auto-induit caractérisant chaque technique. Nous comparons les sensibilités correspondantes aux différentes méthodes et pour chaque cas, nous donnons les conditions dans lesquelles la sensibilité et le rapport signal sur bruit sont optimisés. Ceci afin de faciliter la caractérisation des échantillons en couches minces (typiquement 1 μm d'épaisseur) où le signal est de trois ordres de grandeur plus faible que celui obtenu avec un échantillon massif.

En outre, nous discutons d'une part le problème de la photo-sensibilité des couches minces dans le contexte de détermination de n_2, l'indice de réfraction non linéaire, et de β, le coefficient d'absorption non linéaire, et d'autre part les erreurs induites par un signal faible qui pousse l'expérimentateur à augmenter l'intensité et, ainsi, à détruire les échantillons. Par ailleurs, nous montrons que la méthode Z-scan pourrait être employée pour examiner et caractériser les effets photo-induits et permanents dans la réfraction et l'absorption au niveau du point d'impact. Aussi cette méthode a-t-elle été utilisée pour caractériser les paramètres optiques linéaires des couches minces, telles que l'épaisseur et l'indice de réfraction du film avec une résolution accrue ($\lambda/550$). Une étude théorique complétée par des calculs numériques nous permet d'obtenir des relations simplifiées qui peuvent se révéler très utiles au niveau des estimations des épaisseurs.

Nous rapportons aussi sur des mesures absolues de n_2 dans le disulfure de carbone et la silice fondue, deux matériaux de références utilisés parfois pour étalonner l'intensité dans le plan focal d'une lentille. Les valeurs des coefficients non linéaires sont obtenues dans le régime picoseconde et pour trois longueurs d'ondes différentes (355 nm, 532 nm et 1064 nm). Enfin, nous caractérisons et mesurons les coefficients non linéaires de certains verres exotiques : une famille de verres en chalcogénures (GeS_2-Sb_2S_3-CsI) et des verres en oxyde à base de métaux lourds ($Pb(PO_3)_2$-WO_3). Nous montrons aussi que le modèle développé par Boling et al. en 1978 dénommé modèle BGO pourrait être utilisé de manière appropriée pour prévoir les coefficients de réfraction non linéaire à partir de la mesure de deux indices linéaires pour deux longueurs d'ondes différentes dans la région de transparence du matériau, facilitant ainsi le choix de la composition du verre en fonction des propriétés optiques souhaitées.

Abstract

This study deals with the sensitivity of different experimental technique to characterize the third order optical susceptibility. We combine different well-known experimental techniques inside the $4f$ coherent imaging system in order to simplify the nonlinear optical characterization. We show that by changing the object at the entry and the field-stop at the output of the $4f$ setup it is possible to perform various popular nonlinear characterization methods, such as degenerate four-wave mixing (DFWM), Z-scan, EZ-scan, I-scan and nonlinear imaging technique with phase object (NIT-PO). Moreover we introduce different multi-wave mixing techniques using objects composed of different numbers of circular apertures (top-hat beams). We show that all these methods can be considered as particular cases of the same nonlinear imaging process. For various objects the alterations of the intensity distribution in the image plane of the $4f$ setup, after nonlinear filtering through the material under study placed in proximity of the Fourier plane, provide informations about nonlinearity. To analyze quantitatively nonlinear distortions of images acquired by CCD camera we define the diffraction efficiency as a signal to be measured. Using simple numerical model based on Fourier optics we derive relations between diffraction efficiency and nonlinear phase shift for each characterization techniques. We compare sensitivities corresponding to different methods and for each case we provide the conditions in which the sensitivity and the signal to noise ratio are optimized in order to facilitate characterization of samples in thin film form where the signal is three order of magnitude lower than in the classical measurement. Furthermore we discuss the problem of photo-sensitivity of thin films in the context of determination of n_2, the nonlinear refractive index and β, the nonlinear absorption coefficient. Moreover the well-known Z-scan method, typically exploited for nonlinear characterization, is employed to investigate permanent photo-induced changes in refraction and absorption as well as to characterize linear optical parameters of thin films, such as thickness and refractive index. The theories for such Z-scan experiments in linear regime are developed analytically and numerically. We report also on Z-scan absolute measurements of n_2 in carbon disulfide and fused silica, two standard references materials used to calibrate nonlinear optical experiments. The results of nonlinear coefficients are obtained in picoseconds regime for three different wavelengths (355 nm, 532 nm and 1064 nm). Finally, linear and nonlinear optical characterization of new families of chalcogenide glasses (GeS_2-Sb_2S_3-CsI) and oxide glasses with heavy metals ($Pb(PO_3)_2$-WO_3) is presented. We show also that the theoretical model developed by Boling et al. in 1978 called the BGO model could be used to predict the nonlinear refraction coefficients from the measurement of two linear indices in two different wavelengths in the transparency region of the material. The prediction of nonlinearities on the basis of linear coefficients can facilitate the choice of glass compositions with the desired optical properties.

Acknowledgement

This thesis is the result of work done from February 2008 to January 2011 at the *Laboratoire de Photoniques d'Angers* (LΦA), EA 4464 (the former laboratory of *Proprietes Optiques des Materiaux et Applications* (POMA), FRE CNRS 2988).

I have had a great time as a student in the Photonic Laboratory at the University of Angers and I wish to thank a number of people for contributing to this experience. First of all I would like to express my sincere gratitude to my supervisor Georges Boudebs without whom this work would not be possible. I am grateful to him for accepting me as a PhD student and making possible for me to stay in Angers during these three years. I always enjoyed his style of work and a very enthusiastic attitude to the scientific research. Without his creative ideas and constant support I could not push my studies forward. He introduced me to the various concepts in nonlinear optics and experimental techniques. During this time he was not only the guide but also a good friend. Despite his many responsibilities he had always a time for me and he had never refused to help me in different problems. I am also thankful to his lovely family for being very friendly to me and for the dinners offered by them.

I acknowledge Prof. Herve Leblond for invaluable theoretical support and constructive comments about our work. His positive remarks were always ensuring us that our researches were heading in a good direction.

I am indebt to Prof. Cid B. Araújo from the *Universidade Federalde Pernambuco*, (Recife, Brazil), Dr Dominique Bosc from the *Laboratoire Foton* in Lannion, Prof. Mathieu Chauvet from the *Université de Franche-Comté* and Prof. Philippe Grelu from the *Université de Bourgogne* for accepting to be members of the jury. I express my sincere gratitude to all of them.

I would like to thank Virginie Nazbal, Quentin Coulombier and Johann Troles of the *Université de Rennes 1*, for providing us the samples for characterization. I am also indebted to

Romain Mallet and Robert Filmon from the *Laboratoire S.C.I.A.M* in Angers for supplying us with AFM pictures and profiles.

I acknowledge especially the help of Christophe Cassagne and Alain Mahot in setting up the experiments and to keep the laser in working condition. The practical part of my work could not be done without their technical support. I am thankful to Oksana Krupka for her help in chemical work which I could not avoid during my studies. I appreciate the help of Dr. Jean-Luc Godet in editing some parts of this work in French language. I would also like to thank other members of laboratory for being very kind to me at all times.

I take this opportunity to thank all my friends at Angers. First of all I would like to thank Payman and Ayhan Tajalli-Seifi with whom I shared my apartment and office. We became very good friends and we spent together a lot of exciting moments. It was also a great pleasure to share my office with Ivan Verzhbitskiy. I would like to thank him for friendly atmosphere and interesting discussions. I wish also to thank all my other friends: Kostas, Katia, Fei Chen, Abdeliallah, Frederic, Vânia, Robert and Zac for making the life in Angers exciting and an active one.

I would like to send special thanks to my parents. The effort which they put in my education was priceless. Above all, they encouraged me to start the PhD studies in France and they have always been supportive and showed interest for my work. This thesis is dedicated for them.

Finally I would like to express my feelings of gratitude to my fiancée Sylwia - my good spirit. Without her support and understanding everything would be much more complicated. Thank you so much.

Contents

List of Figures

List of Tables

List of Symbols

E	Amplitude of electric field
I	Intensity
I_{eff}	Effective intensity
I_0	Focal on-axis intensity
L	Sample thickness
L_{eff}	Effective thickness
P	Polarization
S	Linear transmittance of aperture
T	Transmittance
ΔT_{pv}	Peak-valley transmission change
c	Velocity of light in vacuum
e	Natural number ($\exp(1) \approx 2.7183$)
$\widehat{\mathbf{e}}$	Unit vector
e_c	Elementary electric charge
f	Focal length
i	$\sqrt{-1}$
k	Wave number $k = 2\pi/\lambda$
m_e	Electron mass
n_0	Linear refractive index
n_2	Nonlinear refractive index
r	$r = \sqrt{x^2 + y^2}$
$\mathbf{r}$	$r = (x, y, z)$
r_a	Radius of circular aperture
t	Time

x, y, z	Cartesian coordinates
u, v	Spatial frequencies
w_a	Beam waist at the image plane of the $4f$ imaging system
w_e	Beam waist at the entry of the $4f$ imaging system
w_0	Beam waist in the focal plane
z_0	Rayleigh range
$\Delta\Phi_0$	Focal on-axis phase shift
$\Delta\Phi_{NL}$	Nonlinear phase shift
α	Linear absorption coefficient
β	Two absorption coefficient
ϵ_0	Vacuum permitivity
ε	Energy
ε_g	Energy band gap
κ	Extinction coefficient
λ	Wavelength
η or η'	Diffraction efficiency
$\chi^{(1)}$	Linear susceptibility
$\chi^{(3)}$	Third-order susceptibility
ω	Angular frequency

List of Abbreviations

AOS	All-Optical Switching
B-DFWM	Backward Degenerate Four Wave Mixing
DFWM	Degenerate Four Wave Mixing
F-DFWM	Forward Degenerate Four Wave Mixing
FS-DFWM	Forward-Scatering Degenerate Four Wave Mixing
FOM	Figure of Merit
FWHM	Full Width at Half Maximum
NIT-PO	Nonlinear Imaging Technique with Phase Object
NLA	Nonlinear Absorption
NLR	Nonlinear Refraction
PO	Phase Object
PIE	Photo-Induced Effects
TPA	Two Photon Absorption

INTRODUCTION GÉNÉRALE

Avec l'invention du laser en 1960 un domaine nouveau et fascinant de la recherche a été introduit dans la communauté scientifique: "l'optique non linéaire". Historiquement, l'optique non linéaire a commencé avec les travaux expérimentaux de P.A. Franken et al.[1] qui en 1961 ont découvert le phénomène de la génération de la seconde harmonique. Après cette date, l'interaction de la lumière laser intense et cohérente avec la matière est devenue un sujet de recherche de pointe en raison de ses applications potentielles dans des domaines variés. Beaucoup de phénomènes nouveaux ont été découverts. En particulier, il a été constaté que dans la gamme des intensités lumineuses utilisées pour générer des effets optiques non linéaires, les paramètres optiques habituels des matériaux ne peuvent pas être considérés comme constants, mais sont eux-mêmes des fonctions de l'intensité lumineuse. Une grande partie des effets non linéaires peut être expliquée en se référant à des changements d'intensité dépendant de la réfraction et de l'absorption habituellement décrites par l'indice de réfraction non linéaire (n_2) et le coefficient d'absorption non linéaire (β), respectivement. Les effets non linéaires ont été utilisés pour de nombreuses applications pratiques, en particulier dans les dispositifs tout-optiques et électro-optiques utilisés dans les télécommunications, le stockage optique de l'information, les commutateurs optiques, la limitation optique, etc. La double dépendance à n_2 et β a une influence significative sur la performance des applications de certains appareils optiques. Par exemple, le coefficient n_2 est responsable des effets tels que l'auto-modulation de phase et l'auto-focalisation du faisceau laser. Ces deux phénomènes permettent de compenser la tendance naturelle de l'impulsion à la dispersion et à la diffraction créant en définitive des solitons spatio-temporels. C'est un grand pas vers la communication tout-optique. Cependant l'absorption non linéaire caractérisée par β peut réduire considérablement la puissance transmise par la fibre optique ou le guide d'onde. Une situation semblable a lieu pour toutes les applications en commutation optique où un grand n_2 et un petit β sont nécessaires pour la conception de commutateurs tout-optiques ultra-rapides qui peuvent remplacer leurs homologues électroniques relativement plus lents. Par ailleurs, dans le domaine de la limitation optique, les matériaux caractérisés par une forte absorption non linéaire sont souhaitables afin de construire des limiteurs optiques pour réduire la puissance lumineuse à l'entrée d'un système. Ainsi la connaissance de l'indice de réfraction non linéaire, n_2, et du coefficient d'absorption non linéaire, β, des matériaux est d'un grand intérêt en raison de leurs applications potentielles dans la conception de dispositifs optiques ultra-rapides.

En conséquence, diverses techniques pour déterminer les coefficients non linéaires ont été développées. Il s'agit notamment de la génération de la troisième harmonique, de l'interférométrie non linéaire (par exemple Michelson [112] ou Mach-Zender [113]), et l'ellipsométrie [36][41], les techniques de mélange d'ondes (par exemple, mélange à trois ondes [46], mélange à quatre ondes [59]) et diverses méthodes utilisant la distorsion d'un faisceau (par exemple Z-scan [63], I-scan [71]). Toutes ces méthodes présentent des avantages et des inconvénients. En particulier, il s'agit de caractériser et de comparer la sensibilité de chaque méthode en tenant compte d'un rapport signal/bruit maximal. La question de la sensibilité est particulièrement importante dans le contexte de la caractérisation des couches minces. La nouvelle génération des circuits optoélectroniques intégrés, de plus en plus petits avec une vitesse de commutation de plus en plus élevée, s'oriente vers le développement de films minces. Les films minces considérés comme un système à deux dimensions sont d'une grande importance pour de nombreux problèmes pratiques. Le coût du matériau est relativement plus faible et ils remplissent la même fonction quand il s'agit de processus de surface. Ainsi, la détermination des propriétés des couches minces est-il un enjeu important car la connaissance précise de leurs caractéristiques peut être utile pour de futures applications. Dans le domaine de la caractérisation de couches minces en optique non linéaire, la tâche est difficile. La longueur d'interaction avec la lumière est très courte lorsque l'épaisseur du matériau est de l'ordre de plusieurs couches atomiques et, par conséquent, les effets optiques non linéaires générés sont très faibles. On pourrait accroître l'intensité lumineuse afin de renforcer le signal issu de la non-linéarité, mais un tel accroissement est limité par le seuil d'endommagement du matériau. Ce seuil est particulièrement faible pour les matériaux photosensibles. Il est donc nécessaire de disposer de méthodes de caractérisation très sensibles permettant de convertir une petite réponse non linéaire du matériau en une grande quantité mesurable sans pour autant détruire l'échantillon. Parmi les diverses techniques de caractérisation, la méthode Z-scan a été jugée particulièrement efficace dans la transformation des petits changements au niveau de la réfraction et l'absorption non linéaires en signaux détectables. Cette technique est devenue populaire et a été acceptée par la communauté scientifique pour réaliser les mesures de n_2 et β. Elle offre à la fois, la simplicité de la configuration optique et la possibilité de la détermination simultanée du signe et du type de la non-linéarité (réfraction ou absorption). En outre de nombreuses améliorations de la méthode Z-scan ont été proposées afin d'améliorer la sensibilité [69], [74], [77], [81], [86], [87], [88], [93], [94]. En particulier la méthode 'Z-scan éclipsé' (EZ-scan pour Eclipsed Z-scan) [68] a été introduite; elle offre une sensibilité supérieure d'un ordre de grandeur par rapport à la méthode originale. Toutefois, une telle amélioration impressionnante se fait au détriment d'une réduction de la précision parce que le rapport signal sur bruit est sensiblement plus petit en éclipsant les mesures. En général, dans les expériences Z-scan, un équilibre doit être trouvé entre le signal non linéaire et l'amélioration de la sensibilité afin d'obtenir une précision satisfaisante [124].

G. Boudebs et al.[100][101] ont introduit une technique d'imagerie non-linéaire (NIT) qui exploite les propriétés de filtrage d'un système d'imagerie $4f$ cohérent. Il a été démontré qu'il est possible de caractériser les non-linéarités en analysant le profil d'intensité de l'image acquise par une caméra CCD, après filtrage non linéaire à travers le matériau placé dans le plan de Fourier de la configuration. La comparaison de l'image expérimentale avec sa simulation numérique conduit aux coefficients non linéaires de l'échantillon étudié. Différents objets comme les fentes d'Young [100], le profil gaussien, l'objet rectangulaire [103] et l'objet de phase [104] ont été proposés à l'entrée du système $4f$ afin d'optimiser la caractérisation non linéaire. En particulier l'utilisation des objets de phase (PO) permet d'obtenir une sensibilité comparable à Z-scan. Dans cette thèse, les techniques d'imagerie non linéaires sont généralisées par l'introduction du mélange multi-ondes à l'intérieur de la configuration $4f$. En outre, nous montrons qu'en choisissant un objet approprié à l'entrée et un filtre spatial correspondant dans le plan image il est possible d'effectuer diverses expériences connues, comme le mélange quatre ondes (DFWM), Z-scan, EZ-scan et I-scan. Un seul dispositif expérimental pour toutes ces techniques nous permettra de comparer leur sensibilité optique. En outre, nous montrons qu'en définissant le signal mesuré d'une manière appropriée, l'optimisation de la sensibilité peut être accompagnée d'une augmentation du rapport signal sur bruit. Par suite, les conditions optimales pour les mesures seront établies pour chaque méthode afin de tenter et faciliter la caractérisation de couches minces.

La deuxième partie de notre étude porte sur la caractérisation des échantillons minces. En particulier, nous étudions la photosensibilité des films dans le cadre de la caractérisation non linéaire. Les effets photo-induits (PIE) tels que l'ablation ou le photo-noircissement peuvent être compris comme une destruction de l'échantillon ayant entraîné une modification permanente de la réfraction et de l'absorption au niveau de la matière. Ces modifications se produisent lorsque l'échantillon est irradié par des intensités au-dessus du seuil de dommage. Cependant, les fortes intensités sont parfois indispensables afin d'induire une réponse (y compris parfois une diffraction linéaire sur la zone d'impact après ablation), en particulier dans les couches minces. Comme nous le montrons dans cette thèse, les PIE affectent non seulement la caractérisation non linéaire, mais peuvent aussi imiter le signal non linéaire issu de la méthode Z-scan avec ses caractéristiques typiques faisant apparaître un maximum et un minimum dans le profil. Cela peut conduire à des résultats erronés pour la mesure de n_2 et β par cette méthode. Néanmoins, nous montrons qu'il est aussi possible d'exploiter cet effet dans un sens positif. Nous introduisons Z-scan comme une nouvelle technique à mettre en place pour caractériser les effets photo-induits dans les changements permanents au niveau de la réfraction et de l'absorption. Cela pourrait être particulièrement utile pour quantifier le processus d'écriture des guides ondes optiques. Ce dernier est largement étudié en tant que mécanisme potentiel permettant la réduction des coûts de fabrication des guides d'ondes [147]. Le guide pouvant être créé par les changements permanents de l'indice de réfraction linéaire induit localement le long du faisceau laser. La description quantitative d'un tel phénomène serait utile. Nous utilisons également la méthode Z-scan pour mesurer les propriétés optiques linéaires des couches minces transparentes. L'utilité de cette technique va bien au-delà domaine de l'optique non linéaire puisqu'il a été possible de mesurer l'épaisseur (ou l'indice de réfraction linéaire) d'un échantillon mince de profil rectangulaire.

La dernière partie de notre thèse est consacrée à la caractérisation optique non linéaire d'échantillons massifs. Tout d'abord nous procédons à des mesures absolues de réfraction non linéaire dans le disulfure de carbone (CS_2) et la silice fondue (SiO_2) pour trois longueurs d'ondes: 355 nm, 532 nm et 1064 nm. Ces deux matériaux sont souvent utilisés comme références pour calibrer les montages expérimentaux lors de la caractérisation non linéaire.

Pour obtenir des valeurs de n_2 plus précises que celles utilisées depuis quelques dizaines d'années, nous combinons Z-scan à l'intérieur du système $4f$ avec la méthode d'obturation Kerr (Kerr shutter) afin d'analyser avec précision le profil spatio-temporel du faisceau pompe. Les valeurs absolues ainsi obtenues pour n_2 sont comparées à ceux déjà rapportés dans la littérature. Une discussion à la lumière des théories de dispersion de l'indice de réfraction non linéaire en fonction de la longueur d'onde sera réalisée. Enfin, nous présentons les caractérisations optiques linéaires et non linéaires de nouvelles familles de verres en chalcogénures (GeS_2-Sb_3S_2-CSI) et des verres d'oxydes à base de métaux lourds ($Pb(PO_3)_2$-WO_3). Les verres en chalcogénures sont des matériaux vitreux inorganiques qui contiennent toujours un ou plusieurs éléments chalcogènes: S, Se ou Te, mais pas d'oxygène (contrairement à des verres d'oxydes). Les verres chalcogénures sont bien connus pour posséder une grande réfraction linéaire et non linéaire associée à une transparence dans l'infrarouge. Les verres d'oxydes à base des métaux lourds sont intéressants en raison d'une absorption non linéaire relativement faible, en particulier dans le domaine infrarouge. Avec un indice n_2 dix fois plus élevé que celui de la silice fondue, ces verres sont des candidats potentiels pour des applications dans les télécommunications. Les résultats obtenus pour les deux familles de verres sont comparés dans le contexte des applications en commutation et traitement tout-optique du signal. En outre, un modèle théorique introduit par Boling et. al.[18] (que l'on appelle BGO) est adopté afin de prédire le coefficient non linéaire à partir des données expérimentales caractéristiques en optique linéaire. Il est très important d'avoir des expressions théoriques permettant de prédire l'importance des non-linéarités et donc, facilitant le choix de la composition du verre en fonction des propriétés optiques souhaitées. Comme nous le montrons dans cette thèse, le modèle BGO peut fournir des prédictions correctes pour les deux familles des verres que nous avons examinés.

GENERAL INTRODUCTION

With the invention of the laser in 1960's a fascinating new field of research termed "nonlinear" optics was introduced to the scientific and engineering community. Historically, nonlinear optics originated with the experimental work of P. A. Franken et al.[1] who in 1961 discovered the phenomenon of second-harmonic generation. After that the interaction of the intense and coherent laser light with matter became a subject of intensive research owing to its potential applications in a variety of fields. Plenty of new phenomena have been discovered which are not seen with ordinary light. Particularly it was found that in the range of intensities used to generate nonlinear optical effects, the usual optical parameters of materials cannot be considered as constant anymore but become functions of the light intensity. Especially the large part of nonlinear effects can be explained referring to the intensity-dependent changes in refraction and absorption usually described by the nonlinear refractive index (n_2) and the nonlinear absorption coefficient (β), respectively. The nonlinear effects have been employed for many practical applications especially in all-optical and electro-optical devices used for telecommunication, optical storage, optical switching, optical limiting and optical computing. The interplay between n_2 and β significantly influences on the performance of particular optical devices in these applications. For example, the n_2 coefficient is responsible for such effects as the self-phase modulation by the laser pulse and the self-focusing of the laser beam. These two phenomena compensate the natural tendency for the pulse to disperse and for the beam to diverge creating as a result temporal and spatial solitons. This is a major leap towards all-optical communication. However the nonlinear absorption determined by β can substantially reduce the power transmitted through optical fiber or waveguide acting as communication wires. The similar situation takes place for all-optical switching applications where large n_2 and small β are required in order to design ultra-fast optical switches which can replace slower electronic counterparts. In yet another case, in the field of optical limiting, the materials characterized by high nonlinear absorption are desirable in order to build optical limiters reducing the input light power. Thus the knowledge of nonlinear refractive index, n_2, and the nonlinear absorption coefficient, β, of materials is of great interest due to their potential applications in designing particular optical devices.

In consequence, various techniques to determine the nonlinear coefficients were developed. These include the third harmonic generation, nonlinear interferometric techniques (e.g. Michelson [112] or Mach-Zender [113] interferometers), Kerr ellipsometry (e.g. ellipse rotation [36], Kerr gate [41]), wave-mixing techniques (e.g. three wave-mixing [46], degenerate four wave mixing [59]) and various types of beam distortion methods (e.g. Z-scan [63], I-scan [71]). All of them have advantages and disadvantages. Particularly, we would like to characterize and compare the sensitivity for each method taking into account the highest signal to noise ratio. The issue of sensitivity is especially important in the context of thin film characterization. The growing demand for development of smaller and smaller devices with higher speed especially in the new generation of integrated optoelectronic circuits attracts the attention towards the thin film's technology. Thin films as a two dimensional systems are of great importance to many real-world problems. Their material costs are very small as compared to the corresponding bulk material and they perform the same function when it comes to surface processes. Thus, the determination of properties of thin films is an important issue since the accurate knowledge about their features can be valuable for future applications. In the nonlinear optical domain the characterization of thin films is a challenging task. The interaction length with the light is very short when the thickness of the material is of the order of several atomic layers and consequently the generated nonlinear optical effects are very weak. One could increase the incident intensity in order to enhance the nonlinearity; however this is ultimately limited by the damage threshold of the material. The latter is especially low for the photo-sensitive materials. Hence it is necessary to have very sensitive characterization methods allowing converting a small nonlinear response of the material into a measurable quantities without destroying the sample. Among a variety of characterization techniques the Z-scan method was found to be especially efficient in transforming the small nonlinear changes in refraction and absorption into detectable signals. This technique has gained the greatest popularity and has been accepted by the optical community as a standard experiment for measurements of n_2 and β. It offers both, the simplicity of the optical setup and the possibility of simultaneous determination of the sign and the type of nonlinearity (refractive or absorptive). Moreover many different alterations to original Z-scan method have been proposed in order to improve the sensitivity [69], [74], [77], [81], [86], [87], [88], [93], [94]. Particularly an eclipsing Z-scan (EZ-scan) [68] was introduced giving the sensitivity one order of magnitude larger in comparison to the original method. However, such impressive enhancement comes at the expense of a reduction in accuracy because the signal to noise ratio is substantially decreased in eclipsing measurements. In general, in Z-scan experiments, the balance between the nonlinear signal and the sensitivity improvement must be found in order to obtain satisfactory accuracy [124].

G. Boudebs et al. [100][101] introduced the nonlinear imaging technique (NIT) exploiting the filtering properties of a simple $4f$ coherent imaging system. It was shown that it is possible to characterize nonlinearities by analyzing the intensity profile of the image acquired by a CCD camera after nonlinear filtering through the material placed in the Fourier plane of the setup. The comparison of experimental filtered image of an object with its numerical simulation leads to nonlinear coefficients of the investigated sample. Different objects as the Young's double-slit object [100], the Gaussian object, the top-hat object [103] and the phase object [104] have been proposed at the entry of the $4f$ system in order to optimize the nonlinear characterization. Particularly the use of the phase objects (PO) permits to achieve sensitivity comparable with the Z-scan technique. In this thesis the nonlinear imaging techniques are extended by introducing the multi-wave mixing methods inside the $4f$ configuration. Furthermore we will show that by choosing an appropriate object at the entry and a field-stop in the image plane of the $4f$ setup it is possible to perform various well-known experiments, particularly, such popular techniques as Degenerate Four Wave Mixing (DFWM), Z-scan, EZ-scan and I-scan. An application of one experimental setup for all this techniques will permit us to compare their optical sensitivities. Moreover we will show that by defining the measured signal in a proper way the optimization of the sensitivity can be accompanied by an increase of the signal to noise ratio. Consequently the optimized conditions for measurements will be provided for each method in order to facilitate the characterization of thin films.

The second part of our study deals with the characterization of the samples in thin form. Particularly we investigate the photo-sensitivity of films in the context of nonlinear characterization. The photo-induced effects (PIE) such as ablation or photo-darkening can be understood as a destruction of the sample leading to permanent modifications in refraction and absorption of the material. These changes occur when the sample is irradiated by intensities above the damage threshold. But sometimes high intensities are indispensable in order to induce a response, particularly in thin films. As we will show in this thesis, PIE not only hinder the nonlinear characterization but can also imitate the nonlinear signal in such popular method as the Z-scan technique. This can lead to largely erroneous results of n_2 and β determined throughout this kind of experiment. Nevertheless we will show that it is also possible to exploit this effect in a positive way. Z-scan technique will be introduced as a new method to characterize permanent photo-induced changes in refraction and absorption. This could be particularly useful to quantify the optical waveguide writing process. The latter effect is extensively studied as potential mechanism reducing costs of waveguide fabrication [147]. Accordingly, the waveguide can be created through the permanent changes of linear refractive index induced locally along the laser path. The quantitative description of such phenomenon would be valuable. In the further part of the thesis we will employ also the Z-scan method to measure linear optical properties of transparent thin films. Hence the usefulness of this technique will be extended outside the domain of nonlinear optics and the possibility of measuring the thickness (or the linear refractive index) of thin sample by this method will be presented.

The last part of our thesis is devoted to the nonlinear optical characterization of samples in the bulk form. First of all, we report on Z-scan absolute measurements of nonlinear refraction in carbon disulfide (CS_2) and fused silica (SiO_2) for three wavelengths at 355 nm, 532 nm and 1064 nm. Both materials are frequently used as standard references to calibrate experimental setups for nonlinear characterization. To obtain more accurate n_2 values than those already published we combine Z-scan technique inside the $4f$ system with the Kerr shutter method in order to analyze precisely the spatio-temporal profile of the pump beam. The measured absolute values of n_2 are compared with those already reported in the literature and discussed in the light of dispersion theories for nonlinear refractive index. Finally we present linear and nonlinear optical characterization of new families of chalcogenide glasses (GeS_2-Sb_2S_3-CsI) and oxide glasses ($Pb(PO_3)_2$-WO_3). Chalcogenide glasses are inorganic glassy materials which always contains one or more of the chalcogen elements: S, Se or Te, but not O (in contrary to oxide glasses). Chalcogenides glasses are well-known for possessing a large linear and nonlinear refraction combined with infrared transparency. Hence they are promising candidates for optical elements. The oxide glasses including heavy metals are of interest due to a relatively small nonlinear absorption, especially in the infrared region. In connection with n_2 10 times higher than in the fused silica, the oxide glasses become potential candidates for optical communication purposes. The results obtained for both investigated families of glasses are compared and described in the context of all-optical switching applications. Moreover a theoretical model of n_2 introduced by Boling et al.[18] (the so called BGO model) is adopted in order to predict the nonlinear coefficient from the linear experimental data. It is very important to have theoretical expressions allowing to predict the magnitude of nonlinearities and hence facilitating the choice of glass compositions with the desired optical properties. As we will show in this thesis the simple BGO theory can provide very accurate predictions in both examined families of glasses.

Outline of the thesis

Chapter 1: Basic concepts of nonlinear optics

The thesis starts with a brief introduction to nonlinear optics. The basic concepts from linear and nonlinear light-matter interaction are presented. Particularly, the nonlinear refractive index (n_2) and nonlinear absorption coefficient (β) are defined and their fundamental properties are described.

Chapter 2: Measurements techniques

This chapter is a review of few experimental techniques developed to measure n_2 and β. Particularly, the degenerate four-wave mixing (DFWM), the Z-scan and the nonlinear imaging techniques (NIT) are described in details. The $4f$ coherent imaging system is presented.

Chapter 3: Sensitivity of nonlinear characterization techniques inside the 4f imaging system

The multi-wave mixing technique inside the $4f$ coherent imaging system is introduced. The comparison of optical sensitivities corresponding to different experiments combined inside the $4f$ setup, such as DFWM, Z-scan, EZ-scan, I-scan and nonlinear imaging technique with phase object (NIT-PO), is done. The conditions for optimization of the sensitivity with the pure nonlinear refractive signal are provided for each method and the influence of nonlinear absorption is discussed.

Chapter 4: Photo-induced effects in nonlinear optical characterization

In this part of the thesis the problem of photo-induced effects (PIE) in nonlinear optical characterization is discussed. Particularly, the difficulties encountered in the measurements of n_2 and β for photo-sensitive thin films using NIT-PO and Z-scan techniques are emphasized. Moreover new applications for Z-scan method are proposed. First, the Z-scan is introduced as a tool for characterization of permanent modifications in refraction and absorption induced by PIE. Second, the Z-scan technique is presented as method for linear optical characterization of transparent thin films. The possibility of determination of the thickness (or the linear refractive index) of sample with this method is demonstrated.

Chapter 5: Characterization of nonlinear materials

The last part of the thesis deals with linear and nonlinear optical characterization of bulk samples. The Z-scan absolute measurements of nonlinear refraction in carbon disulfide (CS_2) and fused silica (SiO_2) are reported. The absolute values of n_2 are compared with those commonly accepted. Moreover the nonlinear characterization of new families of chalcogenide glasses (GeS_2-Sb_2S_3-CsI) and oxide glasses ($Pb(PO_3)_2$-WO_3) is described in the context of all-optical switching applications. The BGO model is adopted to predict the nonlinearities in these investigated glasses.

Chapter 1

BASIC CONCEPTS OF NONLINEAR OPTICS

1.1 Introduction

Nonlinear optics is the study of optical effects that arise due to interaction of intense laser light and matter. A fundamental parameter in this light-matter interaction is the polarization of a material system. Generally there are two different approaches used to describe this quantity. The first one is based on the semi-classical theory in which the matter is supposed to be a system of atoms and molecules which can be described using quantum mechanics, whereas the light radiation is described as an electromagnetic wave using Maxwell's equations. The semi-classical theory generally gives a description for the macroscopic polarization without intriguing too deeply into the microscopic scale. Hence this approach is characterized by some limitations, nevertheless it can be adopted to explain the majority of nonlinear effects and phenomena. The second approach is based on the quantum electrodynamics which is more rigorous and convincing but it does not bring new physical insight in experiment using large laser intensities. Our studies are mainly concerned with macroscopic effects, and so the semi-classical description will be used in this thesis.

This chapter is devoted to some basic concepts of nonlinear optics in the frame of the semi-classical theory. First we will describe briefly the electromagnetic formulation of laser light. Then we will proceed to the most fundamental description of light-matter interaction. We will introduce such important terms like linear susceptibility, linear polarizability and the complex linear refractive index. Then we will extend all these definitions to nonlinear forms taking into account the intensity-dependent response of the material in presence of high-intensity laser light. Particularly, the third-order nonlinear refractive index (n_2) and the two-photon absorption coefficient (β) will be introduced. The physical origin along with the basic properties of nonlinear refraction and nonlinear absorption will be discussed. Finally theoretical models for prediction of n_2 values in optical solids will be reviewed.

1.2 Laser light in optics

Light is an electromagnetic wave which for majority of optical applications is described by its electric field. Most of the nonlinear optics experiments are performed with laser light, which is monochromatic, coherent and has a highly directional nature. Therefore it is commonly assumed that electric field propagates in one direction, generally taken as z-axis, and the general form of laser light is described by [2]†:

$$\widetilde{\mathbf{E}}\left(\mathbf{r},t\right)=\widehat{\mathbf{e}}E\left(\mathbf{r},t\right)\exp\left(i\left(kz-\omega t\right)\right)+c.c., \tag{1.1}$$

where $\mathbf{r}=(x,y,z)$ is the vector of Cartesian coordinates, ω is the angular frequency, $k=2\pi/\lambda$ is the wave number in vacuum with λ being the wavelength, t is the time and *c.c.* denotes the complex conjugation. The wave amplitude $E\left(\mathbf{r},t\right)$ can have a space- and time-dependence, which is slowly varying compared to the rapidly varying parts (space and time) of the oscillating wave. This amplitude is, in general, complex and includes the possibility of phase accumulation in addition to that contained in the exponent of Eq.(1.1). The unit vector $\widehat{\mathbf{e}}$ denotes the polarization of electric field. Generally for elliptically polarized light this vector has a complex form.

The large number of problems in optics can be described using plane waves, i.e. infinitively extended fields with a constant amplitude and phase in a plane transverse to the direction of propagation. However in the nonlinear optics a lot of phenomena can not always be explained using this approximation. Especially since real laser beams are finite and vary spatially along the transverse direction. In the theoretical formulation the transverse profile

---

†The tilde ($\tilde{}$) is used to denote a quantity rapidly varying with time. Constant and slowly varying quantities are written without the tilde.The bold font indicates vector and tensor quantities.

of laser light is often described by TEM$_{00}$ mode of circular Gaussian beam:

$$\widetilde{\mathbf{E}}\left(r,z,t\right)=\widehat{\mathbf{e}}E_0\left(z,t\right)\frac{w_0}{w\left(z\right)}\exp\left(-\frac{r^2}{w^2\left(z\right)}-\frac{ikr^2}{2R\left(z\right)}+i\tan^{-1}\left(\frac{z}{z_0}\right)\right)\exp\left[i\left(kz-\omega t\right)\right]+c.c.,\tag{1.2}$$

where $r=\sqrt{x^2+y^2}$ is the radial coordinate and $E_0\left(z,t\right)$ is the on-axis (for $r=0$) part of amplitude. The Gaussian beam symmetry is illustrated in Fig.1.1.

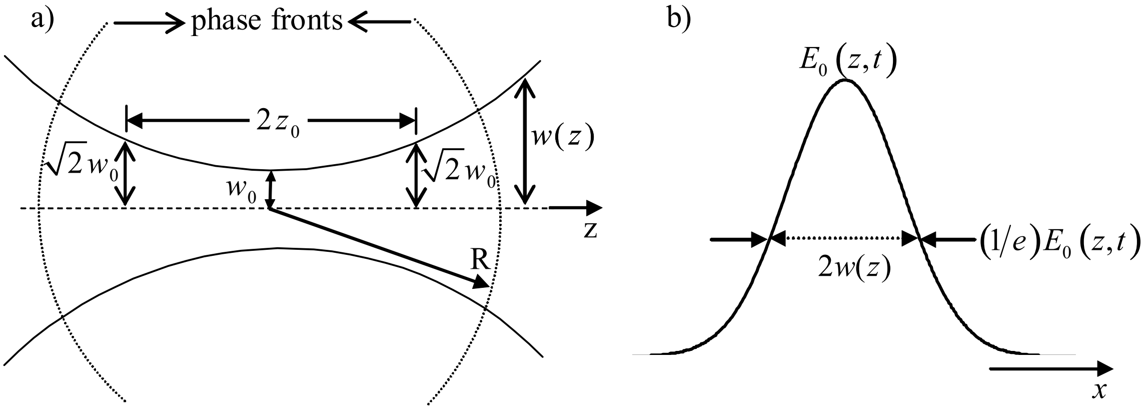

Figure 1.1: Schematic illustration of a TEM$_{00}$ Gaussian beam (a) beam propagation profile (b) beam cross section

The beam cross section is described by radius $w\left(z\right)$ which is defined as the half-width of the Gaussian curve at the point r , where the curve is at $1/e$ of its maximum value. The radius has a minimum, defined by w_0 (so called beam waist), at the plane $z=0$. Outside this plane the waist changes with z according to:

$$w\left(z\right)=w_0\sqrt{1+\frac{z^2}{z_0^2}},\tag{1.3}$$

where z_0 is a Rayleigh range which corresponds to the distance from $z=0$ at which the beam radius increases by a factor of $\sqrt{2}$. The Rayleigh range can be also defined as:

$$z_0=k\frac{w_0^2}{2}.\tag{1.4}$$

The range $|z|<z_0$ is often called as a *near field* of the Gaussian beam while $|z|>z_0$ is described as a *far field*. The radius of the curvature of the Gaussian wave-front is given by

$$R\left(z\right)=z\left(1+\frac{z_0^2}{z^2}\right), \tag{1.5}$$

In the *near field* region the phase has practically an infinite radius of curvature, and hence the Gaussian beam mimics a plane wave. The model of the Gaussian beam is very useful to treat problems in nonlinear optics. We will refer to this approach frequently throughout this thesis.

1.3 Linear optics

The theory of nonlinear optics is built on the well-understood theory of linear optics. Some concepts from linear description of light-matter interaction are brought directly to a nonlinear formulation. Therefore we will present here few useful linear optical relations, which will be generalized to nonlinear forms in next section.

1.3.1 Linear susceptibility

For the majority of situations considered in optics, and for every case treated in this thesis, it can be assumed that the material system is non-magnetic and electrically neutral. Under such assumptions the following wave equation describes the propagation of the light in the medium [3]:

$$\nabla^2\widetilde{\mathbf{E}}-\frac{1}{c^2}\frac{\partial^2}{\partial^2 t}\widetilde{\mathbf{E}}=\frac{1}{\epsilon_0 c^2}\frac{\partial^2}{\partial^2 t}\widetilde{\mathbf{P}}, \tag{1.6}$$

where c is the speed of light in vacuum and ϵ_0 is the vacuum permittivity. Here $\widetilde{\mathbf{P}}$ denotes the polarization vector which represents the response of the material due to the presence of electromagnetic wave. Generally this optical response is dependent on the field strength and in the first approximation $\widetilde{\mathbf{P}}$ is linearly related to $\widetilde{\mathbf{E}}$:

$$\widetilde{P}_i=\epsilon_0\sum_j\chi_{ij}^{(1)}\widetilde{E}_j, \tag{1.7}$$

where the indice i, j refer to the Cartesian components of the field and $\chi_{ij}^{(1)}$ are elements of the second-rank tensor of linear susceptibility. The susceptibility tensor describes linear optical properties of material system. The given relation is valid for lossless and dispersionless materials. In general, the polarization does not have to respond instantaneously to an applied field. This causes losses, which make $\boldsymbol{\chi}^{(1)}$ both complex and frequency-dependent.

1.3.2 Linear indices of refraction and absorption

In the linear optics the wave equation in Eq.(1.6) has homogeneous nature. To simplify the problem it is generally given in terms of the Fourier transform of the electric field, as a time-independent differential equation:

$$\nabla^2 \mathbf{E}(\mathbf{r}, \boldsymbol{\omega}) - \boldsymbol{\epsilon}_r \frac{\omega^2}{c^2} \mathbf{E}(\mathbf{r}, \boldsymbol{\omega}) = 0. \tag{1.8}$$

The latter relation is known also as a Helmholtz equation. Here $\epsilon_{r(ij)} = \delta_{ij} + \chi_{ij}^{(1)}$ is the linear dielectric tensor. For simplicity let us consider a model of plane wave in an isotropic medium where the linear susceptibility becomes a scalar quantity. The latter is ,in general, a complex function of frequency $\chi^{(1)}(\omega) = \chi_R^{(1)}(\omega) + i\chi_I^{(1)}(\omega)$. Therefore the dielectric constant is also complex, but when $\chi_I^{(1)} \ll \chi_R^{(1)}$ it can be written as:

$$\sqrt{\epsilon_r(\omega)} \approx n_0(\omega) + i\frac{c}{2\omega}\alpha(\omega). \tag{1.9}$$

The real part n_0 is the conventional refractive index while the imaginary part $\kappa = c\alpha/2\omega$ is known as extinction coefficient with α denoting the intensity absorption coefficient. The latter describes the attenuation of the electric field in the medium. These angular-frequency dependent components are often called as "optical constants" of the material. The linear refractive index is related to real part of linear susceptibility, while the absorption coefficient is given by the imaginary part:

$$n_0 = \sqrt{1 + \chi_R^{(1)}}, \tag{1.10}$$

$$\alpha = \frac{\omega}{n_0 c}\chi_I^{(1)}. \tag{1.11}$$

In these conditions the plane wave solution of wave equation describing the propagation of the light in isotropic medium in linear regime has the form:

$$\widetilde{\mathbf{E}}\left(z,t\right)=\widehat{\mathbf{e}}E\exp\left(-\frac{1}{2}\alpha z\right)\exp\left(i\left(k'z-\omega t\right)\right)+c.c., \tag{1.12}$$

where E is the amplitude of the wave at $z = 0$. The dispersive dependence of refractive index is included in the wave number $k' = kn_0\left(\omega\right) = n_0\left(\omega\right)2\pi/\lambda = n_0\left(\omega\right)\omega/c = \omega/v$. In the last term $v = c/n_0$ denotes the phase velocity of the wave. This gives a standard physical interpretation of n_0 as the factor by which the light speed in the vacuum must be devided in order to get the light speed inside the medium. It is necessary to mention that the concept of a unique phase velocity is meaningless for ultra-short (femto-second) pulses which are only quasi-monochromatic since they are composed of several frequencies clustered about some carrier frequency. When the frequency spread of the pulse is such that dispersion of the refractive index cannot be ignored, a concept of group velocity must be applied [2].

1.3.3 Linear electronic polarizability

From the microscopic point of view the electronic linear polarization is often considered as dipole moment per unit volume:

$$\widetilde{\mathbf{P}}_L = N\widetilde{\boldsymbol{\mu}}, \tag{1.13}$$

where N is the number density of components (atoms or molecules) and $\widetilde{\boldsymbol{\mu}}$ is the elementary dipole of material system. The dipole induced by a single atom or molecule is represented by:

$$\widetilde{\boldsymbol{\mu}} = \boldsymbol{\gamma}^{(1)}\widetilde{\mathbf{E}}_{loc}, \tag{1.14}$$

where $\widetilde{\mathbf{E}}_{loc}$ is the local electric field (at the atom, at the molecule), which is a superposition of the applied field $\widetilde{\mathbf{E}}$ and the net field due to surrounding dipoles, $\boldsymbol{\gamma}^{(1)}$ is the linear polarizability tensor. For gaseous media the average distance between neighboring components is relatively large and the interaction between them is negligible, so $\widetilde{\mathbf{E}}_{loc} \approx \widetilde{\mathbf{E}}$. However for liquid and solid media the interaction between neighboring components can not be ignored and some correction factor must be applied. An analytical expression for the local field can be obtained only for isotropic and cubic media using the so-called Lorentz model [3] where $\widetilde{\mathbf{E}}_{loc} = \left(n_0^2 + 2\right)\widetilde{\mathbf{E}}/3$. The latter implies the relation between linear susceptibility and polarizability:

$$\chi_{ij}^{(1)} = \epsilon_0^{-1}FN\gamma_{ij}^{(1)}, \tag{1.15}$$

where F is the Lorentz-Lorenz local field correction factor:

$$F = \frac{1}{3}\left(n_0^2 + 2\right). \tag{1.16}$$

1.3.4 Intensity of optical field

Physical photo-detectors cannot respond to the rapidly varying optical frequency, thus the quantity measured experimentally is always a time-averaged (over several optical cycles) field flux. The latter can be expressed using optical intensity (or irradiance) which is related to the amplitude of electric field:

$$I\left(\mathbf{r},t\right) = 2\epsilon_0 n_0 c \left|\mathbf{E}\left(\mathbf{r},t\right)\right|^2. \tag{1.17}$$

Using this quantity the attenuation described in Eq.(1.12) for a plane wave can be generalized to all kind of fields by Beer-Lambert law:

$$\frac{dI\left(\mathbf{r},t\right)}{dz} = -\alpha I\left(\mathbf{r},t\right). \tag{1.18}$$

This relation implies that in the linear approximation for a given propagation distance, the transmitted intensity is linearly related to the initial intensity.

1.4 Nonlinear optics

The linear dependence between polarization and electric field implies that the optical properties of matter as refraction or absorption are constant quantities which values are determined only by intrinsic features of material and optical frequency of incident field. Moreover no coupling between two different monochromatic components passing through a medium is predicted by linear theory. However, in the presence of high intensity irradiation provided by laser light, such approximations were found to be invalid. A large number of new light-matter interactions was observed including intensity-dependent refraction and absorption. Moreover it was found that the presence of one laser beam influences the behavior of the other one and vice versa, leading to the effects which are not predicted by the classical theory. All these phenomena are explained by assuming a nonlinear dependence between $\widetilde{\mathbf{P}}$ and

$\widetilde{\mathbf{E}}$. When the light intensity is sufficiently high a small additional polarization will appear, so that the total polarization can be written as:

$$\widetilde{\mathbf{P}} = \widetilde{\mathbf{P}}_{\mathbf{L}} + \widetilde{\mathbf{P}}_{\mathbf{NL}}, \tag{1.19}$$

where $\widetilde{\mathbf{P}}_{\mathbf{NL}}$ denotes the nonlinear part of polarization.

1.4.1 Nonlinear susceptibility

Using the definition of polarization provided in Eq. (1.19), the propagation of the light inside the nonlinear medium is described by:

$$\nabla^2\widetilde{\mathbf{E}} - \frac{1}{c^2}\frac{\partial^2}{\partial^2 t}\widetilde{\mathbf{E}} - \frac{1}{\epsilon_0 c^2}\frac{\partial^2}{\partial^2 t}\widetilde{\mathbf{P}}_{\mathbf{L}} = \frac{1}{\epsilon_0 c^2}\frac{\partial^2}{\partial^2 t}\widetilde{\mathbf{P}}_{\mathbf{NL}}. \tag{1.20}$$

This relation has the form of a driven (i.e. inhomogeneous) wave equation where the nonlinear response of the medium acts as a source term which appears on the right-hand side of this equation. Generally the nonlinear polarization is expressed as a power series in the electric field. For a lossless and dispersionless medium this dependence is usually written in a following form:

$$\widetilde{P}_i = \widetilde{P}_{L(i)} + \epsilon_0 \sum_{jk} \chi^{(2)}_{ijk} \widetilde{E}_j \widetilde{E}_k + \epsilon_0 \sum_{jkl} \chi^{(3)}_{ijkl} \widetilde{E}_j \widetilde{E}_k \widetilde{E}_l + \ldots = \widetilde{P}_{L(i)} + \widetilde{P}^{(2)}_i + \widetilde{P}^{(3)}_i + \ldots \,. \tag{1.21}$$

Here the indices i, j, k, l refer to the Cartesian components of the fields, $\chi^{(2)}_{ijk}$ and $\chi^{(3)}_{ijkl}$ are the third-rank and fourth-rank tensors of second-order and third-order nonlinear susceptibilities, respectively. Hence $\widetilde{\mathbf{P}}^{(2)}(\mathbf{r}, t) = \epsilon_0 \boldsymbol{\chi}^{(2)} : \widetilde{\mathbf{E}}^{(2)}(\mathbf{r}, t)$ is the second-order polarization, $\widetilde{\mathbf{P}}^{(3)}(\mathbf{r}, t) = \epsilon_0 \boldsymbol{\chi}^{(3)} \vdots \widetilde{\mathbf{E}}^3(\mathbf{r}, t)$ is the third-order polarization, and so on ... The latter quantities are responsible for nonlinear interactions. The most commonly found and well-described nonlinear phenomena are summarized in Tab.(1.1). These effects can have a resonant and non-resonant nature [4]. The interaction can either be a real transition of the atoms or molecules from one eigen state to another or a perturbation of the normal distribution or motion of internal electric charges. In resonant interactions the first kind is more predominant while for near-resonant or non-resonant interaction (where the optical frequency of interacting waves is far from the absorption frequency of the material), there will be no real transitions occurring. Moreover the occurrence of nonlinear interactions is also related to the symmetry of nonlinear medium. For example, the second order effects (and all higher with even order) are observed only in the noncentrosymmetric crystals that is, in crystals that do not display inversion symmetry. All the elements of $\boldsymbol{\chi}^{(2)}$ vanish in centrosymetric media as liquids, gases and amorphous solids. On the other hand $\boldsymbol{\chi}^{(3)}$ has always non-zero elements in all type of media. The detailed description of all these nonlinear interactions can be found in the literature devoted to nonlinear optics, e.g. [2][3][4].

Second-order effects ($\chi^{(2)}$)	Third-order effects ($\chi^{(3)}$)
Second harmonic generation	Third harmonic generation
Optical rectification	Optical Kerr effect
Optical parametric amplification	Self-focusing, self-phase modulation and self-trapping
Pockel's effect	Wave Mixing
Electro-optic beam deflection	Optical phase conjugation
	Stimulated Raman, Brillouin and Rayleigh scattering
	Optical continuum generation
	Two-photon absorption
	Saturable absorption

Table 1.1: The most popular second and third-order nonlinear effects

In general case of materials with loss and dispersion the nonlinear optical susceptibilities become complex quantities. Moreover if the electric vector of the optical field is composed of few discrete frequency components, then the total induced polarization vector is given by [2]:

$$\widetilde{\mathbf{P}}(\mathbf{r},t) = \sum_{m} \mathbf{P}\left(\omega_m\right) \exp\left(i\omega_m t\right), \tag{1.22}$$

where m denotes the number of frequencies involved (alike positive and negative). Here $\mathbf{P}\left(\omega_m\right) = \mathbf{P}\left(\mathbf{r},t\right) \exp\left(i\mathbf{k}_m\mathbf{r}\right)$ is the complex amplitude assigned to component with frequency ω_m. With this notation the nonlinear susceptibility becomes a proportionality factor relating the complex amplitude of the nonlinear polarization to the product of the complex electric field amplitudes ($\mathbf{E}(\omega_m) = \widehat{\mathbf{e}}E(\mathbf{r},t)\exp(i\mathbf{k}_m\mathbf{r})$). For example when three frequencies are present ω_1, ω_2 and ω_3, the third order susceptibility is given by

$$P_i^{(3)}(\omega_1+\omega_2+\omega_3) = \epsilon_0 D \sum_{jkl} \chi^{(3)}_{ijkl}(\omega_1+\omega_2+\omega_3, \omega_1, \omega_2, \omega_3) E_j(\omega_1) E_k(\omega_2) E_l(\omega_3), \quad (1.23)$$

where the degeneracy factor D represents the number of distinct permutations of applied frequencies:

$$D = \begin{cases} 1 & \text{all fields indistingusihable} \\ 3 & \text{two fields indistingusihable} \\ 6 & \text{all fields distingusihable} \end{cases} \quad (1.24)$$

This form of the third-order polarization allows for various combination of frequencies (alike positive and negative) helping to explain many observable third-oder nonlinear effects, particularly the coupling of different monochromatic waves leading to such phenomena as third-harmonic generation or wave-mixing.

1.4.2 Nonlinear index of refraction

Under the action of intense coherent light, the contribution of nonlinear polarization to refractive index can no longer be neglected. To introduce the phenomenon let us consider an isotropic medium ($\chi^{(2)} = 0$), where only the third-order effects are present and the linearly polarized (e.g. along x-axis) plane wave of frequency ω is propagating in z direction. Then the third order polarization is given by (see Eq.(1.23))

$$P^{(3)}(\omega) = 3\epsilon_0 \chi^{(3)}(\omega, \omega, \omega, -\omega) E(\omega) E(\omega) E^*(\omega), \quad (1.25)$$

where $E^*(\omega) = E(-\omega)$. For simplicity we are suppressing vector and tensor indices (e.g. here $\chi^{(3)} = \chi^{(3)}_{xxxx}$). Hence the total polarization of material system is described by (Eq.(1.7) + Eq.(1.23)):

$$P(\omega) = \epsilon_0 \chi_{eff} E(\omega), \quad (1.26)$$

where $\chi_{eff} = \chi^{(1)} + \chi^{(3)} |E(\omega)|^2$ is the effective susceptibility. Assuming that the nonlinear contribution to χ_{eff} is much smaller than the linear one, the general expression for a refractive index can be expressed as:

$$n = \sqrt{1 + \mathrm{Re}\left\{\chi_{eff}\right\}} \approx n_0 + \frac{3}{2n_0}\chi_R^{(3)} \left|E\left(\omega\right)\right|^2 . \tag{1.27}$$

Taking into account the time averaged intensity of optical field defined in Eq.(1.17), the nonlinear part of refraction will be described by:

$$\Delta n = n - n_0 = n_2 I, \tag{1.28}$$

where n_2 is the third order nonlinear refractive index (expressed in meter square per Watt (m^2/W) in SI units). This quantity is related to the real part of the third order susceptibility:

$$n_2 = \frac{3}{4n_0^2\epsilon_0 c}\chi_R^{(3)} . \tag{1.29}$$

From Eqs. (1.27) and (1.28) it is clearly seen that for weak incident beams, the refractive index of a medium remains constant (independent of the incident intensity) since the contribution of Δn is negligible. However, when the incident light is intense enough, the refractive index is no more constant but depends noticeably on the intensity of the incident optical wave. In the first approximation this dependence is linear. This is one of the basic phenomenon in nonlinear optics and it is a source for plenty of other optical effects. Particularly, the intensity-dependent changes in refraction induced by the high-intense laser beam cause modifications of temporal and spatial profiles of the beam itself. Consequently many new self-induced effects occur, as self-focusing, self-defocusing, self-phase modulation, optical phase conjugation, optical bistabilty, self-traping etc... (for more details see [2][3]). Similar expressions to Eq.(1.28) and Eq.(1.29) can be derived for higher order nonlinearities where refractive indices of fifth-order (n_4), seventh-order (n_6) and so on... can be considered. However experimentally it is, in general, difficult to observe phenomena related to these indices because intensities required to induce measurable effects are usually much higher than the damage threshold of materials. As the comparison of optical sensitivities of measurement techniques for the nonlinear refractive index, n_2, is one of the main subjects in this thesis, the theory of intensity dependent refractive index will be presented in greater details in the forthcoming sections.

1.4.3 Physical mechanisms of refractive index changes

Different physical mechanisms can contribute to the nonlinear polarization and consequently to intensity-dependent refractive index changes. All these mechanisms have their own characteristic response time and so their origin depends upon the duration of the applied field. It is important to know what mechanism is dominant under a given set of experimental conditions. The major contributions (which are within the frame of interest in this thesis) to the total nonlinear refractive index can be divided as follow[†]:

$$n_2 = n_2\,(electronic) + n_2\,(molecular\ \ reorientational) + n_2\,(electrostrictive) + n_2\,(thermal)\,. \tag{1.30}$$

The typical values of n_2 along with response times for these processes are given in Tab.(1.2).

Mechanism	n_2 (m^2/W)	$\chi^{(3)}$ (m^2/V^2)	Response time
Electronic polarization	10^{-20}	10^{-22}	10^{-15}
Molecular reorientation	10^{-18}	10^{-20}	10^{-12}
Electrostriction	10^{-18}	10^{-20}	10^{-9}
Thermal effects	10^{-10}	10^{-12}	10^{-9}

Table 1.2: Typical values of nonlinear refractive indices [2]

Non-resonant electronic contribution

Non-resonant electronic nonlinearities occur as the result of the nonlinear response of bound electrons to an applied optical field. This response is extremely fast (10^{-15}s) since it involves only virtual processes. Generally the electronic nonlinearity is not particularly large (typically $\sim 10^{-20}$m^2/W) in comparison to index changes induced by other physical mechanism, but electronic contribution is always present in all dielectric materials. Moreover it can be resonantly enhanced when the frequency of the incident field approaches to the resonance frequency of a material. However this improvement of nonlinear refraction is usually accompanied by (linear or nonlinear) absorption. The electronic cloud distortion is especially

---

[†] Other more specific physical mechanisms which can contribute to n_2 as photo-refraction, saturable atomic absorption or wide class of population redistribution effects (except the free-carrier absorption) are outside the area of interest in this thesis.

important in optical solids as glasses and crystals where the movement of molecules is substantially limited due to the strong internal interactions between them. It must be added that in such materials the electronic response can be often accompanied by nuclear motion which in some glasses can give a noticeable contribution (even 30%) to n_2 [5][6]. This kind of nonlinearity can be enhanced through the resonance Raman-transitions [4].

Microscopically, in the nonlinear regime the electronic polarization can be still considered as an electric dipole per unit volume, as in linear approximation (see section 1.3.3). Consequently, the microscopic nonlinear electronic polarizabilities can be defined. Following the notation of power series of the electric field, Eq.(1.14) (describing elementary dipole of atom or molecule) is generalized to the following form:

$$\widetilde{\boldsymbol{\mu}} = \boldsymbol{\gamma}^{(1)}\widetilde{\mathbf{E}}_{loc} + \boldsymbol{\gamma}^{(2)} : \widetilde{\mathbf{E}}^{2}_{loc} + \boldsymbol{\gamma}^{(3)} \vdots \widetilde{\mathbf{E}}^{3}_{loc} + ..., \tag{1.31}$$

where $\boldsymbol{\gamma}^{(2)}$ and $\boldsymbol{\gamma}^{(3)}$ are the first-order and second-order hyperpolarizabilities tensors, respectively. The detailed analysis of dispersive properties of these quantities is given in [3]. In the particular case of single monochromatic wave propagating inside isotropic medium (characterized by N, the density of its elementary electric dipoles), the relation between the third order nonlinear susceptibility and the corresponding electronic hyprepolarizability is given by:

$$\chi^{(3)}_{ijkl} = \epsilon_0^{-1} F^4 N \gamma^{(3)}_{ijkl}, \tag{1.32}$$

where F, the field correction factor for isotropic medium is defined in Eq.(1.16).

Generally, in the case of nonlinearities originating from different processes than electronic one (molecular reorientation or electrostriction) the macroscopic nonlinear polarization can be always considered as dipole moment per unit volume. However the electronic hyperpolarizability in Eq.(1.32) must be replaced by more complex expressions taking into account specifications of each process. The detailed discussion about microscopic description of nonlinear susceptibilities due to different physical origins can be found in [2][3][4]

Molecular reorientation

This mechanism is particularly important inside media composed of anisotropic molecules (i.e. characterized by anisotropic linear polarizability tensor). In the absence of external electric field the molecules are randomly distributed, therefore the medium is macroscopically isotropic. This situation can be found in several liquids (e.g., CS_2, benzene, toluene and other organic liquids) and in liquid crystals. When a strong electric field is applied to such a system, the induced dipole moments of the molecules experience a torque attempting to twist them in order to align with the applied field. As a result of such light induced-reorientation of molecules, the medium becomes partially anisotropic. In other words, there is an induced anisotropic refractive index change. This refractive index change can be expressed in terms of n_2 as long as the induced dipole–electric field interaction energy is small compared to the thermal energy, which is typically the case. The time period for such mechanisms is usually of the order of a few picoseconds ($10^{-12} - 10^{-13}$ s). The exact time depends on the size of molecules. Smaller molecules rotates faster. Molecular reorientation is often referred to as the optical Kerr effect or AC Kerr effect in analogy to classical Kerr phenomenon, where the anisotropy of the material is induced by DC electric field. The typical nonlinearities associated with small anisotropic molecular systems are $n_2 \sim 10^{-17} - 10^{-19}$ m^2/W [2].

Electrostrictive contribution

Electrostriction is a phenomenon that depends on the presence of an inhomogeneous intensity. This effect can occur, for example, in a case of the superposition of coherent waves forming an interference pattern of bright and dark fringes, or along the transverse direction of propagating Gaussian beam. Such an inhomogeneous field produces a force on the molecules or atoms comprising a medium. The force moves the dipoles into a region of higher intensity. This produces an increase in local density resulting in an increase of the local refractive index. In majority of materials the electristrictive contribution to n_2 is of the same order as the molecular reorientational contribution. However the response time of electrostriction is about three orders of magnitude slower.

Thermal contribution

Thermal processes can lead to large (and often unwanted) nonlinear optical effects. A fraction of the incident light energy can be always absorbed by an optical medium. The temperature of the illuminated portion of the material consequently increases leading to the changes in refraction of the medium. The modifications of index due to a temperature rise ΔT are usually expressed by:

$$\Delta n = \frac{dn}{dT}\Delta T, \tag{1.33}$$

where dn/dT is the thermooptic coefficient. In most liquids and solids this factor has a negative value leading to a negative change of refraction. The thermal effects are prominent in two cases: the first one when the pulse width is of nanosecond order or longer and second one when the medium is illuminated by a train of pulses whose spacing is shorter than the characteristic thermal-diffusion time $t_c = w^2/4D$, where w is the laser beam spot size and D is the thermal diffusion coefficient of the material [7][8]. The latter phenomenon is often referred as cumulative thermal effect and it occurs for a high repetition rate (typically > 10 kHz depending on the material) of laser pulses and for CW laser beam.

Free-carrier absorption

When the frequency of the incident radiation is near a resonant energy transition of material system, then real transitions are induced. Consequently, populations of excited states are redistributed and if their life-time is relatively long, the optical properties of medium can be modified. Such phenomenon is particularly important for semiconductor crystals and semiconductor-like glasses (characterized by relatively small energy gap), where an index change can occur due to a free-carrier absorption effect. In thermal equilibrium there is always a small amount of free carriers in the conduction band which can absorb electromagnetic radiation as they scatter from the lattice (i.e. they experience phonon assisted absorption to higher-lying states in the conduction band). Accompanying this free carrier absorption is a free carrier contrbution to the index of refraction. This contribution depends directly on the density of electronic gas. The latter can be modified through the band-band absorption producing an intensity dependent change in the refractive index: $\Delta n = \sigma_r N(I)$, where σ_r is the free-carrier dispersion coefficient while $N(I)$ is the intensity dependent free-carrier density [9][10]. When the free-carrier population in the conduction band is enhanced via one-photon absorption then Δn is linearly proportional to intensity ($N(I) \sim I$) and thus the effect mimics the third order nonlinear refractive index. However when there is a simultaneous absorption of two-photons (so called two-photon absorption, see paragraph 1.4.5) then $N(I) \sim I^2$ and consequently Δn behaves like fifth-order nonlinear refraction. The magnitude of the refractive index change due to free-carrier absorption is usually few orders of magnitude larger than the one originating from a pure non-resonant electronic response.

1.4.4 Dependency of n_2 on light polarization

In the paragraph 1.4.2 we described the nonlinear modification of the refractive index induced by a linearly polarized beam of frequency ω propagating inside isotropic medium. Here we will extend the problem to elliptically and circularly polarized light. The electric field $\mathbf{E}$ with any polarization can be always decomposed into a sum of left-hand ($\mathbf{E}_+$) and right-hand ($\mathbf{E}_-$) circular components: $\mathbf{E} = \widehat{\mathbf{e}}_+ E_+ + \widehat{\mathbf{e}}_- E_-$. Here $E_\pm$ are the complex amplitudes of circular components and unit vectors are $\widehat{\mathbf{e}}_\pm = (\widehat{\mathbf{e}}_x \pm i\widehat{\mathbf{e}}_y)/\sqrt{2}$. Furthermore, the third-order susceptibility is a fourth-rank tensor, and thus it is described by 81 separate elements. However in the isotropic media, due to the high degree of spatial symmetry, there are only 21 elements with a nonzero values and only 3 of them are independent [3]: $\chi^{(3)}_{xxyy}$, $\chi^{(3)}_{xyxy}$, and $\chi^{(3)}_{xyyx}$. All the other components of the tensor can be described as a combination of these three particular coefficients: $\chi^{(3)}_{ijkl} = \chi^{(3)}_{xxyy}\delta_{ij}\delta_{kl} + \chi^{(3)}_{xyxy}\delta_{ik}\delta_{jl} + \chi^{(3)}_{xyyx}\delta_{il}\delta_{jk}$, where $\delta_{mn} = 1$ for $m = n$ and zero otherwise. Moreover for the choice of frequencies given by $\chi^{(3)}_{ijkl}(\omega, \omega, \omega, -\omega)$ the condition of intrinsic permutation symmetry requires that $\chi^{(3)}_{xxyy}$ is equal to $\chi^{(3)}_{xyxy}$. Hence, there are only two independent elements of the susceptibility tensor describing nonlinear refraction (NLR) experienced by a single beam in isotropic medium. Consequently the third-order nonlinear polarization for isotropic media can be rewritten as [11]:

$$\mathbf{P}^{(3)} = \epsilon_0 A (\mathbf{E} \cdot \mathbf{E}^*) \mathbf{E} + \frac{1}{2} \epsilon_0 B (\mathbf{E} \cdot \mathbf{E}) \mathbf{E}^*, \tag{1.34}$$

where $A = 6\chi^{(3)}_{xxyy} = 3\chi^{(3)}_{xxyy} + 3\chi^{(3)}_{xyxy}$ and $B = 6\chi^{(3)}_{xyyx}$. The relative magnitude of these two coefficients depends on the nature of the physical process that produces the optical nonlinearity. For the most commonly found mechanism we have [3]:

- $A/B = 1$ for non-resonant electronic response

- $A/B = 6$ for molecular reorientation

- $A/B = 0$ for electrostriction

The nonlinear polarization of an isotropic medium given in Eq.(1.34) has two components. The first one produces a nonlinear polarization with the same handedness as $\mathbf{E}$, whereas the second term produces a nonlinear polarization with the opposite handedness (as $\mathbf{E}^*$). Consequently in the case of elliptically polarized light, as explained in Ref.[3], the left ($\mathbf{E}_+$) and the right hand ($\mathbf{E}_-$) circular components experience different refractive index change owing to these two independent parts of the nonlinear polarization. Hence the effective nonlinear refraction is dependent on the beam polarization state. The general expression for the effective nonlinear refractive index in isotropic medium is given by [12]:

$$n_2 = \frac{\left(1-q^2\right) n_{2circ} + 2qn_{2lin}}{\left(1+q^2\right)}, \tag{1.35}$$

where $n_{2circ} = A/4n_0^2\epsilon_0 c$ and $n_{2lin} = \left(A + 0.5B\right)/4n_0^2\epsilon_0 c$ are the NLR coefficients in the case of circular and linear polarizations, respectively. Note that n_{2lin} has been already defined in Eq.(1.29). Here $q = \left(1-\varsigma\right)/\left(1+\varsigma\right)$ where $\varsigma = ||E_+| - |E_-|/|\,||E_+| + |E_-||$ defines the ellipticity of polarization state. If $\varsigma = 0$ the light is polarized linearly while for $\varsigma = 1$ the light is characterized by a circular polarization. The linearly polarized laser beam experiences the largest nonlinear refractive index while the circularly polarized light the smallest one. In general the difference is given by $n_{2lin}/n_{2circ} = 1 + B/2A$:

$$\frac{n_{2lin}}{n_{2circ}} = \begin{cases} 3/2 & \text{for nonresonant electronic response} \\ 4 & \text{for molecular reorientation} \\ 0 & \text{for electrostriction} \end{cases} \tag{1.36}$$

1.4.5 Two photon absorption

Nonlinear absorption effects are resonant phenomena which refer to the change in the transmittance of a material as a function of the intensity. Among these class of effects we can generally distinguish [2][3] excited state absorption (including saturable absorption and free carrier absorption) or multi-photon absorption. The latter one is of particular importance because it often accompanies the the change of the refraction due to non-resonant electronic response. At sufficiently high intensities, the probability of a material absorbing more than one photon before relaxing to the ground state is greatly enhanced. Particularly the simultaneous transition of two photons is a very well-known and most frequently observed phenomenon. The basic theory of two-photon absorption (TPA) was formulated by Göppert-Mayer [13] as early as in 1931 and its first experimental conformation was done by Kaiser and Garrett in 1961 [14]. In general case, two situations are possible. In the first one, two photons from the same optical field of frequency ω are absorbed to make the resonant transition at 2ω. In the second situation, two optical fields at frequencies ω and ω' are present, and one photon from each field is absorbed making an overall transition approximately at $\omega + \omega'$. In this work we are interested in the first case. In this single beam (degenerate) situation the nonlinear absorption is proportional to the square of the intensity. Therefore the linear Beer-Lambert law (Eq.(1.18) describing the optical loss), must be generalized to:

$$\frac{dI}{dz} = -\alpha I - \beta I^2, \tag{1.37}$$

where β is the TPA coefficient (expressed usually in centimeter per GigaWatt (cm/GW) in SI units). This quantity is directly related to the imaginary part of the third order susceptibility:

$$\beta = \frac{3\pi}{n_0^2 \epsilon_0 c \lambda} \chi_I^{(3)}. \tag{1.38}$$

The nonlinear absorption coefficient of a material can be characterized through simple transmission measurements: detecting intensity outgoing from the medium as a function of input irradiance. The quantitative description of this experiment is provided by the exact solution of Eq.(1.37). The latter, taking into account the Fresnel reflection at the interface of the material with air, has a form:

$$I_{out}(r, L, t) = \frac{I(r,0,t)\,(1-R)^2 \exp(-\alpha L)}{1 + \beta I(r,0,t)\,(1-R)\,L_{eff}}, \tag{1.39}$$

where R is the Fresnel reflection coefficient , $I(r,z=0,t)$ is the intensity at the entry of the material and $L_{eff} = (1 - \exp(-\alpha L))/\alpha$ is the effective length with L denoting the physical thickness. However the physical quantity which is usually measured is not exactly the intensity but rather the optical energy. In order to obtain an expression for the energy transmittance, Eq.(1.39) must be integrated spatially and temporally. The exact solutions for CW and pulse laser beams of different intensity profiles are given in Ref.[2].

1.5 Theoretical models for n_2

Nonlinear materials exhibiting large nonlinear refraction have attracted a special attention due to the broad range of possible applications in which they can be found. Optical switching, optical limiting, optical logic gates, optical communications, active elements of high-power lasers, etc. [2][3] are just few particular examples of possible usefulness of nonlinear refraction. Each of these applications requires materials with specific n_2 values in order to optimize an operation of particular devices at some given experimental parameters. Therefore it becomes considerably important to theoretically predict the nonlinear refractive index and to obtain expressions for calculation of n_2 that are convenient for practical application. Particularly it is desirable to predict n_2 from macroscopic parameters of the medium such as the linear refractive index, the bandgap, etc. However generally it is a difficult task to find one universal expression due to the complexity of the problem. The nonlinear refractive index is in fact the third-order susceptibility. Moreover even if the issue is limited to a scalar formalism which is appropriate for linearly polarized light in an isotropic medium (mainly considered in this section) there is still a problem with estimation of local electric fields. Nevertheless several semi-empirical models for n_2 of pure non-resonant electronic origin have been developed providing sufficiently good predictions for specified classes of materials.

1.5.1 Miller's rule and Wang's rule

At the most fundamental level, electrons under light illumination can be considered as an assembly of forced harmonic oscillators and the nonlinear optical response of this system can be related to the deviation of the electronic displacement from harmonic behavior [3]. The classical anharmonic oscillator model was used by Miller [15] in 1961 in order to derive a relation between the second-order nonlinear and linear susceptibilities. He obtained a result $\chi^{(2)} \sim \left(\chi^{(1)}\right)^3$ which has been well validated for a large variety of the second-order nonlinear materials. Later, Wynne (1969) generalized Miller's rule to the third order nonlinear effects [16]: $\chi^{(3)}(\omega_4) = A\chi^{(1)}(\omega_4)\,\chi^{(1)}(\omega_1)\,\chi^{(1)}(\omega_2)\,\chi^{(1)}(\omega_3)$, where $\omega_4 = \omega_1 + \omega_2 + \omega_3$ and A is a constant which is frequency independent and nearly the same for all materials. Wynne has shown [16] that the generalization of Miller's rule is valid for certain optical materials, such as ionic crystals, however, this generalization is not universal.

Wang (1970) has proposed [17] different relationship which seems to be more generally valid than the Miller's rule. Wang's rule states that, in the quasi-static limit ($\omega \to 0$, i.e. for a range of frequencies which are low compared to electronic absorption frequencies but still high compared to the vibrational frequencies) the third order susceptibility should verify [3][17]. :

$$\chi^{(3)} = Q\left(\chi^{(1)}\right)^2, \tag{1.40}$$

where $Q = g/Ns\hbar\omega_0$ is the parameter related to the material properties described in the frame of the harmonic oscilator model. Accordingly, g is the dimensionless anharmocity parameter, N is the molecular density, s is the oscillator strength, ω_0 is the mean oscillator resonance frequency and $\hbar$ denotes the Planck constant. Wang has shown empirically that the predictions of Eq.(1.40) are accurate both for low-pressure gases (where Miller's rule does not make accurate predictions) and for ionic crystals (where Miller's rule does make accurate predictions) when take into account the local field correction factor defined in Eq.(1.16).

1.5.2 BGO model

The Wang's rule was exploited by Boling, Glass and Owyoung (1978) (BGO) who have derived a simple empirical relationship [18] that allows one to predict nonlinear refractive index of transparent optical glasses from the measurements of linear optical properties. The result of the BGO model can be derived assuming that the linear refractive index of a material is described by the Lorentz-Lorenz law (see Eq.(1.15)) and the Lorentz oscillator model (for more details about this model see Ref.[3]):

$$n_0^2 - 1 = F\epsilon_0^{-1}\sum_i N_i\gamma_i^{(1)}, \tag{1.41}$$

where the summation over i is to include all species that constitute the material, F is a local field corrector factor defined in Eq.(1.16) and $\gamma_i^{(1)}$ is the linear polarizability given by the Lorentz oscillator [3]:

$$\gamma_i^{(1)} = \frac{s_i e_c^2/m_e}{\omega_{0i}^2 - \omega^2}, \tag{1.42}$$

where e_c is the elementary charge, and m_e is the electron mass. The relation in Eq.(1.41) is also known as the Clausius-Mossotti equation. The nonlinear analog of the latter relating n_2 with second-order hyperpolarizability (see Eq.(1.29) and Eq.(1.32)) is given by [3]:

$$n_2 = \frac{3}{4n_0^2\epsilon_0^2 c} F^4 \sum_i N_i \gamma_i^{(3)}. \tag{1.43}$$

The microscopic Wang's formula relating $\gamma_i^{(1)}$ and $\gamma_i^{(3)}$ has a form [3]:

$$\gamma_i^{(3)} = \frac{g}{\hbar\omega_0}\left(\gamma_i^{(1)}\right)^2. \tag{1.44}$$

The BGO model assumes that the resonant transition of only one constituent dominates in the sums in Eq.(1.41) and Eq.(1.43). Consequently, when Eq.(1.41) is solved for $\gamma^{(1)}$ which is then introduced into Eq.(1.44) and the latter into Eq.(1.43) we find that the expression for n_2 is given by:

$$n_2\left(m^2/W\right) = \frac{gs\left(n_0^2+2\right)^2\left(n_0^2-1\right)^2}{12n_0^2 c\hbar\omega_0\left(Ns\right)}. \tag{1.45}$$

Moreover the combination of Eq.(1.41) and Eq.(1.42) provides the dispersion model for the linear refractive index:

$$\frac{1}{3}\frac{\left(n_0^2+2\right)}{\left(n_0^2-1\right)} = \frac{\omega_0^2-\omega^2}{\left(e_c^2/m_e\epsilon_0\right)\left(Ns\right)}. \tag{1.46}$$

The latter relation allows to determine two unknown parameters, Ns and ω_0, from any two values of $n_0(\omega)$. Furthermore Boling et al. suggested that the ambiguous parameter g should take a value around unity independently from the material. However it is pointed out in [3] that there does not seem to be any simple physical argument for why the quantity g should be the same for all materials. Nevertheless the authors of [18] found empirically that parameter gs appearing in Eq.(1.45) is between 3 and 4.5 for most glasses. It must be emphasized that the use of the Lorentz-Lorenz local field correction factor in BGO formulas is rigorously applicable only in the case of cubic or isotropic arrays of isolated ions. It is expected that for materials with extended polarizable bonds, the BGO model is less accurate.

1.5.3 K-K model

Sheik-Bahae et al. [19][20] provided a model for the nonlinear refractive index in semiconductors and insulators where the energy band structure is well-defined. The model was derived for the transparency region where photon energy ($\hbar\omega$) is below the energy gap of material (ε_g). Therefore there is no linear absorption and the loss can be induced only by two-photon resonant transitions. Authors used a two-band model to calculate the nonlinear absorption coefficient[21]:

$$\beta\left(cm/GW\right) = \frac{K\sqrt{\varepsilon_p}}{n_0^2\varepsilon_g^3}F_2\left(2\hbar\omega/\varepsilon_g\right), \tag{1.47}$$

where $\varepsilon_p = 21\ eV$, K can be considered to be a single free parameter whose value must be found empirically. The authors found K to be $3.1 \times 10^3\ cm/GW\ eV^{5/2}$ in wide-variety of semiconductors. Here F_2 is the universal function:

$$F_2\left(2x\right) = \frac{\left(2x-1\right)^{3/2}}{\left(2x\right)^5}\ \text{for}\ 2x > 1, \tag{1.48}$$

and $F_2\left(2x\right) = 0$ otherwise. They derived the corresponding nonlinear refractive index using a nonlinear Kramers–Kronig transformation (K-K model)[22]:

$$n_2\left(cm^2/W\right) = \frac{K\hbar c\sqrt{\varepsilon_p}}{2n_0^2\varepsilon_g^4}G_2\left(\hbar\omega/\varepsilon_g\right), \tag{1.49}$$

where the universal function G_2 is given by

$$G_2\left(x\right) = \frac{-2+6x-3x^2-x^3-\frac{3}{4}x^4-\frac{3}{4}x^5+2\left(1-2x\right)^{3/2}\Theta\left(1-2x\right)}{64x^6}, \tag{1.50}$$

with $\Theta\left(y\right)$ denoting a Heaviside step function. The functional forms of F_2 and G_2 are shown in Fig.1.2. It is clearly seen that the process of two-photon absorption vanishes for $\hbar\omega < 0.5\varepsilon_g$. Moreover the nonlinear refractive index becomes negative for $\hbar\omega > 0.69\varepsilon_g$ when photon energy approaches resonance energy. The K-K model predicts especially a good scaling in a wealth of different materials $n_2 \sim \varepsilon_g^{-4}$. Thus narrow-band-gap semiconductors are expected to produce a much larger nonlinear response than large-band-gap semiconductors. Generally, the K-K model works quite well for different classes of semi-conductive crystals. However, it does not provide good predictions for wide-band gap dielectrics [23], as oxide or fluoride glasses, where the densities of states in valance and conduction bands are quite complicated and so the simple two-band model is not sufficiently accurate.

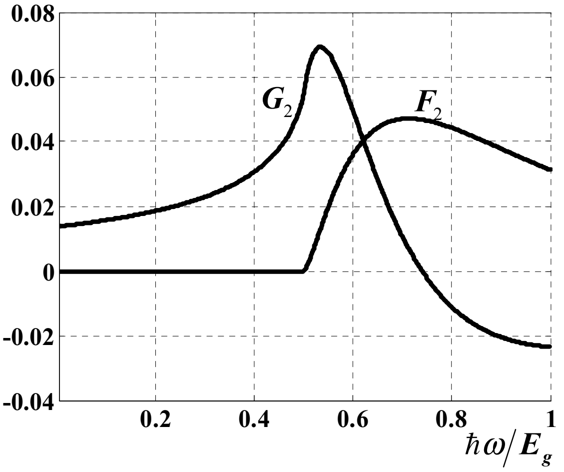

Figure 1.2: Variations of the nonlinear refractive index and two-photon absorption coefficient with photon energy according to K-K model

1.5.4 PERT model

Adair et al. [24] used a perturbation theory in order to derive an expression describing the dispersion of the nonlinear refractive index (so-called PERT model) in a wide-band gap dielectrics. Similarly to BGO theory, the PERT model assume a normal dispersions of n_0 and n_2 which are governed by a single resonance at frequency ω_0. The relation for nonlinear refractive index is given by:

$$\frac{n_2(\omega)}{n_2(0)} = \frac{n_0(0)}{n_0(\omega)} \left[\frac{n_0^2(\omega)+2}{n_0^2(0)+2}\right]^4 \frac{1}{1-x^2} \left\{\frac{1-x^2}{1-4x^2} + \frac{1}{2K'}\left[\frac{1-x^2}{1-4x^2} - \frac{1-x^2/3}{1-x^2}\right]\right\}, \quad (1.51)$$

where $x = \omega/\omega_0$ and K' is the Kurtosis of electronic distribution which value is generally around 0.5 for wide-band gap dielectrics. Here $n_0(0)$ and $n_2(0)$ are the linear and nonlinear refractive indices for frequencies much lower when compared to the resonance frequency (i.e. for the range of frequencies where the dispersion is practically negligible).

1.5.5 Other models

The BGO model has been derived assuming that the dispersion of the linear refractive index is described by Clausius-Mossotti relation (Eq.(1.41)). However frequently n_0 is expressed by an alternative model of Sellmeier: $n_0^2 - 1 = \sum_i A_i\lambda^2/\left(\lambda^2 - \lambda_i^2\right)$, where λ_i^2 are the multiple absorption wavelengths corresponding to the eigenvalues of the oscillator frequencies and A_i are the Sellmeier coefficients. For a dominant single resonance in the system the Sellmeier expression is often presented in a form proposed by Wemple and DiDomenico [25][26]:

$$n_0^2 - 1 = \frac{\varepsilon_d \varepsilon_0}{\varepsilon_0^2 - (\hbar\omega)^2}, \tag{1.52}$$

where ε_0 is the energy of single effective oscillator and ε_d is the dispersion energy (both expressed in eV). These two quantities can be obtained by plotting $(n_0^2 - 1)$ against $(\hbar\omega)^2$. Petkov and Ewen [27] modified the BGO formula taking into account the dispersion model proposed in Eq.(1.52):

$$n_2\left(m^2/W\right) = \frac{\sqrt{3}\,(gs)\left(n_0^2+2\right)^{3/2}\left(n_0^2-1\right)^2 e_c^2\hbar^2}{12 n_0^2 c \epsilon_0 \varepsilon_d \varepsilon_0^2}. \tag{1.53}$$

Another model similar to the BGO was derived by Lines [28] using a two-level bond orbital approximation:

$$n_2\left(m^2/W\right) = 1.7\frac{\left(n_0^2+2\right)^3\left(n_0^2-1\right)d^2}{n_0^2\varepsilon_0^2} \times 10^{-19}, \tag{1.54}$$

where d is nearest-neighbor bond length expressed in nm and ε_0 is in eV. The Sellmeier energy ε_0 is extracted from the refractive index dispersion, but the choice of bond length in inhomogeneous systems like glasses is somewhat arbitrary. Later Lenz et al.[29] combined Eq.(1.54) with the K-K model in order to describe n_2 in particular cases of several chalcogenide glasses:

$$n_2\left(m^2/W\right) = 1.7\frac{\left(n_0^2+2\right)^3\left(n_0^2-1\right)d^2}{n_0^2\varepsilon_0^2} G_2\left(\hbar\omega/\varepsilon_g\right) \times 10^{-17}, \tag{1.55}$$

where d is in nm, ε_0 in eV and G_2 is the universal function defined in Eq.(1.50).

More recently another model based on harmonic oscillator was introduced [30] in order to take into account the general trend in the nonlinear refraction for wide variety of amorphous glasses. It is often observed experimentally that n_2 of these materials is strongly dependent on the normalized band-gap $(\hbar\omega/\varepsilon_g)$ and in contrary to semiconductors it is increasing when

$\hbar\omega/\varepsilon_g \to 1$. It is shown in [30] that nonlinear refractive index in a large variety of amorphous glasses can scale as:

$$n_2 \sim \left\{\frac{1}{\varepsilon_g^6}\right\} \left\{1 - \left(\frac{\hbar\omega}{\varepsilon_g}\right)^2\right\}^{-4}. \tag{1.56}$$

The excellent fit of this relation to the experimental data was obtained over three orders of magnitude range of nonlinearity values for different oxide and chalcogenide glasses.

1.6 Conclusions

In summary, we reviewed some of the most fundamental aspects of nonlinear optics that will be used in our study. The comparison between linear and nonlinear light-matter interactions was done. In conventional optics, the linear refractive index (n_0) and absorption coefficient (α) are related to the real and imaginary part of the linear susceptibility ($\chi^{(1)}$) of material, respectively. Their values are determined only by intrinsic dispersive properties of the medium and they are independent of the input power of incident light. However in the nonlinear regime, in presence of high intensity laser light, both refraction and absorption are dependent on the irradiance of optical field. In the first approximation the induced changes in optical coefficients are linearly proportional to the incident intensity. In such situation a nonlinear part of refraction is described by n_2, the nonlinear refractive index related to the real part of $\chi^{(3)}$, the third-order susceptibility. The nonlinear absorption is given by β, the nonlinear absorption coefficient defined via the imaginary part of $\chi^{(3)}$. Several physical mechanisms giving rise to nonlinear refraction were reviewed. Moreover it was shown that n_2 depends on light polarization due to the tensor nature of nonlinear susceptibility. Some theoretical models for predictions of n_2 on the basis of linear parameters of isotropic optical solids were also analyzed. The intensity dependent losses were introduced by describing the most frequently observed phenomenon of two-photon absorption.

In the next chapter we will describe the various experimental methods used for characterizing the nonlinear refractive index, n_2, and the nonlinear absorption coefficient, β. Physical foundation of each experimental technique will be introduced. We will discuss the comparison between differents methods and the corresponding advantages as well as limitations.

Chapter 2

MEASUREMENTS TECHNIQUES

2.1 Introduction

This chapter is dedicated to present some of the commonly used measurement methods for nonlinear refractive index (n_2) and the nonlinear absorption coefficient (β). There exist plenty of different nonlinear characterization techniques exploiting various nonlinear optical phenomena. Considering the origin of the phenomena we can distinguish the following groups of experimental methods: **(i)** polarization rotation techniques, **(ii)** wave-mixing techniques, **(iii)** beam distortion techniques and **(iv)** nonlinear interferometry techniques. In this chapter we will focus our attention to few particular techniques which will be more or less related to our studies. In this context we will describe briefly the Kerr gating experiment and additionally the related ellipse rotation technique. More extended description will be devoted to wave-mixing methods, particularly to the backward and the forward configuration of degenerate four wave-mixing (DFWM). Finally in the greatest details we will discuss about Z-scan techniques and Nonlinear Imaging Techniques (NIT). Both will be the most heavily employed in our experimental researches. The physical foundation for each technique will be introduced and the methodology used in each experiment will be highlighted. Advantages as well as disadvantages of each technique will be brought out.

2.2 Ellipse rotation and Kerr gate

The earliest characterization techniques were based on optically induced birefringence in third order isotropic media (e.g. [11][31][32][33][34][35]). The nonlinearly induced birefringence affects the polarization properties of optical waves propagating through the medium. In these methods the light of a known polarization state is transmitted through the nonlinear material and the outgoing intensity is measured through an output polarizer. Generally two different experiments are performed: i) ellipse rotation and ii) optical Kerr gate. Since both techniques are based on the polarization effects it is more convenient to describe them in the terms of third-order susceptibility components than in the terms of n_2.

2.2.1 Ellipse rotation

Ellipse rotation is a single-beam experiment performed with an elliptically polarized wave. The general scheme of this method is shown in Fig.2.1. Consider a beam with an arbitrary elliptical polarization incident on a nonlinear medium inducing a birefringence. The latter is occurring in the material due to the fact that left-hand (E_+) and right-hand (E_-) circular components of elliptically polarized beams experience different refractive index changes (as explained in section 1.4.4). In the case of isotropic medium these circular refractive indices are given as [36]:

$$n_\pm \simeq n_0 + \frac{1}{2n_0}\left[A\left|E_\pm\right|^2 + (A+B)\left|E_\mp\right|^2\right], \tag{2.1}$$

where $A = 6\chi^{(3)}_{xxyy}$ and $B = 6\chi^{(3)}_{xyyx}$. Therefore the induced anisotropy is given by:

$$\delta n = n_+ - n_- = \frac{B}{2n_0}\left[\left|E_-\right|^2 - \left|E_+\right|^2\right]. \tag{2.2}$$

Since the left- and right-hand circular components propagate with different phase velocities, the polarization ellipse of the light rotates by angle $\Theta = \delta n\,(\pi z/\lambda)$ as the beam propagates through the nonlinear medium. This phenomenon is similar to the effect occurring in the linear optics inside optically active materials. Note that the rotation is measurable only for elliptically polarized light. In the case of linear polarization $\delta n \simeq 0$ because $|E_-| = |E_+|$, while for circular polarization only one component (left- or right-handed) is present. The output intensity variations due to the nonlinear rotation are verified through the linear analyzer.

Experimentally the elliptical polarization of incident beam is usually obtained from a linearly polarized light passing through the quarter-wave plate. If the direction of the linear polarization makes an angle θ with respect to the fast axis of the wave plate and the nonlinear rotation angle Θ is small, the intensity transmittance through the final polarizer can be written as [2]:

$$T_I \simeq \left(\frac{2\pi}{\lambda} L \frac{3}{4n_0^2 \epsilon_0 c} \left|\chi_{xyyx}^{(3)}\right| I \sin(2\theta) \right)^2 , \tag{2.3}$$

where L is the material thickness, I is the input intensity (before the quarter-wave plate). Note that the term $3\left|\chi_{xyyx}^{(3)}\right| / 4n_0^2 \epsilon_0 c$ can be considered as the nonlinear refractive index.

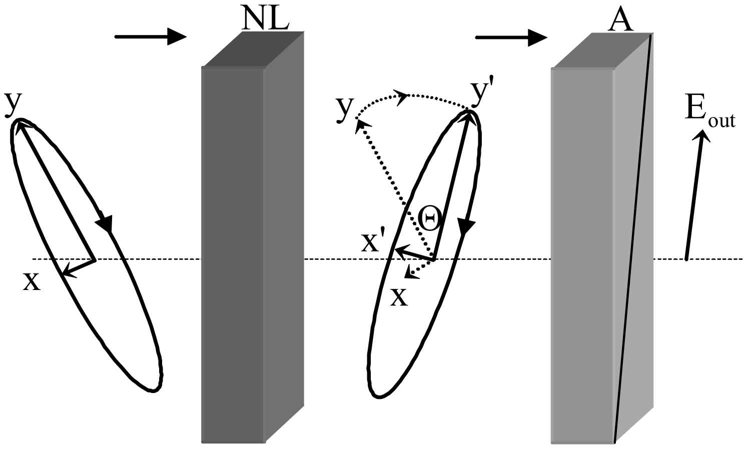

Figure 2.1: The ellipse rotation experiment. The labels refer to: (x, y) - major and minor axes of polarization ellipse of incident electric field, ($x\prime, y\prime$) - major and minor axes of polarization ellipse of the transmitted electric field, Θ - angle of rotation, E_{out} - output electric field, NL - nonlinear medium and A – analyzer.

In a typical experiment, it is the pulse energy and not the intensity that is measured. The energy transmittance has a form:

$$T_\varepsilon \propto C\varepsilon^2, \tag{2.4}$$

where $C = \left(3\pi L \left|\chi_{xyyx}^{(3)}\right| \sin(2\theta) / 2n_0^2 \epsilon_0 c\lambda\right)^2$ and ε is the input energy. Thus the transmittance can be measured as a function of the incident energy, and a fit to experimental data permits to determine C to within a proportionality constant. The comparison with a result obtained for a reference material allows determining the investigated nonlinearity.

2.2.2 Kerr gate

Kerr gate is a pump-probe experiment where the high-intense pump beam is used to induce anisotropy inside the nonlinear medium in order to change a polarization state of weak probe light. The scheme of this technique is shown in Fig.2.2. The nonlinear medium is placed between two crossed polarizers so that in absence of the pump beam the linearly polarized probe light can not pass through the system. Such a setup is often referred as an optical Kerr cell. In presence of a strong pump beam an anisotropic refractive-index is induced. For spatially and temporally overlapping two beams (Pump and Probe) a phase difference is 'written' by the pump and 'read' by the probe. Consequently the polarization plane of the probe beam is changed and a small fraction of light is detected after the analyzer. The expression for the intensity outgoing from the Kerr cell is given analytically by [37][38][39]: $I_{Kerr} = I_{probe} \sin^2(2\theta) \sin^2(\Delta\Phi/2)$, where I_{probe} is the intensity of the incident probe beam, θ is an angle between the polarization planes of the probe and the pump beams and $\Delta\Phi$ is the induced nonlinear phase retardation between the two orthogonal probe components.

Generally, the Kerr gate experiment is performed in such way that the pump and a probe beam propagate in nearly collinear direction (with very small angle between them) and their polarization planes are at $\theta = 45°$ with respect to each other in order to increase the generated signal. In this case the induced birefringence inside the isotropic medium is described by [36]

$$\delta n = n_{\parallel} - n_{\perp} = \frac{3}{n_0}\left(\chi^{(3)}_{xyyx} + \chi^{(3)}_{xyxy}\right)\left|E_{pump}\right|^2, \tag{2.5}$$

where $n_{\parallel}$ and $n_{\perp}$ are the effective refraction indices experienced by the parallel and the perpendicular components of the probe light with respect to the polarization plane of the pump beam. Here E_{pump} is the amplitude of the pump electric field. The relative phase difference between the two orthogonal components of the weak field at the exit face of the sample is expressed as

$$\Delta\Phi = \frac{2\pi}{\lambda_{probe}} L \frac{3}{2n_0^2\epsilon_0 c}\left(\chi^{(3)}_{xyyx} + \chi^{(3)}_{xyxy}\right) I_{pump}. \tag{2.6}$$

Note that the term $3\left(\chi^{(3)}_{xyyx} + \chi^{(3)}_{xyxy}\right)/2n_0^2\epsilon_0 c$ plays here the role of the nonlinear refraction.

Usually an induced phase shift is small so that the intensity transmittance of the Kerr cell can be approximated to:

$$T_I = \frac{I_{Kerr}}{I_{probe}} \simeq \left(\frac{\Delta\Phi}{2}\right)^2 . \tag{2.7}$$

Similarly as in the ellipse rotation experiment, the quantity which is typically measured is the energy transmittance [2]: $T_\varepsilon \propto C\varepsilon^2$ with $C = \left(3\pi L \left|\chi^{(3)}_{xyyx} + \chi^{(3)}_{xyxy}\right| / 2n_0^2\epsilon_0 c\lambda_{probe}\right)^2$. Thus the measurements of the probe energy as a function of the the pump energy provide information about the proportionality factor C and the comparison of the latter with a reference material allows determining the investigated nonlinearity.

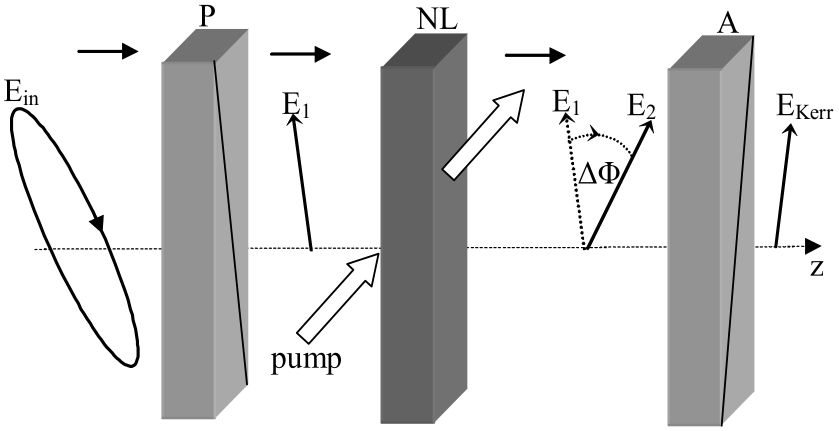

Figure 2.2: The Kerr Gate experiment. The labels refer to: E_{in} - the input electric filed of probe beam with arbitrary polarization, E_1- the incident linearly polarized electric field, E_2 - the nonlinearly rotated electric field, $\Delta\Phi$ - the angle of rotation, E_{Kerr} - the output electric field, NL - the nonlinear medium, P - polarizer and A - analyzer.

The Kerr gate configuration shown in Fig. 2.2 has found a number of additional applications as step-motion photography of laser pulses or measurements of ultra short X-rays pulses emitted by plasma etc. More details can be found in [40]. Especially the Kerr cell is used to study temporal dynamics of nonlinear processes [41] or to investigate pulse duration of laser light as a third-order autocorrelation technique [42]. Such possibilities are provided by time resolved measurements when Kerr signal is measured as a function of the delay time between the probe and the pump beams.

In summary, both the ellipse rotation and the Kerr gate allow together determining two of three independent elements of $\boldsymbol{\chi}^{(3)}$ in isotropic medium, namely $\chi^{(3)}_{xyyx}$ and $\chi^{(3)}_{xyxy}$. Moreover, when the nonlinearity is only due to a pure non-resonance electronic response then $\chi^{(3)}_{xyyx} = \chi^{(3)}_{xyxy} = \chi^{(3)}_{xxxx}/3$, so that the results of both experiments can be also expressed in the terms of $\chi^{(3)}_{xxxx}$. One drawback is that these techniques generally yield only the modulus of the third order susceptibility components. Nevertheless a method was developed in [43] showing that a separate measurements of the real and the imaginary parts of $\chi^{(3)}$ are possible using a modified Kerr cell (the so-called heterodyne Kerr gate technique).

2.3 Wave-Mixing techniques

Frequency mixing represents one of the most general and the most important phenomenon in nonlinear optics. In this process, two or more waves interact in a nonlinear medium to produce output waves at various frequencies. For nonlinear characterization purposes the degenerate four wave mixing (DFWM) process (see for example [44][45][46][47][48][49][50][51][52]) is one of the most heavily employed. This process is degenerate because all the beams are characterized by the same optical frequency. Fig.2.3 shows two the most popular geometrical configurations of DFWM. The first one is, the so-called backward geometry since two of the waves travel in the backward direction and two others travel in the forward direction. The second configuration is named as a forward geometry because all four waves travel in the same direction.

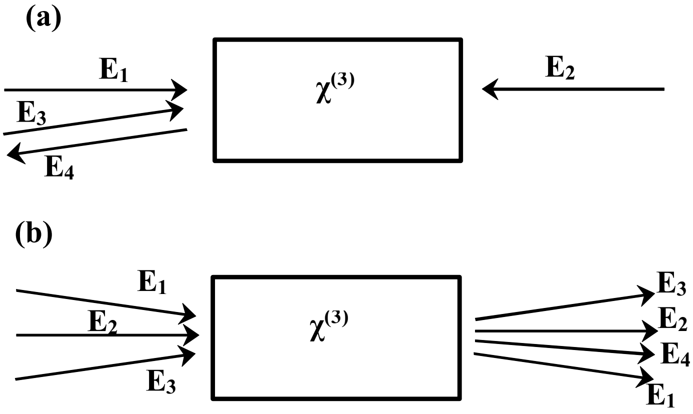

Figure 2.3: General scheme of two configurations of the degenerate four-wave mixing experiment. (a) Backward geometry. (b) Forward geometry.

The wave mixing process in both configurations can be described in terms of the intensity dependent refractive index. Namely, the DFWM can be explained by the interference of two input beams modulating a refractive index and forming a phase grating from which the third beam diffracts generating the fourth wave. Qualitatively the same effects can be obtained when the intensity-dependent two-photon absorption (TPA) is present. In such a case an amplitude grating is induced contributing also to the signal of the fourth wave. Moreover this absorption can lead to contributions to the signal of the fourth beam from effects such as thermal gratings [53], excited state species concentration gratings [54], or free carrier gratings in semiconductors [55].

2.3.1 Degenerate four wave-mixing in backward configuration (B-DFWM)

The backward geometry is the most frequently used DFWM configuration because it produces a phase-conjugate signal. In this configuration, two counter propagating strong pump beams, called forward (E_1) and backward (E_2), and a weak probe beam (E_3) are incident on the nonlinear material. As a result, the fourth wave is induced (E_4) with the same frequency as the other beams and propagates in opposite direction to a probe beam. This phenomenon can be described using a formalism of the third-order nonlinear polarization. The latter quantity produced within the medium by the three input waves will have, in addition to a large number of other terms, a term of the form [2]:

$$P_4^{(3)}(\omega) = 6\epsilon_0 \chi_{eff}^{(3)}(\omega) E_1 E_2 E_3^* \exp\left[i\left(\mathbf{k}_1 + \mathbf{k}_2 - \mathbf{k}_3\right)\cdot \mathbf{r}\right], \tag{2.8}$$

where $\chi_{eff}^{(3)} = \widehat{\mathbf{e}}_4 \cdot \chi^{(3)}(\omega) : \widehat{\mathbf{e}}_1 \widehat{\mathbf{e}}_2 \widehat{\mathbf{e}}_3^*$ represents all susceptibility tensor components involved. Since E_1 and E_2 are collinear, their wave vectors give $\mathbf{k}_1 + \mathbf{k}_2 = 0$. Thus, the polarization $P_4^{(3)}$ induces a fourth wave which is proportional to the conjugate (negative frequency component) of the probe beam: $\mathbf{k}_4 = -\mathbf{k}_3$. The last relation ensures the phase match conditions (when energy and momentum are both conserved) [2][3] which is necessary to obtain the maximum efficiency of the wave coupling.

In general the third-order polarization couples four waves. Similar expressions to Eq.(2.8) can be written for the other three waves. Because of permutation symmetry all the other elements of the nonlinear polarization are described by the same $\chi_{eff}^{(3)}$ [2]. The wave equation employing the slowly varying envelope approximation [2][3] yields the spatial evolution of each wave playing a role in the mixing process. However to simplify the problem, the "non-depleted" pump approximation is usually applied where E_1 and E_2 are assumed to be constant through the medium and so the pump evolutions are ignored [48]. Since the nonlinear material inside the backward configuration behaves as a phase conjugated mirror the useful quantity which is usually defined under such approximations is the reflectivity (R) i.e. the ratio between the reflected conjugated beam amplitude and the incident probe beam amplitude. When the probe beam is incident at a very small angle with respect to the direction of the pump beams (i.e. all the waves are nearly collinear within the medium), R takes the form [2][48]:

$$R = \frac{E_4}{E_3} = \tan^2\left(|\kappa L|\right), \tag{2.9}$$

where $\kappa = 3\omega\chi^{(3)}_{eff}E_1E_2/n_0c$ is the coupling coefficient of pump beams. The pump laser conditions are normally chosen so that $|\kappa L| \ll 1$ and $I_1 = I_2 = I_{pump}$. Moreover if all beams have the same linear polarization (e.g. along x-axis) then only one component of third-order susceptibility can be taken into account in isotropic medium: $\chi^{(3)}_{eff} = \chi^{(3)}_{xxxx} = \chi^{(3)}$. As a result we get

$$R \simeq \left(|\kappa L|\right)^2 = \left(\frac{2\pi}{\lambda}L\frac{3}{2n_0^2\epsilon_0 c}\left|\chi^{(3)}\right|\right)^2 I^2_{pump} \propto \frac{L^2}{\lambda^2}\left|n_2\right|^2 I^2_{pump}. \tag{2.10}$$

Usually it is a phase conjugation intensity which is measured rather than reflectivity. If the probe intensity is related to the pump intensity by $I_3 = \varsigma I_{pump}$, then the intensity of the fourth wave fulfils a relation: $I_4 = \varsigma\left|\kappa L\right|^2 I^3_{pump} = bI^3_{pump}$. Hence, the measurement of the conjugated intensity as a function of the pump intensity allows to determine the unknown parameter b and so the third-order susceptibility. However this procedure requires precise determination of the pump beam spatial profile in order to obtain its irradiance value. It is easier to make relative measurements with respect to some well-known reference material where only the detection of energy is necessary. The expression for the energy of the fourth wave is: $\varepsilon_4 \propto b\varepsilon^3_{pump}$. Thus, both sample and reference experimental data can be fitted to the latter formula and the investigated susceptibility can be obtained from [2]:

$$\left|\chi^{(3)}\right| = \left(\frac{n_0}{n_{ref}}\right)^2 \left(\frac{L_{ref}}{L}\right) \left(\frac{b}{b_{ref}}\right)^{1/2} \left|\chi^{(3)}_{ref}\right|. \tag{2.11}$$

Additionally to the general scheme of backward-DFWM (B-DFWM) presented above, the time-resolved wave-mixing measurements are also possible (see for example [55]). The measurements of the conjugated signal as a function of the delay time between the forward and the backward beams provide useful information about the dynamics of grating formation in the nonlinear medium.

When the wavelength of the laser used in the measurements is in the tail of an absorption band of the sample, or if absorbing impurities are present in the sample, then the phase conjugate signal will be modified. To include the effects of linear absorption the expression on the right side of Eq.(2.11) should be mulitplied by the factor $\alpha L \exp\left(\alpha L/2\right) / \left(1 - \exp\left(\alpha L\right)\right)$ if the following conditions are met [2]: $|\kappa L| \ll \alpha L \ll 1$. However when the linear absorption becomes substantial ($\alpha L \sim 1$), Eq.(2.11) will no longer be appropriate.

The DFWM reveals only the modulus of $\chi^{(3)}$, hence in general the measured signal contains the real and imaginary part of the third order susceptibility. However in some cases it is possible to use DFWM data not only to extract $\chi^{(3)}$ but also to resolve its real and imaginary components. For more details see [55][56].

2.3.2 Degenerate four wave-mixing in forward configuration (F-DFWM)

The phase conjugate signal in B-DFWM is proportional to L^2, the square of the sample thickness (see Eq (2.10)). This quadratic dependence is particularly important in characterization of samples in thin film form, where the induced conjugated signal is relatively low. Therefore it is often necessary to focus the incident beams in order to increase the pump intensity and so to improve the signal-to-noise ratio. Under such conditions, a forward geometry of wave-mixing is usually more preferable. The most popular F-DFWM geometry, the so-called boxcar configuration, is shown in Fig.2.4[51][57][58][59][60]. The three beams are focused by a single lens into the nonlinear material writing a grating that self-diffract these waves. Consequently a multitude of diffracted waves (labeled 4 through 12 in Fig.2.4) appear at the output of the sample. According to Ref.[59] only the beam 4 is perfectly phase-matched. Hence, usually the latter one is chosen as a signal for the nonlinear characterization. In the undepleted pump approximation the expression for this beam intensity is given by [51][52][60]

$$I_4 = const.\, |n_2|^2\, L^2 I_1 I_2 I_3. \tag{2.12}$$

The measurements may be performed with respect to a reference material i.e. measuring I_4 (or energy of this beam) for the investigated film of a known thickness and comparing it with a DFWM signal obtained with the same input light intensity from a reference material. Moreover it was shown in [51] that this technique has the possibility of distinguishing between DFWM signals that are due to the substrate and those from the thin film by monitoring simultaneously two signals: one of phase-matched beam and one of phase-mismatched beam.

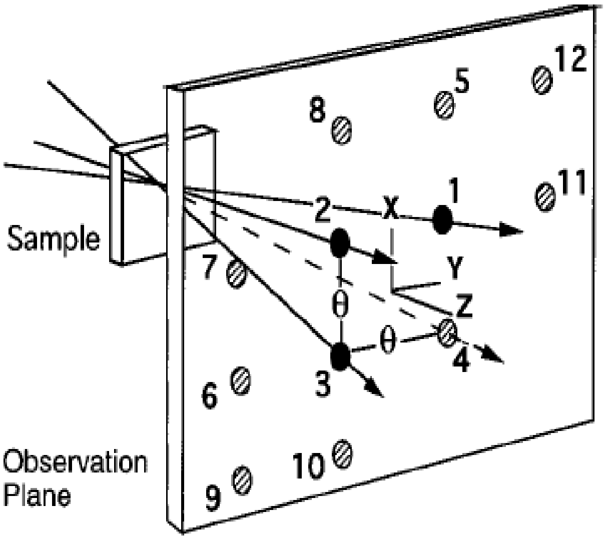

Figure 2.4: Box-car configuration of four wave mixing. Adopted from Ref.[59]

Note that the output signal in Eq.(2.12) is sensitive only to the modulus of $\chi^{(3)}$ as in the B-DFWM configuration. However authors of Ref.[59] showed that the comparison between the intensities of the phase-matched beam and some of the non-phase-matched signals (for various polarizations of the input beams) provides a way to deduce both the magnitude and the phase of each element of the complex fourth-rank nonlinear susceptibility tensor of highly nonlinear thin film deposited on a substrate of low nonlinearity. Moreover in Ref.[60] another technique providing the possibility of measurements of real and imaginary parts of $\chi^{(3)}$ was reported. The authors showed that the use of 2-D phase grating in order to produce an input signal for F-DFWM allows determining the nonlinear refractive index and the nonlinear absorption coefficient through the detection of the single phase-matched beam.

An alternative configuration of F-DFWM described in the literature is shown in Fig.2.5 where two input beams are used instead of three waves [50][61]. In this situation the first-order of diffracted signal is generated in two directions as it is shown in Fig.2.5. Hence there are two additional beams and the method is still considered as four wave mixing process, since four waves are present. This geometry is referred as forward-scattering degenerate four-wave mixing (FS-DFWM). The method was found as a useful tool for analytical chemistry [50].

In summary, the output signals in both the B-DFWM and the F-DFWM configurations are generally sensitive only to the modulus of $\chi^{(3)}$. The most popular is the backward geometry because it provides phase-conjugated and phase-matched fourth wave signal. However this configuration requires quite complicated experimental setup and the optical alignment is difficult. On the other hand an experimental realization of the forward wave-mixing is much simpler. The latter configuration is often used to characterize the samples in thin film form.

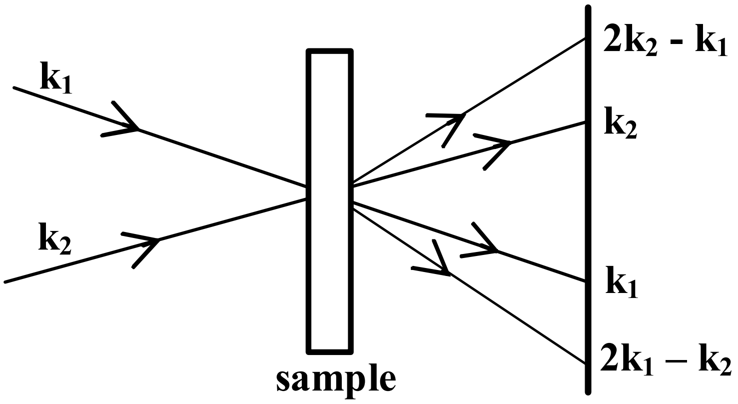

Figure 2.5: Schematic diagram for forward-scattering degenerate four-wave mixing:$\mathbf{k}_1$ and $\mathbf{k}_2$ represents the wave vectors of incident beams

2.4 Z-scan technique

Sheik-Bahae et al.[62][63] introduced a single-beam distortion technique for measuring both the nonlinear refractive index (n_2) and the nonlinear absorption coefficient (β). This method gained very quickly in popularity and it was accepted by the optical community as a standard technique for determination of nonlinearities. The configuration of Z-scan technique is shown in Fig.2.6. In this method the sample is moved along the z-direction (beam propagation direction) of a focused Gaussian beam and the energy transmittance (D2/D1 in Fig.2.6) of nonlinear medium is measured for each sample position through a finite aperture (A) placed in the diffracted far-field. The required range of scanning depends on the experimental parameters (the beam waist, the focal length of converging lens and the wavelength) and the sample thickness, L.

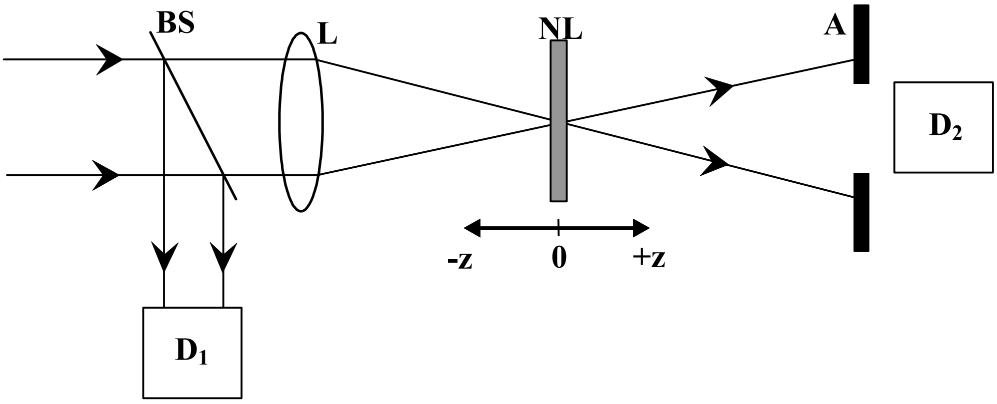

Figure 2.6: Experimental configuration for the Z-scan technique. BS: Beam splitter; L: lens, NL: Nonlinear material; A: aperture; D1, D2: Photodetectors.

The physical origin of this technique is related to the self-focusing phenomenon. The latter occurs when a light beam of non-uniform spatial intensity distribution, as Gaussian one, falls on a medium with a nonlinear index of refraction. Since the nonlinear index follows the shape of the beam, an index gradient is induced in the medium. For a positive nonlinearity, this means that a greater index, and hence the larger phase retardation, is induced in the on-axis center than in the wings of the beam. In the case of negative n_2 we have an inverse situation. The nonlinear focusing has the effect of creating a positive ($n_2 > 0$) or negative ($n_2 < 0$) lens in the medium that tends to focus or defocus slightly the

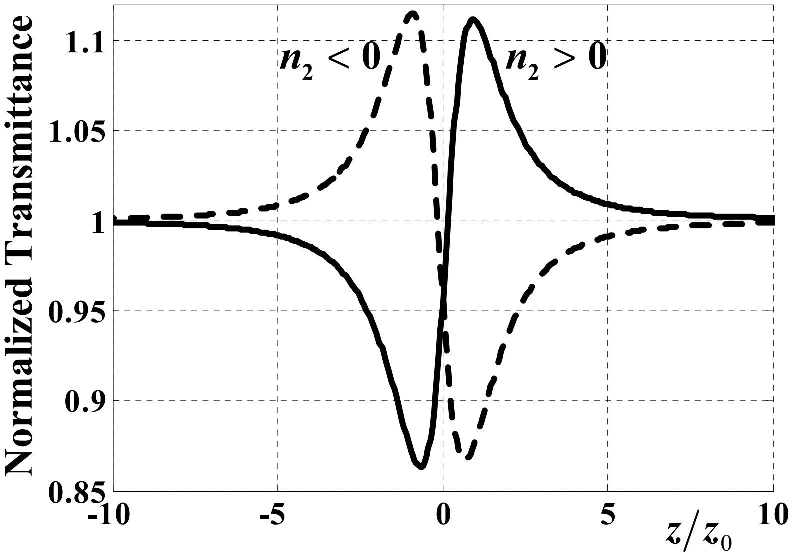

Figure 2.7: A typical Z-scan transmittance for positive (solid line) and negative (dashed line) third-order nonlinear refraction.

beam. Hence, the sample in the Z-scan method can be considered as a lens with variable focal length dependent on z-position. Consequently when the sample is moved along the focal region, the divergence change of beam in the far-field aperture plane leads to changes in the measured transmittance as it is shown in Fig.2.7.

The Z-scan trace is characterized by a peak-valley (a maximum followed by a minimum) configuration for a negative nonlinearity and a valley-peak trace for a positive one. Hence the shape of the transmittance reveals unambiguously the sign of n_2. The signal is normalized in such a way that the transmittance is unity for the sample far from the focus where the incident intensity is low and so the nonlinearity is negligible (no focusing effect occurs).

To describe quantitatively the Z-scan experimental results the following assumptions are made:

i) The incident beam is described by a linearly polarized Gaussian electric field. The latter, defined in Eq.(1.2) after neglecting the terms containing the radially uniform phase variations, takes the form:

$$E\left(r,z,t\right) = E_0\left(z,t\right)\frac{w_0}{w\left(z\right)}\exp\left(-\frac{r^2}{w^2\left(z\right)} - \frac{ikr^2}{2R\left(z\right)}\right), \tag{2.13}$$

where w_0 is the beam waist in the focal plane and all the other parameters are defined in Eqs.(1.2),(1.3), (1.4) and (1.5).

ii) The propagation of the light in the nonlinear medium is described under the slowly varying envelope [2][3] and the thin sample approximations. The first assumption assumes that the magnitude and phase of the wave amplitude vary slowly in space and time over an optical wavelength and period, respectively. In the second assumption the sample is regarded as a "thin sample" in comparison to the depth of the focus ($L < z_0$, where z_0 is the Rayleigh range defined in Eq.(1.4)). So both linear diffraction and nonlinear refraction modifications of the beam profile within the nonlinear sample are negligible. Therefore the propagation of the phase ($\Delta\Phi$) and the amplitude of the electric field ($E = \sqrt{I}$) inside the nonlinear medium can be separated in two equations:

$$\frac{d\Delta\Phi}{dz'} = -k\Delta n\left(I\right), \tag{2.14}$$

$$\frac{dI}{dz'} = -\alpha\left(I\right)I, \tag{2.15}$$

where z' is the propagation length inside the medium. For the third-order nonlinearity $\Delta n\left(I\right) = n_2 I$ and $\alpha\left(I\right) = \alpha + \beta I$. Generally the solutions of this set of equations are considered in two separate cases:

A) Pure nonlinear refraction ($\beta = 0$)

When there is no nonlinear absorption the electric field at the exit face of the sample is given by:

$$E_e\left(r,z,t\right) = E\left(r,z,t\right)\exp\left(-\alpha L/2\right)\exp\left[i\Delta\Phi\left(r,z,t\right)\right], \tag{2.16}$$

where

$$\Delta\Phi\left(r,z,t\right) = \frac{\Delta\Phi_0\left(t\right)}{1+z^2/z_0^2}\exp\left(-\frac{2r^2}{w^2\left(z\right)}\right), \tag{2.17}$$

and $\Delta\Phi_0\left(t\right)$ is the on-axis phase shift in the focus expressed by:

$$\Delta\Phi_0\left(t\right) = kn_2 I_0\left(t\right)L_{eff}. \tag{2.18}$$

Here $L_{eff} = \left(1 - \exp\left(-\alpha L\right)\right)/\alpha$ denotes the effective length due to the linear absorption and $I_0\left(t\right)$ is the focal on-axis intensity (at $z = 0$ and $r = 0$). Once the amplitude and the phase of the beam at the output of the sample are known, the field distribution at the far-field aperture can be calculated using diffraction theory (Huygen's principle) [64]. Sheik-Bahae et al.[63] employed a Gaussian decomposition method [65][66]. Accordingly, the field at the output face of the sample is decomposed through a series expansion of $\exp\left[i\Delta\Phi\left(r,z,t\right)\right]$ and the several Gaussian components propagate in the free space to the aperture plane where they are summed for reconstruction of the beam giving an output electric field $\left(E_{out}\left(r,z,t\right)\right)$[63]. Finally the normalized energy transmittance is calculated by integrating spatially and temporally the output intensity $\left(I_{out}\left(r,z,t\right) \sim \left|E_{out}\right|^2\right)$:

$$T(z) = \frac{\int\limits_{-\infty}^{\infty} dt \int\limits_{0}^{r_a} dr\ r\left|E_{out}\left(r,z,t,\Delta\Phi_0\right)\right|^2}{S\int\limits_{-\infty}^{\infty} dt \int\limits_{0}^{\infty} dr\ r\left|E_{out}\left(r,z,t,0\right)\right|^2}, \tag{2.19}$$

where $\left|E_{out}\left(r,z,t,0\right)\right|^2$ represents the light irradiance in absence of nonlinearity, r_a denotes the radius of the circular aperture and S is the linear transmittance of the aperture defined as:

$$S = 1 - \exp\left(-\frac{2r_a^2}{w_a^2}\right), \tag{2.20}$$

with w_a denoting the beam waist in the aperture plane in the linear regime ($\Delta\Phi_0 = 0$).

The measured normalized energy transmittance in a Z-scan experiment can be fitted numerically to Eq.(2.19) in order to find n_2. However the characterization of nonlinear refraction is usually simplified by exploiting an analytical solution for the normalized transmittance that can be derived for the on-axis intensity ($S \approx 0$, very small aperture) in the far field condition and for very small steady-state nonlinearity ($\left|\Delta\Phi_0\right| \ll 1$) [63]:

$$T\left(z, S\approx 0\right) = 1 + \frac{4x\Delta\Phi_0}{\left(x^2+9\right)\left(x^2+1\right)}, \tag{2.21}$$

where $x = z/z_0$. Sheik-Bahae et al.[63] have shown that a useful experimental parameter is ΔT_{pv}, the difference between the maximum and the minimum of the normalized transmittance. Basing on the analytical relation in Eq.(2.21) it was found numerically that the following expression describes ΔT_{pv} within 3% accuracy for $|\Delta\Phi_0| < \pi$:

$$\Delta T_{pv} = 0.406\,(1-S)^{0.25}\,|\Delta\Phi_0|\,. \tag{2.22}$$

Eq.(2.22) provides an alternative and simple way to determine n_2 from Z-scan traces. Moreover it defines also the sensitivity of the method as the ratio between the detectable transmission change and the corresponding induced nonlinear dephasing $|\Delta\Phi_0|$. Thus from Eq.(2.22) the sensitivity of the measurement for a pin-hole aperture ($S \approx 0$) is 0.406. If the experimental system is able to resolve transmittance changes of about $\Delta T_{pv} \approx 1\%$ for $S \approx 0$ then the related measurable nonlinear phase shift will be about 25 mrad corresponding to an optical path length of $\Delta nL = \lambda/250$. The measurement of such low signal requires good optical quality of the samples apart from the quality of the beam. Surface imperfections and inhomogeneity in the sample can lead to erroneous results. In Ref.[63] it was suggested that such 'parasitic' effects can be reduced substantially by subtracting a low irradiance linear Z-scan from the high irradiance nonlinear Z-scan, after normalizing each of them.

The linear dependence between ΔT_{pv} and $|\Delta\Phi_0|$ makes also convenient to include a time averaging factor due to the transient nonlinearity induced by a pulse radiation which is not taken into account in Eq.(2.22). For an instantaneous nonlinear response of the material and a temporal linear behavior of the photodetector we can use $\langle\Delta\Phi_0\rangle = |\Delta\Phi_0|/\sqrt{2}$ for a Gaussian temporal pulse or $\langle\Delta\Phi_0\rangle = 2\,|\Delta\Phi_0|/3$ for hyperbolic secant squared pulse whereas for a long-lived nonlinearity (much longer than the pulse width), $\langle\Delta\Phi_0\rangle = |\Delta\Phi_0|/2$ independent of the pulse shape [67].

B) Nonlinear refraction with absorption ($\beta \neq 0$)

In the presence of nonlinear absorption the solutions of Eq.(2.14) and Eq.(2.15) for the third-order nonlinearity are given by:

$$\Delta\Phi\,(r,z,t) = \frac{kn_2}{\beta}\ln\left[1+q\,(r,z,t)\right], \tag{2.23}$$

$$I_e\,(r,z,t) = \frac{I\,(r,z,t)\exp(-\alpha L)}{1+q\,(r,z,t)}, \tag{2.24}$$

where $q(r,z,t) = \beta L_{eff} I(r,z,t)$. Since the absorptive and the refractive contributions are coupled inside the phase term, nonlinear absorption will distort the shape of the Z-scan far field transmittance. Two-photon absorption ($\beta > 0$) will enhance the valley and reduce the peak while the saturable absorption ($\beta < 0$) will produce an opposite effect. The typical shape of Z-scan normalized transmittance in presence of two-photon absorption is shown by the solid line in Fig.2.8. The normalized far field transmittance can be calculated numerically following a Gaussian decomposition method and taking into account the results in Eq.(2.23) and (2.24). However Sheik-Bahae et al.[63] proposed a simpler procedure allowing measuring absorption and refraction separately. To do so, firstly the Z-scan experiment should be done without any circular aperture at the output. In such configuration, called as an open aperture Z-scan ($S = 1$), the transmittance is insensitive to beam distortion and is only a function of nonlinear absorption. Thus the output energy transmittance can be obtained by integrating spatially and temporally the intensity outgoing from the sample (Eq.(2.24)) without having to include the free space propagation process. After a spatial integration we get:

$$T(z,t,S=1) = \frac{1+z^2/z_0^2}{q_0} \frac{\int_{-\infty}^{\infty} dt \; \ln\left(1 + q_0 \frac{f(t)}{1+z^2/z_0^2}\right)}{\int_{-\infty}^{\infty} dt \; f(t)}, \tag{2.25}$$

where $f(t)$ is the temporal profile of the laser pulse and $q_0 = \beta L_{eff} I_0$. If one assumes a Gaussian temporal shape, the open aperture normalized transmittance can be approximated by [63]:

$$T(z,S=1) = \sum_{m=0}^{\infty} \frac{[q_0]^m}{\left(1+z^2/z_0^2\right)^m (m+1)^{3/2}}, \tag{2.26}$$

for $|q_0| < 1$. Thus the open aperture Z-scan measurements allow determining unambiguously β, the nonlinear absorption coefficient. Typical open aperture normalized transmittance is shown by the dotted line in Fig.2.8.

When the closed (with an aperture $S < 1$) and the open aperture (without an aperture $S = 1$) data are measured, the nonlinear refractive index can be determined without resorting to numerical propagation if two conditions are met:

$$q_0 < 1 \text{ and } \gamma = \frac{\beta}{2kn_2} < 1. \tag{2.27}$$

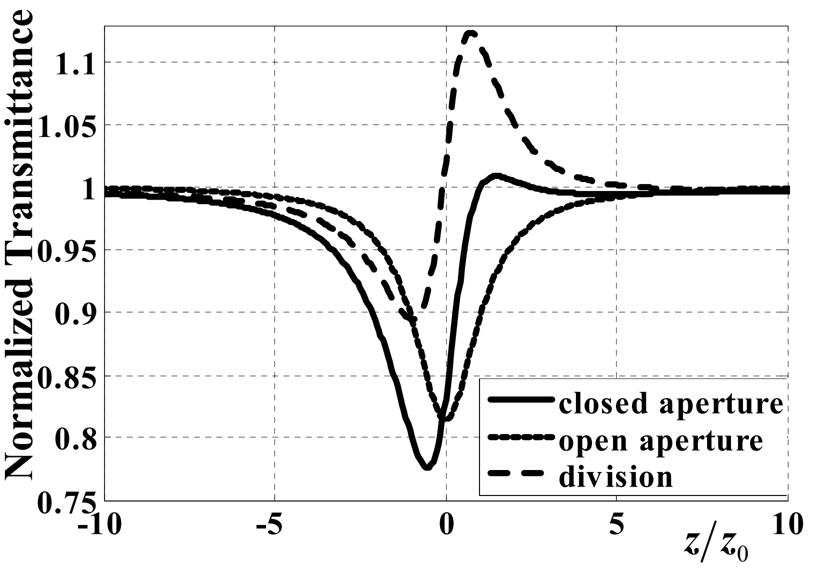

Figure 2.8: Calculations of closed ($S = 0.4$) and open aperture ($S = 1$) Z-scan data along with their ratio for self-focusing ($\Delta\Phi_0 = 1$) accompanied by nonlinear absorption ($q_0 = 0.7$)

The first one can be easily found by adjusting the incident intensity however the second one is an intrinsic property of the material implying that the imaginary part of the third-order susceptibility should not be larger than the real one. This condition is satisfied by most semiconductors, glasses and liquids. Under such circumstances a simple division of the closed aperture ($S < 1$) data by the ones obtained with the open aperture ($S = 1$) gives a valley-peak (or peak-valley) curve where ΔT_{pv} closely approximates (within 10%) a purely refractive Z-scan. The result of the division of the closed aperture curve by the open one in Fig.2.8 is illustrated by a dashed line. After this operation Eq.(2.22) can be employed to determine n_2.

2.4.1 Eclipsing Z-scan technique (EZ-scan)

The on-axis phase shift measured by the Z-scan technique is proportional to the sample thickness; thus, the change of the normalized transmittance is very small for thin films. Hence films can not be easily characterized by Z-scan even when they have large nonlinearity. To improve the signal the incident intensity must be increased. However, the largest intensity is ultimately limited by the damage threshold of the film. The need to characterize samples in thin film form has motivated the development of the eclipsing Z-scan (EZ-scan) technique [68]. In this technique, the far-field aperture is replaced by an obscuration disk, and the transmittance of the beam around this disk is measured. The technique is based on the assumption that the wings of the far-field beam are more noticable when the nonlinear diffraction occurs in a dark region because the contrast is higher in the wings than in the center part of the beam. Consequently the sensitivity of the technique should be increased when a large disk is used instead of small aperture. Using the same analysis as in Z-scan it was found that the peak–valley normalized transmittance has a nearly linear dependence on the on-axis phase shift for $|\Delta\Phi_0| < 0.2$ and $0.98 < S < 0.995$:

$$\Delta T_{pv} = 0.68\left(1 - S\right)^{-0.44}\left|\Delta\Phi_0\right|, \tag{2.28}$$

where S now is related to the amount of the light blocked in the linear regime.

It was shown in [68] that in the optimized experimental conditions EZ-scan can yield sensitivity to $\lambda/10^4$ wave-front distortion. It means that for films of thickness $L \approx \lambda$, the index change $\Delta n \approx 10^{-4}$ can be measured.

2.4.2 Z-scan technique using top-hat beams

Another technique increasing the sensitivity of measurements in comparison to the original Z-scan method was reported by Zhao and Palffy-Muhoray in [69]. The authors noticed that it is not always possible to achieve a good profile of TEM_{00} Gaussian spatial mode necessary for accurate measurements in Z-scan experiments. However, it is often possible to expand the beam and clip it with a small circular aperture of diameter d to approximate a uniform (top-hat) spatial profile. Focusing of such top-hat beam with a lens of focal length f gives a focal spot size defined by the Airy radius $1.22\lambda f/d$. The waist of the beam was chosen to be $w_0 = \lambda f/d$ and thus the Rayleigh range is $z_0 = \pi w_0^2/\lambda$. In the focal plane the field distribution has the well-known Airy profile:

$$E\left(r, z = 0\right) \propto \frac{2J_1\left(\pi r/w_0\right)}{\pi r/w_0}. \tag{2.29}$$

On any plane z around the focus, the transverse field distribution can be described according to the Fresnel diffraction theory [70]:

$$E\left(r,z\right)\propto\frac{2J_1\left(\pi r/w_0\right)}{\pi r/w_0}\otimes\frac{\exp\left(i\pi r^2/\lambda z\right)}{\lambda z}, \tag{2.30}$$

where J_1 is the first-order Bessel function of first kind and $\otimes$ is the operator of convolution.

The electric field is normalized so that the intensity can be expressed as $I(r,z)=|E(r,z)|^2$. If the thin sample approximation is met i.e. L, the sample thickness is much less than the Rayleigh range z_0, then the field distribution at the exit surface of the nonlinear sample is:

$$E_e\left(r,z\right)=E\left(r,z\right)\exp\left(-\alpha L/2\right)\exp\left[ikn_2L_{eff}I(r,z)\right]. \tag{2.31}$$

It is assumed that the output circular aperture is far from the sample at a distance D so that the Fresnel number $F=w_0^2/\lambda D$ is much less than unity. In such conditions the electric field at the output aperture plane can be obtained straightforwardly through the Fourier transform of $E_e\left(r,z\right)$. This simple procedure allows calculating numerically the normalized transmittance. The computations show that the relationship between ΔT_{pv} and $|\Delta\Phi_0|$ is no longer linear in the case of top-hat beams, nevertheless the following empirical expression describes the exact numerical results with 1% accuracy for $|\Delta\Phi_0|<\pi$:

$$|\Delta\Phi_0|=2.7\tanh^{-1}\left[\frac{\Delta T_{pv}}{2.8\left(1-S\right)^{1.14}}\right]. \tag{2.32}$$

Here S is the ratio of power transmitted through the aperture to the total power incident on the plane of the aperture in the limit of low intensity. The simple calculations based on the latter relation show that the normalized transmittance with a top-hat beam is about 2.5 times more sensitive than that obtained with a Gaussian beam. This increase in sensitivity is attributed to the steeper beam curvature gradients encountered by the nonlinear sample at the positions near the focus.

2.4.3 I-scan experiment

Taheri et al.[71] noticed that it is not always convenient to move a sample. Particularly, when one wants to avoid crossing the focal plane where the sample is exposed to large irradiance. The latter can cause an irreversible damage inside materials with absorption. Therefore the authors proposed to fix the sample in one position and to monitor the output transmittance through the circular aperture as a function of variable incident intensity. The analysis of the so-called I-scan method is analogous to that of the Z-scan. Hence in the open aperture configuration (no aperture) the signal is sensitive only to nonlinear absorption. Assuming a spatially and temporally Gaussian incident beam and including single reflection from the front and back surfaces of the sample, the normalized transmission coefficient T for a sample of thickness L is

$$T(z, S = 1) = \sum_{m=0}^{\infty} \frac{\left[-\beta\,(1 - R)\,L_{eff}\right]^m}{(m + 1)^{3/2}} I_0^m, \tag{2.33}$$

where R is a Fresnel reflection coefficient describing the ratio of the reflected intensity to the transmitted intensity for a given position of the sample. The value of β can be determined by a numerical fit of the above equation to the observed transmission.

In the closed aperture configuration (with aperture), as in Z-scan technique, the experimental results should be divided by those obtained from the open aperture giving a transmission approximately due to a pure refractive response of the material. The sign and magnitude of n_2 are, then, directly related to the slope of the normalized transmission given by:

$$T(z, S \approx 0) = 1 + \frac{4kgdn_2L_{eff}}{\sqrt{2}\,(g^2 + 9d^2/d_0^2)\,d_0}, \tag{2.34}$$

where $g = 1 + da/\left(a^2 + z_0^2\right)$ and $d_0 = \pi w_0^2/\lambda$. Here z_0 is the Rayleigh range, a is the sample position with respect to the focal plane of the lens, d is the distance between the sample and the aperture and w_0 is the beam radius at the sample. It is pointed out in [72] that I-scan method is a more practical choice for the measurement of the third-order nonlinearity in inhomogeneous samples, especially in thin film form, because the same part of the sample is investigated during the entire experiment. Thus, the sample's imperfections inducing linear and nonlinear distortions in the signal are significantly decreased. Additionally, the influence of the fluctuation of the output intensity of the laser is substantially reduced. Moreover since no displacement of specimen is necessary, no moving elements (such as step motor) are needed. The advantages include also the reduction of the total exposure time and the simplification of the data fitting.

Alternatively to the most popular Z-scan and I-scan techniques another types of scans can be performed in order to characterize nonlinearity [73]: r-scan, d_a-scan, and r_a-scan, where r is the position of the pinhole in the aperture plane, d_a is the distance from the focal plane to the aperture plane and r_a is the aperture size.

2.4.4 Other types of Z-scan

Since the time when Z-scan method has been discovered, plenty of altenative or improved Z-scan techniques have been developed. Numerous Z-scans experiments were reported considering various types of input beam profiles: e.g. the trimmed Airy beam [74], the elliptic Gaussian beam [75], the Gaussian-Bessel beam [76] and the quasi-one-dimensional slit beam [77]. The Z-scan analysis has been also extended to thick samples ($L > z_0$) [78][79] and to anisotropic media [80]. Furthermore, the use of an off-center aperture was suggested in [81] to increase the Z-scan sensitivity. It was shown in [82] that the nonlinearity can be also characterized by measuring the radius of the output beam instead of the energy transmittance. A reflection Z-scan experiment was demonstrated by Petrov et al.[83][84] to study highly absorbing samples. This technique is particularly useful for studying optical effects in thin films; however, it is very sensitive to surface defects and imperfections. The Z-scan method was also combined with the ellipse rotation technique to determine two of the three independent elements of the third-order susceptibility tensor in isotropic medium [12][85]. Moreover two-color Z-scan [86][87][88] and time-resolved Z-scan [89] using a dual-wavelength were introduced to investigate the non-degenerate nonlinearities. More recently, a Z-scan using white light continuum pulsed laser was reported [90][91][92] to study the spectral dispersions of degenerate nonlinear refractive index and nonlinear absorption coefficient. Marcano et al. [93][94] introduced a non-apertured multi-channel Z-scan, where the total far-field profile distortion was recorded onto a CCD camera. Through image processing, the nonlinearly distorted beam for a given sample position is compared with the undistorted (linear) beam. The moduli of the intensity variation over each pixel of the CCD camera are then summed to define a total profile distortion signal proportional to the nonlinear phase shift. It was reported that this method is sensitive to nonlinear phase distortions less than $\lambda/15000$. Such impressive enhancement of sensitivity in comparison to original Z-scan was explained by the higher ratio of the amount of radiation processed by the CCD camera over the background fluctuations due to the multi-channel nature of detection (i.e. each pixel of CCD can be considered as a singular Z-scan signal).

2.4.5 Limitations of Z-scan technique

In summary, the Z-scan method provides a sensitive and a straightforward method for the determination of the sign as well as the magnitude of n_2 without or with nonlinear absorption. The simplicity of the method made this technique very popular and it was very quickly accepted as a standard for determination of third-order nonlinearities. This method is used now to study a wide variety of different materials including also samples in thin film form. In spite of the aforesaid advantages, there exist some limitations for the Z-scan method. The most fundamental one is related to the impossibility of distinguishing the physical origin of observed self-focusing effect. Hence the Z-scan signal can be simultaneously due to electronic cloud distortion, molecular reorientation, thermal effects, electrostriction, free-carrier absorption and so on. Particularly, the thermo-optical effects mask frequently the Kerr nonlinear response (electronic one) of materials. This is especially true when a pulse laser of nanosecond duration or longer are employed or when the high repetition rate of laser pulses ($>$ 10 kHz) is used [7][8] (even in the femtosecond regime). The cumulative heating occur when the medium is illuminated by a train of pulses whose spacing is shorter than the characteristic thermal-diffusion time $t_c = w^2/4D$, where w is the laser beam spot size and D is the thermal diffusion coefficient of the material. Several techniques to distinguish the Kerr nonlinearity from thermo-optical effects during measurements have been suggested including the use of a mechanical chopper [7][95][96][97]. Additionally, for the particular case of thin films the use of substrates with higher thermal conductivity was proposed to reduce the contribution of cumulative heating [8]. An extra effect which can lead to misinterpretation of Z-scan results is the free-carrier absorption, especially important in semiconductors and low-band-gap optical glasses. The way how to separate this contribution from electronic nonlinearity in Z-scan experiment is provided in [9]. Another drawback of Z-scan method is the use of multiple shots in the sample to obtain the nonlinear coefficients. In case of fragile materials, an exposure to multiple intense pulses can cause ablation and optical damage inside the material. Furthermore, as shown in [98], the presence of the ablation hole inside the thin film during Z-scan measurements can yield the expected peak-valley configuration of normalized transmittance, which can be wrongly assigned to Kerr nonlinearity. Moreover photo-induced changes can occur in some materials due to multiple shots as it was shown in Ref.[99] for silver-nanocluster-doped glasses. During the measurement the composite glass was modified, visibly altering the transmission in the illuminated region of the material and irreversibly changing its nonlinear response. The Z-scan measurements in such cases can lead to erroneous results.

2.5 Nonlinear Imaging Techniques (NIT)

Boudebs et al.[100][101] proposed a nonlinear characterization techniques based on the use of a spatial filtering inside the image processing systems. It was shown that it is possible to characterize nonlinearities by analyzing the intensity profile of the image after nonlinear filtering through the material placed in the Fourier plane of a $4f$ coherent imaging processor. The comparison of the experimental filtered image of an object with its numerical simulation leads to the determination of the nonlinear refractive index of the investigated sample. Hence NIT experiments belong to the group of beam distortion techniques. This technique was also extended to measurements of the nonlinear absorption coefficients.

2.5.1 $4f$ coherent imaging system

A typical $4f$ system for nonlinear characterization is shown in Fig.2.9. An object $O(x, y)$ is placed at the entry of the setup. The transverse structure (in amplitude and/or phase) of this object determines the distribution of the amplitude and phase of electric field $S(u, v)$ in the Fourier plane of the system (focal plane of lens L_1). In absence of nonlinearity this spectrum yields a geometrical image of the object at the output. However in the nonlinear regime the medium placed in the Fourier plane will change spectrum to $S_L(u, v)$. This change in the spectrum is transformed into a change in the field amplitude distribution $U(x, y)$ in the image plane. Hence the alteration of the image intensity $I_{im}(x, y) = |U(x, y)|^2$ will be a signature of the induced nonlinearity. The ratio of the field amplitude transmitted by the medium and the field amplitude incident on the sample defines the nonlinear transmittance $T(u, v)$ of the medium.

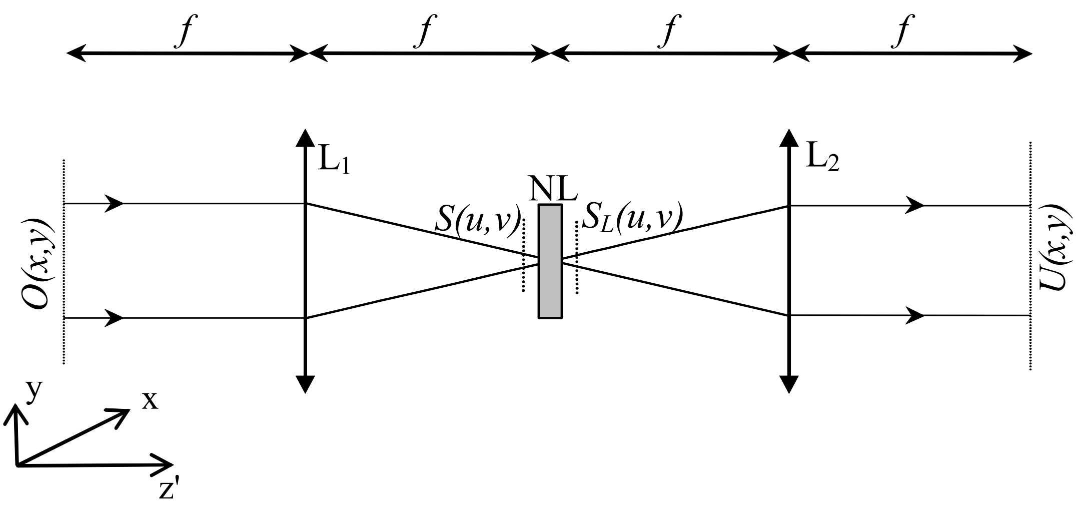

Figure 2.9: Schematic of the $4f$ coherent imaging system. Labels refer to: lenses (L1,L2), nonlinear medium (NL)

The nonlinear image formation inside the $4f$ system can be described on a basis of Fourier optics [64]. A two-dimensional object is illuminated at normal incidence by a linearly polarized monochromatic plane wave defined by $E = E_0\left(t\right)\exp\left[i\left(\omega t - kz\right)\right] + c.c.$, where ω is the angular frequency, k is the wave vector and $E_0\left(t\right)$ is the amplitude of the electric field containing the temporal envelope of the laser pulse. Since we are concerned with the image intensity, the temporal terms can be omitted. If the transmittance of the object is $t(x,y)$, the field amplitude in the focal plane of the first lens L_1 is the spatial Fourier transform of $O(x,y) = E \cdot t(x,y)$:

$$S\left(u,v\right) = \widetilde{F}\left[O(x,y)\right] = \int\limits_{-\infty}^{+\infty}\int\limits_{-\infty}^{+\infty} O(x,y)\exp\left[i2\pi\left(ux+vy\right)\right]dxdy, \tag{2.35}$$

where $\widetilde{F}$ denotes the Fourier transform operation, $u = x/\lambda f$ and $v = y/\lambda f$ are the spatial frequencies in the focal plane, f is the focal length of the lens L_1, and λ is the wavelength of the exciting wave.

In the focal plane the spectrum of the object experiences an alteration due to the presence of the nonlinear medium. Assuming cubic nonlinearity and a medium exhibiting **(i)** linear absorption defined by α **(ii)** two-photon absorption defined by and β **(iii)** nonlinear refraction defined by n_2, the nonlinear transmittance of the medium under the slowly varying envelope and thin sample approximations is defined as [102]

$$T(u,v) = \frac{S_L(u,v)}{S(u,v)} = \{\exp(-\alpha L)(1+q(u,v))\}^{-1/2} \exp\left[i\frac{2\pi n_2}{\lambda\beta}\ln(1+q(u,v))\right], \quad (2.36)$$

where $S_L(u,v)$ is the spectrum at the exit face of the sample, $q(u,v) = \beta L_{eff} I(u,v)$ with $L_{eff} = (1-\exp(-\alpha L))/\alpha$ representing the effective length and $I(u,v)$ denotes the intensity of the laser beam within the sample. The latter quantity is related to the electric field through the expression $I(u,v) = 2\epsilon_0 n_0 c\,|S(u,v)|^2$.

At the output of the $4f$ system, the image intensity is obtained by the inverse Fourier transform of :

$$I_{im}(x,y) = |U(x,y)|^2 = \left|\widetilde{F}^{-1}[S(u,v)\times T(u,v)]\right|^2, \quad (2.37)$$

where $\widetilde{F}^{-1}$ denotes the inverse Fourier transform operation.

2.5.2 Nonlinear Imaging Technique with Phase Object (NIT-PO)

Different objects as Double-slit Object [100] or Top-Hat Object [103], have been proposed as an input for the $4f$ system used for nonlinear characterization. However, the Phase Object (PO) has gained the greatest popularity [104]. The schematic of this object is shown in Fig.2.10. It is composed of circular glass plate of radius R_a on which a transparent dielectric disk (of radius L_p) has been deposited. The disk has a thickness and index of refraction such that it retards the phase of the incident light by $\Delta\Phi_L$ relative to the phase outside the disk.

When the radius of the circular glass plate is much smaller compared to the spatial extension of the beam (i.e. beam waist of the Gaussian beam) the input field can be assumed as plane wave. Then the transmittance of the phase object can be defined as:

$$t(x,y) = \zeta_{Ra}(x,y)\exp\left[i\Delta\phi_L\zeta_{Lp}(x,y)\right], \quad (2.38)$$

where $\zeta_R(x,y)$ is the circular function defined as equal to one if the radius $\sqrt{x^2+y^2}$ is less than R and zero elsewhere.

The examples of the numerical simulations for such object and non-absorbing sample ($\beta = 0$) are shown in Fig.2.11. The increase of the transmitted intensity inside the phase

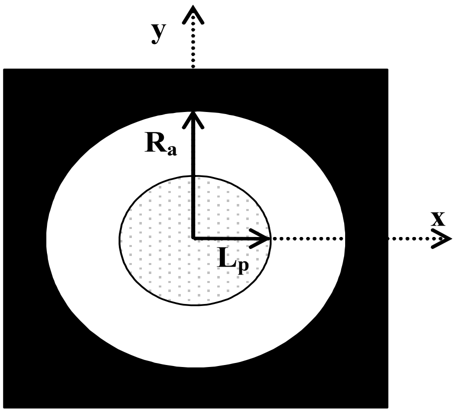

Figure 2.10: Schematic of phase object used at the entry of the 4f system

plate is observed when the nonlinear medium is characterized by a positive n_2. Inversely, for a negative n_2, there is a decrease in the image center. The transmission change ΔT is defined as the difference between the mean value of the diffracted fluence inside the phase plate and the fluence outside. Hence the positive ($\Delta T > 0$) or the negative ($\Delta T < 0$) image contrast indicates unambiguously the sign of the nonlinear refraction. The comparison between numerical simulations and experimental images (acquired by a non-spatially integrated detector as a CCD camera) allows determining nonlinear refractive indices. Moreover, when the sample is nonlinearly absorbing ($\beta \neq 0$) it is possible to obtain a signal that is approximately due to pure nonlinear refraction using two intense laser shot in the material. It is done by subtracting two images obtained with and without the phase object both taken in the nonlinear regime [105]. The NIT-PO technique has many advantages. The optical alignment is easy and no displacement of the material is needed unlike in the Z-scan method. Only one-laser-shot is required, giving the possibility to study materials showing intensity-dependant n_2 as well as the temporal evolution of the refractive index modifications due to the photo-induced effects inside photo-sensitive materials [106]. This technique is particularly advantageous in situations where the optical beam quality of the laser output is poor and when the optical materials under study are fragile. One drawback of this method is that a good optical quality of the material is needed.

Later, various modifications of NIT-PO technique have been developed. In Ref. [107] a positive–negative PO instead of conventional uniform PO was proposed in order to increase the sensitivity of the system. Furthermore a time-resolved pump-probe experiment based on the NIT-PO was presented in [108]. It was shown that dynamic of both degenerate and non-degenerate nonlinear absorption and refraction can be measured simultaneously. In addition, the sensitivity of such NIT-PO time-resolved pump-probe system is more than twice of that based on Z-scan system. Moreover the combination of the NIT-PO technique with a Z-scan method has been also reported in order to measure n_2 and β [105][109] as well as to distinguish the transient thermal lensing effect from the third-order nonlinear refraction [110]. Recently, the reflection NIT-PO technique [111] was introduced to characterize the nonlinear optical properties of the thin films prepared on opaque substrates.

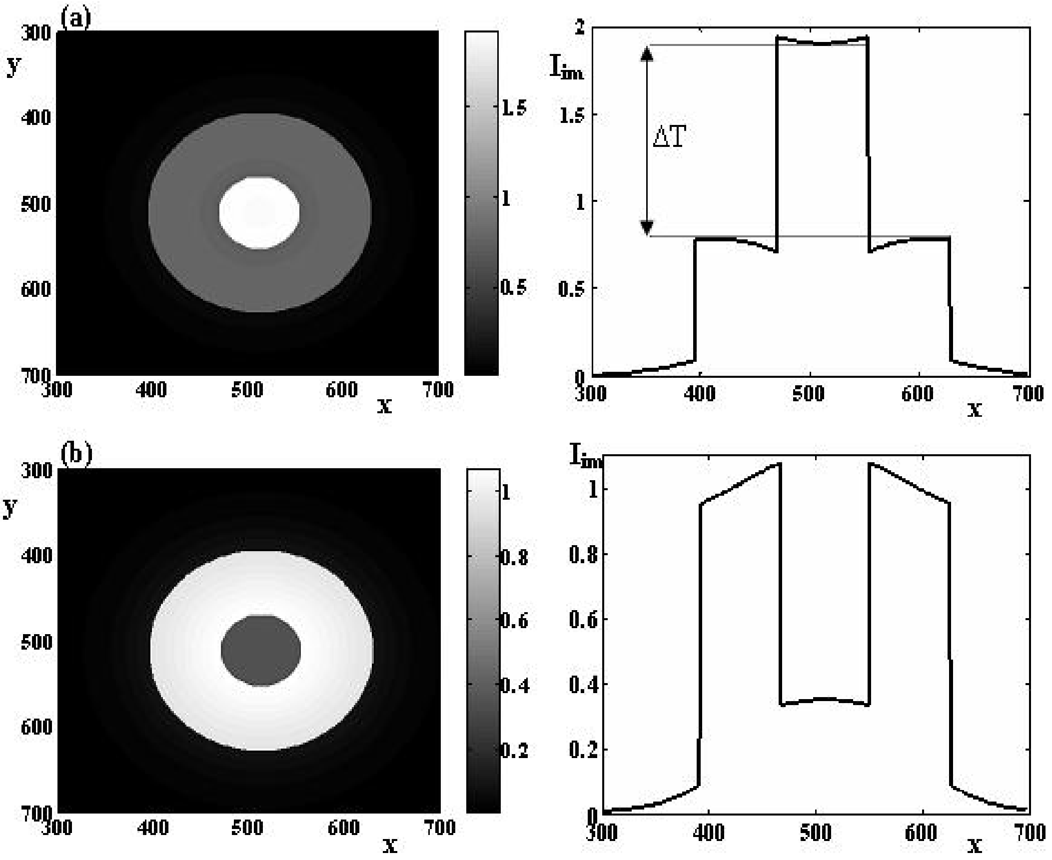

Figure 2.11: Numerical simulation of phase object images and the corresponding image profiles for (a) positive n_2 (b) negative n_2.

2.6 Conclusions

In this chapter we presented several techniques used for the characterization of nonlinear materials. All of them, more or less, will be involved in the studies described in this thesis. All of the presented methods have their own advantages as well as disadvantages. The Kerr gate and ellipse rotation were briefly introduced showing that the optical nonlinearities can be determined by exploiting dependency of nonlinearities on beam polarization state. Some elements of the third-order susceptibility tensor can be estimated with the help of these techniques. Both methods are relatively sensitive however they require very precise alignment of the optical setup. Hence the measurements are preferable with a reference material. The Kerr-gate experiment attracts special attention because as a pump-probe technique it provides the possibility to study the temporal behavior of nonlinear interactions and it can be used as third order autocorelation technique to measure pulse duration.

The degenerate four wave-mixing (DFWM) is a characterization technique making use of spatial frequency mixing process. Three input beams with the same temporal frequency interact inside the medium producing a fourth wave. This method requires a complex experimental apparatus but on the other hand it provides several advantages. The fact that the setup includes temporal and spatial overlapping of three separate beams allows flexibility of measurements, such as the possibility of measuring different tensor components of $\chi^{(3)}$, a straightforward study of the temporal behavior of a sample, low sensitivity to the quality of the beam profile and the optical quality of sample. Similarly to the Kerr gate experiment the measurements are typically performed with respect to a standard material, but it may provide absolute measurements if the lasers are well characterized.

The Z-scan technique has been widely accepted as a standard method allowing to separate measurements of the nonlinear refraction and the nonlinear absorption. It has been extensively employed for characterization of a wide variety of different materials, because of some notable advantages such as the simplicity of the optical setup, the high sensitivity and the simultaneous determinations of the signs and the magnitudes of optical nonlinearity. No complicated numerical fitting is required and the nonlinear coefficients can be obtained directly from the experimental data. Hence the Z-scan technique is a very good method for absolute measurements of optical nonlinearities. Various modifications of the original technique have been developed in order to improve the sensitivity or to adapt this method to different experimental conditions. Unfortunately Z-scan is sensitive to all nonlinear physcial mechanisms induced in the material and each of them should be recognized in given experimental conditions. Moreover Z-scan is a multi-shot technique where cumulative effects such as thermo-optical phenomena and optical damage of fragile material are possible.

The Nonlinear Imaging Technique (NIT) using a $4f$ coherent imaging system was introduced in order to overcome all the problems encountered with multi-shot methods. This technique requires only few laser shots and is suitable to study intensity-dependent phenomena. Particularly, the NIT with a phase objects (PO) has been found to be an attractive method since it provides the possibility of measuring the magnitude as well as the sign of the nonlinear refraction. Moreover many additional advantages are provided by this technique such as: an easy optical alignment, no request for sample displacement, small sensitivity to variation of laser beam characteristics, accurate measurement of the intensity by means of a CCD camera and simple theoretical model based on Fourier optics. The only disadvantage is the requirement of a relatively good optical quality sample.

In this chapter we did not discussed about the interferometric methods. Various configurations including different interferometer as Michelson and Mach-Zehnder have been reported (see for example [112][113][114][115][116]) to characterize the nonlinearity. The interferometric techniques are powerful tools to obtain one laser shot measurement allowing to determine n_2. They can be spatially resolved and show sensitivity comparable to the Z-scan technique [113]. But the great inconvenience is the complexity of the optical set up, especially when one is using unstable beam outputs. Moreover, the numerical processing involved is quite complicated. These methods will not be exploited in this thesis but have been studied in details earlier in our lab (for more details one can see [113][114][115]).

In the next chapter we will introduce the multi-wave mixing technique inside the $4f$ coherent imaging system. Particularly we will demonstrate that it is possible to combine the degenerate four wave-mixing process with the Z-scan method. Hence experiments from two different groups, namely the wave-mixing and the beam distortion, will be unified. Finally we will show that in the low excitation regime by analyzing nonlinearly diffracted energy in the image plane of the $4f$ system it is possible to compare the optical sensitivity of these seemingly different measurement methods.

Chapter 3

SENSITIVITY OF NONLINEAR CHARACTERIZATION TECHNIQUES INSIDE THE $4f$ IMAGING SYSTEM

3.1 Introduction

Three parameters, resolution, sensitivity and accuracy, can be used to characterize each measurement technique. The first parameter describes the smallest change in the measured signal that can be resolved by the experimental apparatus and data acquisition system. The resolution is predominantly determined by the noise level of the detector. The second parameter, the sensitivity, is defined as the ratio between a differential change of the output signal and a corresponding differential change in the input signal [117]. Thus it describes how much the output changes due to the small perturbation at the entry of the setup. In the particular case of nonlinear optical characterization techniques the sensitivity is directly related to the optical nonlinearity. It expresses how much the modifications in the nonlinear response of the material are transferred into changes of the measured signal. Both the resolution and the sensitivity determine the maximum error that occurs during the measurements. The latter defines the accuracy of the system. A need of highly sensitive experimental method is particularly important when one wants to characterize samples in thin film form where the optical interaction length is very short and so the signal to noise ratio is very low. Hence the direct comparison of the optical sensitivity of different techniques is necessary in order to optimize the nonlinear characterization.

In this chapter we will show that it is possible to combine the wave-mixing process with the Z-scan technique inside the $4f$ coherent imaging system. Moreover, we will illustrate that by changing the object at the entry and the field stop in the image plane, it is possible to perform different multi-wave mixing experiments as well as different characterization techniques, such as DFWM, Z-scan, EZ-scan, I-scan or NIT-PO. All of them can be considered as special cases of the same nonlinear imaging process. Such unification of nonlinear characterization techniques will permit us to compare directly their optical sensitivities. Moreover an optimization procedure for the measurements in each case will be proposed.

3.2 Numerical model of beam propagation inside the $4f$ system

The the $4f$ imaging system scheme is shown in Fig.2.9. When the sample position is fixed at the focal plane, the numerical method given in Section 2.5.1 can be used in order to describe image formation as it was done for a NIT-PO technique. However when the sample is not placed at the focus of lens L_1 (see Fig.2.9), the free-space beam propagation methods must be employed. For an object ($O(x,y)$) with circular symmetry (as Gaussian beam, Top Hat beam or Phase Object) one can use the Fresnel-Bessel transformation as in Ref.[105] to propagate the beam from the object plane to the image plane. However when the object has no circular symmetry a more general numerical method must be applied. An application of Fourier optics in scalar diffraction theory provides the possibility of propagating an input field of random distribution in the Fourier space. Accordingly, one can propagate the Fourier spectrum of the object, $S\left(u,v\right) = \widetilde{F}\left[O(x,y) = E \cdot t(x,y)\right]$ defined in Eq.(2.35), using the transfer function of the wave propagation phenomenon (see chap. 3 in Ref.[64]):

$$H\left(u,v,z'\right) = \exp\left[ikz'\sqrt{1-\left(\lambda u\right)^2-\left(\lambda v\right)^2}\right]. \tag{3.1}$$

The origin of this transfer function is based on the Helmholtz equation (see Eq.1.8) defined in the space domain for a given wavelength. The field amplitude after the free space propagation over a distance z' is obtained by computing the inverse Fourier transform:

$$E\left(x,y,z'\right) = \widetilde{F}^{-1}\left[S(u,v) \times H\left(u,v,z'\right)\right]. \tag{3.2}$$

This procedure reduces the computation time substantially in comparison to methods where the beam is propagated in spatial domain [118] and allows to consider different objects having any symmetry. The diagram of the free-space propagation algorithm is shown in Fig.3.1.

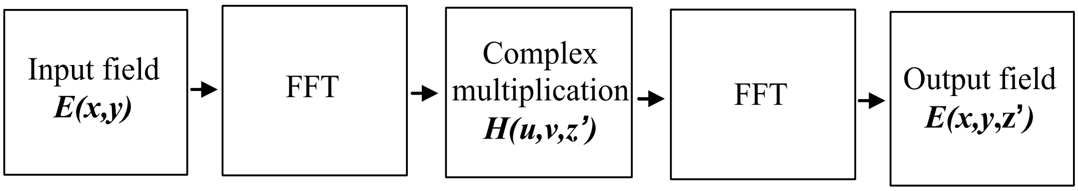

Figure 3.1: Algorithm of the free-space beam propagation over a distance z'. FFT denotes Fast Fourier Transform operation.

To calculate the output beam after passing through a lens of focal length f, the phase transformation related to its thickness variation in the paraxial approximation can be used [64]:

$$t_L\left(x,y\right) = \exp\left[-i\frac{\pi\left(x^2+y^2\right)}{\lambda f}\right]. \tag{3.3}$$

The first propagation is performed on a distance $z' = f$ from the object to the lens L_1 where t_L is applied. After that the beam propagates towards the sample located at z considering $z' = f + z$ in the the optical transfer function H ($z = 0$ at the focus of the lens L_1, negative values of z are considered for the sample situated between the focusing lens and the focus). The nonlinear response of the material is taken into account using $T(u,v)$ defined in Eq.(2.36). Next, the propagation is performed over a distance $z' = f - z$ where the phase transformation due to lens L_2 is applied. The final diffraction, calculated with $z' = f$, gives the field distribution $\left(U\left(x,y\right)\right)$ in the image plane. In this plane we can take into account the field stops or spatial filters (as in the eclipsed Z-scan) before calculating the image intensity.

3.3 Degenerate four-wave mixing using Z-scan technique [119]

To combine Z-scan with Forward Four Wave-Mixing we placed an object composed of three circular apertures (see Fig 3.2(a)) at the entry of the $4f$ setup (see Fig.3.3). The object was illuminated with an expanded laser beam giving a uniform (top-hat) field distribution inside the apertures. The geometrical image of the object was eclipsed in the image plane by one from two possible adapted field stops shown in Fig.3.2 (b) and (c) as well as in Fig.3.3. The first one stops all of the beams except the one fourth wave and the second one blocks just the geometrical image of the object in order to acquire the image of all the diffracted beams. The nonlinearly diffracted energy filtered through these stops was measured versus z, the sample position with respect to the geometrical focus ($z = 0$).

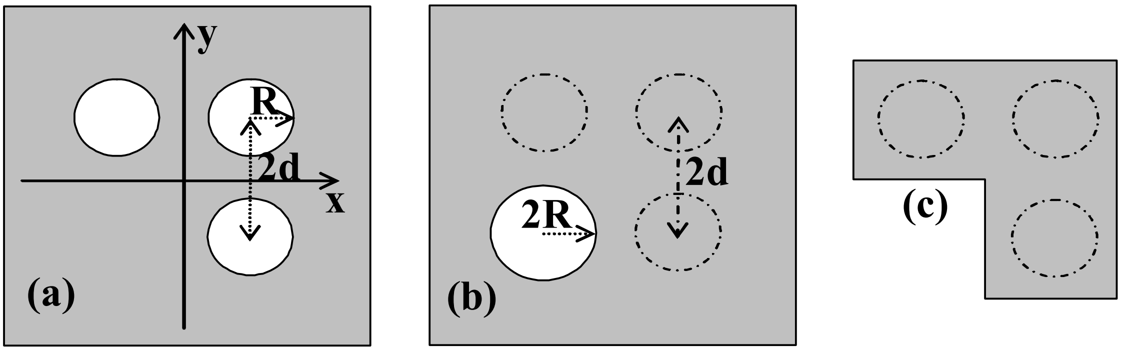

Figure 3.2: (a): The three circular apertures object. (b) and (c): Two different field stops placed in the image plane stopping the geometrical images of the circular apertures.

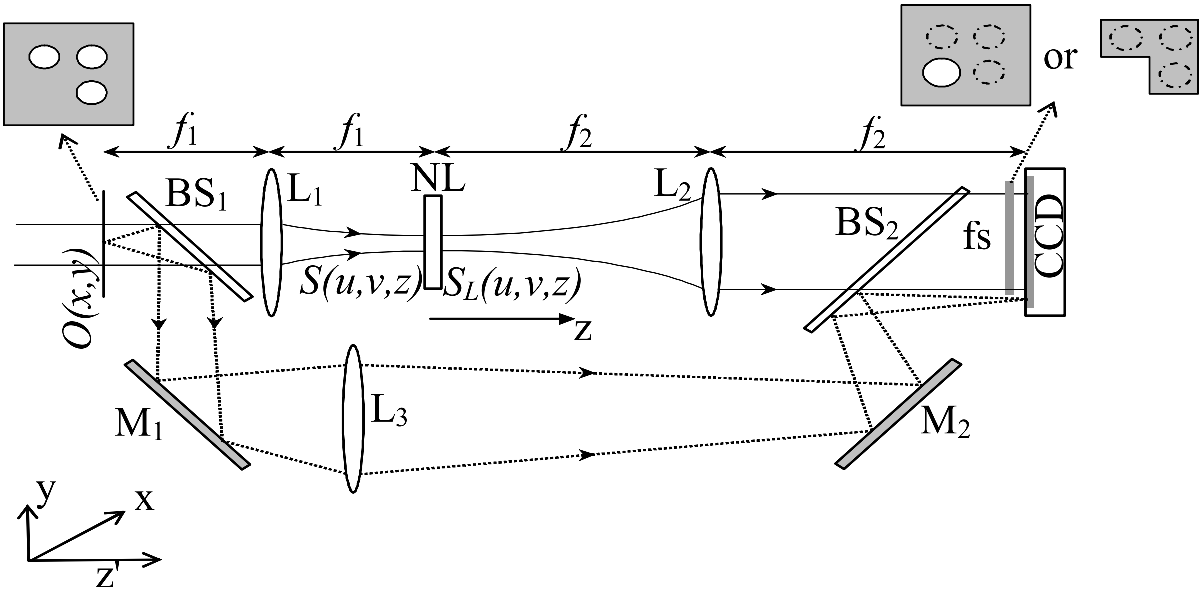

Figure 3.3: Schematic of the $4f$ coherent system imager used for wave-mixing experiment. The sample is located in the focal region. The labels refer to: the object O(x,y); lenses (L_1-L_3); mirrors (M_1,M_2); beam splitters (BS_1, BS_2); nonlinear material (NL), field stops (fs).

3.3.1 Numerical simulations

To simulate the experiment the transmittance of the object shown in Fig.3.2(a) is assumed to be:

$$t(x,y) = \zeta_R(x+d, y-d) + \zeta_R(x-d, y-d) + \zeta_R(x-d, y+d), \tag{3.4}$$

where $\zeta_R(x,y)$ is the circular function defined as equal to one if the radius $\sqrt{x^2+y^2}$ is less than R and zero elsewhere. Here R is the radius of the circular apertures and $2d$ is the distance between their centers. To simplify the problem we considered the particular case of a lossless Kerr material ($\alpha = 0$ and $\beta = 0$) characterized only by a cubic nonlinearity defined by n_2. Hence the transmittance of the relatively thin sample defined in Eq.(2.36) can be simplified to the following form:

$$T(u,v,z) = \frac{S_L(u,v,z)}{S(u,v,z)} = \exp\left[i\frac{2\pi}{\lambda} n_2 L I(u,v,z)\right], \tag{3.5}$$

where $I(u,v,z) \propto |S(u,v,z)|^2$ denotes the intensity of the laser beam within the sample placed in z-position with respect to the focal point. It is generally assumed [63] that Eq.(3.5) remains valid up to a maximum induced (on-axis) nonlinear focal phase shift less than $\Delta\Phi_0 = 2\pi n_2 L I_0/\lambda < \pi$ (I_0 being the on-axis peak intensity at the focus). The beam is propagated from the object up to the image plane using a method described in Section 3.2 (i.e. Eq.(3.1)-(3.3)). The image intensity I_{im} is calculated taking into account the transmittance of the field stop. For the stop shown in Fig.3.2(b) composed of a circular aperture situated at the position where a diffracted fourth wave should appear (induced by the nonlinear regime), this transmittance is given by $fs_b(x,y) = \zeta_{2R}(x+d, y+d)$. The radius of this field stop is two times larger than the radius of the object in order to capture all the energy diffracted through the circular aperture. On the other hand the field stop in Fig.3.2(c) is defined by three disks (circular stop functions) with a radius two times larger than the geometrical images of the three apertures composing the object. Such large opaque filter allows an easy alignment in the image plane: $fs_c(x,y) = 1 - [\zeta_{2R}(x+d, y-d) + \zeta_{2R}(x-d, y-d) + \zeta_{2R}(x-d, y+d)]$. The diffracted energy is calculated after numerically integrating the filtered image intensity: $E_D = \iint I_{im}(x,y) \times fs_i \, dxdy$, where $i = b$ or c.

To describe quantitatively the nonlinearly diffracted energy we define the diffraction efficiency as the quantity to be measured:

$$\eta = \frac{(E_{DNL} - E_{DL})}{E_{TOT}}, \tag{3.6}$$

where E_{DNL} is the diffracted energy in the nonlinear regime (with high laser intensity), E_{DL} is the diffracted energy in the linear regime (with low laser intensity) and E_{TOT} is the total energy detected in the nonlinear regime without any field stop at the output.

3.3.2 Experiment and results

The excitation is provided by a Nd:YAG laser delivering 17 ps single pulses at $\lambda = 1.064\ \mu m$ with 10 Hz repetition rate. The input intensity is varied by means of a half-wave plate and a Glan prism, in order to maintain linear polarization. A beam splitter at the entry of the setup (Fig.3.3) permits to monitor any fluctuation (through lens L_3) occurring in the incident laser beam. Other experimental parameters are: $f_1 = f_2 = 20\ cm$ (focal length of lens L_1 and L_2). The radius of the three circular apertures at the entry is $R = 0.45\ mm$ and the half of the distance between their central points is $d = 1\ mm$. The latter is small compared to the beam-waist of the incident laser beam (1 cm). One millimeter thick fused silica cell filled with non-absorbing CS_2 was used as a nonlinear medium. The image receiver is a cooled CCD camera (-30°C) with 1000×1018 pixels, each of them is $12 \times 12\ \mu m^2$. The camera pixels have 4095 gray levels. The comparison between the experimental nonlinearly filtered image and its numerical simulation for a sample placed at $z = 0$ is shown in Fig.3.4. Physically, in the focal plane region of lens L_1 the intensity distribution pattern creates a combination of circular and sinusoidal gratings inside the nonlinear material. For an instantaneous response of the medium, the self-diffracted spectrum on this induced pattern generates diffracted beams at the output of the sample. Fig.3.4(a) represents the natural logarithm of the acquisition in the image plane in presence of the spatial filter (Fig.3.2(c)) stopping only the geometrical image of the apertures. The on-axis peak intensity of these three interfering beams was $I_0 = 1.9$ GW/cm^2 giving $\Delta\Phi_0 = 0.34$. The focal on-axis intensity (I_0) was calibrated considering the value of n_2 for CS_2 at 1.064 μm given in reference [63]. Each circular beam has an Airy radius large enough to consider the corresponding Rayleigh range as much higher than the sample thickness. Fig.3.4(b) shows the simulation image (natural logarithm of the intensity) obtained with the same experimental parameters. The good agreement between these two images validates our model and the corresponding numerical simulation. Typically as for the classical F-DFWM in a box-car configuration we distinguish nine intense diffracted waves in the acquisition. For $\Delta\Phi_0 = 0.34$, the efficiency of the diffracted energy is about 6×10^{-4} for three of them (see Fig.3.4(b)) and 6 times less for the six others.

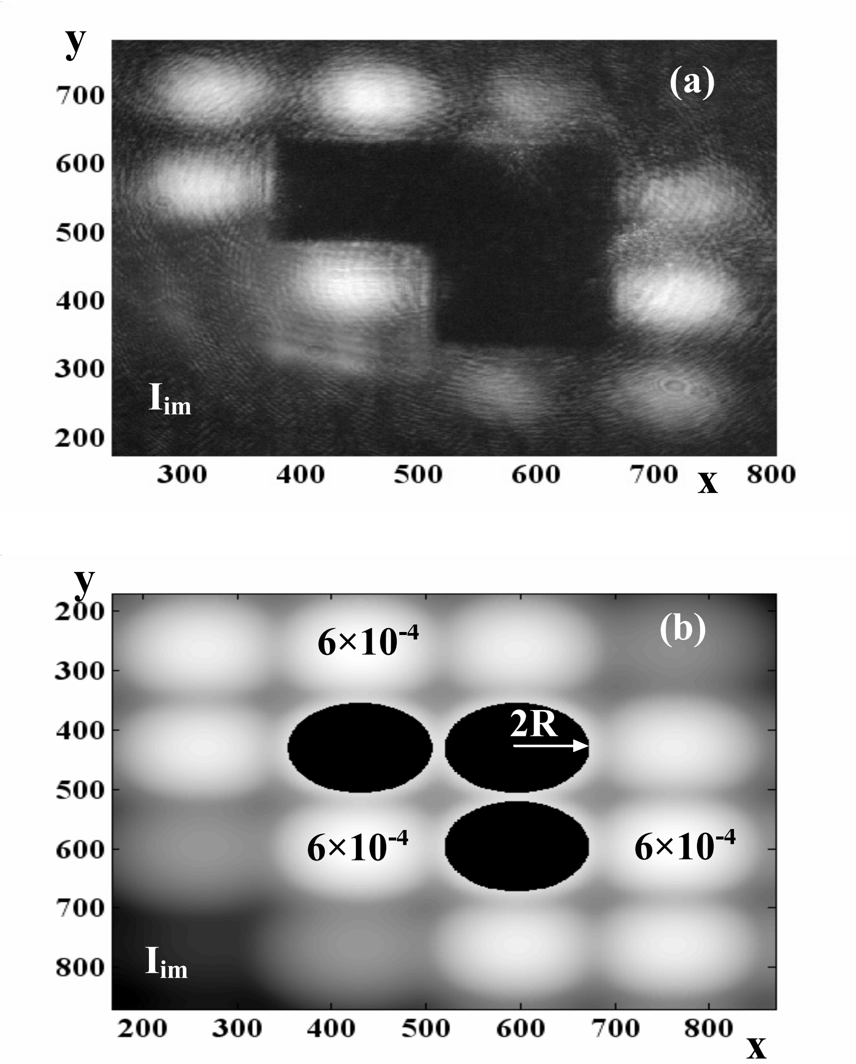

Figure 3.4: Comparison between the experimental acquisition (a) and the numerically calculated one (b) of the images obtained at $z = 0$ for $\Delta\Phi_0 = 0.34$. The "L" pattern appearing in (a) is the spatial filter defined in figure 3.2(c). The coordinates x and y are expressed in number of pixels and the natural logarithm is used to enhance lower intensity.

Two sets of Z-scan acquisitions are carried out for two kinds of field stops placed just in front of the camera. The experimental results as well as the related numerical simulations are shown in Fig.3.5(a). A perfect agreement between theory and experimental data can be noticed. Fig.3.5(b) shows the evolution of the diffracted efficiency (η) versus $I(z)$, the on–axis incident intensity at z, a given sample position. The evolution has a typical quadratic dependence characterizing wave-mixing experiments. Note that, the diffraction efficiency related to all the diffracted beams is 5 times higher than that for one intense diffracted wave. Therefore, the signal to noise ratio is enhanced in the n_2 measurement when one takes into account all diffracted beams. Moreover we found numerically that the diffraction efficiency is independent of geometrical parameters of the object when R, the aperture radius of circular apertures is at least 2 times smaller than d, the half of the distance between their centers. In this geometrical configuration there is no spatial overlapping in the image plane between the diffracted beams and the geometrical image of the object. Based on numerical fitting and assuming a relatively low nonlinearity ($|\Delta\Phi_0| < 1$), we found a simple quadratic expression relating the efficiency of all the diffracted waves to the maximum of the nonlinear phase shift (within 1% accuracy):

$$\eta = 2.41 \times |\Delta\Phi_0|^2 \times 10^{-2}, \tag{3.7}$$

while for the one intense forward diffracted beam, the efficiency is given by $\eta = 5.13 \times |\Delta\Phi_0|^2 \times 10^{-3}$. The sensitivity of the method can be defined as the slope of the curve giving the signal (η) versus $\Delta\Phi_0$ [63]. It easy to notice that by using all diffracted waves the sensitivity is enhanced by a factor of $2.41/0.513 \approx 5$.

One of the most important advantages of this technique is the simplicity of the optical alignment in comparison to F-DFWM. However as in the classical DFWM, the inconvenience of this method is that we are not able to separate measurement of the nonlinear absorption and the nonlinear refraction. Indeed, the signal is sensitive only to the modulus of the third order susceptibility. When compared to Z-scan and EZ-scan, an advantage of this method is that it does not require a perfect Gaussian incident beam. The use of this method with a reference material for calibration is recommended.

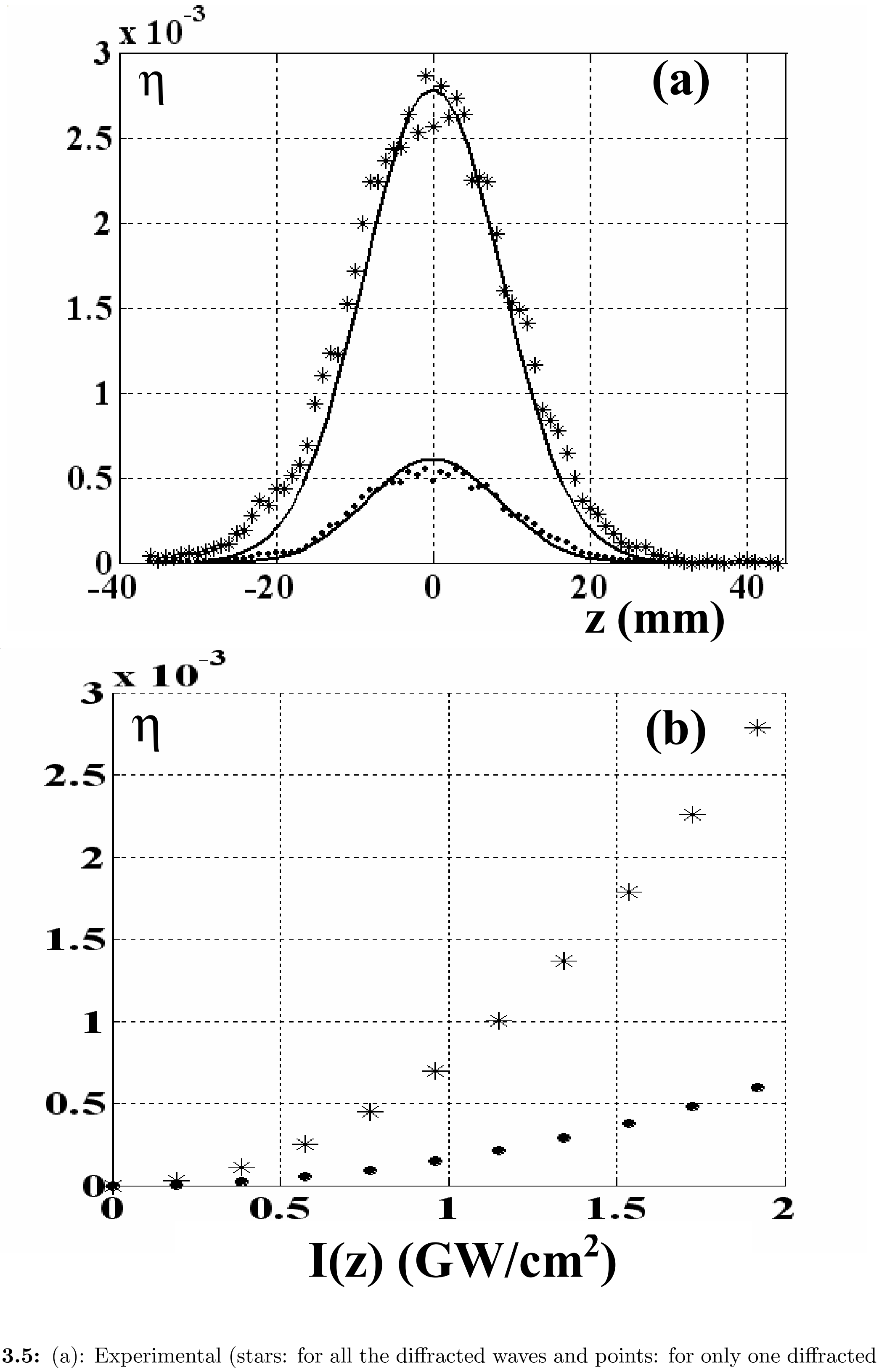

Figure 3.5: (a): Experimental (stars: for all the diffracted waves and points: for only one diffracted beam) and theoretical (solid line) efficiency of the diffracted energy versus z, the sample position for $I_0 = 1.9$ GW/cm^2 in 1 mm CS_2 at 1064 nm ($\Delta\Phi_0 = 0.34$). (b): diffracted efficiency in nonlinear regime versus $I(z)$, the on–axis incident intensity for z, at a given sample position.

3.4 Comparison of sensitivities of nonlinear characterization techniques

The use of three circular aperture objects is just a particular case among all the possible nonlinear imaging processors inside the $4f$ system. One can easily notice a possibility of performing different measuring methods as Z-scan, EZ-scan, I-scan, different wave-mixing or NIT-PO by matching the field stop in the image plane with the object at the entry of the $4f$ system. Therefore all these seemingly different techniques can be considered as special cases of the same nonlinear imaging process in the low excitation regime. Consequently, the measurements of nonlinearly diffracted energy in the image plane of a $4f$ system provide a good tool for comparison of optical sensitivities corresponding to these different techniques. The sensitivity can be defined for all of them as $d\eta/d\left(\Delta\Phi_0\right)$, i.e. the slope of the curve giving the diffraction efficiency (η) versus nonlinear on-axis focal phase shift ($\Delta\Phi_0$). The definition of η given in Eq.(3.6) has a precious advantage to avoid a 'zero division' with non existing energy, what could happen when one performs normalization to the linear regime in eclipsing experiments as in the classical EZ-scan. In such a case when a large field stop is used (e.g. obscuration disk in EZ-scan), the nonlinear signal is divided by a very small quantity (very low linear signal) and consequently the sensitivity is increased artificially sometimes by few orders of magnitude (e.g. EZ-scan is much more sensitive than Z-scan) but experimentally will always reach an asymptotic value defined by the noise level of the photo-detector. Here in Eq.(3.6) the diffracted energy is normalized to $E_{TOT,}$ the total energy which is typically three orders of magnitude higher than the nonlinear signal in the low excitation regime ($|\Delta\Phi_0| < 1$). Thus no problem of "division by zero" can happen and the sensitivity can be compared between all those that have been considered as different techniques (together when taking into account the maximum of the signal to noise ratio).

In this section we will compare directly the sensitivity of the $4f$ system with different objects at the entry representing different wave mixing configurations as well as different techniques as I-scan, Z-scan, EZ-scan and NIT-PO. The relation between η and $\Delta\Phi_0$ will be provided for each case and the optimization of the signal to noise ratio will be proposed. Finally the influence of nonlinear absorption will be also discussed.

3.4.1 Sensitivity of multi-wave mixing techniques in I-scan configuration [120]

One of advantage of the wave-mixing technique is that we can obtain a maximal signal at the focus of the converging lens when the induced nonlinearity is the highest (see Fig.3.5(a)). Furthermore one can avoid Z-scanning the material by placing the sample at $z = 0$ where the signal to noise ratio is optimized and varying the incident intensity i.e. performing I-scan measurement in the focus as it is usually done in DFWM experiments. We will compare here the sensitivity of different wave-mixing configurations inside the $4f$ system for a sample located at the focus. To begin we will consider the simple case of a lossless material ($\alpha = 0$ and $\beta = 0$, Eq.(3.5)). Since the sample is fixed at the focus the simulations can be performed in a I-scan configuration, i.e. using the numerical model described in section 2.5.1. We consider the objects at the entry of the $4f$ system composed of

i) one circular aperture (top-hat beam): $t_1(x, y) = \zeta_R(x, y)$

ii) two circular apertures: $t_2(x, y) = \zeta_R(x + d, y) + \zeta_R(x - d, y)$

iii) three circular apertures:
$t_3(x, y) = \zeta_R(x + d, y - d) + \zeta_R(x - d, y - d) + \zeta_R(x - d, y + d)$

iv) four circular apertures:
$t_4(x, y) = \zeta_R(x + d, y - d) + \zeta_R(x - d, y - d) + \zeta_R(x - d, y + d) + \zeta_R(x + d, y + d)$.

One can find different adapted opaque disks ($fs_i(x, y) = 1 - t_i(x, y)$, $i = 1, 2, 3, 4$) in the image plane. In Fig.3.6(a) we can see the simulated images of the diffracted beams for all considered objects. We can distinguish the zero-order diffraction around the geometrical images of the apertures where the spatial eclipsing filters are placed. It is related to the nonlinear broadening of the fundamental beams. Furthermore we can notice that, for an increasing number of incident waves there are more intense diffracted beams. Note that the two-apertures object corresponds to the Forward-Scattering configuration of DFWM while the three-apertures one is related to the box-car configuration (see Section 2.3.2). In Fig.3.6(b) we can see the variation of the diffraction efficiency versus a, the radius of the output opaque disks (field stops). It is evident that whatever the object is, the maximal signal is obtained for $a = R$. Particularly, for one circular aperture (top hat beam) the matched field stop will be of course the one that stops the geometrical image and let pass the nonlinearly deflected rays. The same evidence is valid for multi-apertures object. Moreover we have checked that we obtain exactly the same results as in Fig.3.6(b) by using circular apertures instead of opaque disks at the output of the system. Indeed, the variation of the diffracted energy outside the holes is the same as the variation of the energy in the central part of fundamental beams passing through output apertures. Furthermore the diffraction efficiency has the same order of magnitude for all objects, however, the best signal is found with one circular aperture at the entry for $a = R$. Under the latter condition the efficiency is decreasing with the number of apertures, but in the case of three and four apertures, the difference is not significant (~1%). For $a = 2R$ (where the optical alignment is easier) as in DFWM combined with Z-scan experiment described in Section 3.3 only the orders of diffraction higher than zero contribute to the signal and the efficiency increases with the number of the apertures.

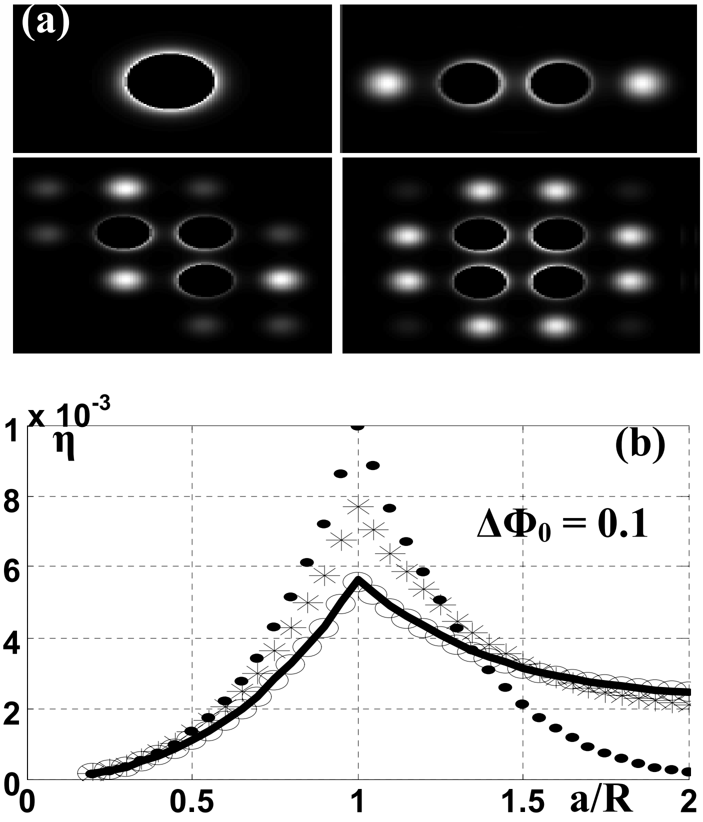

Figure 3.6: (a) Numerical simulation showing the images of the diffracted beams with objects composed of one, two, three or four circular apertures. The adapted field stops appear in black in the image plane. (b) Diffraction efficiency versus the normalized opaque disk radius; filled circles, stars, empty circles and solid line are for one, two, three and four apertures respectively.

The dependence between the signal (η) versus $\Delta\Phi_0$ is shown in Fig.3.7(a) and (b) for $a = R$ and $a = 2R$ respectively. For clarity we do not show the curve for four apertures object giving almost the same result as three apertures one. In all cases we found that η is proportional to $|\Delta\Phi_0|^2$ in the low excitation regime ($|\Delta\Phi_0| < 1$). In the case of $a = R$ we found:

i) one circular aperture (top-hat beam): $\eta = 9.8 \times |\Delta\Phi_0|^2 \times 10^{-2}$
ii) two circular apertures: $\eta = 7.5 \times |\Delta\Phi_0|^2 \times 10^{-2}$
iii) three circular apertures: $\eta = 5.4 \times |\Delta\Phi_0|^2 \times 10^{-2}$
iv) four circular apertures: $\eta = 5.3 \times |\Delta\Phi_0|^2 \times 10^{-2}$

These results indicate that the highest sensitivity ($d\eta/d\,(\Delta\Phi_0)$) at a given intensity ($\Delta\Phi_0$) is obtained for one circular aperture object (top hat beam). Hence the highest sensitivity is obtained for the object giving the highest signal to noise ratio. It is because the variation of the diffraction efficiency expresses the variation of the optical energy contributing to the captured signal in the photodetector.

The optical alignment of the field stop is easy when the radius of the eclipsing disks is higher than the radius of the apertures at the entry. The simulation for $a = 2R$ shown in Fig.3.7(b) gives the following results:

i) one circular aperture (top-hat beam): $\eta = 0.2 \times |\Delta\Phi_0|^2 \times 10^{-2}$
ii) two circular apertures: $\eta = 2.1 \times |\Delta\Phi_0|^2 \times 10^{-2}$
iii) three circular apertures: $\eta = 2.4 \times |\Delta\Phi_0|^2 \times 10^{-2}$
iv) four circular apertures: $\eta = 2.4 \times |\Delta\Phi_0|^2 \times 10^{-2}$

In this case the results indicate that the sensitivity increases with the number of the mixing waves and reaches an asymptotic value for more than three circular apertures.

Finally, in order to validate our numerical simulation we have also performed the experimental acquisitions. In Fig.3.7(c) we can see the variation of the experimental diffraction efficiency versus the nonlinear phase-shift obtained with CS_2 and three circular apertures object which image is eclipsed by three obscuration disks with radii $a = 2R$. All the experimental parameters are the same as described in Section 3.3. The numerical fitting of the experimental points gives exactly the same quadratic relation ($\eta = 2.4 \times |\Delta\Phi_0|^2 \times 10^{-2}$) as in our simulation therefore validating all our numerical study.

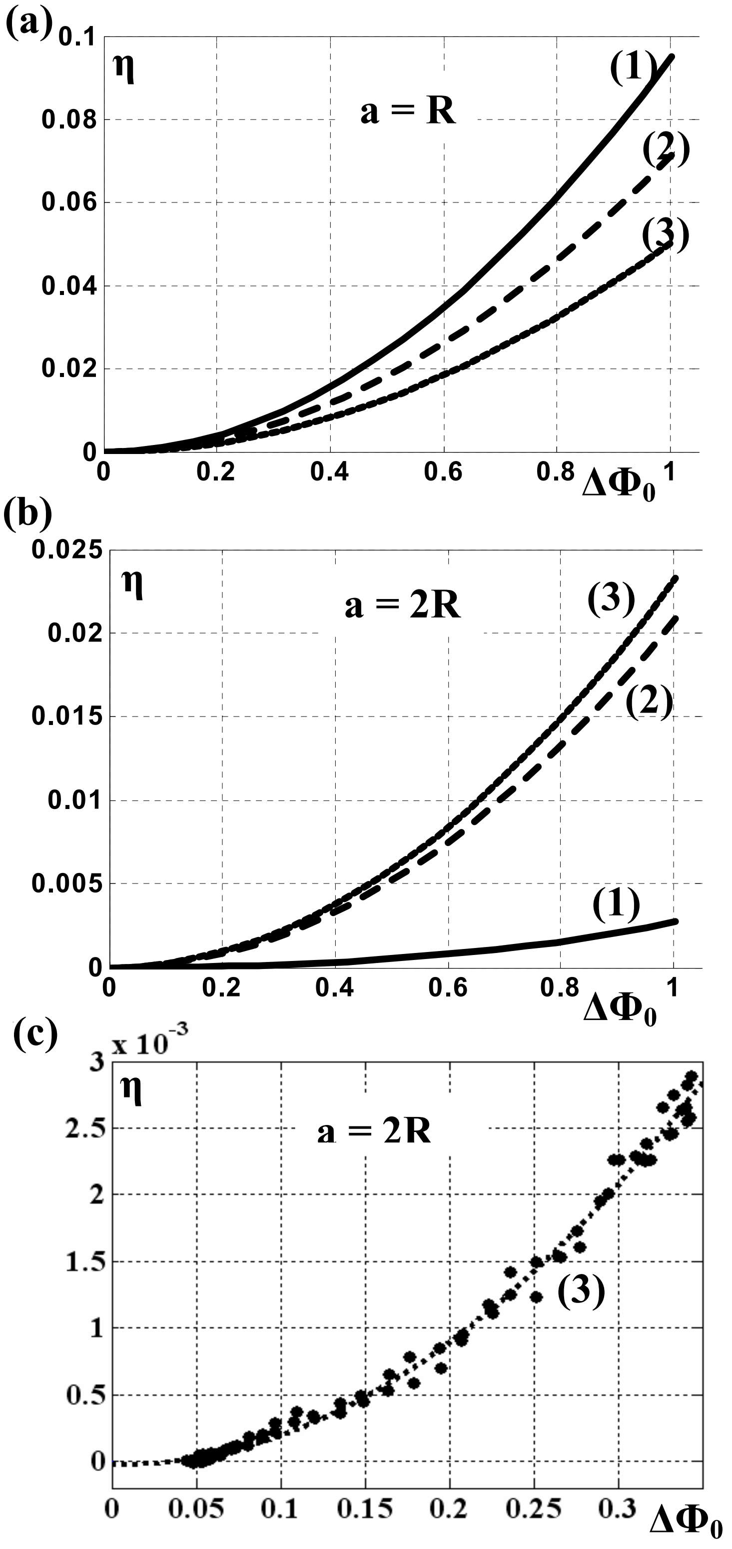

Figure 3.7: Diffraction efficiency versus the nonlinear phase shift ($\Delta\Phi_0$): (1), (2) and (3) for one, two and three apertures respectively, (a) simulation with opaque disks of radii $a = R$, (b) simulation with opaque disks of radii $a = 2R$, (c) experimental data obtained with object composed of three circular apertures and adapted field stops with radii $a = 2R$. The dotted curve is the numerical simulation (3) in Fig.3.7(b).

3.4.2 Multi-wave mixing experiments in presence of nonlinear absorption [121]

In the previous section we discussed different configurations of wave-mixing inside the $4f$ system for a pure refractive case (i.e. $\alpha = 0$ and $\beta = 0$). In such situation Eq.(3.5) was sufficient to describe nonlinear response of the material. In this section we will discuss an influence of absorption on sensitivity of wave-mixing experiments. In this more general case in presence of linear and nonlinear absorption ($\alpha \neq 0$ and $\beta \neq 0$), the more general Eq.(2.36) must be used in order to describe the nonlinear response of the medium. This relation can be rewritten in a more convenient way using the concept of the effective nonlinear phase shift:

$$T(u,v) = \frac{S_L(u,v)}{S(u,v)} = \left\{\exp(-\alpha L)\left(1+q(u,v)\right)\right\}^{-1/2} \exp\left[i\Delta\Phi_{NL}^{eff}(u,v)\right]. \tag{3.8}$$

Let us recall $q(u,v) = \beta L_{eff} I(u,v)$ with $L_{eff} = \left(1-\exp(-\alpha L)\right)/\alpha$ representing the effective length and $I(u,v) = 2\epsilon_0 n_0 c \left|S(u,v)\right|^2$ denotes the intensity of the laser beam within the sample. Here $\Delta\Phi_{NL}^{eff}$ can be considered as the effective nonlinear phase shift:

$$\Delta\Phi_{NL}^{eff} = \frac{2\pi}{\lambda} n_2 L_{eff} I_{eff}, \tag{3.9}$$

where $I_{eff}(u,v) = I(u,v)\ln\left(1+q(u,v)\right)/q(u,v)$ is the effective intensity. In the particular case when the linear absorption $\alpha = 0$ and the nonlinear one $\beta = 0$ (no losses), $\Delta\Phi_{NL}^{eff}$ reduces to $\Delta\Phi_{NL} = 2\pi n_2 L I/\lambda$ describing phase shift in non-absorbing medium (see Eq.(3.5)). The idea of the effective length (L_{eff}) and the effective intensity (I_{eff}) is commonly used to simplify the calculation when linear and nonlinear absorptions are present [101][122] respectively. It allows the nonlinearity to be computed using the same expressions as for non-absorbing materials. To clarify the influence of nonlinear absorption on wave-mixing processes inside the $4f$ system we will derive analytical calculations explaining the distribution of the diffracted intensity in the image plane for the three apertures objects. Moreover numerical calculations will be performed in order to compare the sensitivity of wave-mixing techniques in I-scan configuration with and without absorption.

Analytical calculations

Let us consider now the object composed of three circular apertures as seen in Fig.3.2(a). For numerical simulation the transmittance of this object can be described by three circular functions as in Eq.(3.4). In the analytical calculations presented here, we will simplify the problem by approximating the three apertures to three single points placed at the center of each circle. Hence the transmittance of the object can be expressed by:

$$t(x,y) = \delta(x-d,y) + \delta(x,y-d) + \delta(x-d,y-d), \tag{3.10}$$

where $\delta(x,y)$ is the Dirac distribution and d is the shift of these distributions from the origin of the coordinate system (see Fig.3.8) along x and y directions. The amplitude $S(u,v)$ of the electric field in the back focal plane ($z = 0$) of lens L_1 is given by the Fourier transform defined in Eq.(2.35). Calculating the Fourier transform of $O(x,y) = E \cdot t(x,y)$ in this simple case we get

$$S(u,v) = E\left[e^{-i2\pi ud} + e^{-i2\pi vd} + e^{-i2\pi(u+v)d}\right]. \tag{3.11}$$

The electric field at the exit face of the sample is $S_L(u,v) = T(u,v)\,S(u,v)$, where the transmittance $T(u,v)$ is given by Eq.(3.8). For convenience, we rewrite $q(u,v)$ defined in this equation as

$$q(u,v) = 2Q\left|S(u,v)\right|^2, \tag{3.12}$$

where $Q = \beta L_{eff}K/2$, with $K = 2\epsilon_0 n_0 c$. We also set $\xi = 2\pi n_2 L_{eff} K/\lambda$. Assuming both a small nonlinear absorption ($q(u,v) \ll 1$) and a small effective phase shift ($\Delta\Phi_{NL}^{eff} \ll 1$), we can expand the transmittance $T(u,v)$ to the first order in intensity, so that

$$S_L(u,v) \approx e^{-\alpha L/2}\left[1 + (i\xi - Q)\left|S(u,v)\right|^2\right] S(u,v). \tag{3.13}$$

By developing the latter we get

$$\begin{aligned} S_L(u,v) \approx\ & E e^{-\alpha L/2}\left(1 + 5(i\xi - Q)E^2\right)\left[e^{-i2\pi ud} + e^{-i2\pi vd} + e^{-i2\pi(u+v)d}\right] \\ & + e^{-\alpha L/2}(i\xi - Q)E^3[2 + 2e^{-i4\pi ud} + 2e^{-i4\pi vd} + e^{i2\pi(u-v)d} \\ & + e^{i2\pi(v-u)d} + e^{i2\pi(v-2u)d} + e^{i2\pi(u-2v)d} + e^{-i2\pi(v+2u)d} + e^{-i2\pi(u+2v)d}]. \end{aligned} \tag{3.14}$$

Then the output electric field is obtained through the inverse Fourier transform: $U(x,y) = \widetilde{F}^{-1}[S_L(u,v)]$ which, using Eq.(3.14), reduces to:

$$\begin{aligned} U(x,y) \approx\ & Ee^{-\alpha L/2}\left(1 + 5(i\xi - Q)E^2\right)t(x,y) \\ & + e^{-\alpha L/2}(i\xi - Q)E^3[2\delta(x,y) + 2\delta(x-2d,y) \\ & + 2\delta(x,y-2d) + \delta(x+d,y-d) + \delta(x-d,y+d) \\ & + \delta(x-2d,y+d) + \delta(x+d,y-2d) + \delta(x-2d,y-d) + \delta(x-d,y-2d)], \end{aligned} \tag{3.15}$$

where $t(x,y)$ (corresponding to the geometrical image) is defined by Eq.(3.10). The expression in Eq.(3.15) is schematically represented in Fig.3.8. It can be seen that the spatial distribution of the intensity (squared electric field) is similar to the experimental one shown in Fig.3.4(a). Moreover three diffracted beams (with their centers located at $(0,0)$, $(0,2d)$ and $(2d,0)$) have their intensities four times higher than that of the other diffracted beams laying outside the geometrical image of the input apertures. This result is also in very good agreement with the experimental observation and the numerical simulation. What is the

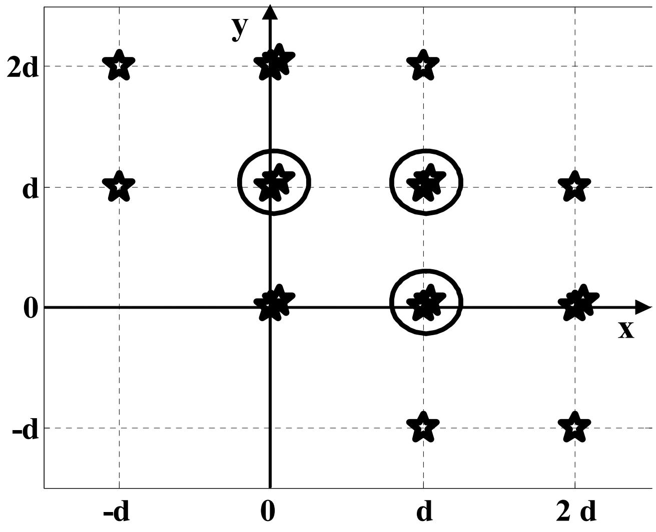

Figure 3.8: The amplitude $U(x,y)$ of the output electric field. Each star corresponds to a quantity $e^{-\alpha L/2}(i\xi - Q)E^3$, the circles represent the output geometrical image of the apertures with an amplitude $Ee^{-\alpha L/2}\left[1 + 5(i\xi - Q)E^2\right]$.

most important is the fact that both the nonlinear refraction (ξ) and the nonlinear absorption (Q) contribute to the output intensity due to diffraction on the induced phase and amplitude gratings. The theoretical analysis presented here can be easily extended for any objects with a random number of the apertures.

Numerical calculations

Since the absorptive (Q) and refractive (ξ) contributions to the output signal are coupled (see Eq.(3.15)), the contribution due to nonlinear refractive index (n_2) cannot be separated from that of nonlinear absorption coefficient (β). Hence we have to proceed as usually; β (together with α) has to be determined separately through transmission measurements by acquiring the output intensity versus the input one. Knowing α and β, the nonlinear refractive index can be found using the wave-mixing technique. It is advantageous to determine n_2 by using a simple quadratic expression relating the diffraction efficiency (η) with the maximal phase shift as it is done for non-absorbing media. However, for the nonlinearly absorbing materials, we have to take into account additionally the coupling between the nonlinear absorption and the nonlinear refraction, both contributing to the diffracted signal. For this purpose, let us define a coupling factor as $\gamma = Q/\xi = q_0/2\Delta\Phi_0 = \beta/2kn_2$, where $q_0 = \beta L_{eff} I_0$ with I_0 denoting the focal on-axis intensity. In the transparency region the coupling coefficient is generally less than one ($\gamma < 1$) in a wide variety of different materials [63]. The latter condition means that the imaginary part of the third order susceptibility is not larger than the real part. In order to find a relation between η, $\Delta\Phi_0$ and γ we have performed numerical simulations using the model described in section 2.5.1 with the three circular aperture object given in Eq.(3.4) and a field stop composed of three opaque disks with radius blocking the geometrical image of the apertures along with the diffraction occurring in the vicinity. When $\gamma < 1$ we found that the following relation describes the variations of η within 10% accuracy for $|\Delta\Phi_0| < 1$:

$$\eta = 2.41 \times |\Omega|^2 \times 10^{-2}, \tag{3.16}$$

where $\Omega = (1+\gamma^2)^{1/2}\,\Delta\Phi_0^{eff}$ is defined as the generalized effective phase shift in focus. Here $\Delta\Phi_0^{eff} = \Delta\Phi_{NL}^{eff}(0,0)$ is the effective on-axis phase shift in focus defined in Eq.(3.8)-(3.9). In Fig.3.9(a) we can see the comparison between this relation (solid lines) and the numerically calculated η versus the effective phase shift ($\Delta\Phi_0^{eff}$) for $\gamma = 0$ (filled dots), $\gamma = 0.5$ (empty circles) and $\gamma = 1$ (stars). The same η is plotted versus the generalized effective phase shift Ω in Fig.3.9(b), proving that whatever the absorption is ($\gamma < 1$), the diffraction efficiency is always described by the more general Eq.(3.16). Note that in the limiting case where there is no absorption ($\alpha = 0$ and $\beta = 0$), Ω reduces to $\Delta\Phi_0$ and then Eq.(3.16) is identical to Eq.(3.7).

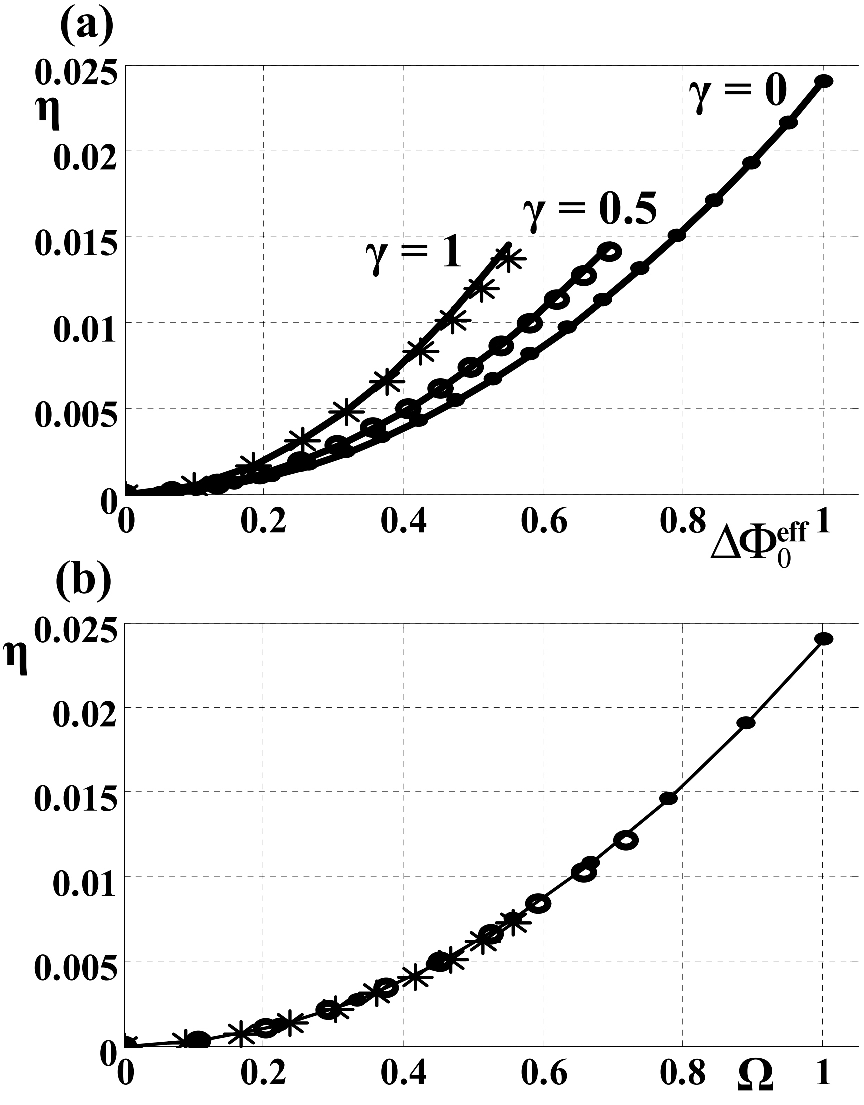

Figure 3.9: Calculated diffraction efficiency for $\gamma = 0$ (filled dots), $\gamma = 0.5$ (empty circles) and $\gamma = 1$ (stars) (a) versus $\Delta\Phi_0^{eff}$, the effective nonlinear phase shift, (b) versus Ω, the generalized effective nonlinear phase shift The solid lines are described by Eq.(3.16)

The same numerical simulations can be performed for objects composed of one, two, and four circular apertures. We have checked that the quadratic relations provided in previous section for each object in the pure refractive case can be easily extended by replacing $\Delta\Phi_0$ by Ω to include absorptive effects. These relations are summarized in Tab.(3.1), where column 2 contains the expressions which are valid when the radius a of the opaque disks composing the field stop (placed at the output of the system) is equal to the radius R of the circular apertures composing the object. In column 3 we can find the relations which hold when a is twice larger than R (advantageous for optical easy alignment).

Object	$a = R$	$a = 2R$
one aperture	$\eta = 9.8 \times \lvert\Omega\rvert^2 \times 10^{-2}$	-
two apertures	$\eta = 7.5 \times \lvert\Omega\rvert^2 \times 10^{-2}$	$\eta = 2.1 \times \lvert\Omega\rvert^2 \times 10^{-2}$
three apertures	$\eta = 5.4 \times \lvert\Omega\rvert^2 \times 10^{-2}$	$\eta = 2.4 \times \lvert\Omega\rvert^2 \times 10^{-2}$
four apertures	$\eta = 5.3 \times \lvert\Omega\rvert^2 \times 10^{-2}$	$\eta = 2.4 \times \lvert\Omega\rvert^2 \times 10^{-2}$

Table 3.1: Quadratic relationships relating the diffraction efficiency to the generalized input effective phase shift in the wave-mixing techniques using the 4f system with different objects at the entry (composed of one, two, three and four circular apertures).

These simple quadratic relations have an interesting implication for the evaluation of the sensitivity of the wave-mixing techniques. For pure nonlinear refraction the sensitivity is defined by $d\eta/d\Delta\Phi_0$. In the more general case, when the absorption is present and because the contribution to the signal is due to both absorptive and refractive grating effects we should use Ω as the input, therefore generalizing the sensitivity to $d\eta/d\Omega$. Following this definition and according to the relations given in Tab.(3.1), one can easily notice that the nonlinear absorption does not affect the sensitivity of the wave-mixing techniques when compared to pure refractive case. Physically, this could be understood by the fact that the sensitivity should be independent from the material. The absorption in the low excitation regime should not change the performance of the measurement system.

In summary, for a given material the nonlinear characterization should begin by measuring α and β using the square modulus of Eq.(3.8) and by performing simple transmission measurements without any object at the entry and any field stop at the output. After that, the wave mixing experiment provides the diffraction efficiency using the $4f$ imaging system. Finally the nonlinear coefficient can be determined by simply fitting the quadratic relation (for a given object) to the measured data of η. The only unknown parameter in this relation is n_2, since the on-axis intensity I_0 can be calibrated using well known reference non-absorbing materials.

3.4.3 Input Gaussian beam using an I-scan configuration [121]

In this section we will consider a single Gaussian beam at the entry of the $4f$ system and a sample placed at the focal plane (see Fig.3.10). In such a case the object is defined as $E = E_0 \exp\left[-\left(x^2+y^2\right)/w_e^2\right]$, where E_0 denotes the on-axis amplitude of electric field and w_e is the beam waist at the entry of the setup (at the object plane). The question here is to know what is the optimized field stop in this case. The circular symmetry of the input beam at the entry imposes a circular field stop at the output. The spatial extension of the amplitude field is theoretically infinite so the question is to find the radius of this circular aperture or disk in order to increase the optical signal for a given noise inside the system.

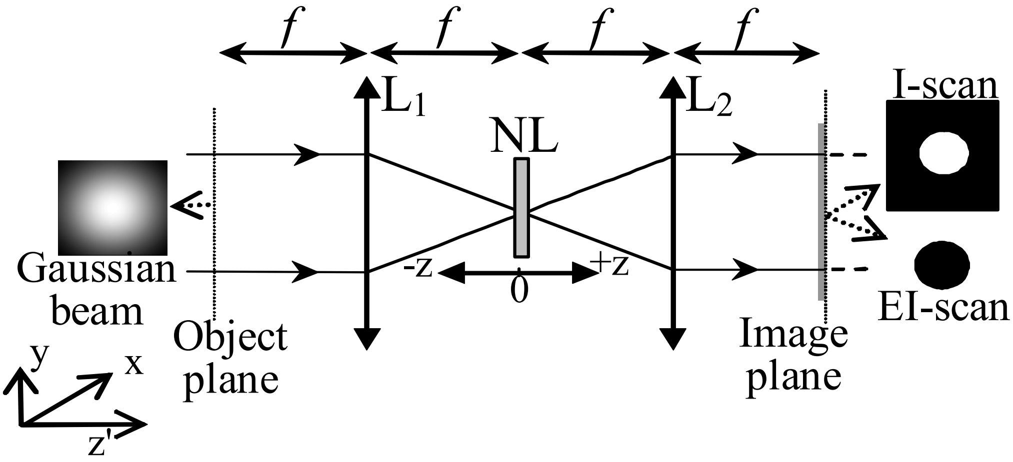

Figure 3.10: Schematic of the $4f$ imaging system. The labels refer to: lenses (L_1-L_2) and their focal lengths (f), nonlinear medium (NL). The object at the entry is the Gaussian beam, while a circular aperture or an opaque disc is placed in the image plane to obtain I-scan or EI-scan configuration, respectively.

First we performed numerical simulation without any field stops in the image plane (as in Ref.[103]) in order to show the alteration of the image profile after nonlinear filtering due to a pure nonlinear refraction (i.e. $\alpha = 0$ and $\beta = 0$). In Fig.3.11(a) we can see profiles of the far-field spatial distortions of an input Gaussian beam after passing through the nonlinear medium for four different nonlinear phase shifts $\Delta\Phi_0$ $(0, 1\ rad, 2\ rad, 2.7\ rad)$. We clearly

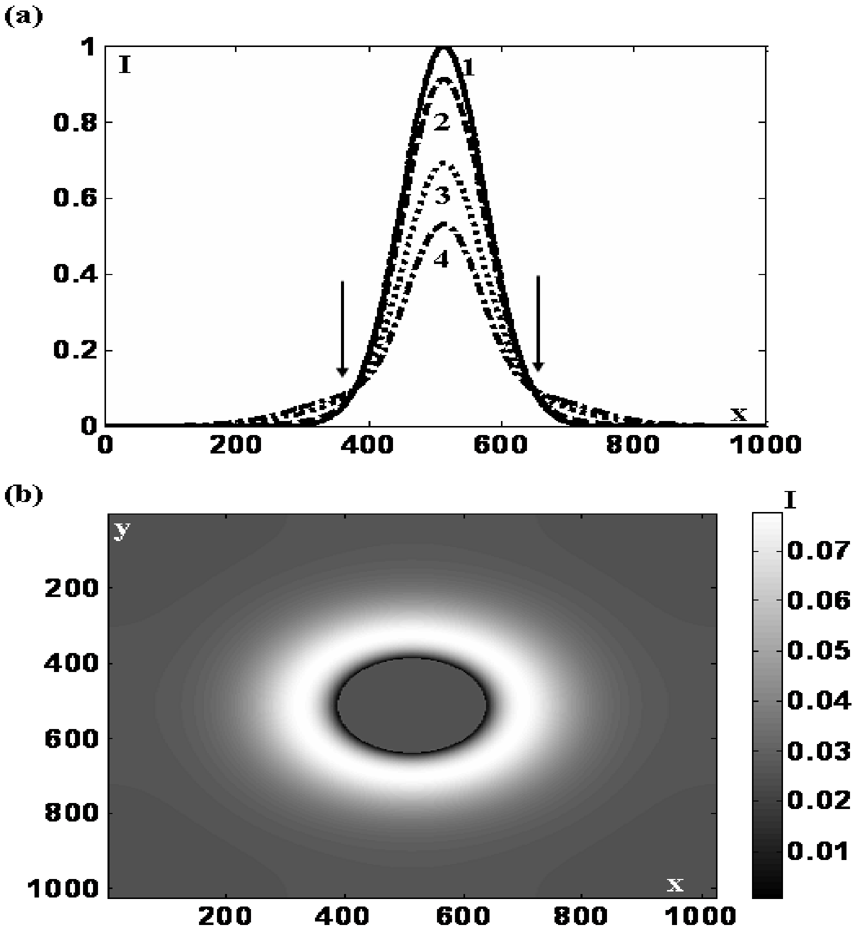

Figure 3.11: (a) The output beam image profiles for different nonlinear phase shift: The solid curve (1) is obtained for $\Delta\Phi_0 = 0$ (linear regime), the curves (2), (3) and (4) are obtained for $\Delta\Phi_0 = 1\ rad$, $2\ rad$ and $2.7\ rad$, respectively. The arrows indicate the points of intersection corresponding to all these profiles. (b) Numerical simulation showing the positive part of the image subtraction corresponding to (4) - (1). The coordinates (x, y) are in pixels.

observe a diffracted energy into the wings of the transmitted beam (nonlinear broadening). One can notice that for higher $\Delta\Phi_0$ more energy is transferred from the central area of the beam to its borders. Fig.3.11(b) presents the simulated image showing the positive area after subtraction of the image calculated in the nonlinear regime (related to profile 4) minus the one obtained in the linear regime (profile 1). We can see the diffracted ring occurring at the wings of the Gaussian beam. So in absence of absorption, the variation of the energy inside the central part of the beam is the same as the diffracted one in the wings. This result is a consequence of the energy conservation.

Next, we placed an circular aperture ($fs\,(x,y) = \zeta_{r_a}\,(x,y)$, the so-called I-scan configuration, see section 2.4.3) or circular obscuration disk ($fs\,(x,y) = 1 - \zeta_{r_a}\,(x,y)$, the so-called EI-scan configuration) in the image plane in order to show the influence of its radius r_a on the measurements of the nonlinearly diffracted energy. The fraction of the light transmitted by the aperture or blocked by the disk is defined by Eq.(2.20): $S = 1 - \exp\left(-2r_a^2/w_a^2\right)$ where w_a is the beam-waist at the output in the aperture/disk plane evaluated in the linear regime. The latter is physically equal to the beam radius at the entry $w_a = w_e$, because the magnification of the considered here the $4f$ imaging system is unity. Fig.3.12(a) shows the variation of η versus S which is related to different radius r_a in the aperture. In both cases the maximum of the absolute value of η is obtained for $S_{max} \approx 0.89$ (giving $r_a = 1.05w_a$). To understand physically this important result, let us come back to Fig.3.11(a) where we distinguish clearly two different parts. The central part of the beam is damped and the energy is diffracted outside to the external part (wings of the beam). The border between these central and external parts of the beam is a circle of radius $r_a = 1.05w_a$ where the diffraction efficiency is maximal ($S_{max} \approx 0.89$). It means that the maximum of the absolute value of η is obtained when only the energy from the central part is measured using the aperture or only the energy diffracted in the wings is measured using the disk. In Fig.3.12(b) we can see the variation of η versus $\Delta\Phi_0$ calculated for S_{max}. Based on a quadratic numerical fitting we obtained the following simple relation which can be used to determine n_2 values in nonlinear optical characterization:

$$\eta = 7.0 \times \left|\Delta\Phi_0\right|^2 \times 10^{-2} \tag{3.17}$$

The advantage of this relation is that it is independent of the size of the beam-waist of the incident beam. When we compare the I-scan method using Gaussian and top-hat beams (see section 3.4.1, $\eta = 9.8 \times \left|\Delta\Phi_0\right|^2 \times 10^{-2}$), it easy to notice that the latter enhance the sensitivity by a factor of $9.8/7.0 \approx 1.4$. Our result is coherent with experiments using top hat beams in a Z-scan configuration [69].

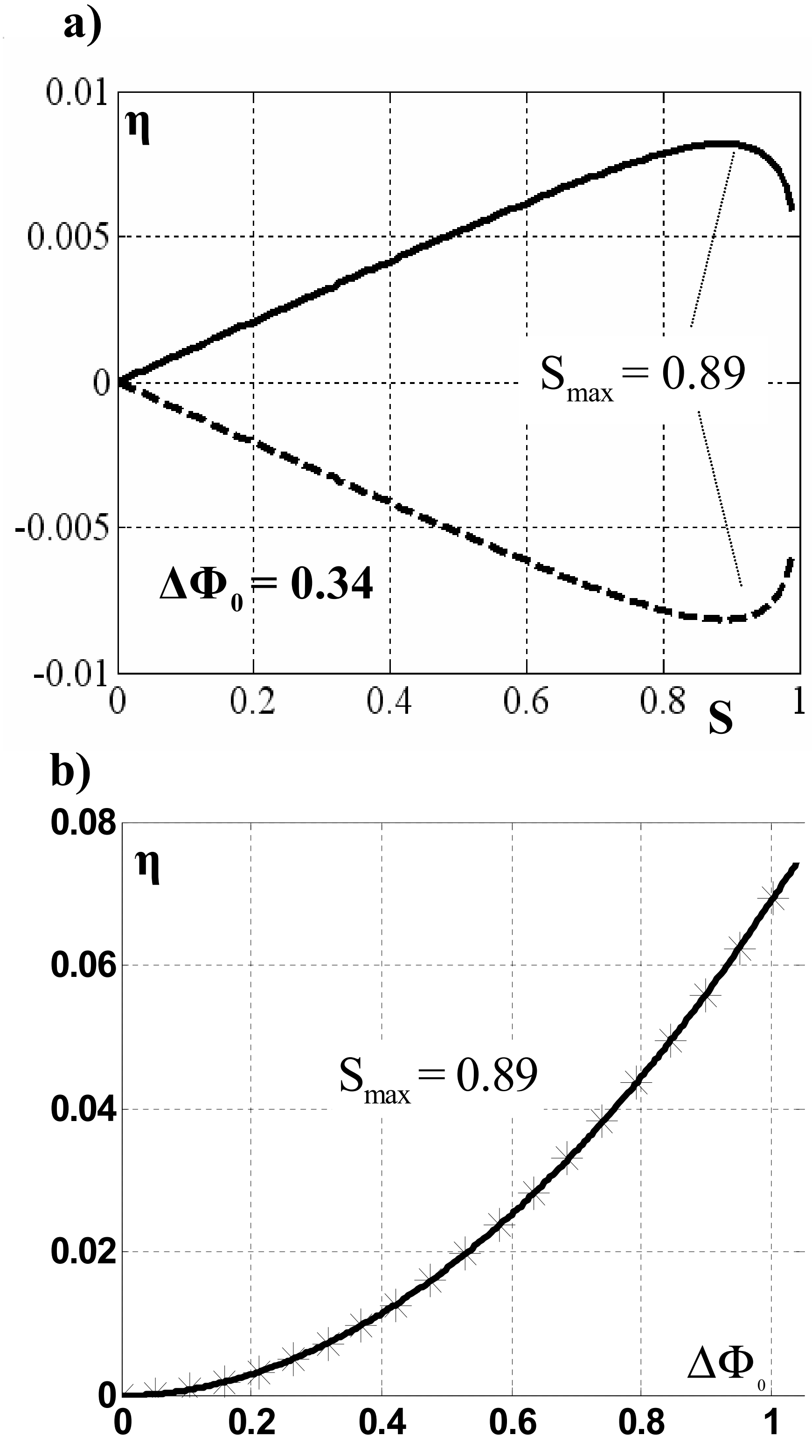

Figure 3.12: The case of the Gaussian beam at the entry and the circular aperture or the eclipsing disk in the image plane. (a) The diffraction efficiency versus S, the fraction of light blocked by the obscuration disk (solid line) and the transmitted light through the circular aperture (dotted line) ($\Delta\Phi_0 = 0.34$). (b) The absolute values of diffraction efficiency versus $\Delta\Phi_0$ for $S = 0.89$.

3.4.4 Sensitivity of Z-scan and EZ-scan using diffraction efficiency [123]

Let us now consider the $4f$ system with the Gaussian beam at the entry and a circular aperture or an opaque disk at the output (see Fig.3.10) with a sample changing its position in the focal region. This configuration of the $4f$ system corresponds to the classical Z-scan with a circular aperture and EZ-scan with an obscuration disk. It has been already checked [105] numerically and experimentally that the addition of lens L_2 does not affect the results of Z-scan. In fact, this lens contributes to produce the Fourier transform of the field at the exit surface of the sample, which is physically similar to the far field diffraction pattern obtained with the original Z-scan method. Originally, using Z-scan and EZ-scan techniques the energy detected in the nonlinear regime (with the high intensity) is normalized to the energy obtained in the linear regime (with the low intensity) giving a normalized transmittance (Eq.(2.19)) of the nonlinear medium. Such a procedure allows to enhance the sensitivity significantly when a large disk (EZ-scan) is used instead of a small circular aperture (Z-scan) [68]. This improvement is mainly due to the reduction of the linear signal in the eclipsing experiment. Unfortunately this kind of normalization suffers couple of disadvantages. First of all, when the nonlinear transmittance is divided by a very small quantity (very low linear signal) the sensitivity can be increased artificially sometimes by few orders of magnitude but experimentally will always reach an asymptotic value defined by the noise level of the photodetector when there is no light at all. This problem has been already emphasized in [124], where the combination of the Z-scan technique with the binary diffractive elements has been proposed. Moreover the enhancement of the sensitivity related to the decrease/increase of the size of the aperture/disc in the classical Z-scan/EZ-scan experiment always comes at the expense of a reduction in accuracy due to the decrease of the signal to noise ratio. We will show here experimentally and numerically that these problems can be overcome by applying a modified definition of the diffraction efficiency (similar to the one given in Eq.(3.6)) instead of using the normalized transmittance containing a zero division:

$$\eta' = \frac{E_{DNL}}{E_{TNL}} - \frac{E_{DL}}{E_{TL}} \tag{3.18}$$

where E_{DNL} and E_{DL} are the energies inside the aperture or outside the opaque disk in nonlinear and linear regimes, respectively. Whereas E_{TNL} and E_{TL} denote the total energies in the image plane in nonlinear and linear regimes. The subtraction of the low irradiance background Z-scan (E_{DL}/E_{TL}) from the high irradiance scan (E_{DNL}/E_{TNL}) is applied here in order reduce a noise due to a sample imperfections similarly as it was proposed in the original Z-scan method [63]. We have checked that the last definition of the diffraction efficiency can be used interchangeably with Eq.(3.6) when one investigates the diffracted energy in all wave-mixing experiments for a sample placed in the focus. However here, for a particular case of single beam Z-scan/ EZ-scan experiment where sample changes its position around the focal plane, the separate evaluation of η in the linear and the nonlinear regimes is more appropriate (as we will show below) because it will additionally facilitates the signal processing in presence of nonlinear absorption.

Experiments and simulations

Excitation is provided by a Nd:YAG laser delivering 17 ps single pulses at $\lambda = 1.064\ \mu m$ with 10 Hz repetition rate. The Rayleigh range of the input Gaussian beam is much higher than the thicknesses of the used samples. To detect the light in the image plane we use a 1000×1018 pixels cooled ($-30°C$) CCD camera with fixed linear gain. The camera pixels have 4095 gray levels and each pixel is $12\times12\ \mu m^2$. Open and closed aperture Z-scan/EZ-scan signals can be numerically processed from the acquired images, by integrating over all the pixels of the CCD camera in the first case and over a circular numerical aperture or an annular area outside the numerical disk in the second one. One can easily notice an advantage of using a non-spatially integrated detector as CCD camera which allows performing Z-scan and EZ-scan experiments for the same set of acquisitions. Generally in the classical experiments the sensitivity is improved using a very small diaphragm (with $S \longrightarrow 0$) in Z-scan and a very large opaque disk ($S \longrightarrow 1$) in EZ-scan. The maximum of the enhancement is achieved for the latter case. The transmittance of the aperture/disk (S) is defined in Eq.(2.20). Fig.3.13(a) shows Z-scan (filled dots) and EZ-scan (empty circles) experimental results obtained for non-absorbing CS_2 using $S = 0.7$ and classically normalizing the nonlinear signal to the linear one (E_{DNL}/E_{DL}). The solid lines in Fig.3.13(a) are the corresponding numerical simulations obtained with $\Delta\Phi_0 = 0.75$ and $q_0 = \beta L_{eff} I_0 \approx 0$ (no nonlinear absorption). The numerical simulation were performed using the theoretical model described in section 3.2 (Eqs.(3.1)-(3.3)). As expected the difference between the peak and the valley of the

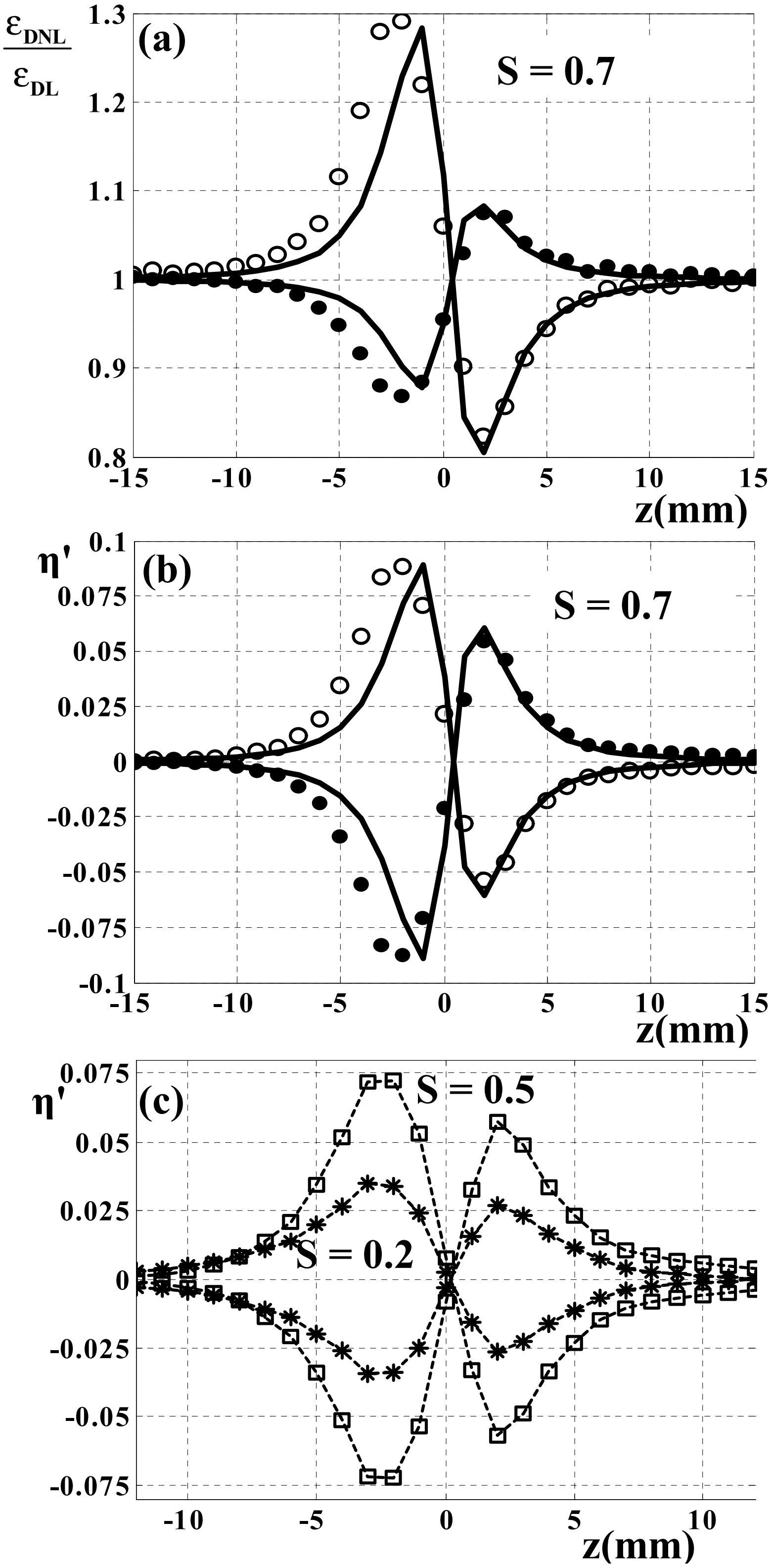

Figure 3.13: Experimental comparison of Z-scan (filled dots) and EZ-scan (empty circles) of CS_2 under identical experimental conditions using (a) the normalized transmittance as in ref.[63] and (b) the diffraction efficiency defined in Eq.(3.18), both evaluated for $S = 0.7$, solid lines are the numerical simulations; c) experimental Z-scan and EZ-scan diffraction efficiencies obtained with $S = 0.5$ (empty squares) $S = 0.2$ (stars), the dotted lines are provided to improve the visibility

normalized transmittance (ΔT_{pv}) is higher for the eclipsing experiment indicating higher sensitivity. The results of the same experimental acquisitions are shown in Fig.3.13(b), however this time the signal is processed using the diffraction efficiency normalization defined in Eq.(3.18). We can see that the classical peak-valley configuration is preserved with this normalization but the obtained traces are symmetrical and $\Delta\eta_{pv}$, the difference between the maximum and the minimum of the diffraction efficiency is exactly the same for both experiments. Therefore there is no discrepancy in the pure optical sensitivities of the Z-scan and the EZ-scan configurations. Fig.3.13(c) shows the experimental results using $S = 0.2$ (stars) and $S = 0.5$ (empty squares) proving that for same size of the aperture and the disk the optical sensitivity is always identical. Obviously these results are the direct consequences of the choice of the normalization procedure. However the use of the diffraction efficiency has a more physical meaning than the use of the classical normalized transmittance, since the first one is maximizing to the optical response of the system. Diffraction efficiency proves that the variations of energy in the central part of the Gaussian beam (detected in Z-scan) are accompanied by the opposite variations in wings of the beam (sensed in EZ-scan).

One of the advantages of the Z-scan method [62][63] comes from the simple expression relating ΔT_{pv} to $\Delta\Phi_0$ allowing nonlinear optical characterization of the material without resorting to complicated computer fits. Following the same way, we have to introduce similar expression for diffraction efficiency. We have found that $\Delta\eta_{pv}$ is linearly dependent on $|\Delta\Phi_0| < \pi$ for $S \leq 0.7$:

$$\Delta\eta_{pv} = \vartheta\,|\Delta\Phi_0| \tag{3.19}$$

where ϑ is a proportionality factor dependent on S. These variations of $\Delta\eta_{pv}$ for different sizes of the far-field apertures/disks are shown in Fig.3.14(a). Note that the sensitivity of the method indicated by the slope of the curve is increasing with the size of the aperture. This behavior is unlike that which occurs in the classical Z-scan experiment [63]. Hence, the enhancement of the sensitivity is accompanied by an increase of the signal to noise ratio. Numerically we have found that for a very large aperture/disk defined by $S > 0.7$ the deviation from the linear dependence occurs. This change manifests itself in Fig.3.14(b) where ϑ is plotted versus S for two nonlinear phase shifts $|\Delta\Phi_0| = 0.1$ (filled dots) and $|\Delta\Phi_0| = \pi$ (empty circles). One can see that for $S \leq 0.7$ the proportionality factor is

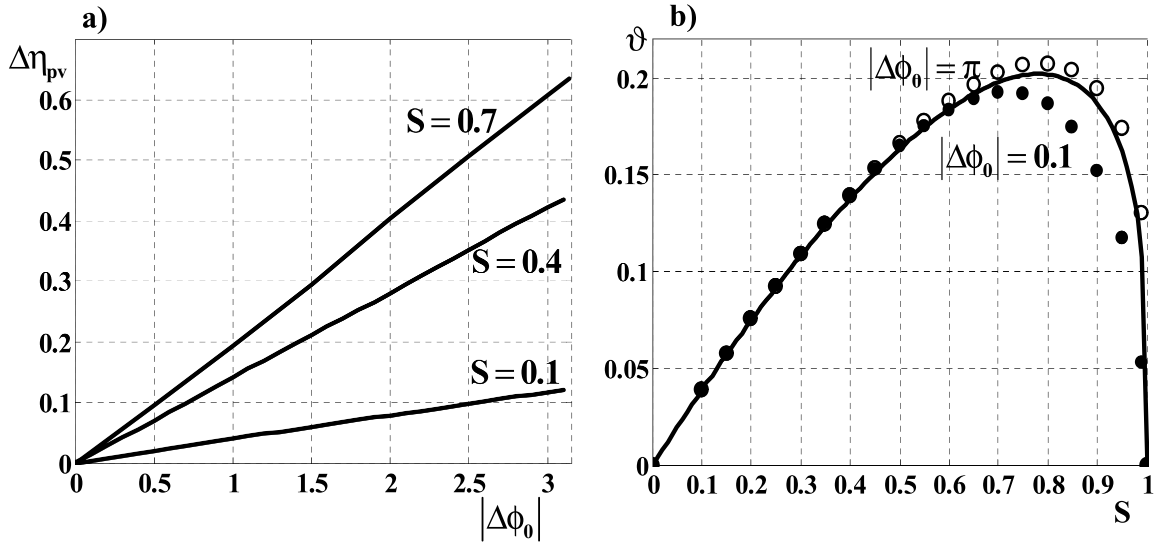

Figure 3.14: (a) Calculated $\Delta\eta_{pv}$ as a function of the focal on-axis phase shift ($\Delta\Phi_0$); (b) the proportionality factor ϑ versus S calculated for two phase shifts: $\Delta\Phi_0 = 0.1$ (filled dots) and $\Delta\Phi_0 = \pi$ (empty circles). The solid line is described by Eq.3.20.

practically independent from $|\Delta\Phi_0|$ while for larger S a significant discrepancy occurs. The maximum of the efficiency appears around $S = 0.73 \sim 0.78$ dependently on the nonlinear phase shift. Through careful numerical evaluation, we have found that for $S \leq 0.7$ the following relation (shown by the solid line in Fig.3.14(b)) includes variations of ϑ versus S within 5% accuracy:

$$\vartheta = 0.44S\left[\cosh\left(1 - S\right) - 1\right]^{0.14} \tag{3.20}$$

The combination of Eq.(3.19) and Eq.(3.20) provides a tool allowing to characterize quantitatively optical nonlinearities using either Z-scan or EZ-scan experiments and considering diffraction efficiency. Moreover these two equations reveal the highly sensitive nature of the Z-scan/EZ-scan experiments. If the experimental apparatus is able to resolve diffraction efficiency changes as low as 1×10^{-3}, the corresponding measured phase value will be equal to $|\Delta\Phi_0| \approx 10^{-3}/0.2$ using an optimized filter $S \approx 0.7$. Thus the minimum optical path length which can be measured (corresponding to a wave front distortion) is $\approx \lambda/1250$.

In Fig.3.15 we can see a comparison of Z-scan experimental diffraction efficiencies obtained with $S = 0.1$ (stars), $S = 0.7$ (filled dots) and $S = 0.86$ (empty circles). The highest $\Delta\eta_{pv}$ is achieved for $S = 0.7$ confirming the numerical predictions shown in Fig.3.14(b).

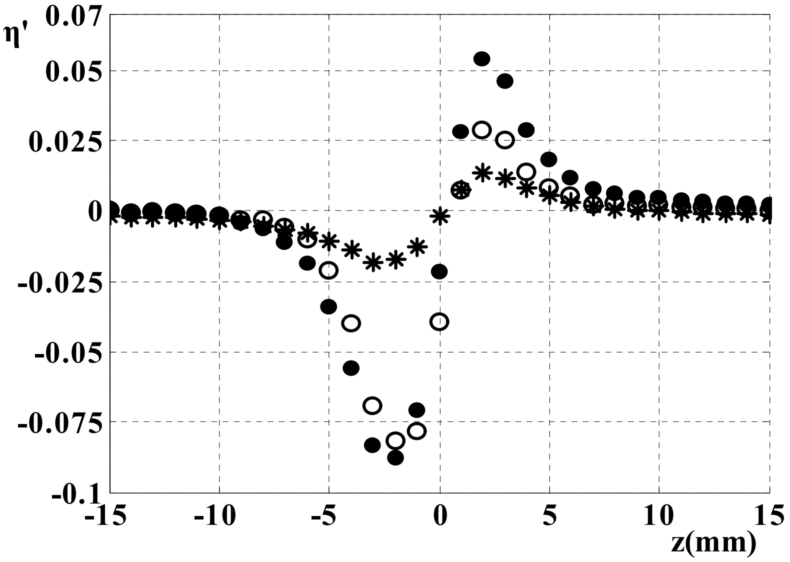

Figure 3.15: Comparison of Z-scan diffraction efficiencies obtained with $S = 0.1$ (stars), $S = 0.7$ (filled dots) and $S = 0.86$ (empty circles).

It must be mentioned that the size of the aperture/disc optimizing the nonlinear signal in the Z-scan/EZ-scan does not coincide with the size of an optimized filter used in the I-scan configuration (see section 3.4.3). In the latter the best results were obtained for $S \approx 0.86$, corresponding to the situation where r_a, the radius of the aperture/disc is equal to w_a, the beam waist in the image plane in the linear regime. Considering only the particular point at $z = 0$ in Fig.3.15 one can easily notice that the absolute variations of the diffraction efficiency are indeed maximum for $S = 0.86$. Moreover the measured absolute value of η' at this point is in very good agreement with the prediction of the quadratic relation $\eta'_{(z=0)} = \eta = 7.0 \times |\Delta\Phi_0|^2 \times 10^{-2}$ (Eq.(3.17)) provided for the optimized filter ($S \approx 0.86$).

Fig.3.16(a) shows the diffraction efficiency (filled dots) and the normalized transmittance (stars) calculated (with $S = 0.7$) from the Z-scan data acquired for a nonlinearly absorbing sample (at 1064 nm) of chalcogenide glass (GeS$_2$(26.25%)Sb$_2$S$_3$(66.25%)CsI(7.5%)). The solid lines in Fig.3.16(a) are the corresponding numerical simulations obtained with $\Delta\Phi_0 = 0.73$ and $q_0 = 0.28$. The normalized transmittance exhibits a typical shape in presence of two-photon absorption: the enhanced valley and the suppressed peak. While the trace of the diffraction efficiency preserves quite well the symmetrical peak-valley configuration. Hence

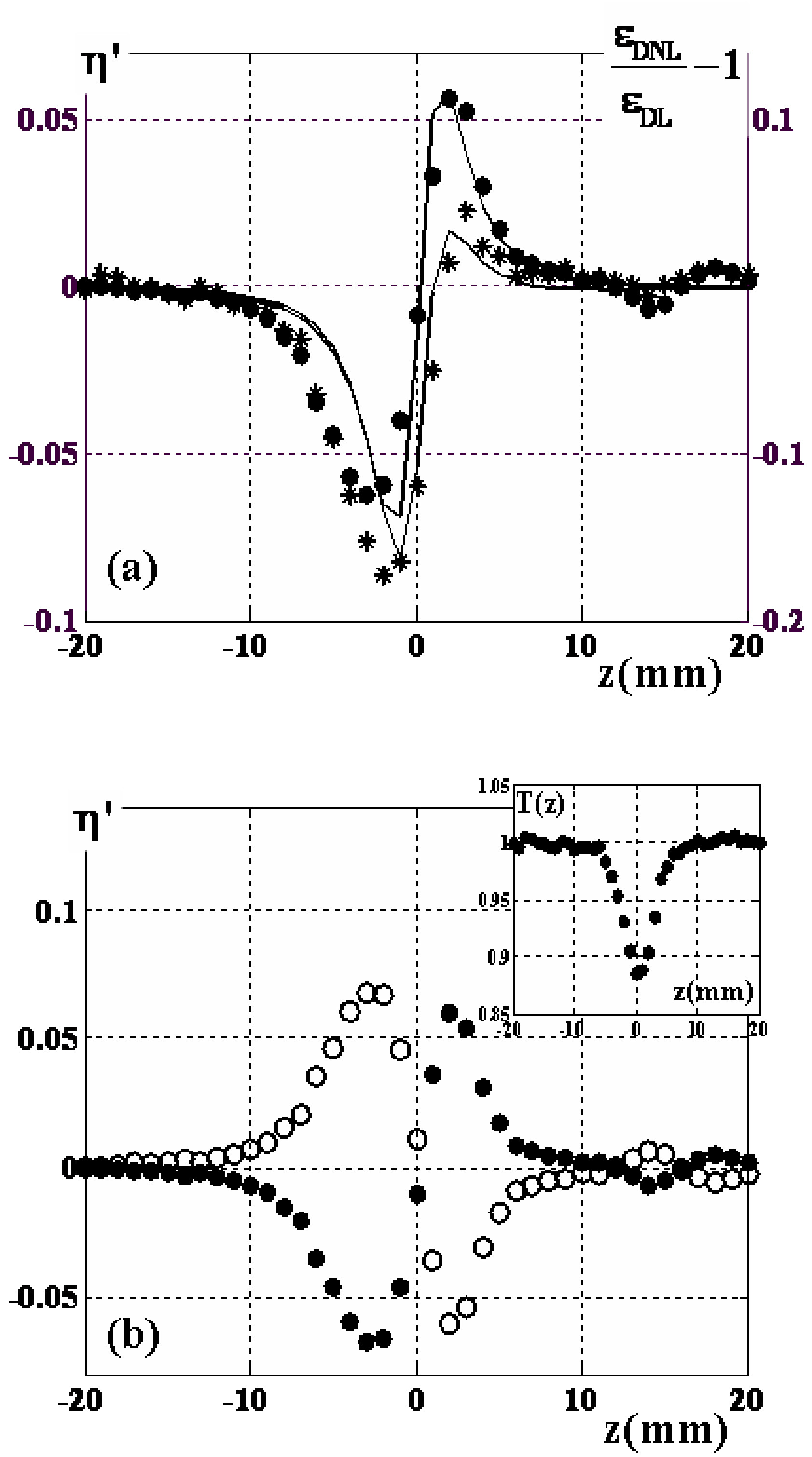

Figure 3.16: (a) Z-scan normalized transmittance (stars) and diffraction efficiency (filled dots) of a nonlinearly absorbing chalcogenide glass (b) the results of the division of the diffraction efficiency by the open aperture normalized transmittance for Z-scan (filled dots) and EZ-scan (empty circles) efficiency by the open aperture normalized transmittance. The open aperture normalized transmittance is shown in the inset.

the closed aperture η' is much less sensitive to nonlinear absorption than the closed aperture normalized transmittance. It is due to the first component in the difference of Eq.(3.18), namely E_{DNL}/E_{TNL}. It compensates partially the influence of the nonlinear absorption because both, the energy inside (outside) the aperture (disc) and the total energy in the nonlinear regime suffer the nonlinear absorption inside the sample. This also explains why we have decided to evaluate separately diffraction efficiency in linear and nonlinear regimes instead of using Eq.(3.6). Numerical simulations show that under the same conditions $q_0 < 1$ and $q_0/2\Delta\Phi_0 < 1$ as used for classical Z-scan [63] and for a relatively small phase shift $|\Delta\Phi_0| \leq 0.7$, $\Delta\eta_{pv}$ agrees to within less than 10% with that obtained from the purely refractive experiment. No division by an open aperture normalized transmittance $T(z) = E_{TNL}/E_{TL}$ is necessary as it is usually done in Z-scan experiments. What is more, the results of the division are even less accurate when the phase shift is low. However for the higher phase shift $|\Delta\Phi_0| > 0.7$ the division should be applied in order to obtain peak and valley traces from which measurements could be done within 10% accuracy. In Fig.3.16(b) we can see the effect of this procedure for our experimental data in Z-scan and EZ-scan configuration. The open aperture trace is shown in the inset. It is clearly seen that even in the presence of nonlinear absorption the signal given by Z-scan or EZ-scan remains the same.

3.4.5 Sensitivity of the NIT-PO using diffraction efficiency

Let us now consider the phase object shown in Fig.2.10 and defined in Eq.(2.38). Typically, in the NIT-PO experiments (see section 2.5.2), the nonlinear phase contrast defined in Fig.2.11 is taken into account as the signal to measure. In a given experimental conditions (i.e. for a given nonlinear phase shift) the contrast depends only on $\Delta\phi_L$, the linear phase retardation provided by the object and L_p/R_a, the ratio between radius of the phase plate and the radius of the input top-hat beam [104][125][126]. Here, as in the previous sections, we will consider the diffraction efficiency as a measured signal. The latter can be defined as the ratio between energy inside the phase plate and total energy in the image plane. In Fig.3.17(a) and 3.17(b) we can see the calculated absolute values of the diffraction efficiency due to a pure nonlinear refraction versus $\Delta\phi_L$ and L_p/R_a for positive and negative nonlinearity,

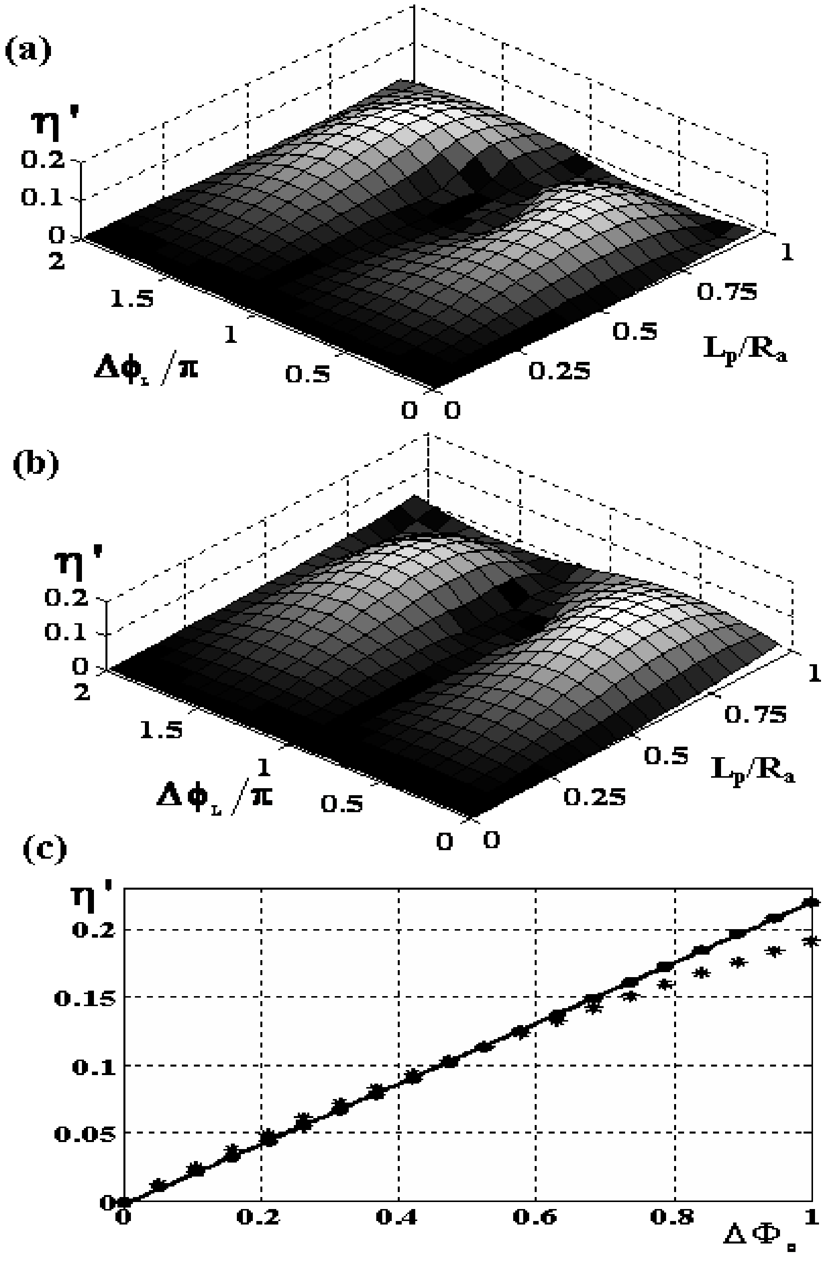

Figure 3.17: Calculated absolute values of diffraction efficiency in the pure nonlinear refraction case versus $\Delta\phi_L/\pi$ and L_p/R_a for (a) a positive nonlinearity ($\Delta\Phi_0 > 0$) and (b) a negative nonlinearity ($\Delta\Phi_0 < 0$); (c) Diffraction efficiency versus nonlinear phase shift calculated for an optimized phase object parameters: $L_p/R_a = 0.75$ and $\Delta\phi_L/\pi = 0.5$ ($n_2 > 0$) or $\Delta\phi_L/\pi = 1.5$ ($n_2 < 0$). Filled dots are calculated in absence of nonlinear absorption ($q_0 = 0$ and $\gamma = 0$) while stars are the results obtained for $q_0 = 1$ and $\gamma = 0.5$.

respectively. We can distinguish clearly two non-equal maxima in each figure appearing for $L_p/R_a \approx 0.75$ and for two linear phase retardations: $\Delta\phi_L \approx 0.5$ and $\Delta\phi_L \approx 1.5$. For a positive nonlinearity ($\Delta\Phi_0 > 0$) a higher maximum appears at $\Delta\phi_L \approx 1.5$ while for a negative nonlinear refraction ($\Delta\Phi_0 < 0$) it appears at $\Delta\phi_L \approx 0.5$. It is important to emphasize that the optimized parameters of the phase object using diffraction efficiency do not correspond to the optimized parameters evaluated for the phase contrast in [104][125][126]. We have found that in the optimized conditions the diffraction efficiency is linearly dependent on nonlinear phase shift $|\Delta\Phi_0| < 1$:

$$\eta' = 0.22\,|\Delta\Phi_0| \tag{3.21}$$

The comparison of the latter equation with the exact numerical results is shown in Fig.3.17(c). Moreover when the diffraction efficiency is evaluated separately in the linear and the nonlinear regimes, as in Eq.(3.18), the numerical calculations show that Eq.(3.21) remains valid within 10% accuracy in presence of nonlinear absorption under the same approximations as the ones used in wave-mixing or Z-scan experiments, i.e. $q_0 < 1$ and $\gamma = q_0/2\Delta\Phi_0 < 1$. The results obtained for $q_0 = 1$ and $\gamma = 0.5$ are shown by stars in Fig.3.17(c). Hence the NIT-PO technique is practically insensitive to nonlinear absorption in the given optimized conditions.

3.5 Conclusions

We have shown that the well-known Forward-Degenerate Four Wave Mixing (F-DFWM) experiment can be performed inside the $4f$ imaging system by using three circular aperture object at the entry and matched field-stop (three opaque circular disks blocking geomtrical image of the object) in the image plane. A few intense diffracted orders were recorded by a CCD camera in the image plane outside the field stop, as a result of the self-diffraction of the fundamental beams on a phase grating nonlinearly induced inside the sample placed in the focal region. To analyze quantitatively the nonlinearly diffracted energy in the image plane we have introduced the diffraction efficiency (η) as a new physical quantity allowing to characterize optical nonlinearities. Moreover we have shown that the simple arrangement of $4f$ setup provides a lot of flexibility in nonlinear characterization enabling the wave-mixing experiment either in Z-scan configuration (i.e. measuring η as function of sample position) or I-scan configuration (i.e. measuring η as function of incident intensity for a sample position fixed in the focus). What is more important we have also shown that it is possible to perform different popular nonlinear characterization techniques inside the $4f$ setup, such as DFWM, Z-scan, EZ-scan, I-scan and NIT-PO, simply by changing the object at the entry and the field-stop in the image plane. All these methods can be considered as particular cases of the same imaging process. Consequently the analysis of the diffracted energy at the output of the $4f$ system allows comparing pure optical sensitivities corresponding to what has been considered up to now as different methods.

At the beginning we compared the sensitivities of multi-wave mixing experiments using objects composed of one, two, three and four circular apertures. We considered the sample fixed at the focus where the maximal nonlinear response is obtained in wave-mixing processes. We have shown that by matching the object at the entry with a field stop in the image plane we can maximize the measured signal, therefore optimizing the signal to noise ratio. We have provided simple quadratic relationships relating the diffraction efficiency (η) to the focal on-axis nonlinear phase shift (Φ_0) in order to characterize the cubic optical nonlinearity in the low excitation regime ($|\Phi_0| < 1$). The sensitivities ($d\eta/d\Delta\Phi_0$) for all the objects were found to be of the same order of magnitude but the highest one was obtained with the one circular aperture (top-hat beam). Moreover the influence of both the linear and the third order nonlinear absorptions on the nonlinear characterization using wave-mixing has been also studied. We have presented a theoretical analysis explaining the distribution of the diffracted intensity in the image plane and illustrating that both refractive and absorptive effects can contribute to the diffracted signal. We have generalized the simple quadratic relations derived for the pure refractive case in order to include the absorptive effects. Consequently we have shown that the sensitivity of the measurement is not affected by the presence of nonlinear absorption inside the material in the low excitation regime.

The case of a Gaussian beam at the entry of the $4f$ system has been also studied. First we investigated the I-scan experiment with a sample placed at the focus. We have shown that the maximum of the diffraction efficiency can be obtained by placing in the image plane a circular aperture or disk having a radius approximately equal to the beam-waist of

Gaussian beam in this plane in linear regime. The linear transmittance of such aperture (or the fraction of light blocked by the disk) is equal to $S \approx 0.89$. Next we have examined the same configuration of the $4f$ system for different position of the sample in the focal region. The latter arrangement corresponds to Z-scan (circular aperture in the image plane) and EZ-scan (obscuration disk in the image plane) experiments. We have shown that the sensitivity of both methods is identical when the diffraction efficiency is considered as the signal to be measured. Moreover using this physical quantity we have shown that the sensitivity and the signal to noise ratio can be maximized simultaneously in Z-scan experiments. The optical signal is optimized for the measurements when the size of the far-field aperture/disk is defined by $S \approx 0.7$. Furthermore we have demonstrated that the diffraction efficiency gives more accurate results in presence of nonlinear absorption than the classical closed aperture Z-scan normalized transmittance. Finally a simple linear relation between diffraction efficiency and nonlinear phase shift for Z-scan experiment has been provided to characterize nonlinear refraction in presence of linear and nonlinear absorptions.

The NIT-PO technique using the diffraction efficiency as the signal to be measured has been also discussed. Numerical calculations show that the diffraction efficiency is optimized for the measurements when the ratio between the radius of the phase plate and the radius of the input top-hat beam is $L_p/R_a \approx 0.75$ while the linear phase retardations of the phase object is $\Delta\phi_L \approx 0.5\pi$ for negative nonlinearity ($\Delta\Phi_0 < 0$) or $\Delta\phi_L \approx 1.5\pi$ for positive nonlinearity ($\Delta\Phi_0 > 0$). In these optimized conditions the diffraction efficiency is linearly dependent on the nonlinear induced phase shift and is almost insensitive to nonlinear absorption.

The comparison of the sensitivities (pure refractive ones) of all the considered techniques is summarized in table 3.2. It is clearly seen that Z-scan/EZ-scan and NIT-PO techniques have the highest and comparable sensitivities (i.e. $d\Delta\eta_{pv}/d\Delta\Phi_0 \approx d\eta/d\Delta\Phi_0$). Consequently both of them are the most appropriate methods for characterization of samples in a thin film form where the optical interaction length is very low. However in the next chapter we will show that high sensitivities of both methods do not ensure the accurate nonlinear characterization of thin films. We will show that the photo-sensitivity of the material under study can considerably hinder or even make impossible to measure the nonlinear coefficients.

Characterization technique	Optimization	Relation	Validity
I-scan with Gaussian beam	$S \approx 0.89$	$\eta = 7.0 \times \lvert\Delta\Phi_0\rvert^2 \times 10^{-2}$	$\lvert\Delta\Phi_0\rvert < 1$
I-scan with Top-Hat beam	$a = R$	$\eta = 9.8 \times \lvert\Delta\Phi_0\rvert^2 \times 10^{-2}$	$\lvert\Delta\Phi_0\rvert < 1$
I-scan with two input beam	$a = R$	$\eta = 7.5 \times \lvert\Delta\Phi_0\rvert^2 \times 10^{-2}$	$\lvert\Delta\Phi_0\rvert < 1$
I-scan with three input beam	$a = R$	$\eta = 5.4 \times \lvert\Delta\Phi_0\rvert^2 \times 10^{-2}$	$\lvert\Delta\Phi_0\rvert < 1$
I-scan with four input beam	$a = R$	$\eta = 5.3 \times \lvert\Delta\Phi_0\rvert^2 \times 10^{-2}$	$\lvert\Delta\Phi_0\rvert < 1$
Z-scan/EZ-scan	$S \approx 0.7$	$\Delta\eta_{pv} \approx 0.2 \times \lvert\Delta\Phi_0\rvert$	$\lvert\Delta\Phi_0\rvert < \pi$
NIT-PO (I-scan configuration)	$L_p/R_a \approx 0.75$ **i)** $\Delta\phi_L \approx 0.5$ for $\Delta\Phi_0 < 0$ **ii)** $\Delta\phi_L \approx 1.5$ for $\Delta\Phi_0 > 0$	$\eta = 0.22 \times \lvert\Delta\Phi_0\rvert$	$\lvert\Delta\Phi_0\rvert < 1$

Table 3.2: Comparison the optical sensitivities of the most used characterization techniques. Column 2 gives parameters (defined throughout the text) necessary to obtain optimized conditions for measurements (maximizing the signal to noise ratio). Column 3 presents expressions relating diffraction efficiency with nonlinear focal on-axis phase shift in optimized conditions, while column 4 gives the range of validity of these relations.

Chapter 4

PHOTO-INDUCED EFFECTS IN NONLINEAR OPTICAL CHARACTERIZATION

4.1 Introduction

This chapter is mainly devoted to the optical characterization of thin films. Particularly we will discuss the influence of photo-induced effects (PIE) on the measurements of nonlinear refractive indices and nonlinear absorption coefficients. Both NIT-PO and Z-scan technique will be employed in our study. By PIE we understand all phenomena which cause the damage or permanent modifications inside the material (e.g. ablation, photo-darkening, photo-oxidation, carbonization etc.) leading to permanent changes in linear refraction and absorption. We will show that PIE can mimic the nonlinear response in both NIT-PO and Z-scan measurements significantly hindering the nonlinear characterization. The NIT-PO technique will be employed to verify the presence of photo-induced modifications inside the sample. The intensity threshold for damage as well as the kinetics of photo-induced changes in thin films of chalcogenide glasses will be studied using this method. On the other hand we will show that the Z-scan technique masks completely the PIE contribution in both closed and open aperture configurations. Consequently the measurements of n_2 and β can be erroneous when one investigates nonlinearities in fragile materials using this technique. Nevertheless we will show that it is possible to exploit this effect in a positive way. We will employ the Z-scan technique to investigate simultaneously the magnitude and the sign of the refractive index (Δn_0) and the absorption coefficient changes ($\Delta\alpha_0$) induced by PIE. Following this way we will also extend the usefulness of Z-scan technique for characterization of linear optical parameters. The Z-scan will be presented as a new tool to determine the thickness (L) or the linear refractive index (n_0) of thin samples. Such possibility will be demonstrated by Z-scanning a rectangular groove (i.e. rectangular permanent phase shift) inside a transparent thin film.

4.2 Photo-induced effects in thin films during nonlinear characterization

In this section we will investigate the photo-sensitivity in thin films by considering the ones made of amorphous chalcogenide glasses. These materials are based on the chalcogen elements (S, Se, Te) and are well-known for possessing a large optical nonlinear refraction combined with an infrared transparency [127][128]. Hence they are promising candidates for linear and nonlinear optical elements and so their optical properties are widely studied. However chalcogenide glasses are also well-known to be highly photo-sensitive on laser irradiation due to their flexible molecular structure and unique electronic configuration. Numerous photo-induced effects have been observed in this family of glasses as ablation, photo-darkening, photo-bleaching etc. [127][128][129][130][131] all of them accompanied by changes in the optical constants, i.e., changes in the electronic band gap, refractive index and optical absorption coefficient. However in the majority of publications dealing with nonlinear characterization, PIE occurring during the measurements has been ignored, especially in the infrared region of the incident light. Here we will compare the experimental results obtained for photo-sensitive thin films using both NIT-PO and Z-scan techniques at $\lambda = 1.064\ \mu m$ in the picosecond regime.

4.2.1 PIE with phase object [132]

In this paragraph we investigate photo-induced effects for various compositions of chalcogenide $\mathrm{Ge}_x\mathrm{As}_y\mathrm{Se}_{100-x-y}$ amorphous glasses (see table 4.1). The samples were prepared by the *Équipe Verres et Céramiques*, Université de Rennes 1 (UMR-CNRS 6226) using pulsed laser deposition [132][133]. The compositions of glasses as well as their thicknesses (L), the refractive indices (n_0) and the energy gaps (ε_g, from Tauc's plot) are given in table 4.1. The linear optical parameters were estimated from ellipsometry measurement. For more details about the properties of the investigated specimens see Ref.[132]. The NIT-PO experiment was performed by placing the phase object at the entry of the $4f$ imaging system without any filed stop in the image plane (see section 2.5.2). The object is composed of circular glass plate of radius $R_a = 1.45\ mm$ on which a transparent dielectric disk of radius $L_p = 0.5\ mm$ has been deposited. The linear phase retardation provided by the PO is $\Delta\phi_L = \pi/2$ radians at $\lambda = 1.064\ \mu m$. A Gaussian laser beam with beam waist $w_e = 1.8\ mm$ was used at the entry of the $4f$ system. The focal on-axis intensity (I_0) was calibrated considering the value of $n_2 = 3 \times 10^{-18}\ m^2/W$ for CS_2 given in reference [63].

Composition	n_0(at 1.064 μm)	$\varepsilon_g\,(eV)$, Tauc plot	$L\,(nm)$,	$I_{0T}\,(GW/cm^2)$,	$\varepsilon_{pulse}\,(\mu J)$,
$Ge_{10}As_{40}Se_{50}$	2.79	1.65	1083	3.1	8.8
$Ge_{10}As_{35}Se_{55}$	2.77	1.70	1040	3.9	10.8
$Ge_{15}As_{30}Se_{55}$	2.71	1.71	941	2.9	8.3
$Ge_{10}As_{30}Se_{60}$	2.70	1.77	994	2.5	7
$Ge_{20}As_{20}Se_{60}$	2.62	1.81	820	4.7	13

Table 4.1: Optical parameters of the investigated thin films of chalcogenide glasses: refractive index (n_0), energy band gap (ε_g), thickness (L), on-axis intensity threshold (I_{0T}) for PIE and corresponding energy pulse (ε_{pulse}).

In the first experiment using PO we were increasing the input intensity slowly in order to find the intensity for which the nonlinear response of the sample becomes detectable. When the on-axis irradiance reached the intensity threshold (I_{0T}, given in the column 5 of table 4.1), the phase contrast appeared showing an image similar to the nonlinear image that one would obtain with the optical Kerr effect. However by decreasing the intensity to a very low level again, the phase contrast remained in the image showing a PIE memorized inside the nonlinear sample. Moreover the contrast did not vary with the input pulse intensity. Furthermore we found that the phase contrast can be positive or negative being dependent on the glass composition. In addition the phase contrast could change with the illumination time. The examples of the experimental images acquired in presence of PIE are shown in Fig.4.1(b) and Fig.4.1(d). These experimental observations lead us to the conclusion that our modified images should be related to a damage of the sample. To understand physically the occurrence of intensity-independent phase contrast we performed numerical simulation for NIT-PO experiment (see section 2.5). Since the beam intensity distribution at the entry is Gaussian, so that it is not a uniform (top-hat) as supposed in the original experiment, the transmittance of the phase object given in Eq.(2.38) should be modified to: $t\left(x,y\right) = \exp\left[-\left(x^2+y^2\right)/w_e^2\right] \times \zeta_{Ra}\left(x,y\right)\exp\left[i\Delta\phi_L\zeta_{Lp}\left(x,y\right)\right]$. We assume also that the laser light induces inside the sample a small circular spot (of radius w_{spot}) of a permanently modified refractive index and absorption coefficient. The linear transmittance of such medium can be written as $T_L = \exp\left[i2\pi\left(\Delta n_{spot} + i\Delta\kappa_{spot}\right)L/\lambda\right]$ for $\rho < w_{spot}$ and $T_L = 1$ for $\rho > w_{spot}$. Here Δn_{spot}, $\Delta\kappa_{spot}$ and ρ are the refractive index change, the extinction coefficient change and the radial coordinate in the focal plane, respectively. Calculations show that in the presence of an optically modified spot inside the sample, the filtering process of the spatial frequencies composing the object in the Fourier plane contributes to energy deflection or absorption inside the image of the phase plate. Consequently the images are qualitatively similar to those obtained in presence of Kerr nonlinearities (as it can be seen in Fig.4.1(c) and 4.1(e)). Moreover the phase contrast can be positive or negative and dependent on the magnitude and the sign of both, Δn_{spot} and $\Delta\kappa_{spot}$. Hence, the occurrence of a permanent phase contrast is due to the interplay between the photo-induced permanent changes in refraction and absorption.

In the next step we investigated the temporal behavior of PIE illuminating each sample during 250 seconds with 10 Hz repetition rate and acquiring one image every successive 50 laser shots. For a quantitative description of our experiment we defined the signal to measure using the diffraction efficiency $\eta(t)$ as follow: $\eta(t) = \left(\varepsilon_{phnl}\left(t\right) - \varepsilon_{phnl}\left(0\right)\right)/\varepsilon_{tot}\left(0\right)$, where ε_{phnl} is the energy in the phase plate and ε_{tot} is the total energy in the first image (at $t = 0$). An example of evolution of the signal (η) versus t, the time behaviour for intensities below and above the threshold value is given in Fig.4.2. For $I_0 < I_{0T}$, the η is constant (~ 0) during the time characterizing undamaged samples. No phase contrast was

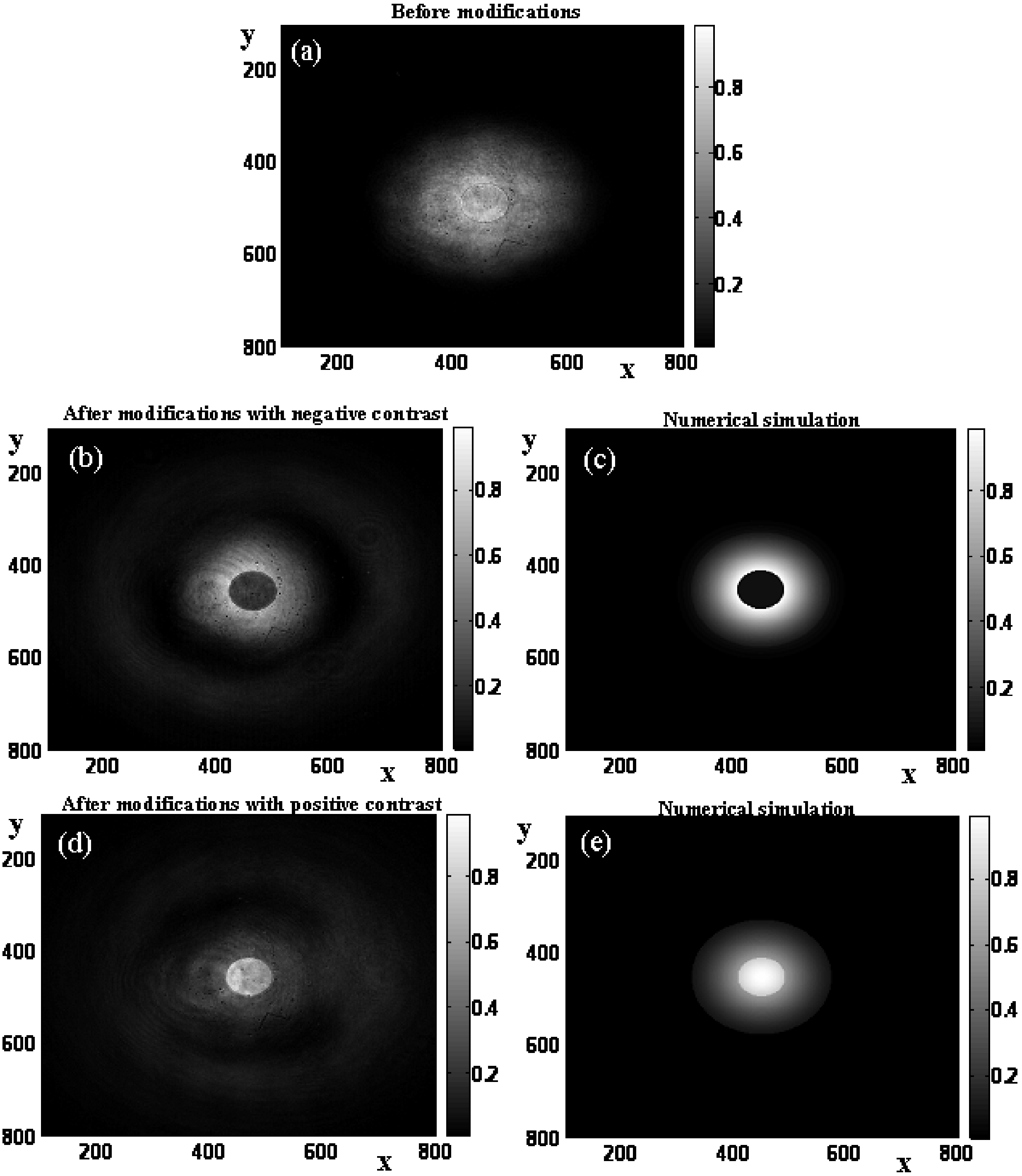

Figure 4.1: Experimentally acquired images of the phase object at the output of the imaging system: (a) before and after the photo-induced modifications indicated by a negative contrast (b) and a positive contrast (d). The circular shape appearing at the centre of the images is the phase object. Numerical simulations supposing (c) $\Delta n_{spot} = -0.1$ and $\Delta \kappa_{spot} = 0$, (e) $\Delta n_{spot} = 0$ and $\Delta \kappa_{spot} = 0.05$. The size of the spot used in calculations is $w_{spot} = 36$ μm. The coordinates x and y are expressed in number of pixels.

observed in this range of input intensities indicating the absence of detectable nonlinearity in all the investigated specimens. For intensities above the threshold ($I_0 > I_{0T}$), the phase contrast appears imitating the nonlinear behavior. The breakpoint position that appears in the Fig.4.2 for each film varies from 10 to 110 s depending on the composition but it can be also related to the value of the intensity threshold. Higher is the incident power density, faster is the kinetic to reach the optical threshold leading to a damage of the thin film.

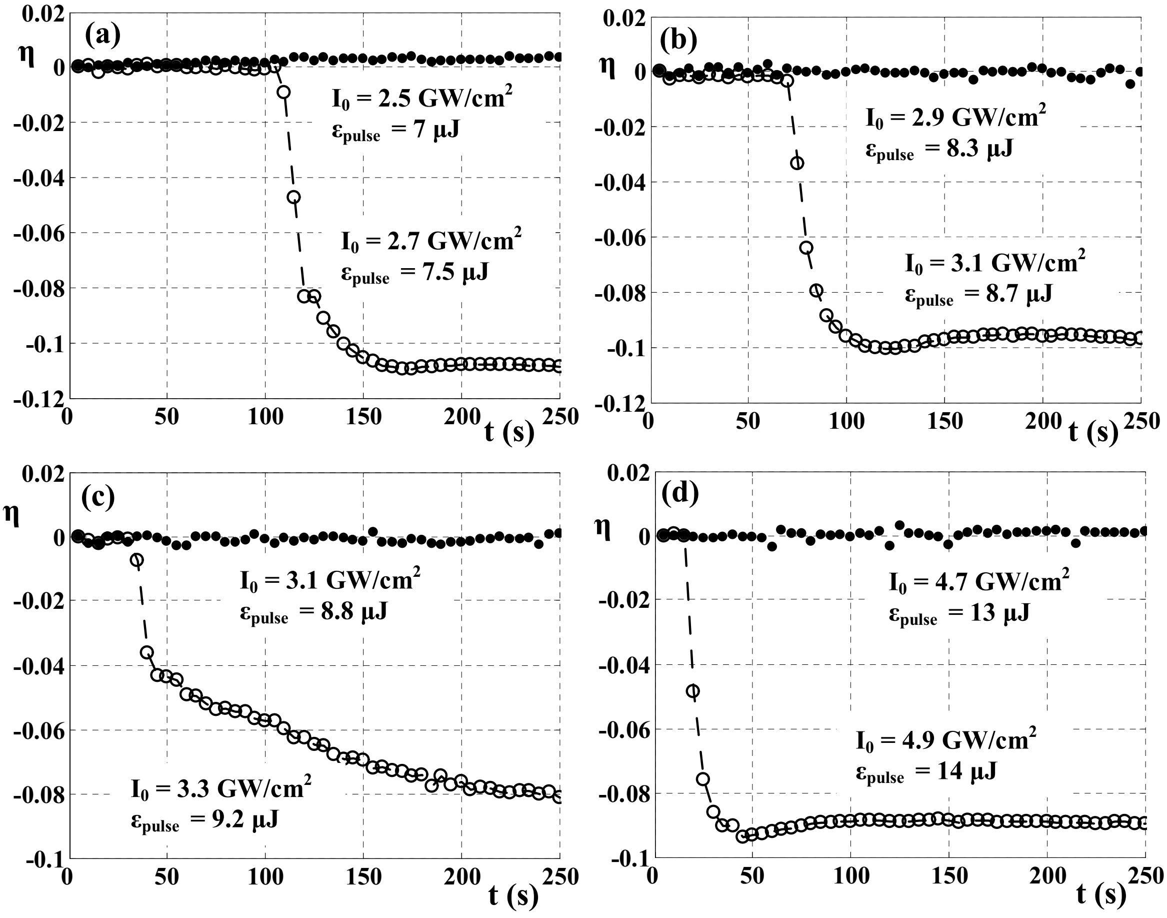

Figure 4.2: Time evolution of the diffraction efficiency for the intensities below the threshold value (full circles) and above the threshold (open circles) obtained with **(a)** $Ge_{10}As_{30}Se_{60}$, **(b)** $Ge_{15}As_{30}Se_{55}$ **(c)** $Ge_{10}As_{40}Se_{50}$ and **(d)** $Ge_{20}As_{20}Se_{60}$.

The intensity threshold values (I_{0T}) could be expected to follow the band-gap (ε_g) variation as a direct effect on the two-photon absorption which should increase with decreasing of the band-gap energy. However the process seems to be more complex (see table 4.1) and it is therefore difficult to predict an optical damage threshold of the material directly from the energy band gap. Other parameters related to the optical quality of the films or the hyperpolarizability of the elements constituting the layer seem to be important. It must be added that we also investigated different types of thin films of chalcogenide glasses, oxide glasses and organic polymers using NIT-PO technique. For all the examined thin films we have obtained qualitatively similar results as the ones described above. Though it is difficult to relate directly I_{0T} with the effective energy gap ε_g, nevertheless we have found that generally the intensity threshold is increased when the transparency of the film (indicated by the specimen's color) is shifted significantly towards the shorter wavelength. For example, the black or red films are found to be much more sensitive to excitation light at 1.064 μm than yellow or blue samples. Hence the absorption (one-photon or two-photon) plays an important role in PIE, however as shown above it is not the only phenomenon determining the photo-sensitivity of materials.

Taking into account the results given in table 3.2 one can find that in the optimized conditions a phase shift as small as $\Delta\Phi_0 \approx 5\ mrad$ can be measured if a resolution in the measured diffraction efficiency is of order of 10^{-3}. Moreover table 4.1 shows that the intensity thresholds are $I_{0T} > 1\ GW/cm^2$ for all the investigated specimens in this paragraph. Then one can estimate the minimal value of n_2 characterizing the thin film in order to induce measurable nonlinear response without destroying the material for lower intensities. Assuming $L = 1\ \mu m$, $\lambda = 1.064\ \mu m$, $I_0 = 1\ GW/cm^2$ and at least the signal to noise ratio equal to 3 we can find $n_2 = 3 \times \Delta\Phi_0\lambda/2\pi L I_0 \approx 255 \times 10^{-18}\ m^2/W$. This is about 2 orders of magnitude higher than the n_2 value of CS_2. Such large nonlinear refractive indices are rarely available in chalcogenide glasses (generally $n_2 < 20 \times 10^{-18}\ m^2/W$). The measurements of these values of n_2 will be possible only when the resolution in the measured signal related to the photo-detector is enhanced, the input laser energy fluctuation is reduced and the optical quality of the specimen is improved (i.e. the noise threshold is reduced) allowing detecting smaller phase shifts.

4.2.2 PIE in Z-scan experiments [134]

In the previous paragraph we investigated samples where PIEs were not accompanied by a detectable nonlinearity. The nonlinear characterization was not possible because the nonlinearity was too small to induce measurable effects before exceeding the damage threshold intensity. Here we report on optical characterization of 4.8 μm thick $Te_{20}As_{30}Se_{50}$ chalcogenide glass film (black color specimen) which has sufficiently high nonlinearity to induce measurable nonlinear signal in our experimental system. The samples were prepared using the electron deposition method. The detailed description of the film deposition procedure is given in [135]. The sample has an energy gap $\varepsilon_g = 1.56\ eV$ ($\approx 800\ nm$) and its linear optical absorption at 1.064 μm is smaller than the sensitivity of the measurement apparatus [135][136]. The nonlinear experiments were performed inside the $4f$ imaging system using a Nd:YAG laser (1.064 μm, 17 ps, 10 Hz) and employing both Z-scan and NIT-PO techniques.

To reveal PIE and to find the intensity threshold inside the investigated specimen we performed the NIT-PO experiment (with the same parameters as in the previous paragraph)

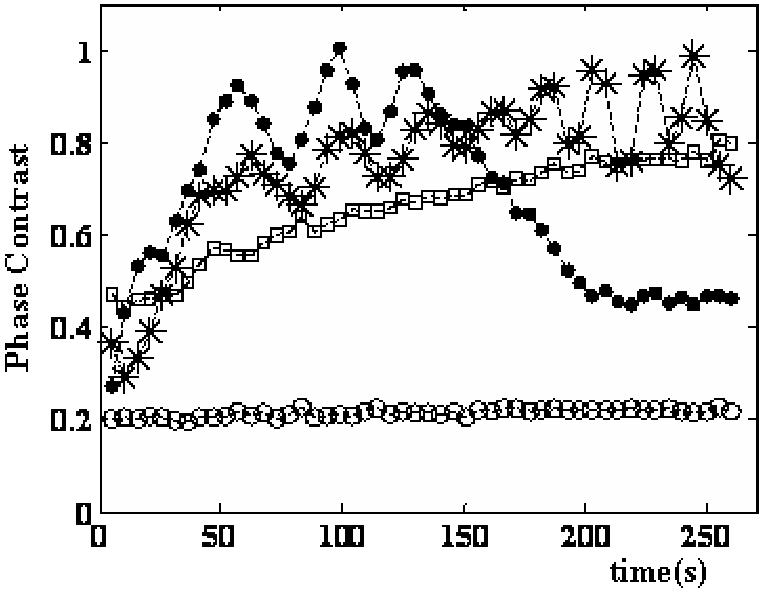

Figure 4.3: Phase contrast versus time: empty circles, stars, empty squares and filled circles are for incident intensity of 1.2 GW/cm^2, 2.0 GW/cm^2, 2.8 GW/cm^2, and 3.3 GW/cm^2, respectively

by measuring the phase contrast (defined as $\Delta T = \langle I(r) \rangle_{r \in [0,L_p]} - \langle I(r) \rangle_{r \in [L_p,R_a]}$, a difference between the mean light intensity passing through the PO and the mean intensity passing outside) in function of the illumination time. Fig.4.3 shows the variations of the measured signal for four different peak intensities (I_0) inside the sample: 1.2 GW/cm^2, 2.0 GW/cm^2, 2.8 GW/cm^2 and 3.3 GW/cm^2. There are 50 laser shots between each successive data points. The temporal variations of the phase contrast for intensities above 1.2 GW/cm^2 reveals the presence of cumulative PIE and indicates damage threshold for the sample between 1.2 GW/cm^2 and 2 GW/cm^2. The oscillatory behavior observed for 2.8 GW/cm^2 and 3.3 GW/cm^2 is related to high phase shift values and has been predicted and explained theoretically in [137]. Each oscillation period shown in Fig.4.3 corresponds to a phase shift change of 2π. The phase shift should be attributed to the third order nonlinearity and to the damage occurring for each laser shot. In the competition between the two contributions the PIE processes becomes dominant very rapidly. For $I_0 = 3.3$ GW/cm^2 we observed contrast reduction after 1500 laser shots that can be explained by almost total ablation of the thin film in the impact region, confirmed by scanning the sample surface using an Atomic Force Microscope (AFM, see Fig. 4.5(b)). According to [137], for high phase shift it is difficult to know from the image contrast when the induced dephasing is positive or negative. A correspondence between negative contrast and negative dephasing is only valid for phase shift smaller than π. Here Fig.4.3 is presented not to show absolute variations of sign and magnitude of phase contrast but to illustrate its relative changes with time in order to verify the presence of PIE.

Sequential Z-scan traces were made in three regimes of intensity: low, high and low. The first experiment with low intensity, not shown here, was made in order to be sure that the fresh laser impact region has no holes or defects diffracting linearly. Flat normalized transmittance curves were obtained in the absence of nonlinear contributions. Afterwards nonlinear acquisitions with large intensity were performed. The insets of Fig.4.4(a) and 4.4(b) show the experimental Z-scan results (filled circles) using the closed- and open-aperture schemes, respectively. The laser intensity was 3.3 GW/cm^2 and the transmittance of the numerical aperture in the closed-aperture Z-scan experiment was equal to $S = 0.4$. The obtained Z-scan profiles indicate positive values for $n_2 = (9.0 \pm 1.4) \times 10^{-16}$ m^2/W and $\beta = (760 \pm 80)$ cm/GW. The profile obtained in the open-aperture scheme is narrower than the profile expected when only a two - photon absorption (TPA) process occurs. However, the data can be fitted considering the contribution of TPA together with the absorption of

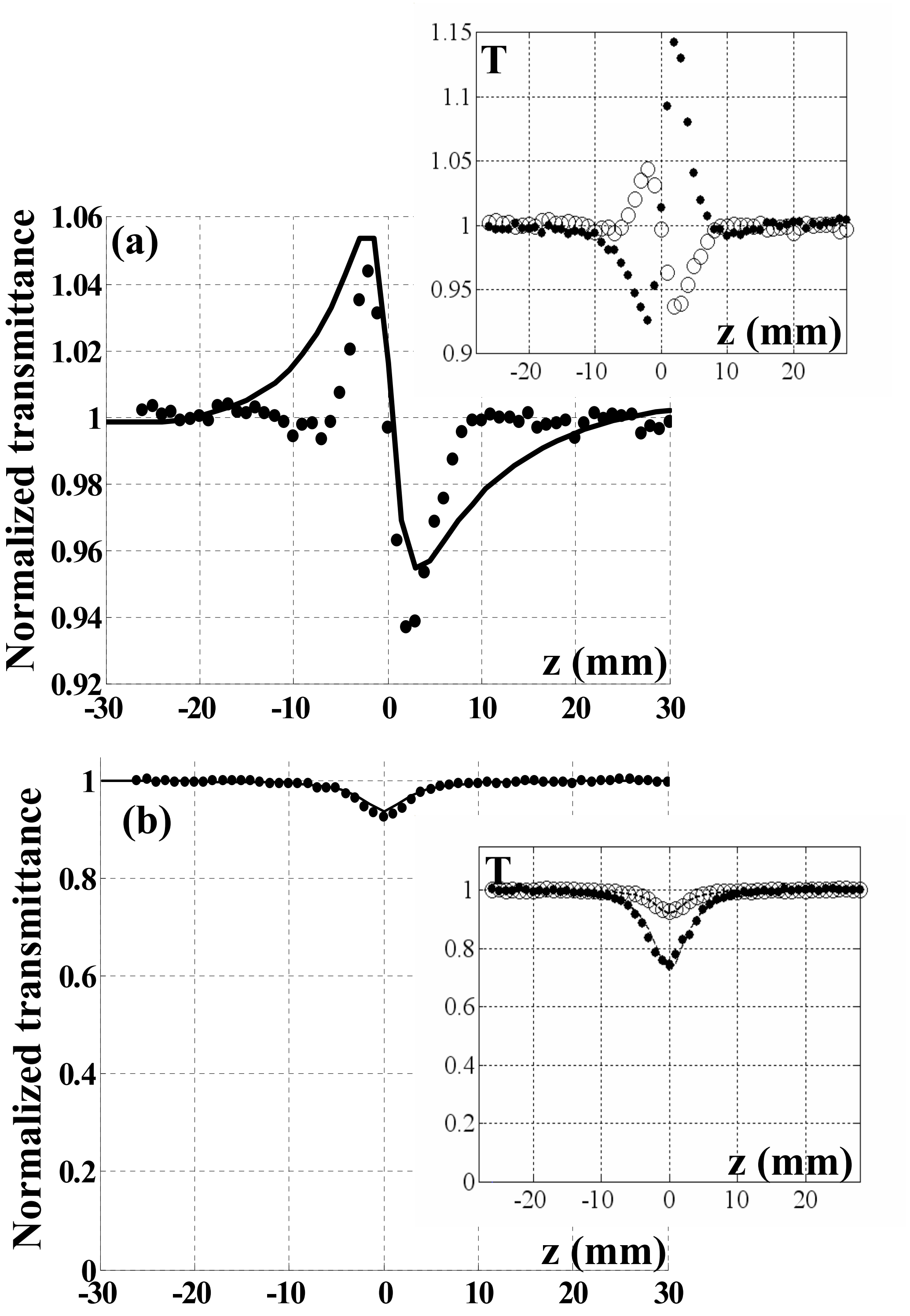

Figure 4.4: Experimental data (filled dots) and numerical results (lines). (a) closed-aperture and (b) open-aperture Z-scan transmittance (T) in low intensity regime (with negligible nonlinearity) showing the presence of ablated region and photo-darkening effect, respectively. The inset of Fig. 34(a) shows the closed aperture Z-scan trace in the nonlinear regime (filled circles) at $I_0 = 3.3\ GW/cm^2$, and in the linear regime (empty circles). The inset of Fig. 34(b) shows the open aperture Z-scan trace in the nonlinear regime at 3.3 GW/cm^2 (filled circles) and in the linear regime (empty circles)

excited carriers [9]. The latter seems to be very probable in the studied sample since the excitation energy is not far away from energy gap of material. The free carrier absorption phenomenon could also explain such high nonlinear refraction of the investigated sample. After the nonlinear regime experiment, a Z-scan trace was obtained with very low intensity to prevent relevant nonlinear contribution. The laser beam was incident on the same impact point as the strong laser in the nonlinear experiments. The same experimental results are shown in Fig.4.4(a) (filled circles) and in the inset of Fig.4.4(a) (empty circles). These results indicate that the sample changes due to the laser pulses and it behaves as a divergent lens for low intensity acting as a material having negative n_2. The closed-aperture Z-scan profile at low intensity can be explained considering the presence of a hole [98], while the decrease of the transmittance around the focus ($z = 0$) shown in Fig.4.4(b) (filled circles) and in the inset of Fig.4.4(b) (empty circles) are attributed to the photo-darkening effect. To support our interpretation we performed numerical simulation of Z-scan low intensity acquisitions using the beam propagation method inside the $4f$ system described in section 3.2. We considered that the sample contributes for a constant linear phase shift due to a hole having the same spatial Gaussian shape as the focused beam. The permanent change in the linear phase shift, created by PIE during the nonlinear regime is assumed to be $\Delta\Phi_L = 2\pi\left(n_0 - i\kappa\right) l_0 \exp\left(-\rho^2/w_0^2\right)/\lambda$, where $n_0 = 2.9$ is the linear refractive index of the film at 1.064 μm [135][136], l_0 is the peak depth inside the hole, ρ is the radial coordinate in the focal plane and w_0 is the beam waist of the focused beam. The imaginary part of the linear refractive index, κ, describes an absorption effect due to photo-darkening. Then, the linear transmittance of the sample in the impact region is described by $T_L = \exp\left(-i\Delta\Phi_L\right)$. In Fig.4.4(a) and 4.4(b) we present experimental (filled circles) and numerical simulation (lines) results for low intensity. The best agreement was obtained for $\kappa = 1.1\ m^{-1}$ and $l_0 = 10\ nm$. The value of l_0 is in good agreement with the hole deepness measured by AFM ($\sim 15\ nm$) (see Fig.4.5(a)). However, the experimental closed-aperture Z-scan profile is narrower than the theoretical curve. This may be due to the threshold intensity to be reached in order produce ablation in the film. Indeed, the pattern used in the numerical calculation is Gaussian with beam waist of 25 μm, while the AFM image shows a steep profile with a hole diameter of $\approx 15\ \mu m$. It should be added that the inspection of the

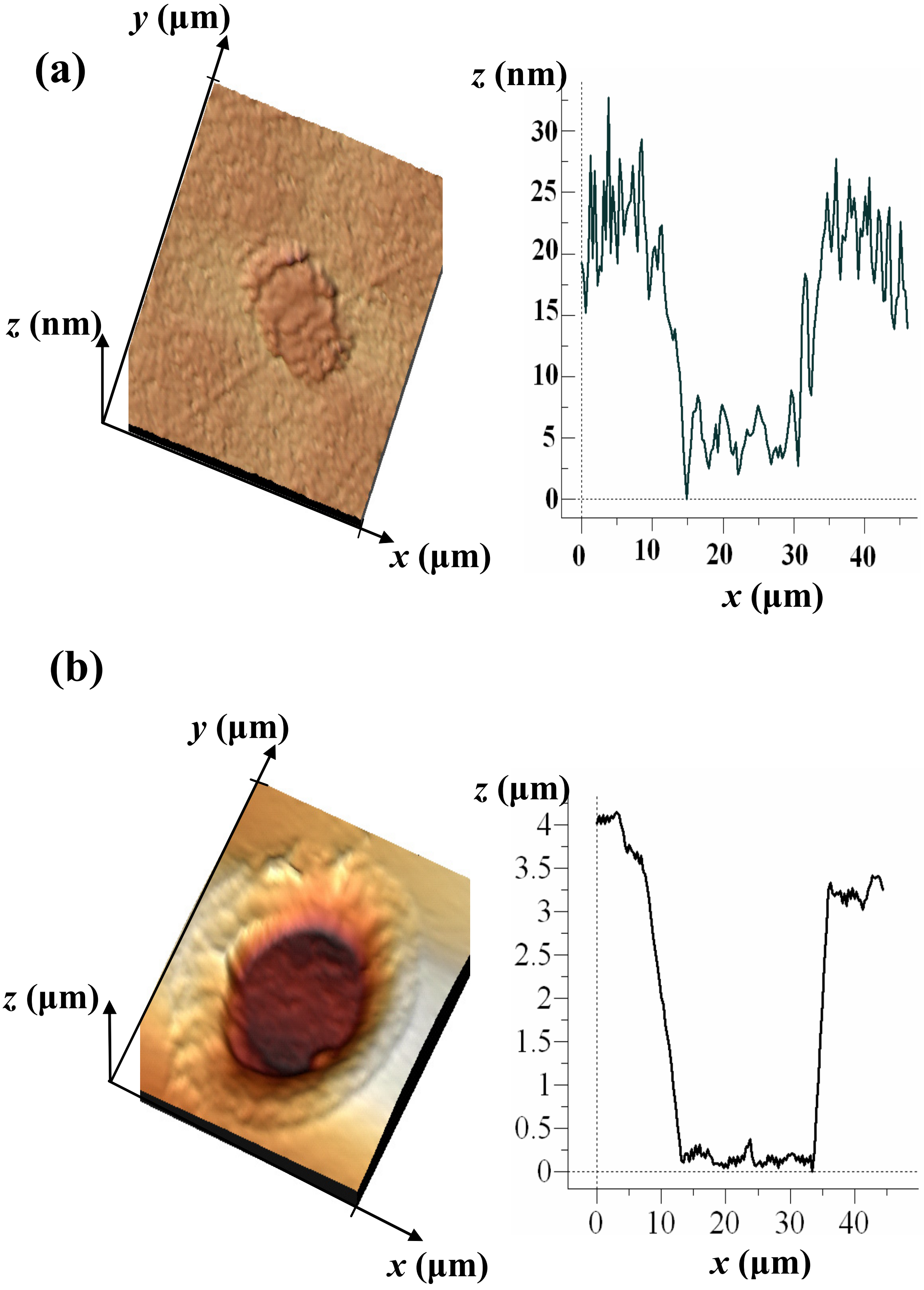

Figure 4.5: AFM images of the ablated regions and their profiles (a) created during Z-scan measurements (∼50 laser shots) and (b) created in NIT-PO experiment (∼2500 laser shots), both with $I_0 = 3.27\ GW/cm^2$ in the focus.

ablated film shown in Fig.4.5 (a) under the optical microscope did not reveal any damage.

To summarize, the optical response of the studied $Te_{20}As_{30}Se_{50}$ film is attributed not only to the optical nonlinearity but also to nano-ablation of the sample. The good agreement between experiment and numerical simulation proves that holes as well as photo-darkening can appear during the Z-scan measurements in the picosecond regime masking the nonlinear response of the sample. Another important result is the use of the Z-scan technique that allows measurement of very small holes with $\approx 10\ nm$ deepness showing the high sensitivity of this method to estimate not only n_2 and β but also the film thickness and optical absorption coefficients due to the photo-darkening phenomenon. In the next two sections we will exploit the latter properties. Firstly we will show that it is possible to quantify PIE by measuring the sign and the magnitude of permanent modifications in refraction and absorption. Secondly we will use Z-scan for characterization of thickness or linear refractive index in transparent thin films using rectangular hole inside the sample

4.3 Determination of photo-induced changes in linear coefficients by Z-scan [138]

In the previous section we showed that PIE can mask the nonlinear optical response of the materials using NIT-PO as well as Z-scan. Hence photo-induced effects are unwanted in nonlinear optical characterization. On the other hand the photosensitivity of various materials is also a subject of intense research due to the wide range of possible applications of PIE. Particularly, the permanent modifications in optical constants (Δn and $\Delta \alpha$) have been successfully utilized for the creation of directly written waveguides and Bragg gratings [139][140][141][142][143][144][145][146][147] in both thin films and bulk slabs of photosensitive materials. One of the tasks is to measure accurately the permanent alterations in refraction and absorption inside the specimen in order to optimize the optical writing processes. These changes can be determined in different ways, using for example: i) microelipsometer [148], ii) aperture-angle method [149], iii) the transmission spectrum [150], or by monitoring the variation of the beam waist at the output of the material during the optical writing process [151]. Here, we present another contribution to the measurements of the permanent modification in optical coefficients by using Z-scan technique. In this section we consider a permanent Gaussian phase shift written inside As_2S_3 chalcogenide glass by a high intensity focused Gaussian beam. It is well-known that photo-induced changes are intensity dependent and when a Gaussian beam is focused into the medium, relatively low induced alterations have the same spatial distribution in the impact area [142][143]. We will show analytically, numerically and experimentally, that Z-scan traces obtained in the linear regime before and after the writing process contain measurable information about the permanent modification in the linear refraction and absorption of the material.

4.3.1 Theory

We assume a TEM_{00} Gaussian distribution beam (travelling in the $+z$ direction) in a focal region of focusing lens (with $z = 0$ in a focal point):

$$E_e\left(r,z\right) = E_0\frac{w_0}{w\left(z\right)}\exp\left(-\frac{r^2}{w^2\left(z\right)}\right)\exp\left(-\frac{i\pi r^2}{\lambda R\left(z\right)}\right), \tag{4.1}$$

where E_0 denotes the on-axis amplitude of the electric field, r is the radial coordinate, λ is the laser wavelength, $R\left(z\right) = z\left(1 + z_0^2/z^2\right)$ is the radius of the curvature of the wave-front, $z_0 = \pi w_0^2/\lambda$ is the Rayleigh range and w_0 is the beam waist at the focal plane. Outside the focal plane the waist changes with z: $w\left(z\right) = w_0\left(1 + z^2/z_0^2\right)^{1/2}$. Since we are concerned with the permanent phase-shift and the image distribution acquired with a CCD, the temporal term will be omitted. The sample is considered as thin, with L, the thickness of the material smaller than the Rayleigh range ($L < z_0$). At the beginning the sample is fixed at $z = 0$ and irradiated with a given intensity during a given period of time. We suppose that the permanent modifications written inside the sample during this process have the same Gaussian distribution in the whole volume of the medium and are identical to the spatial profile of the focal beam intensity used in the writing process:

$$\Delta n\left(r\right) = \Delta n_0\exp\left(-\frac{2r^2}{w_0^2}\right), \tag{4.2}$$

$$\alpha\left(r\right) = \alpha_s + \Delta\alpha_0\exp\left(-\frac{2r^2}{w_0^2}\right), \tag{4.3}$$

where Δn_0 and $\Delta\alpha_0$ are the photo-induced on-axis refractive index and absorption coefficient respectively, α_s is the absorption coefficient of the material. Thus the electric field at the exit surface of the sample situated at z can be expressed by:

$$E_{out}(r,z) = E_e(r,z)\, e^{-\alpha_s L/2} \exp\left[-\left(i\Delta\Phi_0 + \frac{\Delta\alpha_0 L}{2}\right)\exp\left(-\frac{2r^2}{w_0^2}\right)\right], \tag{4.4}$$

where $\Delta\Phi_0 = 2\pi\Delta n_0 L/\lambda$.

Z-scan acquisitions are performed with and without circular aperture in the far field [63]. When there is no aperture at the exit of the setup, the Z-scan transmittance is sensitive only to the absorption. Therefore, $P(z)$, the output power can be obtained by spatially integrating the intensity distribution (proportional to $\int_0^\infty |E_{out}(r,z)|^2\, rdr$) at the exit surface of the sample. To obtain an analytical result, we applied an incomplete gamma function theory (see appendix A) in order to integrate the exponential of an exponential as it has been done in [152]. By defining the normalized open aperture Z-scan transmittance as $T_o(z) = P(z,\Delta\alpha_0)/P(z,0)$, we have found that the far-field signal varies with z, according to the following:

$$T_o(z) = \sum_{m=0}^{\infty} \frac{(-1)^m}{m!} \frac{(\Delta\alpha_0 L)^m}{(1 + m(1 + z^2/z_0^2))}. \tag{4.5}$$

This relation will be used in order to characterize the photodarkening phenomenon by calculating $\Delta\alpha_0$ from the experimental open aperture Z-scan transmittance. Moreover, numerically, we have found (Fig.4.6(a)) that only 5 terms in the sum in Eq.(4.5) are needed to be accurate within 1%.

When the aperture is placed at the exit of the setup, the beam must be propagated from the output face of the sample up to the aperture plane where the photodetector is placed. To calculate this far-field pattern we applied the Gaussian decomposition method [63][65][66]. Accordingly, the electric field at the output face of the sample is decomposed through a series expansion of exponential phase factor in Eq.(4.4) and the several Gaussian components propagate in the free space to the aperture plane where they are summed for reconstruction of the beam (see Appendix A). Finally, the normalized power transmittance

$T_c\left(z\right)$ through the aperture can be expressed by

$$T_c(z) = \frac{\int\limits_0^{r_a} \left|E_a\left(r,z\right)\right|^2 rdr}{S\int\limits_0^{\infty} \left|E_a\left(r,z,\Delta\Phi_0=0,\Delta\alpha_0=0\right)\right|^2 rdr}, \tag{4.6}$$

where E_a is the electric field at the aperture plane, r_a is an aperture radius and $S = 1-\exp\left(-2r_a^2/w_a^2\right)$ is the aperture transmittance, with w_a denoting the beam radius at the aperture plane in absence of any permanent phase modification. The evolution of the closed aperture (for very small $S = 0.01$) normalized transmittance is shown in Fig.4.6(b) by the dashed line ($\Delta\alpha_0 L = 1$ and $\Delta\Phi_0 = 0.3$). This is the case when both, strong absorption and refraction, contribute to the signal. However, assuming a very small aperture ($S \approx 0$) placed in the far-field region, a negligible absorption modification (i.e.$\Delta\alpha_0 L \ll \Delta\Phi_0$) and low phase shift $|\Delta\Phi_0| \ll 1$ we found an analytical expression for the normalized on-axis transmittance

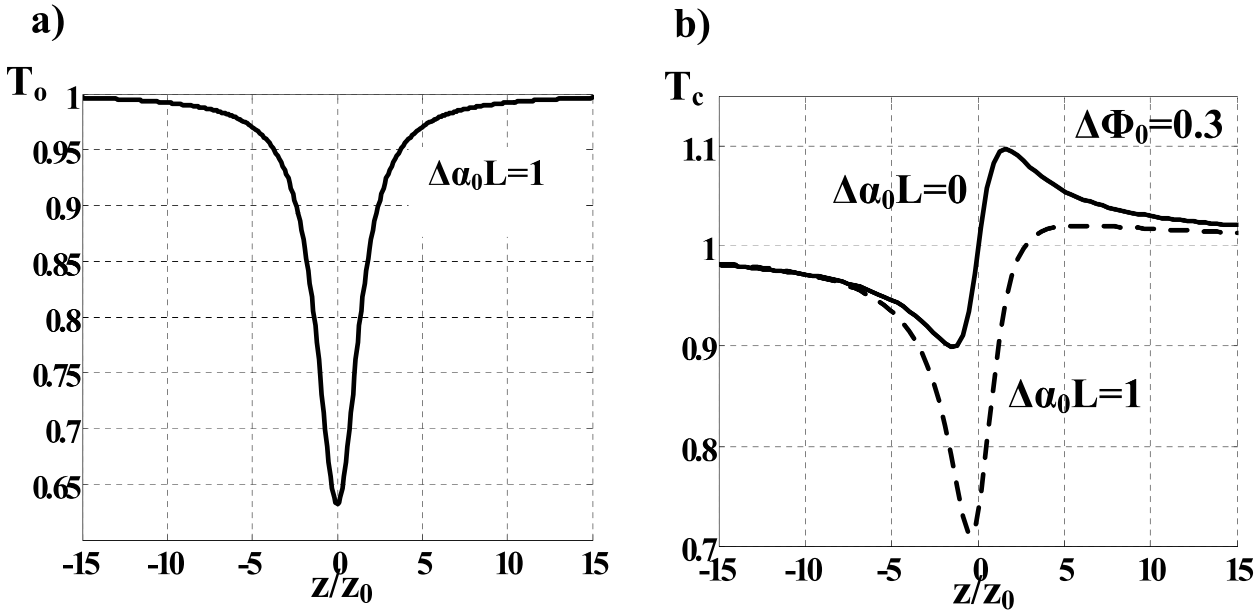

Figure 4.6: Calculated a) open aperture normalized transmittance (T_o) with $\Delta\alpha_0 L = 1$; b) closed aperture on–axis ($S = 0.01$) normalized Z-scan transmittance (T_c) for $\Delta\Phi_0 = 0.3$ with absorption $\Delta\alpha_0 L = 1$ (dashed line) and without absorption $\Delta\alpha_0 L = 0$ (solid line).

following the calculation procedure given in the appendix A:

$$T_c(z, S \approx 0) = 1 + \frac{4\Delta\Phi_0 x}{4x^2 + 9}, \tag{4.7}$$

where $x = z/z_0$. Our analytical result was checked by using an alternative theory based on Huygens-Fresnel principle (see appendix B) as introduced in [152] and the final relation was the same. The curve obtained from Eq.(4.7) has the same valley-peak (a minimum followed by a maximum) configuration (solid line in Fig.4.6(b)) as the one obtained by measuring positive nonlinear refraction in absence of nonlinear absorption. It is evident that the sign of Δn_0 will be given here without any ambiguity. By comparing the curves (dashed and solid lines) in Fig.4.6(b), we can see that the presence of absorption suppress the peak and enhance the valley of the normalized transmittance. The extrema of Z-scan transmittance can be calculated by solving the equation $dT_c(z, S \approx 0)/dz = 0$. Solutions are at $x_{p,v} = \pm 3/2$ therefore the difference between the maximum (peak) and the minimum (valley) in the transmittance is given by:

$$\Delta T_{pv} = \frac{2}{3}\Delta\Phi_0. \tag{4.8}$$

Numerical calculations show that this relation is accurate within 6% for $|\Delta\Phi_0| = 1$. It becomes more and more accurate for lower phase shift and for $|\Delta\Phi_0| \leq 0.3$ the error is negligible (less than 1%). For $|\Delta\Phi_0| > 1$ the linearity of Eq.(4.8) is no more valid (see Fig.4.7). Moreover, we found that the proportionality constant in Eq.(4.8) decreases with the size of the aperture, giving 0.63, 0.60, 0.55, 0.50, 0.44 for $S = 0.1$, 0.2, 0.3, 0.4 and 0.5 respectively. Similarly to the nonlinear Z-scan traces the distance between the peak and valley is constant ($\approx 3z_0$) whatever the phase shift is for $S \leq 0.5$. For larger apertures ($0.5 < S < 1$) the classical peak-valley transmittance configuration is disturbed significantly by additional signal appearing before and after the primary minimum and maximum. Therefore taking into account only $S \leq 0.5$ the following relation includes variations of proportionality constant within 3% accuracy:

$$\Delta T_{pv} = \frac{2}{3}(1 - S)^{0.56}\,\Delta\Phi_0. \tag{4.9}$$

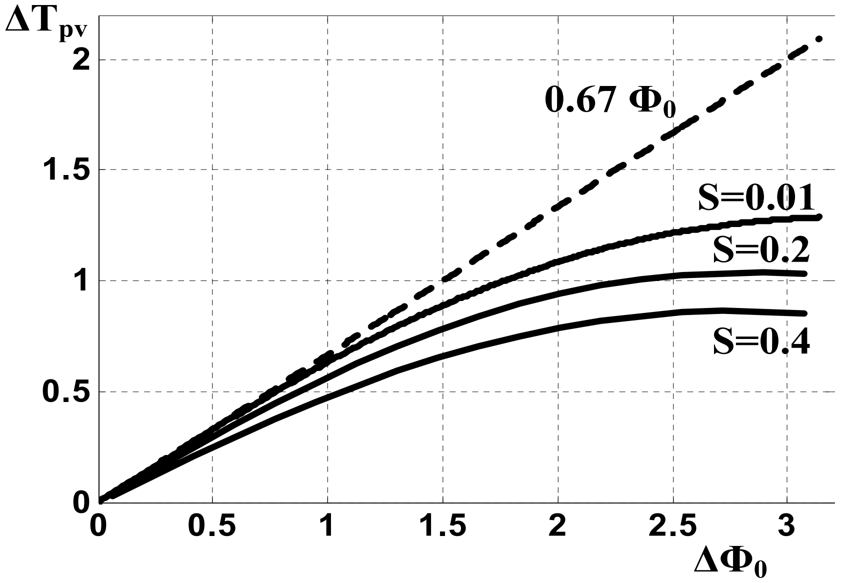

Figure 4.7: Calculated ΔT_{pv} versus the on-axis phase shift for aperture transmittance $S = 0.01$, 0.2 and 0.4, the dashed line is a curve described by Eq.(4.8).

This simple relation can be used to estimate the on-axis refractive index modification (related to $|\Delta\Phi_0| < 1$) in the absence of absorption change directly from the linear Z-scan traces. In presence of low absorption changes (photodarkening with $\Delta\alpha_0 L \leq \Delta\Phi_0$), we checked numerically that Eq.(4.9) can be used by dividing the closed aperture transmittance by the open aperture one. As for nonlinear measurements, the result is a new Z-scan where the signal agrees to within 5% to that obtained from purely refractive Z-scan transmittance.

4.3.2 Experiment and results

In order to confirm the above theoretical analysis we performed experiments using the $4f$ imaging system (Fig.4.8) with As_2S_3 glass. The focal length of the two lenses (L_1 and L_2) composing the setup was $f_1 = f_2 = 20\ cm$. It is important to note that in this configuration one can measure directly and precisely the waists of the Gaussian beam at the entry of the setup because the magnification is equal to 1. This allows to determine precisely, the focal beam waist and z_0, the Rayleigh range. The excitation is provided by a Nd:YAG laser delivering linearly polarized 17 ps single pulses at 1064 nm with 10 Hz repetition rate. The beam waist at the focal plane of lens L_1 is $w_0 = 27\ \mu m$ giving a Rayleigh range $z_0 = 2.1\ mm$. A beam splitter (BS_1) at the entry of the setup allows to monitor fluctuations (through lens L_3) occurring in the incident laser beam. The photoreceptor is a 1000×1018 pixels cooled ($-30°C$) CCD camera with fixed linear gain. The camera pixels have 4095 gray levels and each pixel is $12 \times 12\ \mu m^2$. In order to perform the writing process, the specimen was placed in focal plane ($z = 0$) of the focusing lens L_1.

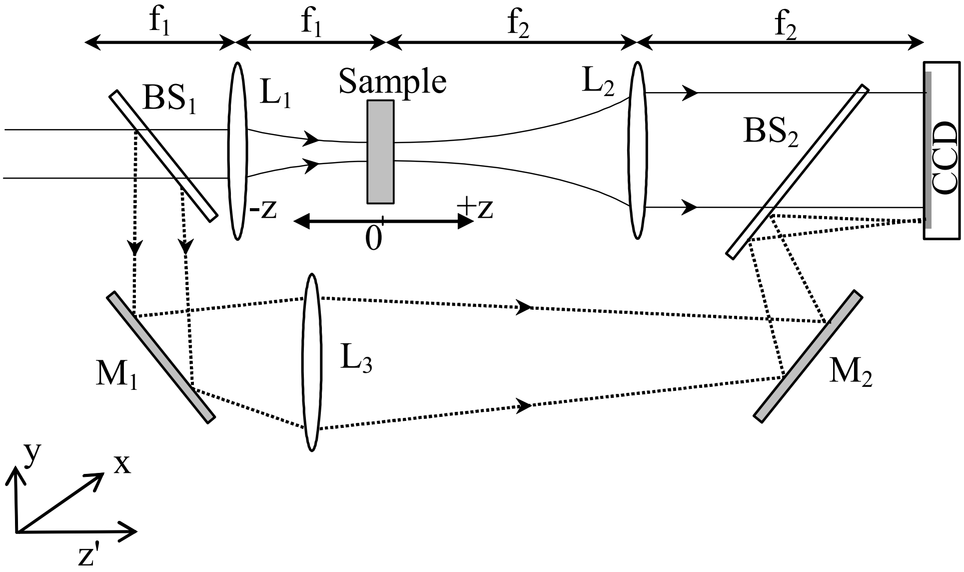

Figure 4.8: Schematic of the $4f$ imaging system. The sample is moved around the focal region. The labels refer to: lenses (L_1-L_3); mirrors (M_1,M_2); beam splitters (BS_1, BS_2).

Since As_2S_3 has a semiconductor-like structure characterized by an optical band gap around 2.35 eV [146] which is much higher than the energy of our laser beam (1.17 eV), the modifications of the linear optical coefficients can be induced only for a high intensity regime when a two-photon absorption or a multi-step one photon absorption through the mid-gap states can occur [130]. Therefore the writing process was performed with the on-axis focal intensity of the order of few GW/cm^2, which is a typical irradiance range where some photo-induced effects were observed in As_2S_3 at 1064 nm [129][130] or 1550 nm [144]. The intensity was calibrated using CS_2, and considering its nonlinear refractive index at 1064 nm in the picosecond regime given in [63]. The thickness of the glass was 1.4 mm which is smaller than the Rayleigh range, thus we can consider that the written modifications have the same distribution in the whole volume of the sample. Two sets of Z-scan acquisitions in the linear regime were made with very low intensity, one before and one after the writing process. Open and closed aperture Z-scan normalized transmittances can be numerically processed from the acquired images by integrating over all the CCD pixels in the first case and over a circular numerical filter in the second one. The comparison of the Z-scan results before and after the writing process can reveal the existence of the photo-induced changes in the material. In order to obtain good Z-scan traces for measurements, the specimen must be illuminated on the same impact region during all the experimental procedure. Therefore the motor translation stage (Z-scan axis) must be well aligned to be parallel with the direction of the light propagation. One should avoid any lateral movement of the sample as well as a lateral shift of the beam as for example at the output of neutral filters that we might add or take off in writing and reading processes. It is preferable to change the regime of the intensity by using a half-wave plate and a polarizer system. A good spatial quality of the beam is also required and the samples should have very good optical quality.

We performed writing processes with different intensities (from 2 GW/cm^2 to 10 GW/cm^2) and different cumulative energies (E_c) inside the specimen (from 1 mJ to 20 mJ). We observed a photodarkening effect for intensities above a threshold value of 3 GW/cm^2 whatever the cumulated energy was. Below this irradiance only changes in closed aperture transmittance (pure refractive index modification) were detected for long illumination time (high accumulated energy inside the specimen $E_c > 5\ mJ$) (Fig.4.9). According to Eq.(4.9), the variation of the transmittance ($\Delta T_{pv} = 0.072$) in Fig.4.9(a) obtained with $S = 0.4$ corresponds to $\Delta n_0 = 1.7 \times 10^{-5}$. The sign of the Δn_0 is positive according to the minimum followed by a maximum in the Z-scan trace of Fig.4.9(a). The solid line is the simulation given by Eq.(4.6) using the same experimental parameters. A very good agreement is obtained validating our theoretical approach.

In Fig.4.10, we can see an example of a closed and an open aperture Z-scan transmittances in the linear regime characterizing the permanent modifications when the writing intensity is 6 GW/cm^2 ($E_c = 5\ mJ$). Fig.4.10(b) reveals a photodarkening effect inside the specimen and the numerical fitting using Eq.(4.5) gives $\Delta\alpha_0 = 840\ m^{-1}$. The dots in Fig.4.10(a) give the result of the division between the closed and the open aperture Z-scan traces. The solid

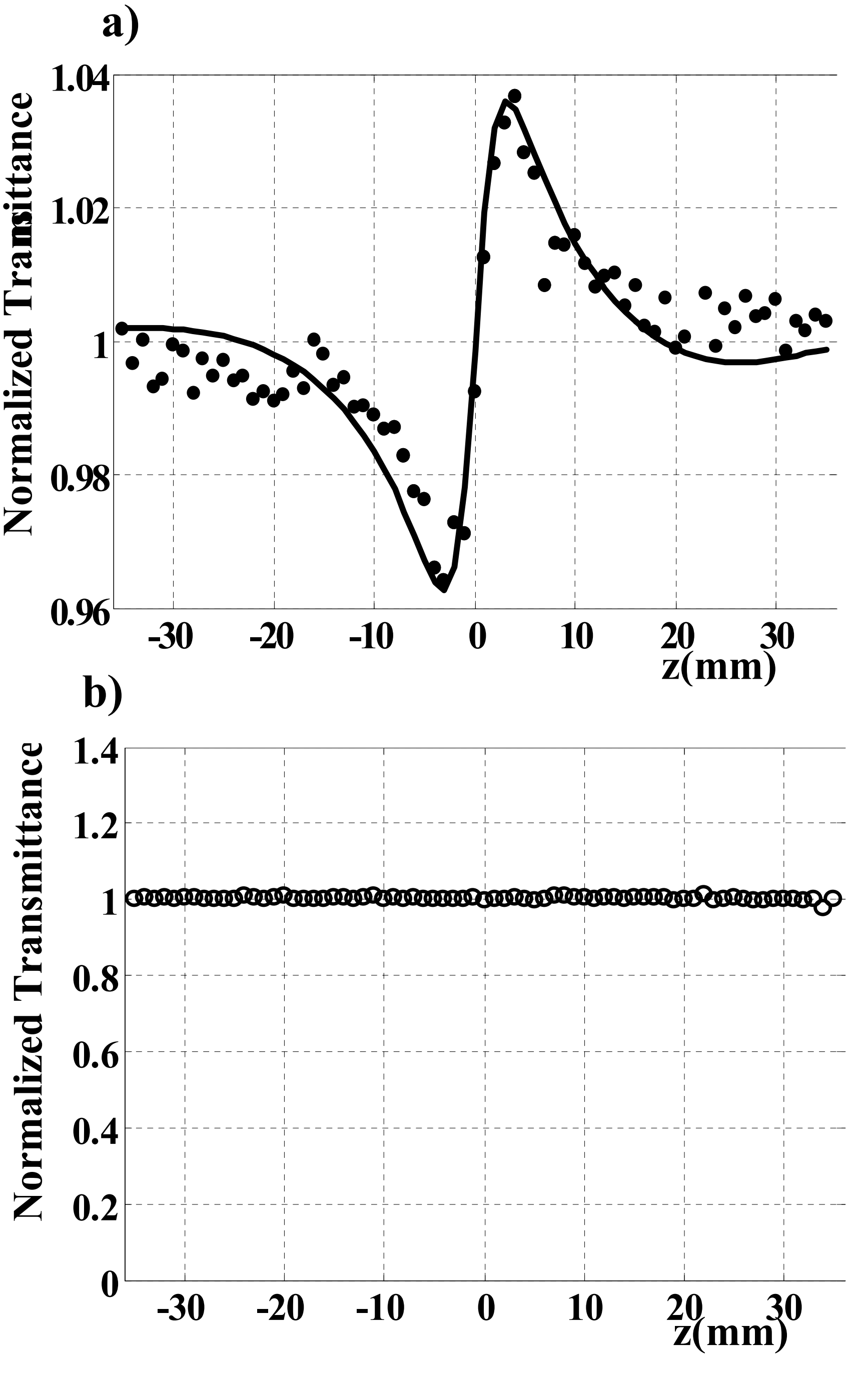

Figure 4.9: Normalized Z-scan transmittance revealing the permanent phase shift written inside 1.4 *mm* thick As_2S_3 glass slab by a Gaussian beam with 3 GW/cm^2 intensity and cumulative energy $E_c = 18$ mJ: (a) experimental (filled dots) closed aperture normalized transmittance obtained with $S = 0.4$ giving $\Delta n_0 = 1.7 \times 10^{-5}$ ($\Delta\Phi_0 = 0.14$), the solid line is the calculated result with the same parameters (b) experimental (empty circles) open aperture data showing the absence of photodarkening ($\Delta\alpha_0 = 0$).

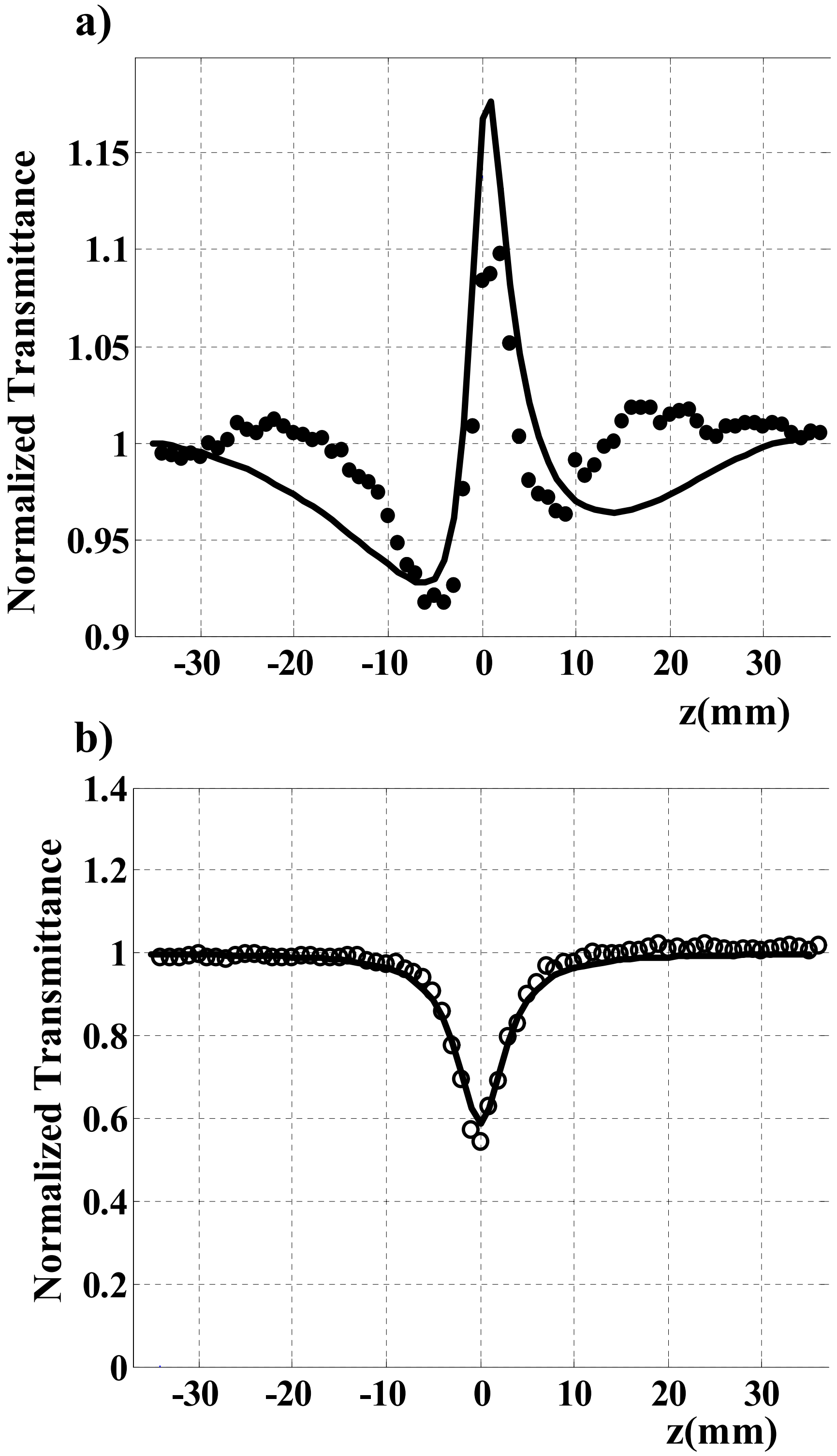

Figure 4.10: Normalized Z-scan transmittance revealing the permanent phase shift written inside 1.4 mm thick As_2S_3 glass slab by a Gaussian beam with 6 GW/cm^2 intensity and cumulative energy $E_c = 5\ mJ$: : (a) experimental (filled dots) closed aperture data after division by open aperture ones and calculated (solid line) transmittance obtained with $S = 0.4$ and $\Delta n_0 = 4.3 \times 10^{-5}$ ($\Delta\Phi_0 = 0.35$) (b) experimental (empty circles) open aperture data; the solid line is a theoretical fit giving $\Delta\alpha_0 = 840\ m^{-1}$.

line is the theoretical result taking into account $\Delta n_0 = 4.3 \times 10^{-5}$ obtained from Eq.(4.9) by considering the experimental ΔT_{pv}. In this case where $\Delta\alpha_0 L > \Delta\Phi_0$, we have to be careful using the simplified Eq.(4.9) because the absorption is relatively high and the refractive signal is hidden by the related deep valley. Although the theoretical result resembles the experimental data, the fitting in Fig.4.10(a) is far from perfect. Anyway, Fig.4.10 is shown here in order to demonstrate principally the experimental evidence of the photodarkening effect and the possibility to quantify it by the open Z-scan trace as shown in Fig.4.10(b).

It must be added that Eq.(4.9) reveals the high sensitivity of the Z-scan technique to characterize linear Gaussian phase shift. Our experimental apparatus is able to resolve normalized transmittance changes as low as 3×10^{-3}. Considering a signal to noise ratio approximately equal to 3 we are able to measure more than $\approx 1\%$ transmittance change. The corresponding measured phase value will be equal to $|\Delta\Phi_0| = 10^{-2}/0.67 \approx 15\ mrad$ for $S \approx 0$. Thus the minimum optical path length which can be measured (corresponding to a wave front distortion) is $\Delta n_0 \times L = 15 \times 10^{-3} \times \lambda/2\pi \approx \lambda/420$. Similarly, when considering Eq.(4.5) we can measure as low as $\Delta\alpha_0 L = 0.02$.

4.4 Linear characterization of transparent thin films by Z-scan [153]

In this section we analyze the influence of a rectangular phase line embedded in transparent thin film on the far field normalized transmittance using Z-scan closed aperture configuration. We will show that under certain conditions (detailed below), we can obtain a peak - valley shape of the Z-scan profile as in the nonlinear measurement. The difference between the maximum (peak) and the minimum (valley) of the transmittance (usually called ΔT_{pv}) will be related linearly to the permanent phase shift, therefore providing simple formula for optical parameter characterization as, n_0, the linear refractive index or L, the thickness. Several optical techniques allow to determine these quantities, see for example [154] and references therein. But, the interferometric and the ellipsometric systems [112][155] are the most popular due to their non-contact character and high sensitivity along with their imaging derivatives [156][157][158][159][160]. Although, all of these methods are very precise, they require relatively complex and expensive experimental apparatus in contrary to the technique reported here which offers simplicity in both, optical setup as well as the derived measurement formulas given hereafter.

4.4.1 Theoretical model

Z-scan measurements were performed inside the $4f$ imaging system shown in Fig.4.8. To support our experiment we performed Z-scan numerical simulations using the beam propagation method described in section 3.2. As usual we suppose that the amplitude of electric field distribution at the object plane (front focal plane of lens L$_1$) is Gaussian, $E = E_0 \exp\left[-\left(x^2+y^2\right)/w_e^2\right]$, where x, y are the spatial coordinates, E_0 denotes the on-axis amplitude and w_e is the beam waist at the entry of the setup. The transmission of a sample with a rectangular phase line of size l_x and l_y along x and y axes, respectively ($l_x \gg l_y$), is defined as $T(x,y) = \exp\left[-i\Delta\Phi\left(x,y\right)\right]$ where $\Delta\Phi\left(x,y\right) = \left[2\pi\left(\widehat{n}-1\right)L \times \mathrm{rect}\left(x/l_x\right) \times \mathrm{rect}\left(y/l_y\right)\right]/\lambda$ is the phase shift. Here $\widehat{n} = n_0 - i\kappa$ is the complex refractive index with n_0 denoting the linear refractive index and κ is the extinction coefficient. The rectangular function rect(x) is defined as equal to one if $|x| < 1/2$ and zero elsewhere. The closed aperture normalized Z-scan transmittance is obtained by integrating spatially the calculated output intensity over a circular aperture in the image. The radius of the aparture is defined as $r_a = w_a\left[\ln\left(1/\left(1-S\right)\right)\right]^{1/2}$, where S is the aperture linear transmission and w_a is the beam waist in the image plane measured in absence of the sample. The latter is equal to the beam waist at the entry ($w_a = w_e$) since the magnification of the considered $4f$ system is equal to one.

4.4.2 Experiment and results

Usually, our setup and experiment are used for nonlinear optical measurements. That is why the excitation was provided here by a Nd:YAG laser delivering 17 ps single pulses at 1064 nm with a 1 Hz repetition rate. Nevertheless, a more energy stable CW laser can be beneficially used. The focal length of the two lenses composing the $4f$ system (Fig.4.8 in section 4.3.2) is $f_1 = f_2 = 20\ cm$. The photoreceptor is a 1000×1018 pixels cooled ($-30°C$) CCD camera with fixed linear gain. The camera pixels have 4095 gray levels and each pixel is $12 \times 12\ \mu m^2$. The laser intensity is kept in low regime in order to avoid any nonlinear optical phenomena and destruction of the material. A beam splitter (BS_1) at the entry of the setup allows to monitor the fluctuations (through lens L_3) occurring in the incident laser beam independently from the absorption that might occur inside the material. Open and closed aperture Z-scan normalized transmittances can be numerically processed from the acquired images, by integrating over all the CCD pixels in the first case and over a circular numerical filter in the second one. We choose a linear transmission of the filter $S = 0.4$. The sample is a thin film of polymethyl methacrylate (PMMA) deposited on a glass substrate by spin coating method. The material is completely transparent in the infrared region ($\kappa = 0$) and its refractive index is $n_0 = 1.48$ [161]. The rectangular shape phase line in the film was made by carefully scratching the film with a sharp edge over a distance l_x long enough ($2\ cm$) in comparison with the focused beam waist in order to neglect its diffracting effects along the x direction. The profile of the scratch (Fig.4.11) was measured by a probing mechanical stylus giving a deepness $L = 120 \pm 10\ nm$ and a width $l_y = 55 \pm 5\ \mu m$. We aligned very carefully i) the motor translation stage (Z-scan axis) to be parallel with the direction of the light propagation, ii) using the image given by the CCD at different z position of the sample, the groove line was centered in the middle of the beam in order to have symmetrical diffracted intensity distribution on its border. In Fig.4.12(a) one can see the experimental acquisition of the image at the output of the $4f$ system for a sample location at $z = -45$

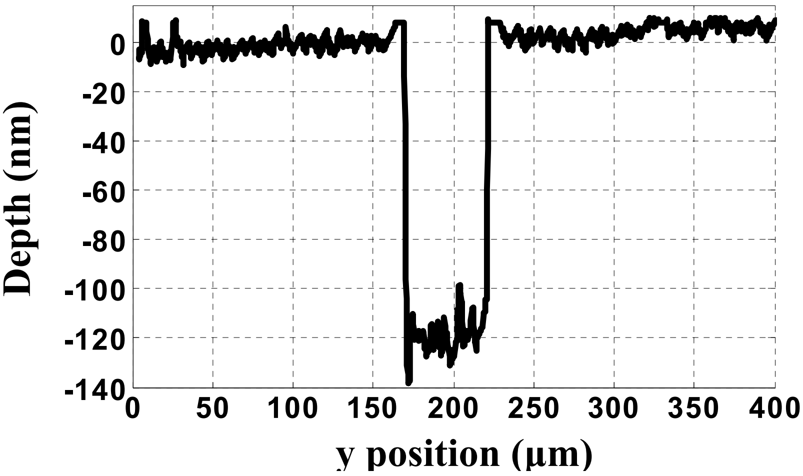

Figure 4.11: Scan made by mechanical profile meter showing the geometrical parameters of the rectangular groove (width and deepness).

mm and for $w_e = 2.52$ *mm*. The latter value gives a beam waist in the focal plane ($z = 0$) $w_0 = 27$ *µm*. Negative z is related to the sample position close to the first converging lens (L_1). In Fig.4.12 (b) we can see the corresponding simulated image obtained with the same experimental parameters. In order to define the numerical parameters of the phase object we used the width and the deepness given by the profilemeter. The qualitative good agreement between these two images was the first step to validate our numerical calculations.

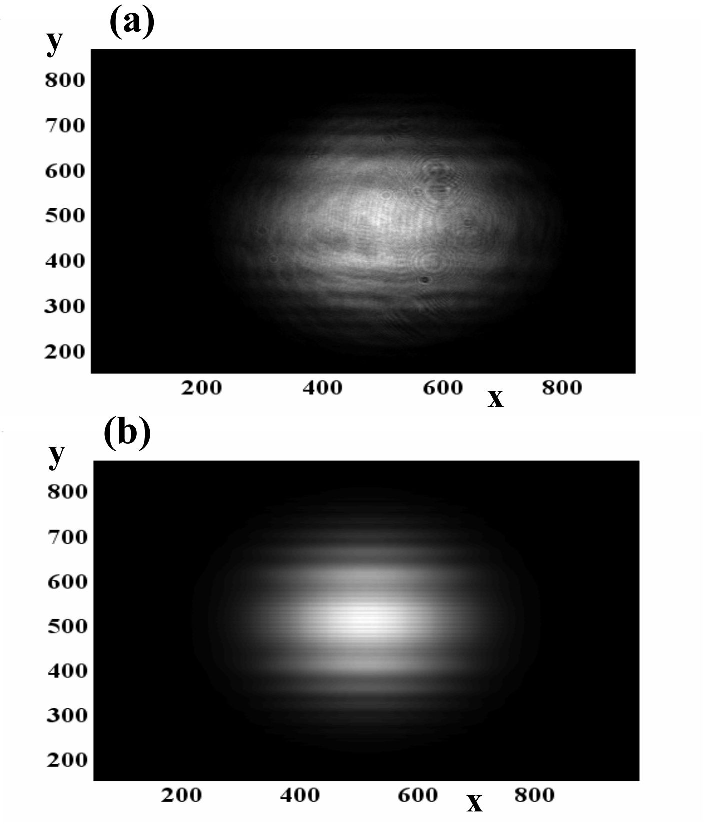

Figure 4.12: Images at the output of the $4f$ system for $z = -45$ *mm*: (a) experimental acquisition, (b) numerical simulation. The coordinates (x, y) are in pixels.

The Z-scan measurements were performed within a range of $z = \pm 45$ *mm*, displacing the sample with 1 *mm* step and acquiring one image for every position. In Fig.4.13 we can see a comparison between the experimental closed aperture normalized transmittance and its numerical simulation obtained for $S = 0.4$ with the previous mentioned experimental parameters ($w_0 = 27$ *µm*, $l_x = 1.2$ *mm*, $l_y = 60$ *µm* and $\Delta\Phi(0,0) = \Delta\Phi_0 = 0.34$). The remarkable good agreement between experiment and theory validates totally our numerical

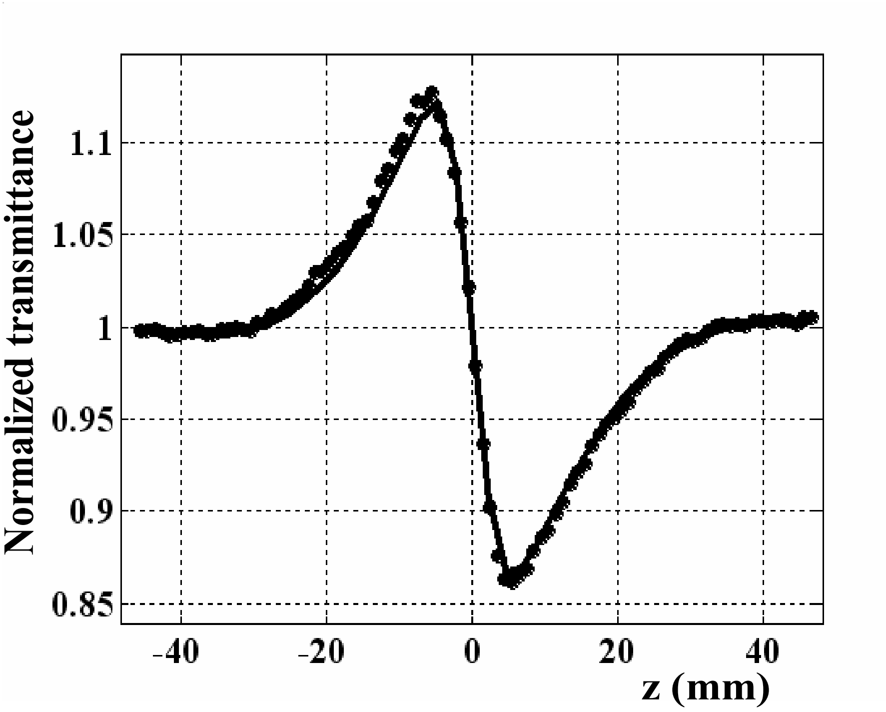

Figure 4.13: Experimental (dots) closed-aperture Z-scan normalized transmittance $T(z)$ and the corresponding theoretical simulation (solid line).

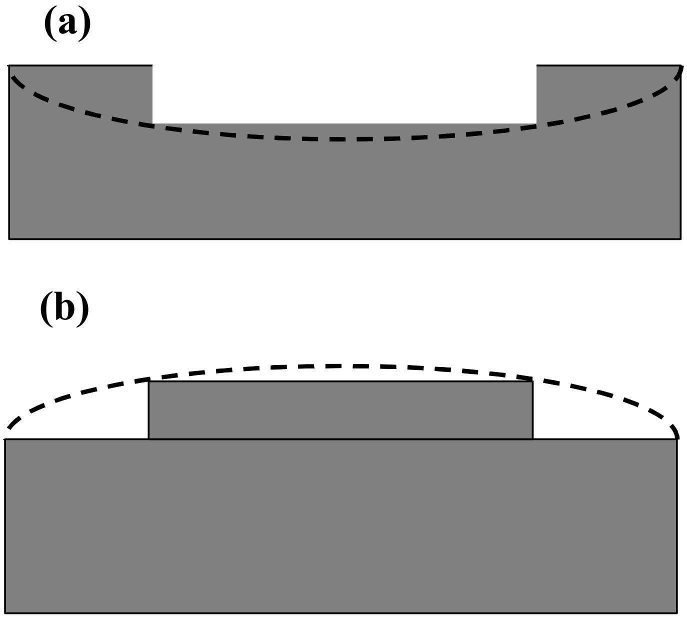

Figure 4.14: Similarity between the cross-section of a) rectangular groove embedded in thin film and the diverging lens (dashed line), b) rectangular strip layer on thin film and the converging lens (dashed line)

simulation. The prefocal transmittance maximum (peak) followed by postfocal transmittance minimum (valley) can be physically explained by noting that the phase object has an approximate sampled shape of thin diverging lens (see Fig.4.14(a)). For a strip line deposited on the film (Fig.4.14(b)) the simulation of the normalized Z-scan transmittance shows a minimum followed by a maximum therefore indicating a positive phase shift. The peak followed by the valley is similar to the one provided for Z-scan traces where a negative nonlinear coefficient (n_2) characterizes the nonlinear material. When the sample is far away from the focus, the beam waist is large compared to the width of the phase line, only a small part of the beam is diffracted and the transmittance remains relatively constant with respect to the position. When the sample is brought closer to the focus, the phase object starts to act as a focusing or defocusing lens since the beam waist becomes smaller: more energy interact with the area of the phase steps diffracting outside or inside the aperture more or less light depending on z position. When the sample is in the focal region and for large l_y compared to w_0, there are no significant changes in the transmittance because the focused light does not encounter the phase step. In Fig.4.15 the dashed line ($l_y = 250\ \mu m \gg 2w_0 = 54\ \mu m$, $\Delta\Phi_0 = 0.34$) represents such situation revealing a flattened central part included between points A and A'. In this figure we can see the simulated transmittance for two different widths of the phase line. One of them (the solid line) is the simulation reported in Fig.4.13 and plotted here for comparison purposes. Using simple geometrical optics approximation and calculating $z_A(z_{A'})$, the position of point A (A') where the beam waist of the converging (diverging) beam is equal to the half width of the rectangular line, we obtain $z_A = l_y f/2w_e$ (see Fig.4.15, where the variations of the transmittance become significant). For small on-axis phase shift ($|\Delta\Phi_0| < 1$), the peak and valley occur at the same distance with respect to the focus. Empirically we have found that the maximum (minimum) is situated approximately at twice the $z_A(z_{A'})$ value. Introducing the beam waist at the focus $w_0 = \lambda f/\pi w_e$, the maximum and the minimum are separated by $\Delta z_{pv} = 2\pi l_y w_0/\lambda$. Numerically, we have found a more precise value (less than 2% error) valid for large Δz_{pv} ($\geq 10\ mm$): $\Delta z_{pv} \approx 2.4\pi l_y w_0/\lambda$. Theoretically, every lateral size of the phase objects can be seen by the light as a diverging or a converging lens depending on the beam waist size with respect to z position.

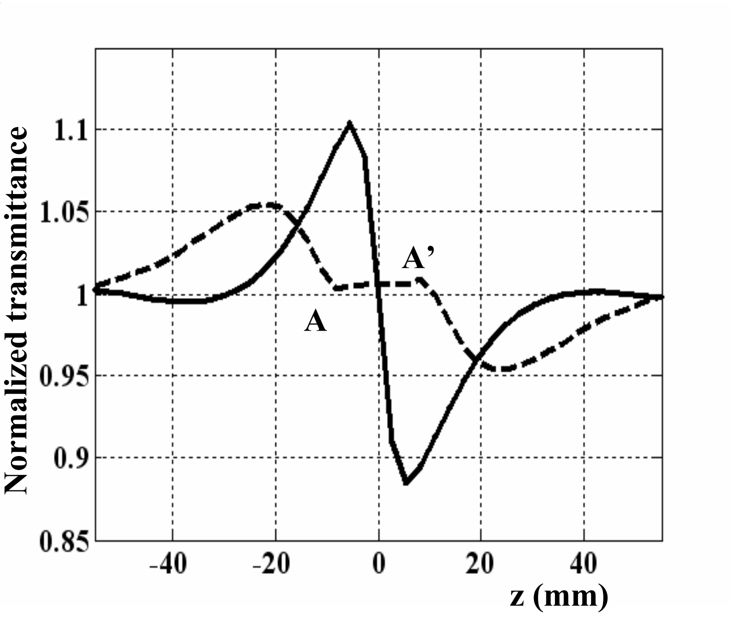

Figure 4.15: Comparison of the Z-scan normalized transmittances. The solid line is the simulation reported in Fig.4.13 for ($l_x = 1.2$ mm, $l_y = 60$ μm). The dashed line is the simulation given for the same parameters with a larger width of the rectangular phase object: $l_y = 250$ μm.

One of the advantages of the Z-scan method [63] comes from the simple expression relating ΔT_{pv} to the induced Gaussian nonlinear phase shift allowing nonlinear optical characterization of the material without resorting to complicated computer fits. Following the same way, we have to introduce similar expression for permanent rectangular phase shift line. Numerically, we have found that for small on-axis dephasing $|\Delta\Phi_0| \leq 1$ the following relation is fulfilled within less than 10% error:

$$\Delta T_{pv} = a\,|\Delta\Phi_0|\,, \tag{4.10}$$

where a is a proportionality factor. The linearity of this relationship becomes more and more accurate for lower on-axis phase shift and for $|\Delta\Phi_0| \leq 0.3$ the error is negligible (less than 1%) (see Fig.4.16(a)). We have found that in general the proportionality factor is dependent on the aperture size (S), the beam waist (w_0), and the lateral geometrical dimensions (l_x and l_y) of the rectangular phase object. Since this problem is quite complicated and possesses many parameters, we fixed $S = 0.4$ and $w_0 = 27$ μm. Let us focus on the importance of the size of the rectangular line with respect to the beam waist. In Fig.4.16(a) we can see ΔT_{pv} versus $|\Delta\Phi_0|$ calculated with the size of the phase line close to that measured experimentally ($l_y = 60\ \mu m$ and $l_x \gg l_y \approx 2w_0$). The slope of the curve is $a = 0.9$. This slope defines the sensitivity of the method. In our case with a pulsed laser having relatively higher energy fluctuation than CW one, the resolution of the measurement is not optimized. Nevertheless, we are able to resolve normalized transmittance changes as low as 3×10^{-3}. Considering a signal to noise ratio approximately equal to 3 we are able to measure more than $\approx 1\%$ transmittance change. According to Eq.(4.10) the measured phase value will be equal to $|\Delta\Phi_0| = 10^{-2}/0.9 \approx 11.1\ mrad$. Thus the minimum optical path length that we can measure (corresponding to a wave front distortion) is $\Delta n_0 \times L = 11.1 \times 10^{-3} \times \lambda/2\pi \approx \lambda/550$.

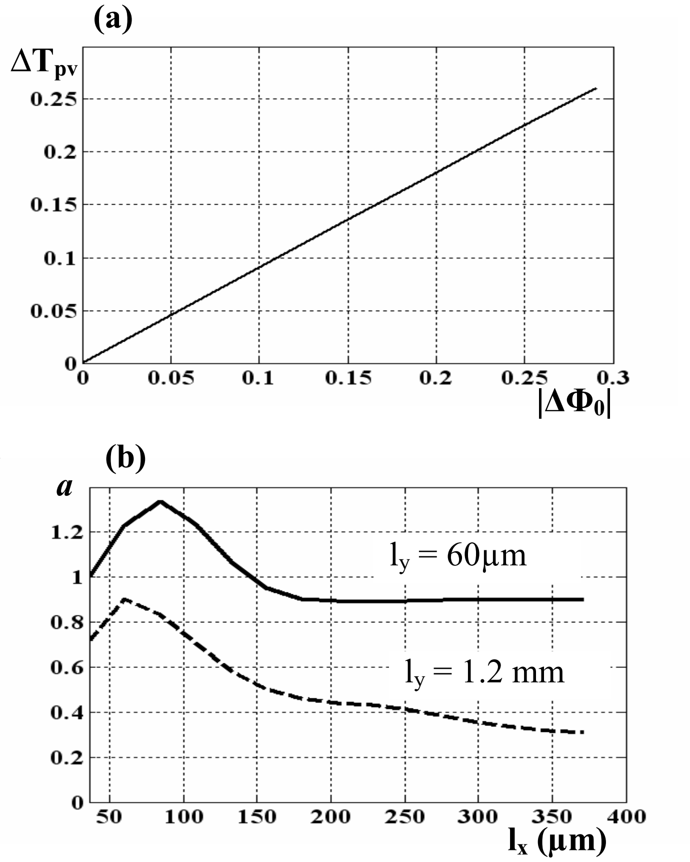

Figure 4.16: (a) Calculated ΔT_{pv} as function of the on-axis phase shift ($\Delta\Phi_0$) for $S = 0.4$, and (b) Calculated influence of l_x on the proportionality factor a for a fixed value of l_y: solid line $l_y \sim 2w_0$ ($= 60\ \mu m$), dashed line $l_y \gg 2w_0$.

The dashed line in Fig.4.16(b) shows the variations of a versus l_x for very large l_y (1.2 mm). The highest value ($a = 0.9$) is obtained for $l_y \approx 2w_0$. Therefore, for a given one lateral dimension of the rectangular phase object, the maximum of the sensitivity appears when the second dimension is comparable with the focal beam diameter. Moreover, by fixing one dimension at this maximum ($l_y \approx 2w_0$) and by varying the other one, a is constant when $l_x \gg l_y$ as it is shown by the solid line in Fig.4.16(b). The experimental acquisitions shown previously (see Fig.4.13) correspond to this case. Note that when all the geometrical dimensions are comparable ($l_x \approx l_y \approx 2w_0$), a is not constant any more and reaches a maximum as we can see at the beginning of the solid line in Fig.4.16(b). One should avoid this region where the diffraction occurs in both directions contributing to very large variation in the Z-scan signal with the lateral dimension of the phase shift. The enhancement of the sensitivity will come at the expense of a reduction in accuracy. Nevertheless, the order of magnitude of the measured phase shift is preserved. It has to be added that the same experimental setup could be used to estimate the lateral size (l_x and l_y) of the phase object by recording an image of its diffracting borders when the object is located at the entry of the $4f$ system.

4.5 Conclusions

It this chapter we have shown that photo-induced effects (PIE), creating permanent changes in refraction and absorption, can hinder considerably the nonlinear optical characterization using both NIT-PO and Z-scan methods. We illustrated this problem by investigating nonlinearities in thin films of chalcogenide glasses ($Ge_xAs_ySe_{100-x-y}$ and $Te_{20}As_{30}Se_{50}$). Firstly, we used the NIT-PO technique to verify the presence of PIE by observing the variation of the phase contrast with the input intensity. We employed this method to study the kinetics of PIE and especially to determine the intensity threshold for damage. We have shown that very small thicknesses of thin films combined with relatively low nonlinearity make nonlinear characterization impossible. In such conditions the optical interaction length is simply too short to induce measurable nonlinear signal before exceeding the intensity threshold for damage. Even the high sensitivity of NIT-PO or Z-scan is not enough to characterize thin sample if the resolution of the measured transmission given by photo-detector is not sufficiently high. Theoretically one can enhance the nonlinear response by illuminating the sample with light of wavelength not far from the resonance of the material. In this situation it is possible to obtain detectable signal from thin film as we have shown for $Te_{20}A_{30}Se_{50}$ glass using Z-scan technique. However in this spectral region the enhancement of the nonlinear refraction is accompanied by relatively strong (linear and/or nonlinear) absorption decreasing the intensity threshold for damage. Moreover in the particular case of the studied chalcogenide glass the high nonlinearity can be attributed to the free carrier absorption effect. We have shown that for intensities above the damage threshold, PIE can contribute to both, open and closed aperture Z-scan normalized transmittances, masking pure nonlinear response of the sample and leading to erroneous results of n_2 and β. To verify the presence of photo-induced changes three scans are necessary to be performed: in low, high and once again in low intensity regime, respectively. We showed that the comparison of low intensity scans (preventing the relevant nonlinearity) in the closed and open aperture configurations can reveal the presence of the ablated hole and the photo-darkening effect created inside the sample in the nonlinear regime. Such linear measurements can provide information about deepness of the region where the modifications occured. It was shown that the changes as low as one tenth of nanometer depth can be sensed by Z-scan technique.

Following the latter results we have demonstrated theoretically and experimentally that the Z-scan technique can be a useful tool to investigate Gaussian profile photo-induced permanent modifications of optical coefficients inside photosensitive materials. The magnitude and the sign of linear alterations in refraction and absorption can be separately determined. Particularly we have studied the photo-induced changes in the linear optical constants of bulk slab of As_2S_3 caused by sub-band gap irradiation. Measuring photo-induced changes in refraction and absorption using Z-scan technique to investigate quantitatively the photosensitivity in various materials can be advantageous to quantify the process before waveguide optical writing.

We have also shown that the Z-scan method can be used to investigate thickness or linear refractive index in thin films. It was demonstrated that the closed aperture Z-scan profiles with a peak-valley configuration can be obtained by Z-scanning a rectangular phase object (rectangular groove or scratch inside the film) as in nonlinear measurements. We have introduced a simple relation in order to determine the magnitude of permanent phase shift directly from the Z-scan data. The validity of this relation has been discussed taking into account the lateral geometrical size of the rectangular phase object with respect to the focal beam waist. The method shows high sensitivity that allows the optical path length as low as $\lambda/550$ to be measured permitting to determine precisely the thickness or the refractive index of transparent thin film.

In the next chapter we will describe the Z-scan measurement of nonlinear optical coefficients for different optical materials. Particularly we will focus on Z-scan absolute measurements of n_2 in CS_2 and fused silica, both materials frequently used as references in nonlinear optics. The problem of calibration of measurement systems will be discussed. Finally the Z-scan results for new families of chalcogenide and oxide glasses will be presented and compared with the BGO theoretical model in order to predict the nonlinear coefficient from the linear experimental data.

Chapter 5

CHARACTERIZATION OF NONLINEAR MATERIALS

5.1 Introduction

In the first part of this chapter we report on Z-scan absolute measurements of the nonlinear refractive indices in carbon disulfide (CS_2) and fused silica (SiO_2). These materials are commonly used as standard references in nonlinear optical experiments. To obtain more accurate values than those usually used since approximately 30 years, we combine the Z-scan method inside a $4f$ imaging system (in order to analyze the spatial distortion of the diffracted pump beam) with the Kerr Shutter experiment (to evaluate the temporal pulse width durations for three different wavelengths 1064 nm, 532 nm and 355 nm). The obtained n_2 values are surprisingly one order of magnitude less than the ones usually taken into account in the picosecond regime and a more significant dispersion of the nonlinear refractive index is found. Experimental and simulated Z-scan transmittance profiles as well as acquired autocorrelation functions in the Kerr-gating experiments are presented in order to validate our measurements.

In the second part of the chapter we present the results of Z-scan measurements (1064 nm, 17 ps) of nonlinear refractive indices and nonlinear absorption coefficients for different compositions of chalcogenide glasses in GeS_2-Sb_2S_3-CsI system and oxide glasses $Pb(PO_3)_2$-WO_3. We show that the simple well known BGO model based on the theory of the semi-classical harmonic oscillator can be a useful tool for theoretical predictions of the nonlinear refractive index in these infrared glasses. The figure of merit (FOM) $2\beta\lambda/n_2$ of these materials is studied and their potential usefulness for optical switching applications is discussed.

5.2 Absolute measurements of n_2 in CS_2 and fused silica [162]

Generally in nonlinear optical characterization the measurements have relative character. It is much easier to determine nonlinear coefficients with respect to some standard and accepted values than to perform absolute characterization. Indeed, the latter requires an accurate knowledge about spatio-temporal profile of the pump beam as the beam spot size, the beam intensity distribution, the pulse energy, the pulse shape and the pulse duration. All these parameters are usually those where the greatest experimental errors reside. The relative measurements simplify the problem and minimize the error. However the precise values of n_2 and β for reference materials are required in order to determine trustworthy relative results. In this section we present absolute measurements for carbon disulfide (CS_2) and fused silica (SiO_2), two standard references materials used in nonlinear experiments. Both of these optical-Kerr media have negligible nonlinear absorption in the range of the low third order optical nonlinearities. CS_2 is generally used to calibrate the incident intensities in the experimental setup for characterizing materials having relatively high nonlinear refractive index (n_2 of about 10^{-18} m^2/W). While fused silica is used for materials with nonlinearities two order of magnitude lower. Nowadays, the absolute n_2 measurements are rare. The order of magnitude is sufficient sometimes to compare nonlinearities together but more precise and accurate absolute values will allow us to better understanding the physical properties of nonlinear phenomena. Moreover the absolute values in glasses are also of interest for high-power laser because of their wide use as optical components inside the system. When a physical quantity is investigated it is necessary to make as many measurements as possible with different experimental parameters and different operators in order to obtain a final reliable mean value. To characterize precisely spatio-temporal profile of pump laser beam we performed Z-scan and Kerr shutter experiments similarly as it was done in [163][164]. The far-field diffraction pattern in a Z-scan experiment is an excellent way to obtain precisely the spatial parameters of the focused laser beam inducing nonlinearities. On the contrary, it is more difficult to obtain information about the temporal profile of the beam. Generally, one relies on the pulse duration values given by the laser manufacturers. Rarely, even though the second order autocorrelation technique is used to determine the pulse duration in the fundamental wavelength (1064 nm with Nd:YAG laser), the pulse durations of the generated harmonics (532 nm, 355 $nm\ldots$) are theoretically deduced by dividing the obtained result at 1.064 μm with $\sqrt{2}$, $\sqrt{3}$,...[23]. In this section, we will show that such theoretical prediction can be one of the sources of important errors.

First we will review the nonlinear refractive indices for CS_2 and fused silica available in the literature. Then we will introduce the principles of our absolute measurements as well as the details of Z-scan and Kerr shutter experiments. Finally the obtained n_2 values will be presented and the comparison with already existing results will be done.

5.2.1 Nonlinear refractive index in CS_2

The nonlinear refractive indices for CS_2 reported in the literature are summarized in table 5.1. The values of n_2 are ordered according to the increasing pulse duration because the nonlinear response of CS_2 is mainly governed by the pulse-width of the incident laser beam. Molecular reorientational relaxation time of neat CS_2 was estimated to be around ≈ 2 ps [35][165][166]. Hence it is expected that the nonlinear refraction in the picoseconds range is mostly determined by the molecular reorientation process, while for shorter laser pulses, in the femtosecond regime, the nonlinear response of CS_2 has an electronic origin combined with the molecular libration mechanism (> 100 fs) [166][167]. Indeed, most of the results, given in table 5.1, show that there is approximately one order of magnitude difference in n_2 values between pico- and femtosecond regimes. For a long nanosecond pulses thermal effects start to play an important role [63]. The absolute measurements reported below in this section are performed in the picosecond regime ($7 - 17$ ps). Most research groups agree that in this range the nonlinear coefficient takes a value around $n_2 \approx 3 \times 10^{-18} m^2/W$. As it is shown in table 5.1 this value is relatively independent of the wavelength over the visible and near infrared region.

n_2 $(10^{-19} \times m^2/W)$	**wavelength** (nm)	**Pulse duration**	**Experimental technique**	**Reference**
3.99	620	60 fs	Kerr gate	[168]
5.96	635 – 640	65 fs	Kerr gate	[169]
4.89	616	75 fs	Beam deflection	[170]
12	775	100 fs	Z-scan, 80 MHz	[171]
7.72	630	100 fs	interferometry	[172]
2.5 (±0.3)	800	110 fs	interferometry	[173]
3.1 (±1.0)	800	110 fs	Z-scan, 10 Hz	[173]
3.0 (±0.6)	795	110 fs	Z-scan, 10 Hz	[174]
2.1	770	120 fs	Z-scan, 76 MHz	[96]
2.3	770	130 fs	Z-scan, 76 MHz	[95]
0.13	497	500 fs	Z-scan, DFWM, 5 Hz	[175]
51.5	1064	9 – 10 ps	Kerr gate	[35]
28 (±8)	1064	20 ps	interferometry	[176]
38	532	25 ps	interferometry	[177]
31 (±5)	532	27 ps	Z-scan	[63]
33 (±8)	1064	27 ps	Z-scan	[63]
38 (±16)	10600	27 ps	Z-scan	[63]
38 (±8)	1064	40 ps	self-focusing	[178]
32 (±16)	1054	300 ps	Z-scan, 1 Hz	[174]
54 (±18)	10600	3 ns	self-focusing	[179]
36 (±3)	532	6.5 ns	Z-scan	[78]
35 (±7)	795	8 ns	Z-scan, 10 Hz	[174]
40 (±20)	795	75 ns	Z-scan, 10 Hz	[174]
3.4	1907	-	Third harmonic generation	[180]

Table 5.1: Some literature reported values of n_2 for CS_2

5.2.2 Nonlinear refractive index in fused silica

The values of n_2 for fused silica available in the literature were summarized by D. Milam in Ref.[181] and are presented here in table 5.2. The latter is also supplemented by few additional results (shown without error bars) which were not taken into account in [181]. In contrary to CS$_2$, the nonlinear coefficient of silica depends relatively weakly on the pulse duration [182] in the femto- and picosenod regimes and it is expected that n_2 values increase noticeably from near infrared to UV region where the resonance of silica occurs. Therefore the nonlinear refractive indices given in table 5.2 are ordered according to the increasing wavelength of incident light. One can easily notice a large scattering of the presented results. It is emphasized in [181] that more than 30 absolute measurements of n_2 in silica have been made at wavelengths ranging from 249 to 1550 nm and the measured values differ sometimes even by a factor of more than 3 at some identical wavelengths. However despite the high discrepancy, all values are of the order $\sim 10^{-20}\ m^2/W$.

Milam made an effort [181] to assess the experimental results presented in table 5.2 and to select the best currently available values for 351 nm, 527 nm and 1053 nm. The optimized results for these three wavelengths were selected by a procedure that was somewhat arbitrary. Accordingly, the author determined the value of $n_2 = (2.74 \pm 0.17) \times 10^{-20}\ m^2/W$ at 1053 nm using an error-bar weighted averaging of selected experimental data at the infrared region (at 804 nm, 1053 nm, 1064 nm and 1550 nm), where the dispersion of n_2 is expected to be negligible. The coefficients for the other two wavelengths were estimated supposing a normal dispersion described by the PERT model (see section 1.5.4). The PERT curve was scaled in amplitude so that it passed through the selected infrared value and the resonance was adjusted in a way to find the best agreement with the selected UV experimental data (see Fig.5.1). The coefficients at $n_2 = (3.0 \pm 0.35) \times 10^{-20}\ m^2/W$ at 527 nm and $n_2 = (3.6 \pm 0.64) \times 10^{-20}\ m^2/W$ at 351 nm were read directly from the obtained theoretical curve shown in Fig.5.1.

$\mathbf{n_2}\,(10^{-20} \times m^2/W)$	**wavelength** (nm)	**Reference**
5.6 (±0.8)	248	[183]
3.4 (±1.6)	248	[183]
7.8 (±0.17)	266	[23]
3.0 (±0.22)	308	[184]
1.7 (±0.7)	351	[185]
2.5 (±1.2)	351	[186]
2.41 (±0.48)	355	[23]
2.62 (±0.6)	355	[187]
3.4	400	[188]
3.42 (±0.37)	402	[189]
3.0 (±0.45)	514	[190]
1.72 (±0.34)	532	[191]
2.24 (±0.46)	532	[23]
3.3 (±1.7)	694	[192]
3.2	800	[188]
2.48 (±0.23)	804	[189]
2.77 (±0.14)	1053	[181]
2.83 (±0.14)	1053	[181]
1.9 (±0.95)	1064	[193]
2.73 (±0.27)	1064	[194]
3.3 (±1.0)	1064	[195]
2.14 (±0.43)	1064	[23]
5.83	1064	[196]
3.75	1064	[197]
2.66 (±0.13)	1319	[198]
2.5	1500	[188]
2.79 (±0.14)	1550	[199]

Table 5.2: Some literature reported values of n_2 for fused silica. Part of the table adapted from Ref.[168].

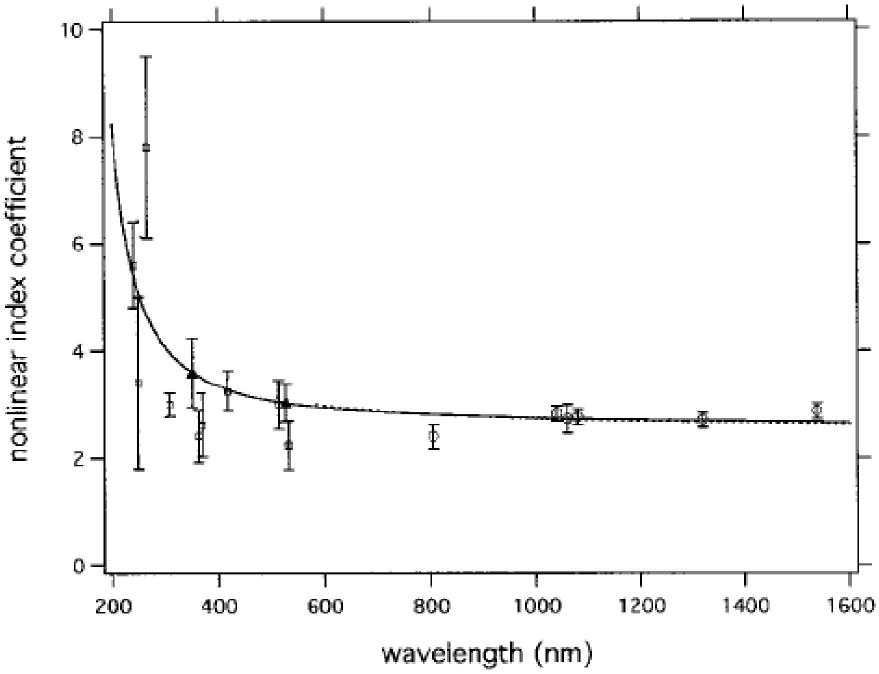

Figure 5.1: Some of experimental values of n_2 for fused silica selected from table 5.2. Coefficients are plotted in multiples of $\times 10^{-20}\ m^2/W$. The solid line is the PERT curve derived by D. Milam in [181]. The figure is adopted from Ref.[181].

5.2.3 Principle of the measurements

In our experiment the Z-scan method is combined with a $4f$ coherent imaging system shown in Fig.4.8 (in section 4.3.2). When the focal lengths of two converging lenses (L$_1$ and L$_2$) composing the system are the same , $f_1 = f_2$, then the image magnification is equal to one. It is important to note that in this configuration one can measure directly and precisely w_e, the beam waist of the Gaussian beam at the entry of the setup. This facilitates the determination of I_0, the central peak intensity in the focal plane of the focusing lens L$_1$. By considering a spatial and temporal Gaussian profiles of the pulse pump beam and after integration on these both coordinates (see Appendix C), we obtain:

$$I_0 = 4\sqrt{\pi \ln(2)} \left(\frac{w_e}{\lambda f_1}\right)^2 \frac{\varepsilon}{\tau}, \tag{5.1}$$

where τ is the pulse duration (full width at the half maximum, FWHM), f_1 is the focal length of lens L$_1$ and ε is the energy given by the joulemeter. It has been already checked [105] numerically and experimentally that the addition of lens L$_2$ (necessary to obtain the image of the Gaussian beam at the entry in the linear regime) does not affect the results of Z-scan. By applying this method, one can determine $\Delta\Phi_0$, the on-axis nonlinear phase shift in the focal plane from the measurement of ΔT_{pv}, the difference between the normalized peak and valley transmittance by using [63]:

$$\Delta T_{pv} = 0.406\,(1-S)^{0.25}\,|\Delta\Phi_0|\,, \tag{5.2}$$

where S is the linear transmittance of the aperture (numerical one in our case). In the case of negligible nonlinear absorption, this allows us to evaluate n_2 with the following relationship: $\Delta\Phi_0 = 2\pi L n_2 I_0/\lambda$ where L is the thickness of the material. It is clear that the measurement of $\Delta\Phi_0$ is quiet easy and direct to determine. But the problem in nonlinear measurements comes from the uncertainty that we have in measuring I_0. One can see from Eq.(5.1) that if ε is given by a calibrated joulemeter, a significant source of errors can originates from the measurement of w_e (especially for experiments using photodiodes) and τ (especially for the harmonics of the Nd:YAG laser). Thereby, we will focus our attention on how to evaluate these two parameters with more accuracy.

5.2.4 Z-scan experiments

The scheme of Z-scan setup is shown in Fig.4.8 in section 4.3.2. The excitation is provided by a Nd:YAG laser delivering linearly polarized pulse at 1064 nm and its harmonics (532 nm and 355 nm). The nominal pulse duration at 1064 nm is given to be $\tau = 17$ ps at FWHM. The image receiver is a 1000 × 1018 pixels (12×12 μm^2) cooled camera (-30 $°C$) with a fixed gain placed in the image plane of the $4f$ setup. Thermo-optical effects are negligible in the picosecond range and low repetition rate (10 Hz) [96]. A beam splitter (BS$_1$) at the entry of the setup allows to monitor fluctuations occurring in the incident laser beam. The focal lengths of lenses L$_1$ and L$_2$ are both equal to 20 cm. In Fig.5.2(a), we show the variation of the measured value of the beam-waist at the output of the experimental setup versus z, the sample position for a positive n_2 material without nonlinear absorption (CS$_2$).

This figure clearly shows the broadening and the narrowing of the output beam for prefocal and postfocal positions, respectively. In the linear regime, we obtain a more constant value and generally, we calculate the mean value by averaging the linear and the nonlinear regime acquisitions. It has to be added that the minimum in the variation of the beam-waist shown in Fig.5.2(a) corresponds to a maximum of the normalized transmittance shown in Fig.5.2(b). In the latter, we can see the Z-scan trace for 1 mm thick cell of CS_2 at 1064 nm and 17 ps pulse duration with 1% linear transmittance of the numerical aperture. Using Eq.(5.2), we evaluate the nonlinear dephasing, $\Delta\Phi_0 = 0.77\ rad$. The 23 GW/cm^2 of central peak incident intensity was obtained using Eq.(5.1) and taking into account the measured energy 6.5 μJ (with a PE10 pyroelectric head OPHIR joulemeter). The pulse duration is estimated using the Kerr shutter experiment that we will briefly describe hereafter.

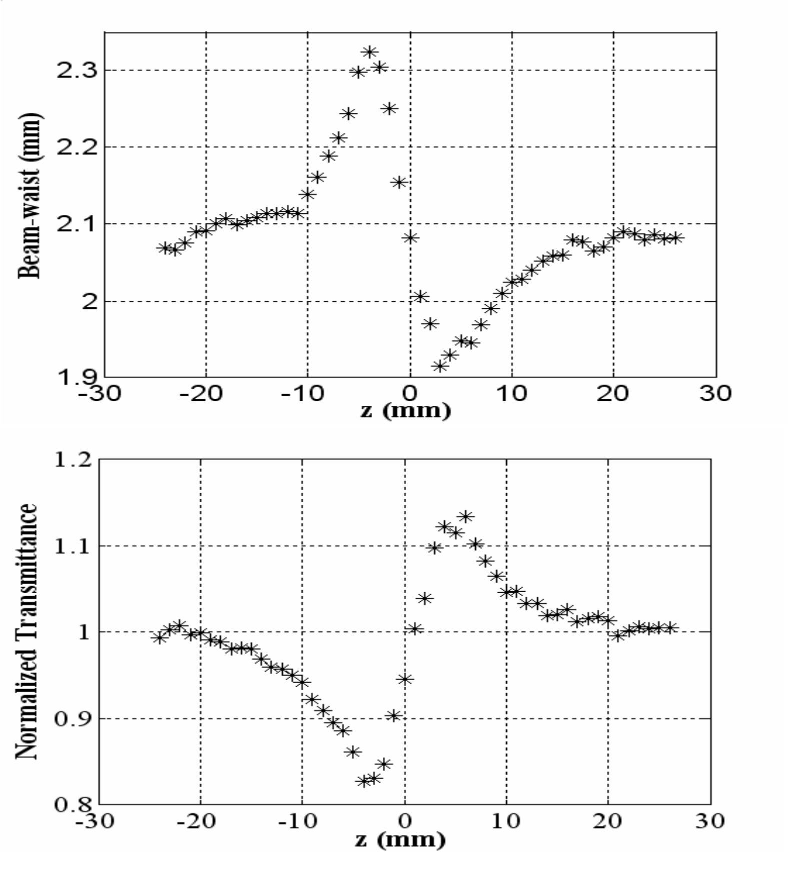

Figure 5.2: (a) Measurement of the beam-waist at the output of the experimental setup versus z, the sample position at 1064 nm in the nonlinear regime (b) Z-scan normalized transmittance for 1 mm thick cell of CS_2 at 1064 nm, 17 ps pulse-duration and 1% linear transmittance of the numerical aperture. The central peak incident intensity is 23 GW/cm^2.

5.2.5 Kerr shutter experiments

The ultrafast optical Kerr shutter setup shown on Fig.5.3 is a well-known experimental configuration for determining pulse-width in the picosecond time scale [40][42][163][170]. The beam splitter (BS) at the entry of the setup divides a linearly polarized beam into two parts: a high intensity pump beam and a low intensity probe beam. Both beams propagate in non-parallel directions and intersect each other inside the sample (NL) at a small angle (6°). This non-collinear configuration of the setup does not require using expensive polarizing elements and gives great flexibility to work with beams of the same polarization. The sample is inserted between two crossed polarizers (P_1 and P_2), thus, generally in absence of nonlinearity, the probe beam can not reach the detector (CCD).

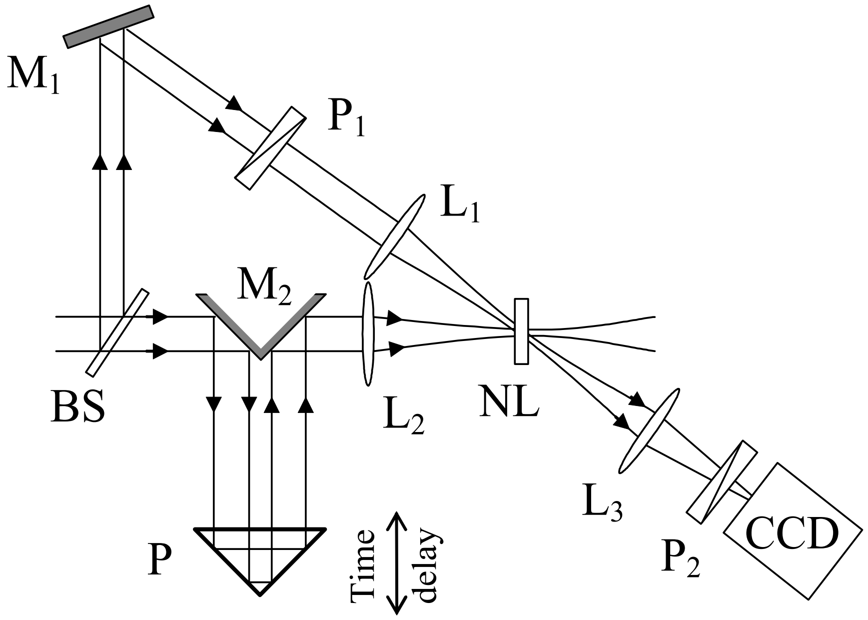

Figure 5.3: Kerr shutter experimental setup: M_i : mirrors, L_i : lenses, P_i : polarizers, BS : beam splitter, P: prism, NL : nonlinear material.

In order to improve the efficiency of the signal obtained by the optical shutter: **(i)** polarizers P_1 and P_2 have their axis at ±45° with respect to the polarization plane of the pump beam; **(ii)** we used lens L_3 to obtain a magnified image of the exit surface of the sample; **(iii)** the probe beam is slightly focused by lens L_1 into the impact region of the pump beam (being careful to have always an area at least 10 times greater than the focused pump beam area). Generally the sample is placed in the focal plane of lens L$_2$ where an intense pulse induces nonlinear change of the refractive index inside the material. During the presence of the pump beam, the induced birefringence (see chap.2 sec.2.2.2) causes the rotation of the probe beam polarization and consequently, a fraction of light can pass through the analyzer (P$_2$) and reaches the CCD . When the response time of the nonlinearity is very fast (much faster than the pulse duration) and in the regime of small nonlinearity the output intensity in the Kerr cell is proportional to $\sim I_p^2(t)\, I_{pr}(t)$ (see section 2.2.2) where I_p and I_{pr} are the pump and the probe beam intensities, respectively [163][200]. Therefore the spatial integration on the acquired images provides a temporally averaged signal which is considered as proportional to a third-order autocorrelation function :

$$G_3(t_d) = \int I_p^2(t)\, I_{pr}(t - t_d)\, dt, \tag{5.3}$$

where t_d is the delay time between incident pump and probe pulses. We have used two different nonlinear liquid materials: CS$_2$ in the infrared and the green (at 355 nm its transmittance is null) and chlorobenzene for all the considered wavelengths. The comparison of the measured values shows that the response time of the materials is smaller than the laser pulse duration. Fig.5.4 presents the autocorrelation functions fitted to the experimental data at 1064 nm (the stars) and 532 nm (the points). The data for 355 nm are not shown here for clarity. A deconvolution program was performed to obtain the assumed Gaussian temporal profile of the pump beam and its pulse-width. The measured pulse durations (FWHM)) are given to be 17 ps at 1064 nm, 7 ps at 532 nm and 12 ps at 355 nm. The value at 1064 nm validates our measurement procedure because our laser has been already tested using the second order autocorrelation technique and the result was in excellent agreement with the obtained value here. At 532 nm, the 7 ps pulse that we obtain is very far from the expected one which is 12 ps $(17/\sqrt{2})$. Therefore one should be very careful to evaluate the incident intensity at the second and third harmonics of the Nd:YAG laser even if the fundamental wavelength was measured by the second order autocorrelation technique. The scale rule for pulse duration for higher harmonics has to hold only if we work in the linear part of the energy conversion efficiency with respect to the incident intensity. But in order to increase the output energy, the laser manufacturers generally use the asymptotic values of this conversion. May be the beam is no more Gaussian as we can guess from the autocorrelation plots (in the green and UV) but it is more accurate to estimate the pulse width from experimental data by supposing so than to believe in theoretical prediction.

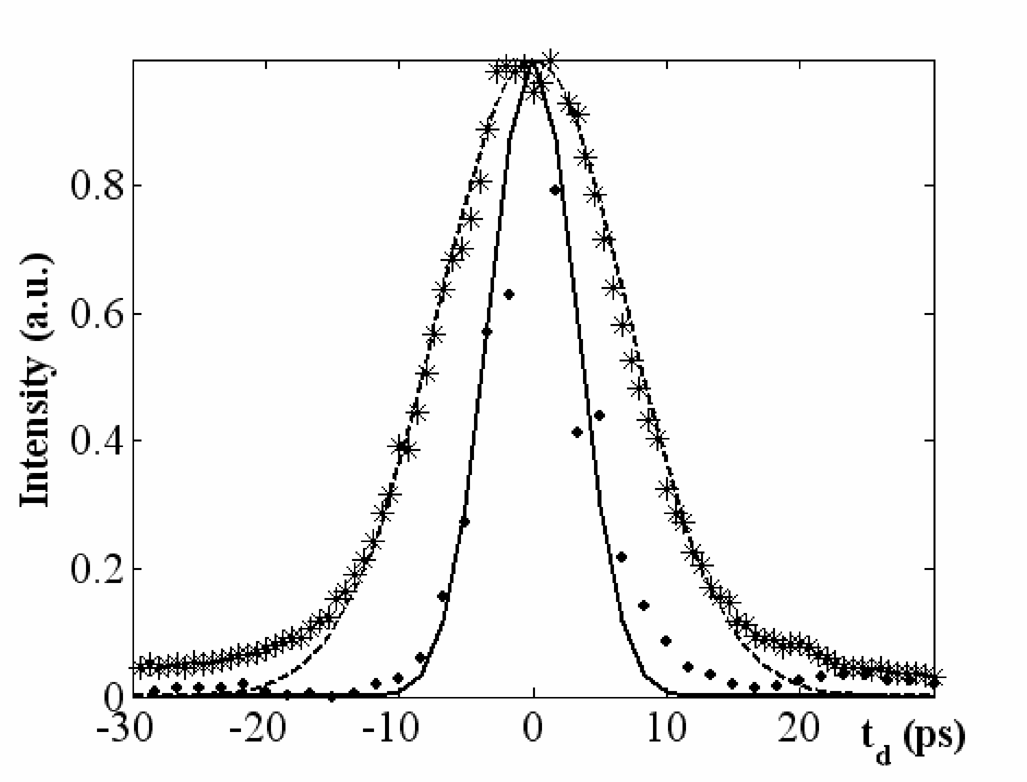

Figure 5.4: Third-order autocorrelation function of 17 *ps* pulses at 1064 *nm* (stars for experimental data and dashed line for numerical fitting) and 7 *ps* pulses at 532 *nm* (points for experimental data and solid line for numerical fitting).

5.2.6 Results and discussion

The measurements were performed more than 10 times with different samples in different experimental conditions to check the reproducibility of the measurements. The incident energy was controlled with two different joulemeter. The overall experimental uncertainty was approximately ±20% (mainly originating from energy calibration of the joulemeter) and depending on the variation of the incident laser energy during the scan. We can see in table 5.3 the absolute measurement of the nonlinear refractive indices for two of the most frequently used reference materials in nonlinear optical experiments. The beam waist at the entry of the setup (w_e) was taken in order to obtain a Rayleigh range larger than L, the thickness of the materials (shown in the third column). This is necessary because the sample should be regarded as thin when applying Eq.(5.2) to calculate $\Delta\Phi_0$, the nonlinear phase shift. We have been careful not to use too high intensities in order to stay within the validity of Eq.(5.2) ($|\Delta\Phi_0| < 1$) and not to destroy the specimen. We can notice the increasing of the measurement sensitivity of the system with the decreasing of the wavelength. Indeed, the required intensity (I_0 in column 6) in the UV is 6 times less than the one used in the infrared. In column 5 appears β, the two-photon absorption coefficient. It is clear that for both materials and for the considered wavelengths the nonlinear absorption is negligible at the corresponding intensities.

Material	$\lambda\,(nm)$	$L\,(mm)$	$n_2 \times 10^{-20}\ m^2/W$	$\beta \times 10^{-3}\ cm/GW$	$I_0\,(GW/cm^2)$
SiO_2	355	3.76	$\mathbf{2.0 \pm 0.4}$	< 2	37
SiO_2	532	3.76	$\mathbf{0.9 \pm 0.3}$	< 0.2	76
SiO_2	1064	3.76	$\mathbf{0.4 \pm 0.07}$	< 0.2	221
CS_2	532	1	$\mathbf{80 \pm 17}$	< 17	5.5
CS_2	1064	1	$\mathbf{40 \pm 6}$	< 7	23

Table 5.3: Values of the experimentally measured nonlinear coefficients corresponding to the studied reference materials at different wavelengths.

One of the main results of this paper is the obtained n_2 absolute values for CS_2 and SiO_2 in the infrared and in the picosecond regime. Our values are one order of magnitude less than those found in the literature (see table 5.1 and 5.2). We notice also a large dispersion of the results with respect to the wavelengths than the one considered up to now. For example, the n_2 value for CS_2 in the green is found to be two times larger than the one obtained in the infrared, while the previous reported results do not indicate any significant dispersion in this range of wavelengths. The similar comment is valid also for the fused silica. The already existing dispersion theories for transparent glasses as fused silica do not predict our experimental results. The first theory proposed by Boling–Glass–Owyoung (BGO, see section 1.5.2) was built on a simple model of harmonic oscillator providing the relation between linear and nonlinear refractive indices. The model is applicable to the low frequency nonlinearity and it predicts no differential dispersion between linear and nonlinear indices. Later, this theory was improved by two other models. The first one employs the Kramers–Kronig transformation of calculated two-photon absorption spectrum in the two-band configuration (see section 1.5.3) in order to determine n_2. This model provides better description of dispersion rather in semiconductors than in wide-band gap glasses as fused silica. The second one (PERT) is based on a fourth-order perturbation theory which assumes that the dispersion of n_2 in the visible and near IR can be attributed to a single resonance in the UV (see section 1.5.4). Both models indicate a normal dispersion, i.e. n_2 in UV is larger than n_2 in IR. In both cases the ratio between nonlinear indices obtained in 355 nm and 1064 nm is about $n_2\left(355\ nm\right)/n_2\left(1064\ nm\right) \approx 1.3$ [24][181][201] which is about 3 times less than the value found in this work ($n_2\left(355\ nm\right)/n_2\left(1064\ nm\right) \approx 4$). All these theoretical models generally depend on a constant that the authors "adapt" (to the material) in order to fit the experimental results or to translate the theoretical curve to match some "important data". In light of our results, we have to consider that the already existing theories should be improved. Note, that our n_2 value for silica in UV is in a good agreement with values obtained in Refs [23], [185], [186] and [187] (see table 5.2).

Moreover, our experimental results give a new look at the dependence of the nonlinear refraction on the pulse duration and its repetition rate. It is well known that only the instantaneous electronic processes and the molecular reorientation contribute to the nonlinear response under picosecond irradiation since the thermal effects are significantly slower processes [2][3]. Hence, the picoseconds range and low repetition rate (10 Hz) in our work exclude thermal component. On the one hand, considering fused silica one can neglect the molecular reorientation [202]. Therefore we can assume that the z-scan technique gives only the electronic part of the cubic susceptibility and n_2 of fused silica is weakly dependent on the pulse duration [182]. On the other hand, the picosecond rotation of molecules gives an important contribution to Kerr susceptibility in CS_2 [3][202] and its n_2 is dependent on pulse duration between pico- and femtosecond regimes as shown by table 5.1. The obtained value in femtosecond regime (due to the pure electronic response) is about $(2-3)\times 10^{-19}$ m^2/W in the infrared at 800 nm [95][96][173][174] (see table 5.1). Up to now we have been considering that the n_2 of CS_2 in the picosecond range should be one order of magnitude larger due to the molecular contribution. Taking into account the large dispersion obtained in our picosecond work, the n_2 value measured at 1064 nm is about two times larger but still in the same order of magnitude as the one obtained in the femtosecond regime.

We think that the beam-waist and the pulse-width precise measurements are very critical parameters in all n_2 measurement experimental procedure. This could explain the discrepancy of the absolute measurements obtained by different authors and worse with different experimental techniques. At the light of our results, more effort should be done in the measurement of the focal plane intensity of a lens which is a very critical parameter in absolute measurements.

5.3 Nonlinear characterization of glasses for optical switching applications

All-optical switching (AOS) is considered as one of the key technologies for high-speed optical communication networks [203]. Third-order nonlinear changes in refraction have been postulated in [204][205] as a potential mechanism for switching applications. Examples of optical switches (e.g., non-linear coupler, non-linear Fabry-Perot etalon) have been discussed in details in [205]. In general the nonlinear optical switching requires materials with fast nonlinear response ($\sim 10^{-15}\ s$), large nonlinear refraction and relatively low linear and nonlinear absorption. The latter can considerably limit the performance of switching devices by limiting the propagation depth inside the nonlinear medium. A convenient way to quantify the importance of the losses is by considering the appropriate figure of merit (FOM) defined below in Eq.(5.6). Conventional all-optical switching devices are based on generation of a light-induced phase shift of the order of $p\pi$, where $4 \geq p \geq 1$ for a range of devices [206]. For example, a nonlinear directional coupler requires $p = 4$ [206] while a Mach-Zehnder interferometer $p = 1$ [207]. Considering the most restrictive case of $p = 4$, the criterion for switching is given as [206]:

$$4\pi = \frac{2\pi I\left(0\right) n_2 L}{\lambda}, \tag{5.4}$$

where $I\left(0\right)$ is the light intensity at the entry of the material with thickness L. Most of the

AOS devices operate in the infrared region where linear absorption is generally negligible and only the two photon absorption (TPA) can cause losses. A general criterion to avoid large TPA is [206]:

$$\beta I\,(0)\,L < 1. \tag{5.5}$$

The combination of Eq.(5.4) and Eq.(5.5) provides a definition of FOM and the criterion for optical switching in presence of nonlinear absorption:

$$FOM = \frac{2\beta\lambda}{n_2} < 1. \tag{5.6}$$

This geometry-independent factor was widely adopted in the literature to classify different nonlinear materials for optical switching applications. Among many nonlinear materials different types of amorphous glasses are found to be promising media for the development of photonic devices. Particularly large family of chalcogenide glasses [127][208][209][210][211] as well as different kind of oxide glasses containing heavy metals (e.g. antimony [212][213] and tungsten [214][215]) were the subject of intense investigation due to the potentially low FOM. In this section we will report another contribution to the characterization of nonlinear materials for AOS applications. Namely we will present results of linear and nonlinear characterization of chalcogenide glasses GeS_2-Sb_2S_3-CsI and oxide glasses of $Pb(PO_3)_2$-WO_3. Moreover we will show that the simple BGO model can be a useful tool for theoretical prediction of n_2 values for these families of glasses even for materials having non negligible nonlinear absorption.

5.3.1 Experimental details

The measurements of n_2 and β for both families of glasses have been done at 1064 nm in the picosecond regime using Z-scan method inside a $4f$ imaging system (shown in Fig.4.8 in section 4.3.2). Other experimental parameters are similar to those depicted in section 5.2.4. To avoid the contribution of any permanent linear change of the refractive index attributed to photo-induced effects (PIE), a shutter is mounted at the input of the setup letting only one laser-shot-interaction with the material for each step of the Z-scan motor. The overall repetition rate is about 0.1 Hz to 0.2 Hz depending on the size of the acquired CCD images (to be stored to the hard disk). To check the absence of the permanent PIE, three sequential Z-scan acquisitions, in the linear, the nonlinear and again in the linear regime were carried out illuminating the sample on the same impact region. No photo-induced modifications were observed for investigated bulk materials. The calibration of the intensity in the focal plane (I_0) was done using CS_2 and considering $n_2 = 0.4 \times 10^{-18}\ m^2/W$ as obtained in our absolute measurements described in section 5.2. It should be added that for comparison purpose n_2 and β given here have to be multiplied by a factor 7.5 in order to obtain the equivalent of the nonlinear coefficients when the calibration is done taking into account the $n_2 \approx 3 \times 10^{-18}\ m^2/W$ of CS_2 found in [63].

5.3.2 Nonlinear characterization of glasses in GeS_2-Sb_2S_3-CsI system [216]

The samples were provided by the *Equipe Verres et Céramiques*, (UMR-CNRS 6226), from Université de Rennes I. The different compositions were prepared according to the method described in [217]. High purity materials (99.999% for Ge Sb, S and 99.99% for CsI) are used for the glass preparation in a silica tube under vacuum (10^{-5} $mbar$). The sealed silica tube is heated to 850°C in a rocking furnace and maintained 10 hours at this temperature to ensure a good reaction between the starting materials and a good homogenization of the melt. The glass is obtained by quenching the tube in water and by annealing the sample near its glass temperature, before cooling down to room temperature in order to release stresses induced by quenching. The glass is then cut into discs of about 1 mm thick, which are then polished to obtain 2 parallel faces.

The optical absorption measurements performed with a UV-visible-NIR spectrometer (CARY500) show negligible linear absorption in the infrared region for all the compositions and particularly at 1064 nm. The other linear optical coefficients along with the compositions of glasses are given in table 5.4. The energy band gap (ε_g) was determined from absorption spectra as the wavelength for which the linear absorption coefficient (α) is equal to 10 cm^{-1}. The linear refractive indices (n_0) were measured at two wavelengths, 1331 nm and 1551 nm, using a polarized laser with TE incidence in a Metricon prism coupler system.

	Percentage composition			**Linear optical properties**		
No	GeS_2	Sb_2S_3	CsI	$\hbar\omega/\varepsilon_g{}^{\dagger}$	$n_0{}^{\ddagger}$ $(1331nm)$	$n_0{}^{\ddagger}$ $(1551nm)$
A	90%	10%	0	0.470	2.146	2.140
B	75%	10%	15%	0.560	2.154	2.146
C	51.25%	26.25%	22.5%	0.571	2.274	2.265
D	66.25%	26.25%	7.5%	0.556	2.303	2.293
E	35%	35%	30%	0.584	2.309	2.299
F	42.5%	42.5%	15%	0.590	2.420	2.408
G	26.25%	51.25%	22.5%	0.622	2.457	2.444
H	10%	60%	30%	0.629	2.484	2.469
I	26.25%	66.25%	7.5%	0.660	2.619	2.602
J	10%	75%	15%	0.652	2.646	2.629

Table 5.4: Compositions of the investigated glasses (GeS_2+Sb_2S_3+CsI) and their linear optical coefficients: the normalized energy gap ($\hbar/\omega$) with the refractive indicies (n_0) at λ=1331 nm and 1551 nm.

The results of the Z-scan measurements of the investigated glasses are summarized in table 5.5. The n_2 values are given in column 2 (within the parenthesis is the ratio of n_2 to that of the fused silica $n_2 = 0.4 \times 10^{-20}\ m^2/W$ obtained in our absolute measurements). The nonlinearity of the investigated glasses is at least 50 times higher than that of the fused silica. Sample J exhibits the highest nonlinear refraction index. A careful revision of the experimental data shown in tables 5.4 and 5.5 could suggest that the optical properties of the investigated glasses depend strongly on the antimony (Sb) content. One can notice an improvement of n_2 (table 5.5), a red-shift of the optical gap ($\hbar\omega/\varepsilon_g$ in table 5.4) and an increase of the linear refractive index (n_0 in table 5.4) with the amount of Sb_2S_3 (table 5.4). A similar behaviour has been already observed in [218] and [219] dealing with linear and nonlinear optical properties of glass-host system xGeS$_2$–$(1-x)$Sb$_2$S$_3$, respectively. Changes in n_2 by $\approx$ 400% were observed when varying x from 10 to 40%. It was shown in [211] that in

---

[†] ε_g is defined as the energy for which the linear absorption coefficient is 10 cm^{-1}

[‡] The measurements done by the Equipe Verres et Céramiques, (UMR-CNRS 6226), from Université de Rennes I

Ge-Sb-S systems, the nonlinear refractive index is correlated to a number of heteropolar Sb-S and Ge-S bonds and n_2 is enhanced with decreasing Ge/Sb ratio. A careful analysis show that n_2 decreases with increasing Ge/Sb ratio for the glasses investigated here. The deviation from this tendency can be attributed to CsI component. Generally, the introduction of halide component reduces the linear refraction and moves the energy gap towards the blue region of the visible spectrum [220]. Therefore higher amounts of CsI elements should decrease the nonlinear refractive index.

	Nonlinear coefficients		
No	$n_2 \times 10^{-19}$ (m^2/W)	$\beta \times 10^{-2}$ (cm/GW)	$FOM = 2\beta\lambda/n_2$
A	2.0 ± 0.4 (50)	< 0.2	< 0.22
B	3.6 ± 0.9 (90)	1.0 ± 0.4	0.6
C	3.9 ± 0.6 (97.5)	2.0 ± 0.4	1.08
D	3.9 ± 0.6 (97.5)	1.0 ± 0.3	0.54
E	4.7 ± 0.7 (117.5)	3.0 ± 0.7	1.36
F	5.6 ± 1.8 (140)	3.0 ± 1.0	1.14
G	7.5 ± 2.2 (187.5)	10 ± 1	2.84
H	9.0 ± 2.0 (225)	19 ± 2	4.50
I	9.7 ± 1.9 (242.5)	20 ± 2	4.38
J	10.3 ± 3.0 (270)	16 ± 5	3.16

Table 5.5: Nonlinear optical coefficients of (GeS_2+Sb_2S_3+CsI) chalcogenide glasses. Column 2 presents n_2 values where within the parenthesis the ratio of n_2 to that of the fused silica is given.

In the column 4 of table 5.5, we give the figure of merit (FOM) defined as in Eq.(5.6). It can be seen that only samples A, B and D fulfil the criterion provided by this equation ($FOM < 1$) and they could potentially be useful for optical switching applications. However, the expected decrease of β at the telecommunication wavelength (1550 nm), where most of the opto-electronic devices operate, could give lower values of FOM [221] for other compositions. In Fig.5.5 we show the FOM versus the normalized photon energy. As it is pointed out in [222][223], the FOM in chalcogenides depends on the proximity of the light frequency to two-photon absorption edge and it reaches a minimum for $\hbar\omega$ just below 0.5. Our experimental results agree with this observation.

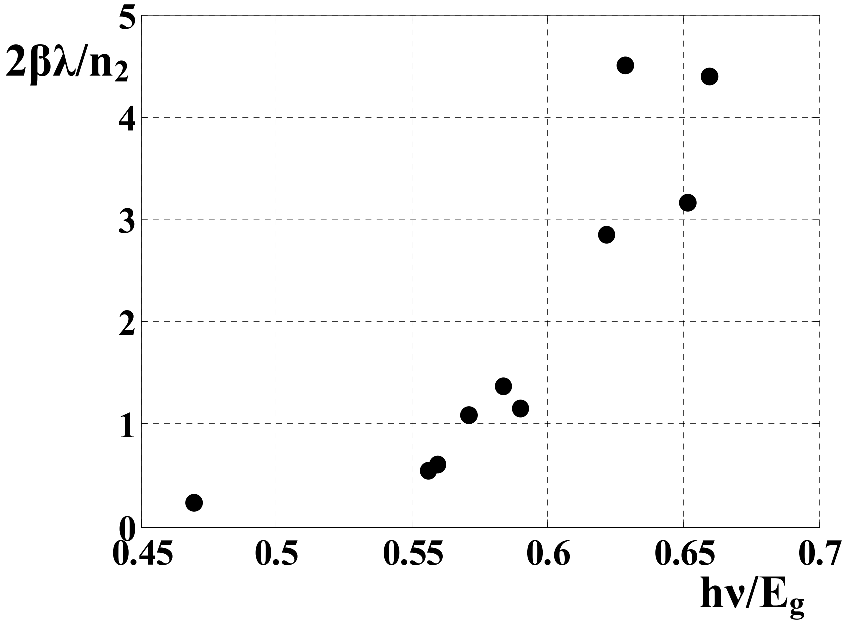

Figure 5.5: Figure of merit (FOM) defined as $2\beta\lambda/n_2$ versus normalized photon energy ($\hbar\omega/\varepsilon_g$)

From the optical point of view the nonlinearities in chalcogenides are correlated to the optical gap and the linear refraction. On the one hand, high third order susceptibility in chalcogenide glasses is attributed to their high n_0 accordingly to the Miller's generalized rule [128] (see section 1.5.1). However there are many experimental results revealing an increase of nonlinearities with $\hbar\omega$ for different families of chalcogenide glasses (see for example [30][222][223]). Figs.5.6(a) and 5.6(b) show n_2 and β as a function of the normalized photon energy for our specimens. The observed variations confirm the strong dependence on absorption gap for a fixed excitation wavelength.

The interdependence of nonlinearities on n_0 and ε_g comes from the fact that the linear refractive index and energy gap are generally related. In crystals the correlation between n_0 and ε_g is usually expressed by the Moss rule [224] stating that $n_0 = \gamma/\varepsilon_g^x$, where $x = 0.25$ and γ is a material dependent constant. In amorphous materials as chalcogenide glasses a similar behaviour between n_0 and ε_g also seems to be valid. In Fig.5.7 we can see the

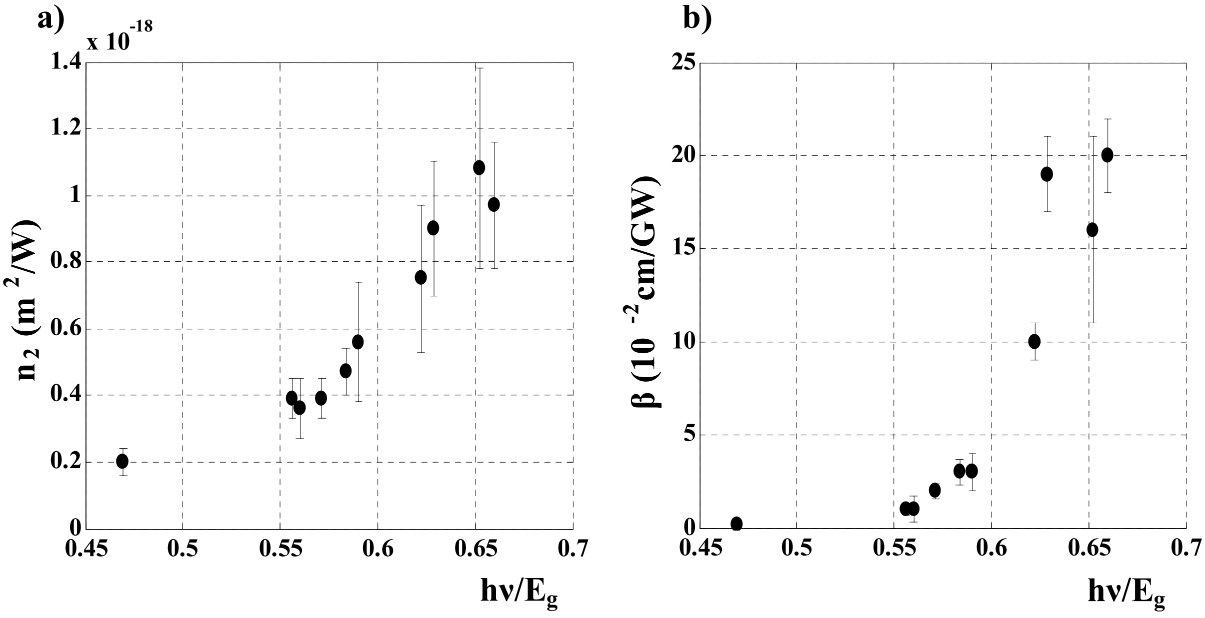

Figure 5.6: Variations of (a) n_2 and (b) β as a function of the normalized photon energy ($\hbar\omega/\varepsilon_g$)

refractive index at 1064 nm versus the energy gap for our specimens (filled circle) as well as for another two families of chalcogenides, namely tellurium (empty circles) (from [210]) and germanium (stars) (from [211]) based glasses. In all cases the energy band gap is defined as the wavelength for which the linear absorption coefficient $\alpha = 10\ cm^{-1}$. The values of n_0 at 1064 nm in the glasses investigated here were obtained from the experimental data at 1331 nm and 1551 nm using the dispersion model described in Eq.(5.8) (given below). The dashed line in Fig.5.7 is the best fit to the experimental data of $n_0 = \gamma/\varepsilon_g^x$ (obtaining $x = 0.37$ and $\gamma = 3.1$ when ε_g is expressed in eV). The absolute values of x and γ are not important because these coefficients are dependent on the energy gap definition which is ambiguous in amorphous materials [225][226]. It is well-known that optical absorption edge in amorphous glasses is not sharp as in crystals. In fact it is generally divided by three spectral regions from high to low absorption: Tauc region ($\alpha \geq 10^4\ cm^{-1}$), Urbach tail ($\alpha \sim 10^2\ cm^{-1}$) and weak absorption tail ($\alpha \sim 10^0\ cm^{-1}$) [227][228]. The interpretation of these three spectral regions still remains ambiguous. Therefore the modified Moss relation should be considered here as a rough approximation in order to show a general tendency in the relationship between ε_g and n_0. This dependency allows us **(i)** to use indifferently one of these parameters to predict the nonlinearities and **(ii)** to explain qualitatively why a model (as the one to come hereafter) using only one of these parameters can be considered valid from the physical point of view.

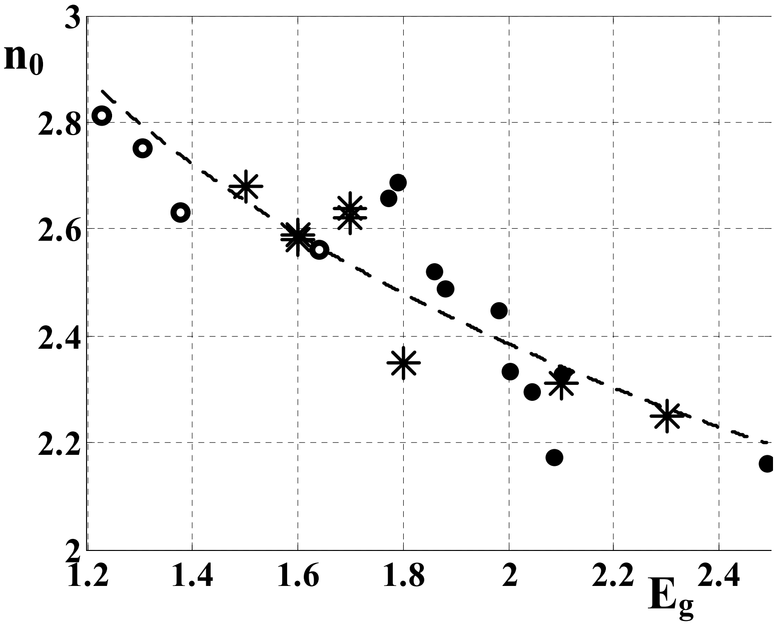

Figure 5.7: Linear refractive index (n_0) at 1064 *nm* versus the energy gap (ε_g) for GeS_2+Sb_2S_3+CsI glass system (filled circle) as well as for tellurium (empty circles) [from [210]] and germanium [from [211]] (stars) based chalcogenide glasses. The solid line is a modified Moss curve.

One of the important tasks is to have simple theoretical expressions allowing to predict the magnitude of nonlinearities and hence, facilitating the choice of glass compositions with the desired optical properties. The estimation of n_2 rather on the basis of the linear refraction index than normalized energy gap would be preferable in amorphous materials because no ambiguity in the measurements of n_0 can appear especially in the transparency region. The BGO model (see section 1.5.2) offers such an advantage. This model assumes that the third-order hyperpolarizability is proportional to the square of the linear polarizability. It supposes also that the linear optical dispersion of the medium is determined by only one resonance frequency ω_0 and the frequency of the light is far away from the resonance ($\omega \ll \omega_0$). Moreover the dielectric response should have a pure electronic nature. The BGO model is expressed by Eq.(1.45) which is rewritten here for self-consistency

$$n_2\left(m^2/W\right) = \frac{gs\left(n_0^2+2\right)^2\left(n_0^2-1\right)^2}{12n_0^2c\hbar\omega_0\left(Ns\right)}, \tag{5.7}$$

where g is a dimensionless anharmocity parameter, s is the effective oscillator strength, N is the ion density depending on the composition and c is the speed of light. The linear refractive index for a wavelength λ fulfils the following expression (see also Eq.(1.46)):

$$\frac{1}{3}\frac{\left(n_0^2+2\right)}{\left(n_0^2-1\right)} = \frac{\omega_0^2-\omega^2}{\left(e_c^2/m_e\epsilon_0\right)\left(Ns\right)}, \tag{5.8}$$

where ϵ_0 is the vacuum permittivity, e_c and m_e are the charge and the mass of the electron respectively. The parameters Ns and ω_0 are obtained from the values of $n_0\left(\lambda = 1331\ nm\right)$ and $n_0\left(\lambda = 1551\ nm\right)$ measured for each sample. Then, the values of Ns and ω_0 are introduced into Eq.(5.7) to determine n_2. The best agreement with experimental data was obtained for a scaling factor $gs = 0.59$. The comparisons of the experimental and the theoretical values are shown in Fig.5.8 as a function of the linear refractive index at 1064 nm.

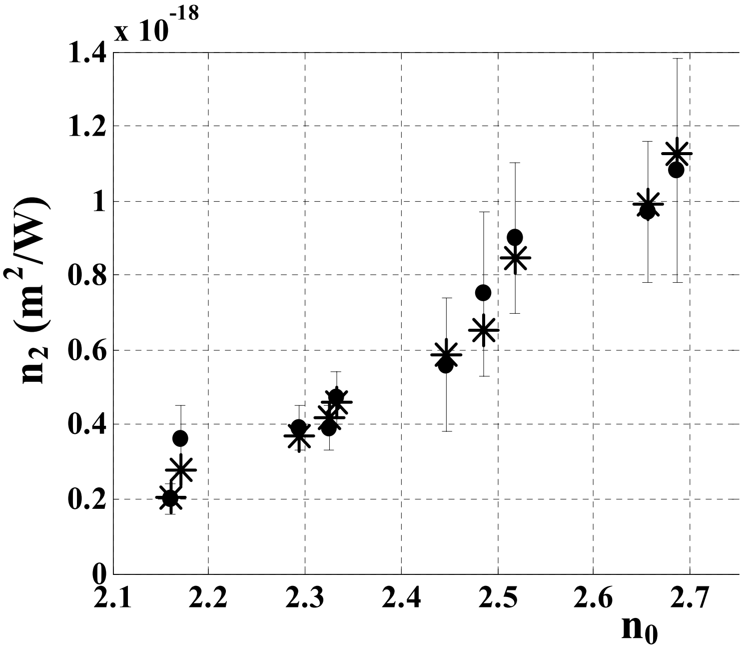

Figure 5.8: Comparison between experimental n_2 data (filled dots) and values calculated from the BGO formula (Eq. (5.7)) (stars)

The values of $n_0\,(\lambda = 1064\ nm)$ were determined using Eq.(5.8) with the values of Ns and ω_0 obtained for each sample. A very good agreement is found between the experimental and theoretical values. Note that due to the new calibration the obtained value of gs is approximately 7.5 less than the ones adopted up to now. The latter values (between 3 and 4.5) [18] have been always chosen empirically in order to fit the experimental results. Anyway the effect of the calibration produces only a vertical shift into the predicted n_2 values but does not change the variation inside Fig.5.8. Moreover, note that the presence of the nonlinear absorption does not affect the predictions of the BGO model. The FOM factor defined in Eq.(5.6) can be related to coefficient $\gamma = \beta/2kn_2$ (defined in Eq.(2.27) in the chapter 2) as: $FOM = 8\pi\gamma$. As mentioned in the chapter 2 the coefficient γ expreses the ratio between imaginary ($\chi_I^{(3)}$) and real ($\chi_R^{(3)}$) part of the third order susceptibility [63]. It easy to calculate that $\gamma \ll 1$ for all the investiagted compositions (for the most absorbing sample $\gamma \approx 0.18$) and thus the nonlinear refractive effects are predominant over the nonlinear absorptive ones ($\chi_R^{(3)} \gg \chi_I^{(3)}$). Consequently the predictions of BGO model are not disturbed in the region of the two-photon absorption resonance even if this effect is not included in the theory derivied by Boling at al.[18].

5.3.3 Nonlinear characterization of $Pb(PO_3)_2$-WO_3 oxide glasses

We obtained the samples from prof. C. B. de Araújo from *Departamento de Física, Universidade Federal de Pernambuco*, (50670-901 Recife, PE, Brazil). The samples were prepared at the Chemistry Institute of UNESP-Araraguara in Brazil. The preparation procedure is given in brief below. The glass samples were synthesized by a melting – quenching method. The starting powdered materials were tungsten oxide, WO_3, and lead orthophosphate, ($PbHPO_4$). In the first step, the powders were mixed and heated at 250^oC for $3h$ to remove water and adsorbed gases. Then, the batch was melted at a temperature ranging from 900^oC to 1050^oC, depending on the WO_3 content. The obtained liquid was kept at this temperature for 40 min to ensure homogenization and fining. Finally, the melt was cooled in a metal mold preheated at 20^oC below the glass transition temperature, T_g. Annealing was implemented at this temperature for $2h$ in order to minimize mechanical stress resulting from thermal gradients upon cooling. Four bulk samples were prepared according to the compositional rule (in *mol* %): $(100-x)\mathrm{Pb(PO_3)_2}$–$x\mathrm{WO_3}$, with $x = 30$, 40, 50, and 60. The bulk samples were cut and polished before performing optical measurements. All samples yielded from pale yellow to green homogeneous transparent glasses free of strains.

The linear and nonlinear characterization of considered glasses were performed in collaboration with group of prof. C. B. de Araújo from *Universidade Federal de Pernambuco* in Recife, Brazil. The dispersion of the linear refractive index was measured for each sample using Horiba Jobin Yvon ellipsometer. The measurements were done for a spectrum range between 320 nm to 500 nm with a step of 30 *nm*. The results are shown in Fig.5.9.

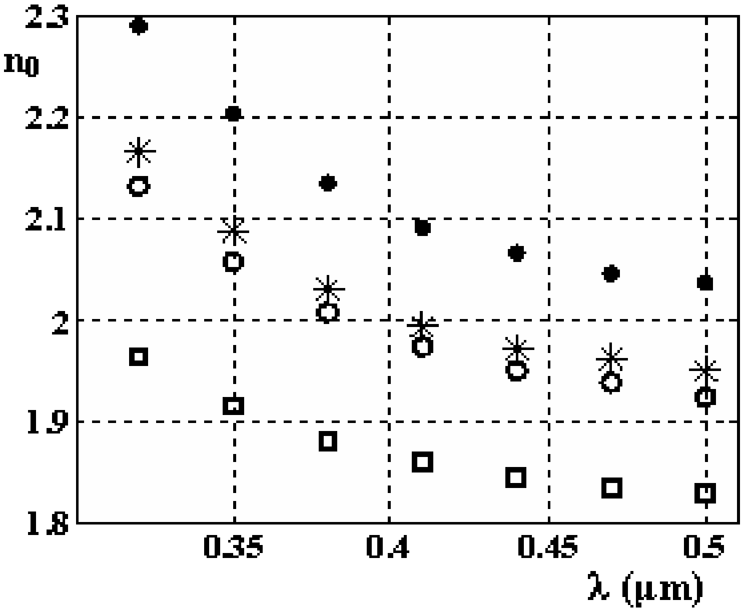

Figure 5.9: Linear refractive index (n_0) versus wavelength (λ) for $40\mathrm{Pb(PO_3)_2}$-$60\mathrm{WO_3}$ (filled dots), $50\mathrm{Pb(PO_3)_2}$-$50\mathrm{WO_3}$ (stars), $60\mathrm{Pb(PO_3)_2}$-$40\mathrm{WO_3}$ (empty circles) and $70\mathrm{Pb(PO_3)_2}$-$30\mathrm{WO_3}$ (squares)

The absorption coefficients (α) were determined using a spectrophotometer[†]. The linear optical parameters for the investigated glasses are summarized in table 5.6. The refractive indices (n_0) in 800 *nm* and 1064 *nm* (column 3 and 5) were determined by fitting the dispersion model given in Eq.(5.8) to experimental data ($n_0(\lambda)$) shown in Fig.5.9.

[†] The measurements done by group of prof. C. B. de Araújo at Departamento de Física, Universidade Federal de Pernambuco, (50670-901 Recife, PE, Brazil)

Sample	Composition	$n_0\,(800\ nm)$	$\alpha\,(cm^{-1})$ $(800\ nm)^{\dagger}$	$n_0\,(1064\ nm)$	$\alpha\,(cm^{-1})$ $(1064\ nm)^{\dagger}$
A	$70Pb(PO_3)_2$-$30WO_3$	1.78	0.13	1.77	0.005
B	$60Pb(PO_3)_2$-$40WO_3$	1.85	0.48	1.84	0.29
C	$50Pb(PO_3)_2$-$50WO_3$	1.87	1.45	1.86	1.18
D	$40Pb(PO_3)_2$-$60WO_3$	1.95	2.94	1.93	1.16

Table 5.6: Linear optical coefficients of $Pb(PO_3)_2$-WO_3 glasses.

The nonlinear characterization was done by performing our Z-scan measurements in 1064 nm in the picosecond regime (17 ps) as well as by doing Kerr shutter[†] experiment in 800 nm in the femtosecond regime (100 fs). The latter was calibrated by CS_2 considering the value of $n_2 = 3 \times 10^{-19}\ m^2/W$. This value was measured in the femtosecond regime by various groups (see table 5.1). More details about Kerr gate experiment can be found in [200]. The Kerr shutter and Z-scan results were compared with predictions of the BGO model. The best agreement with the experimental data was obtained for a scaling factor $gs = 0.37$ (see Eq. (5.7)). The experimental and theoretical data are summarized in table 5.7.

Sample	n_2^{EXP} $(800\ nm)^{\dagger}$	n_2^{BGO} $(800\ nm)$	n_2^{EXP} $(1064\ nm)$	n_2^{BGO} $(1064\ nm)$	$\beta\times10^{-3}$ (cm/GW)	$2\beta\lambda/n_2$
A	(4.2 ± 0.4)	3.2	(4.0 ± 0.6)	3.0	< 0.7	< 0.37
B	(5.1 ± 0.5)	5.2	(4.7 ± 1.0)	4.9	< 1.5	< 0.68
C	(5.6 ± 0.6)	5.5	(4.7 ± 0.8)	5.2	< 3.0	< 1.68
D	(6.2 ± 0.6)	6.8	(6.0 ± 1.1)	6.4	(3.0 ± 0.7)	1.1

Table 5.7: Nonlinear optical coefficients of $Pb(PO_3)_2$-WO_3 and theoretical predictions with basis on the BGO model. Coefficients n_2 are given in multiples of $10^{-20}\ m^2/W$.

It is easy to notice that the nonlinear refractive index is slightly increasing with an amount of tungsten component (WO_3). However this improvement is accompanied by an increase in

---

[†] The measurements done by group of prof. C. B. de Araújo at Departamento de Física, Universidade Federal de Pernambuco, (50670-901 Recife, PE, Brazil)

linear and nonlinear absorption. All values of n_2 are one order of magnitude higher than that of fused silica ($n_2 = 4 \times 10^{-21}\ m^2/W$). The two-photon absorption (TPA) coefficients (β) in 1064 nm are given in column 6 of table 5.7. The obtained results indicate negligible (below the resolution of the experimental setup) TPA for samples A, B and C. The presented values of β for these specimens can be related to the scattering from the samples surface. In the last column of table 5.7 we present the FOM coefficients in 1064 nm. It is clearly seen that these factors are relatively low (around unity or less) and hence all the investigated compositions are quite promising materials for AOS applications.

The presented results of n_2 are also important in the light of our absolute measurements for references materials described in section 5.2. The optical response of transparent glasses in the picosecond and in the femtosecond regime is expected to be approximately equal in infrared region (800 nm and 1064 nm) since only the electronic nonlinearity is being probed. The calibration of Z-scan setup based on our results (i.e. $n_2 = 4 \times 10^{-19}\ m^2/W$ for CS_2) is in agreement with the above statements while the calibration considering the "old" reference value (i.e. $n_2 = 30 \times 10^{-19}\ m^2/W$ for CS_2) will give results approximately one order of magnitude higher in the picosecond regime for the same glasses. No physical explanation could justify such large discrepancy in n_2 values between picosecond and femtosecond regimes in these solid materials. If one considers our absolute values at 1064 nm the results become coherent between two different operators, two different wavelengths, two different pulsewidth regimes and two different laboratories.

5.4 Conclusions

In this chapter we reported on absolute measurements of the nonlinear refractive index for two standard reference materials (CS_2 and SiO_2). Inside a $4f$ Z-scan imaging system we have analyzed the spatial distortion of the diffracted pump beam to measure precisely its beam waist at the entry of the setup. The Kerr Shutter technique was applied to evaluate the temporal pulse-width for three harmonics delivered by a pulsed Nd:YAG laser (1064 nm, 532 nm and 355 nm) in the picosecond regime. In the infrared and the green wavelengths we obtained n_2 values one order of magnitude less than the one usually taken into account. Another important result comes from the more significant dispersion of the nonlinear refraction index for both materials. Only in UV the n_2 value of fused silica is in good agreement with some values found in the literature.

In the second part of the chapter we have characterized the nonlinear refractive indices (n_2) and the nonlinear absorption coefficients (β) for GeS_2-Sb_2S_3-CsI chalcogenide glasses and $Pb(PO_3)_2$–WO_3 oxide glasses in the context of their suitability for all-optical switching (AOS) applications. Chalcogenide glasses were found to have n_2 values approximately one order of magnitude higher than the investigated oxide glasses and two orders higher then that in fused silica. However only three compositions of GeS_2-Sb_2S_3-CsI glasses among ten have a figure of merit (FOM) $2\beta\lambda/n_2 < 1$, making them suitable candidates for optical switching applications. On the other hand all four examined oxide glasses have FOM sufficiently small to use them as materials for AOS. Furthermore we have confirmed that the nonlinear refractive index behaviour is closely related to the linear one in both families of glasses. Following this property we have shown that the BGO model could be a useful tool to estimate n_2 values in both groups of materials. Moreover we have shown that the criterion used to derive this model, namely that the frequency of the light must be far away from the resonance ($\omega \ll \omega_0$), is more restricted than it need to be. The predictions of the BGO fomula are quite accurate in the low excitation regime even if we are in the two-photon absorption resonance region which is not taken into account in the model.

GENERAL CONCLUSIONS

This study deals with the third-order nonlinear optical characterization of thin films and bulk materials. We have combined different well-known characterization techniques inside the $4f$ coherent imaging system in order to optimize the sensitivity with the highest optical signal to noise ratio (S/N) for measurements of the nonlinear refractive indices (n_2) and the nonlinear absorption coefficients (β). We have shown that by using various objects at the entry and different field-stops at the output of the imaging system it is possible to perform various experiments such as degenerate four wave mixing (DFWM), I-scan, Z-scan, eclipsing Z-scan (EZ-scan) and the nonlinear imaging technique with phase object (NIT-PO). All these techniques can be considered as particular cases of the same imaging process where the alteration of the intensity distribution in the image plane, after nonlinear filtering through the tested material placed in proximity of the Fourier plane, leads to the information about the nonlinear coefficients. Moreover we have unified theoretical description of all these seemingly different experimental methods using a simple model based on Fourier optics. To analyze quantitatively nonlinear distortions of images acquired by a CCD camera we have defined the diffraction efficiency as a signal to be measured. We have derived relations between this quantity and the nonlinear refractive phase shift for each technique to characterize materials in the low excitation regime. The influence of the nonlinear absorption was discussed as well. We have found that the Z-scan/EZ-scan and the NIT-PO techniques reveal the highest sensitivity and the best signal to noise ratio among all the considered experimental methods allowing to measure signals corresponding to at least $\sim \lambda/500$ of the nonlinear phase front distortion.

Under these conclusions we have shown that the high optical sensitivity of the Z-scan and the NIT-PO does not ensure the accurate characterization of thin films. We have shown that even in the optimized conditions it is impossible to induce measurable nonlinear signal if the optical interaction length is too low. The enhancement of the nonlinear response of thin samples by increasing the incident intensity was ultimately limited by the damage intensity threshold. Thanks to a CCD camera we were able to see the changes in the diffracted beam due to the photo-induced effects (PIE). This can not be done when one uses spatially integrated detectors as photodiodes or photomultipliers. Exploiting the facility provided by the two-dimensional detection we employed NIT-PO technique to investigate PIE. We have shown that by analyzing the phase contrast as a function of the input intensity and the time it is possible to estimate the damage intensity threshold as well as to study kinetics of PIE. Particularly, we have investigated the photo-sensitivity of thin films of amorphous chalcogenide glasses $\mathrm{Ge}_x\mathrm{As}_y\mathrm{Se}_{100-x-y}$ and $\mathrm{Te}_{20}\mathrm{As}_{30}\mathrm{Se}_{50}$. Furthermore we have shown that the permanent modifications in refraction and absorption induced by PIE can contribute to the nonlinear response in Z-scan measurements. To verify the presence of PIE during Z-scan experiment it is necessary to perform three scans: in low, high and once again in low intensity regime, respectively. The comparison of the low intensity scans reveals permanent changes in refraction and absorption written inside the sample in the nonlinear regime. It was shown that the photo-induced changes in linear optical parameters as ablation depth of few nanometers can be sensed by Z-scan and so leading to erroneous results in n_2 and β values.

Moreover we have demonstrated experimentally that the Z-scan technique can be a useful tool to investigate Gaussian profile photo-induced permanent modifications of optical coefficients inside photosensitive materials. A semi-analytical theory for Z-scan measurements in linear regime was developed. It was shown that the magnitude and the sign of linear alterations in refraction and absorption can be separately determined. Particularly we have studied the photo-induced changes in the linear optical parameters in bulk slab of $\mathrm{As}_2\mathrm{S}_3$ caused by sub-band gap irradiation. Another application was found to study linear optical properties of thin films. It was demonstrated that the closed aperture Z-scan profiles with a peak-valley configuration can be obtained when Z-scanning rectangular phase object (rectangular groove or scratch inside the film). The difference between the peak and the valley of the normalized transmittance was related linearly to the permanent refractive phase shift.

We have also reported on absolute measurements of n_2 in carbon disulfide (CS_2) and fused silica (SiO_2), two standard references materials used in nonlinear optical experiments. The Z-scan method inside the $4f$ imaging system was combined with the Kerr shutter experiment in order to analyze precisely the spatio-temporal profiles of the pump beams at 355 nm, 532 nm and 1064 nm in the picoseconds regime. The obtained absolute values of n_2 were found to be 7.5 times smaller than those commonly used up to now and measured few decades ago. Moreover more significant dispersion of the n_2 value as a function of the wavelength was found.

We have also characterized the nonlinear refractive indices (n_2) and the nonlinear absorption coefficients (β) for different compositions of bulk GeS_2-Sb_2S_3-CsI chalcogenide glasses and $Pb(PO_2)_3$-WO_3 oxide glasses in the context of their suitability for all-optical switching (AOS) applications. We have found that only three compositions among ten investigated chalcogenides glasses have a figure of merit (FOM) $2\beta\lambda/n_2 < 1$, making them suitable for AOS. On the other hand, all studied oxide glasses fulfils the chosen criterion for AOS. Furthermore we have confirmed that the nonlinear refractive index behavior is closely related to the linear one in both families of glasses. Following this property we have shown that the BGO model could be a useful tool to estimate n_2 values in both groups of materials taking into account our absolute measurements. Moreover the predictions of the model are not influenced by the presence of low nonlinear absorption.

In summary, our study deals with the broad range of the issues concerning the third-order nonlinear optical characterization. Beginning from the optimization of sensitivity and the signal to noise ratio in nonlinear measurements, through the problem of the photo-sensitivity of thin films and ending on the nonlinear characterization of different bulk materials. There are few points which are worth to consider for future perspectives. Lower energy fluctuations at the laser output combined with a lower noise threshold are indispensable in order to achieve measurements of nonlinear coefficients in good conditions. Ultimately, effort of experimenters should be done in the measurement of the focal plane intensity of a lens. We are convinced that this is the key to obtain reproducible, coherent and more accurate results in third order optical coefficient measurements and further in the field of nonlinear optics.

CONCLUSIONS GÉNÉRALES

Cette étude traite des caractérisations optiques non-linéaires du troisième ordre des couches minces et des matériaux massifs. Nous avons combiné différentes techniques de caractérisation bien connues à l'intérieur du système d'imagerie $4f$ afin d'optimiser la sensibilité avec un rapport signal sur bruit maximum pour les mesures des indices de réfraction non linéaire (n_2) et les coefficients d'absorption non linéaire (β). Nous avons montré que, dans le régime de faible excitation non linéaire, à l'aide de divers objets à l'entrée et des filtres spatiaux adaptés en sortie du système imageur, il est possible de réaliser diverses expériences telles que le mélange à quatre ondes dégénérées (DFWM), I-scan , Z-scan, Z-scan éclipsant (EZ-scan) et la technique d'imagerie non linéaire avec l'objet de phase (NIT-PO). Nous avons montré que toutes ces techniques peuvent être considérées comme des cas particuliers du même processus d'imagerie où la modification de la répartition de l'intensité dans le plan de l'image, après filtrage non linéaire à travers le matériau testé, placé à proximité du plan de Fourier, conduit à une information sur les coefficients non linéaires. En outre, nous avons unifié leur description théorique en utilisant un modèle simple basé sur l'optique de Fourier. Pour analyser quantitativement les distorsions non linéaires des images acquises par la caméra CCD, nous avons défini le rendement de diffraction comme le signal à mesurer. Nous en avons tiré des relations entre cette quantité et le déphasage non linéaire pour chacune des techniques de caractérisations considérées. L'influence de l'absorption non linéaire a été également traitée. Nous avons établi que Z-scan/EZ-scan ainsi que la technique NIT-PO possèdent les sensibilités les plus élevées tout en gardant les meilleurs rapports signal/bruit. Ces techniques permettent de mesurer des signaux correspondant à $\sim \lambda/500$ au niveau de la distorsion du front de phase.

Suivant ces conclusions, nous avons montré que la sensibilité optique de Z-scan et NIT-PO ne garantissent pas la caractérisation précise des couches minces en optique non linéaire. Nous avons montré que, même dans les conditions optimisées, il est impossible d'induire un signal non linéaire si la longueur d'interaction optique est trop faible. L'amélioration de la réponse non linéaire des échantillons minces en augmentant l'intensité incidente est finalement limitée par le seuil des dommages. Grace à une caméra CCD, nous avons pu voir les changements dans le faisceau diffracté à l'infini à cause des effets photo-induits (PIE). Ce qui ne peut être fait lorsque l'on utilise des photodiodes ou des photomultiplicateurs. Par ailleurs, nous avons utilisé la technique NIT-PO pour caractériser les PIE. Nous avons montré que l'analyse par le contraste de phase en fonction du temps et de l'intensité incidente permet d'estimer le seuil des dommages ainsi que d'étudier la cinétique des PIEs. En particulier, nous avons étudié la photosensibilité des films minces chalcogénures $\mathrm{Ge}_x\mathrm{As}_y\mathrm{Se}_{100-x-y}$ et $\mathrm{Te}_{20}\mathrm{As}_{30}\mathrm{Se}_{50}$. En outre, nous avons montré que les modifications permanentes de la réfraction et l'absorption induite par les PIEs peuvent contribuer à la réponse non linéaire mesurée avec Z-scan. Pour vérifier la présence de PIE au cours de Z-scan, il est nécessaire d'effectuer trois scans: en régime linéaire, puis en régime non linéaire et de nouveau en linéaire. La comparaison des scans en régime linéaires avant et après la mesure permet de révéler les changements permanents dans la réfraction et l'absorption inscrit à l'intérieur de l'échantillon. Il a été montré qu'une ablation d'une dizaine de nanomètres peut être détectée par Z-scan et ceci aboutit à des résultats erronés dans les valeurs de n_2 et β.

De plus nous avons démontré expérimentalement que la technique Z-scan peut être un outil très utile pour étudier le profil gaussien des modifications permanentes photo-induites au niveau des coefficients optiques à l'intérieur des matériaux photosensibles. Une théorie semi-analytique pour Z-scan donnant les mesures en régime linéaire a été développée. Il a été montré que le signe de la réfraction et de l'absorption peuvent être déterminé sans aucune ambigüité. En particulier, nous avons étudié les PIEs dans les paramètres optiques linéaires d'un verre chalcogénure massif $\mathrm{As}_2\mathrm{S}_3$ causés par une irradiation infrarouge. Une autre application a été trouvée pour la mesure de l'épaisseur ou l'indice des couches minces. Il a été démontré qu'en présence d'objets de phase rectangulaire (rainure rectangulaire sur film d'épaisseur très faible devant λ) il est possible d'obtenir une configuration pic-vallée avec la technique Z-scan. La différence entre le pic et la vallée de la transmission normalisée est liée linéairement au déphasage dû à la réfraction permanente.

Nous avons également réalisé des mesures absolues de n_2 dans le disulfure de carbone (CS_2) et la silice fondue (SiO_2), deux matériaux standards utilisés dans les expériences d'optique non linéaire. La méthode Z-scan à l'intérieur du système d'imagerie $4f$ a été combinée avec l'expérience 'Kerr-Shutter' afin d'analyser précisément le profil spatio-temporel des faisceaux de pompe à 355 nm, 532 nm et 1064 nm dans le régime de picoseconde. Les valeurs absolues obtenues de n_2 ont été trouvées 7.5 fois plus petites que celles couramment utilisées jusqu'à présent et mesurées il y a quelques décennies. En outre une dispersion plus importante de n_2 en fonction de la longueur d'onde a été trouvée.

Nous avons également caractérisé les indices de réfraction non linéaire (n_2) et les coefficients d'absorption non linéaire (β) pour différentes compositions de verres massifs en chalcogénures GeS_2-Sb_2S_3-CsI et en oxyde de métaux lourds $Pb(PO_2)_3$-WO_3 dans le cadre de leur aptitude à des applications de commutation tout optique (AOS). Nous avons constaté que seulement trois compositions parmi les dix étudiés en verres chalcogénures ont un facteur de mérite $2\beta\lambda/n_2$ (FOM) < 1, les rendant aptes à l'AOS. Au contraire, tous les verres d'oxydes étudiés remplissent le critère retenu. En outre, nous avons confirmé que l'indice de réfraction non linéaire a un comportement étroitement liée à l'indice linéaire dans les deux familles de verres. De plus, nous avons montré que le modèle BGO pourrait être un outil très utile pour estimer les valeurs n_2 dans les deux groupes de matériaux en tenant compte de nos mesures absolues. Par ailleurs, on constate que les prédictions du modèle BGO ne sont pas influencées par la présence d'une faible absorption non linéaire.

En résumé, notre étude a porté sur le large éventail des questions concernant la caractérisation optique non linéaire de la susceptibilité du troisième ordre: à partir de l'optimisation de la sensibilité et le rapport signal / bruit dans les techniques de mesures, en passant par le problème de la photosensibilité et les effets photo-induits dans les films minces et pour finir sur la mesure absolue des matériaux massifs. Il y a quelques points qui valent la peine d'être envisager pour les perspectives d'avenir. Des fluctuations d'énergie moindres à la sortie du laser combiné avec un seuil de bruit plus faible au niveau du capteur sont indispensables pour réaliser des mesures de coefficients non linéaires dans des bonnes conditions. Nous sommes convaincus que la précision de la mesure absolue de l'intensité dans le plan focal d'une lentille reste la clé conduisant à des résultats plus reproductibles et cohérents pour toutes les expériences menées en optique non linéaire.

Appendix A

Z-scan theory for a permanent Gaussian phase shift

We assume a single Gaussian laser beam in traveling $+z$ direction. The amplitude of electric at the entry of the sample is given by:

$$E_e\left(r,z\right)=E_0\frac{w_0}{w\left(z\right)}\exp\left(-\frac{r^2}{w^2\left(z\right)}\right)\exp\left(-\frac{i\pi r^2}{\lambda R\left(z\right)}\right), \tag{A.1}$$

where E_0 denotes the on-axis amplitude of the electric field, r is the radial coordinate, λ is the laser wavelength, $R\left(z\right)=z\left(1+z_0^2/z^2\right)$ is the radius of the curvature of the wave-front, $z_0=\pi w_0^2/\lambda$ is the Rayleigh range and w_0 is the beam waist at the focal plane. Outside the focal plane the waist changes with z: $w\left(z\right)=w_0\left(1+z^2/z_0^2\right)^{1/2}$. Since we are concerned with the permanent phase-shift, the temporal term are omitted. The sample is considered as thin, with L, the thickness smaller than the Rayleigh range ($L<z_0$). Thus, we can neglect any changes in laser beam irradiance distribution inside the medium due to linear diffraction phenomenon. We suppose the sample with permanently written modifications in refraction and absorption. We assume also that these changes have the same Gaussian distribution in the whole volume of the medium and identical with the spatial profile of the focal beam intensity:

$$\Delta n\left(r\right)=\Delta n_0\exp\left(-\frac{2r^2}{w_0^2}\right), \tag{A.2}$$

$$\alpha\left(r\right)=\alpha_s+\Delta\alpha_0\exp\left(-\frac{2r^2}{w_0^2}\right), \tag{A.3}$$

where Δn_0 and $\Delta\alpha_0$ are the photo-induced on-axis refractive index and absorption coefficient respectively, α_s is the absorption coefficient of the material. Under such assumptions, the amplitude $\sqrt{I}$ and phase Φ of the electric field as a function of z', the propagation depth inside the sample, are governed in slowly varying amplitude approximation by a pair of simple equations:

$$\frac{d\Delta\Phi}{dz'} = \frac{2\pi}{\lambda}\Delta n\left(r\right), \tag{A.4}$$

$$\frac{dI}{dz'} = -\alpha\left(r\right)I. \tag{A.5}$$

The solutions of theses equations at the exit face of the sample take a form:

$$\Delta\Phi\left(r\right) = \Delta\Phi_0 \exp\left(-\frac{2r^2}{w_0^2}\right), \tag{A.6}$$

where $\Delta\Phi_0 = 2\pi\Delta n_0 L/\lambda$ is the on-axis phase shift. The output intensity is given by

$$I_{out}\left(r,z\right) = I_e\left(r,z\right)e^{-\alpha_s L}\exp\left[-\Delta\alpha_0 L\exp\left(-\frac{2r^2}{w_0^2}\right)\right], \tag{A.7}$$

where $I_e\left(r,z\right) = \left|E_e\left(r,z\right)\right|^2$. Hence the electric field outgoing from the sample is expressed as:

$$E_{out}\left(r,z\right) = E_e\left(r,z\right)e^{-\alpha_s L/2}\exp\left[-\left(i\Delta\Phi_0 + \frac{1}{2}\Delta\alpha_0 L\right)\exp\left(-\frac{2r^2}{w_0^2}\right)\right]. \tag{A.8}$$

Open aperture configuration

In the open aperture configuration of Z-scan technique there is no aperture in the far-field in front of detector and the measured signal is insensitive to permanent modifications in refraction. Therefore, $P\left(z\right)$, the output power can be obtained by spatially integrating the intensity distribution at the exit face of the sample given in (A.7):

$$P\left(z,\Delta\alpha_0\right) = \int_0^{2\pi} d\Theta \int_0^{\infty} I_{out}\left(r,z\right)rdr = 2\pi\frac{I_0 e^{-\alpha_s L}}{1+z^2/z_0^2}\times\int_0^{\infty}\exp\left(-\frac{2r^2}{w^2\left(z\right)}\right)\exp\left[-\Delta\alpha_0 L\exp\left(-\frac{2r^2}{w_0^2}\right)\right]rdr \tag{A.9}$$

The explicit solution of the integral can not be found. The difficulty in integrating (A.9) resides in the term where there is an exponential of an exponential. To obtain an analytical result more suitable for numerical evaluation, we applied an incomplete gamma function as it has been done in [152] for a similar integral. Accordingly, we make the substitutions:

$$\Lambda = 2\pi \frac{I_0 e^{-\alpha_s L}}{1 + z^2/z_0^2}, \tag{A.10}$$

$$\upsilon = \frac{2}{w_0^2}, \tag{A.11}$$

$$\vartheta = \frac{2r^2}{w^2(z)}. \tag{A.12}$$

Then we can write the integral to be solved as:

$$P(z, \Delta\alpha_0) = \Lambda \int_0^\infty \exp\left(-\vartheta r^2\right) \exp\left[-\Delta\alpha_0 L \exp\left(-\upsilon r^2\right)\right] r dr. \tag{A.13}$$

After that the following substitutions are made $\xi = \upsilon r^2$ and $\exp(-\xi) = \varsigma$, obtaining an expression to be integrated in the variable ς. Substituting $\mu = \vartheta/\upsilon - 1$ and $\nu = \Delta\alpha_0 L\varsigma$, equation (A.13) is reduced to:

$$P = \frac{\Lambda}{2\upsilon\left(\Delta\alpha_0 L\right)^{\mu+1}} \int_0^{\Delta\alpha_0 L} d\nu \nu^\mu \exp(-\nu). \tag{A.14}$$

Equation (A.14) is the integral representation of the incomplete gamma function [152]:

$$\Gamma(\gamma, x) = \int_0^x d\nu \nu^{\gamma-1} \exp(-\nu) = x^\gamma \sum_{m=0}^\infty \frac{(-1)^m}{m!} \frac{x^m}{(\gamma + m)}. \tag{A.15}$$

In our case $\gamma = \mu + 1 = \left(1 + z^2/z_0^2\right)^{-1}$ and $x = \Delta\alpha_0 L$. Combining (A.14) with (A.15) the normalized open aperture Z-scan transmittance for a sample with a permanent Gaussian phase shift can be expressed as:

$$T_o(z) = \frac{P(z, \Delta\alpha_0)}{P(z, \Delta\alpha_0 = 0)} = \sum_{m=0}^\infty \frac{(-1)^m}{m!} \frac{(\Delta\alpha_0 L)^m}{(1 + m(1 + z^2/z_0^2))}. \tag{A.16}$$

Closed aperture configuration

In the closed aperture configuration of the Z-scan technique there is a circular aperture placed in front of detector in the far-field. Hence the beam must propagate from the exit face of the sample to the aperture plane. Because the beam and the phase shift have Gaussian profiles, we can apply a Gaussian decomposition method [63][65][66] to obtain E_a, the electric field pattern in the aperture plane. Accordingly, we decompose the complex electric field at the exit face of the sample into a summation of the Gaussian beams through the Taylor series expansion of the permanent phase term $\exp\left[-\left(i\Delta\Phi_0 + \Delta\alpha_0 L/2\right)\exp\left(-2r^2/w_0^2\right)\right]$ in (A.8):

$$E_a\left(r,z\right) = E_e\left(r=0,z\right)e^{-\alpha_s L/2}\sum_{m=0}^{\infty}\frac{\left[-\left(i\Delta\Phi_0+\frac{1}{2}\Delta\alpha_0 L\right)\right]^m}{m!}\frac{w_{m0}}{w_m}\exp\left[-\frac{r^2}{w_m^2}-i\frac{\pi r^2}{\lambda R_m}+i\Theta_m\right]. \tag{A.17}$$

Defining d as the propagation distance in the free space from sample to the aperture plane and $g = 1 + d/R\left(z\right)$, the remaining parameters in (A.17) are expressed as:

$$w_{m0}^2 = \frac{w_0^2}{2m + \left(1 + z^2/z_0^2\right)^{-1}}, \tag{A.18}$$

$$d_m = \frac{\pi w_{m0}^2}{\lambda}, \tag{A.19}$$

$$w_m^2 = w_{m0}^2\left[g^2 + \frac{d^2}{d_m^2}\right], \tag{A.20}$$

$$R_m = d\left[1 - \frac{g}{g^2 + d^2/d_m^2}\right]^{-1}, \tag{A.21}$$

$$\Theta_m = \tan^{-1}\left[\frac{d/d_m}{g}\right]. \tag{A.22}$$

The normalized closed aperture Z-scan transmittance is defined as

$$T_c(z) = \frac{\int\limits_0^{r_a}\left|E_a\left(r,z\right)\right|^2 r dr}{S\int\limits_0^{\infty}\left|E_a\left(r,z,\Delta\Phi_0=0,\Delta\alpha_0=0\right)\right|^2 r dr}, \tag{A.23}$$

where $S = 1 - \exp\left(-2r_a^2/w_a^2\right)$ is the linear transmittance of circular aperture with r_a and w_a denoting the aperture radius and beam waist in aperture plane in absence of any permanent phase modification, respectively. The analytical solution for pure refractive (i.e. $\Delta\alpha_0 L \ll \Delta\Phi_0$) transmittance can be derived for on-axis signal ($r = 0$ in (A.17)) and low phase shift $|\Delta\Phi_0| \ll 1$. In such conditions only two terms in the sum of (A.17) need be retained and the on-axis transmittance in the far field conditions ($d \gg z_0$) takes a form:

$$\begin{aligned} T_c(z, S &= 0) = \lim_{d\to\infty} \frac{\left|E_a\left(z, r=0, \Delta\Phi_0\right)\right|^2}{\left|E_a\left(z, r=0, \Delta\Phi_0=0\right)\right|^2} = \\ &\lim_{d\to\infty} \frac{\left|\left(g^2+d^2/d_0^2\right)^{-1/2}\exp\left(i\Theta_0\right) - i\Delta\Phi_0\left(g^2+d^2/d_1^2\right)^{-1/2}\exp\left(i\Theta_1\right)\right|^2}{\left|\left(g^2+d^2/d_0^2\right)^{-1/2}\exp\left(i\Theta_0\right)\right|^2}. \end{aligned} \tag{A.24}$$

The limit ($d \to \infty$) of this expression, after disregarding terms of second order, is given by

$$T_c(z, S \approx 0) = 1 + \frac{4\Delta\Phi_0 x}{4x^2+9}, \tag{A.25}$$

where $x = z/z_0$.

Appendix B

Huygens-Fresnel principle in Z-scan theory

Samad et al.[152] introduced a theory based on the Huygens-Fresnel principle allowing determining Z-scan normalized on-axis transmittance in the closed aperture configuration alternatively to the Gaussian Decomposition Method presented in appendix A. Here we will use this theory to derive the on-axis transmittance in a case of a sample with permanently written Gaussian refractive modifications in order to confirm the result (equation (A.25)) obtained in appendix A. The system under consideration is shown in Fig.B.1.

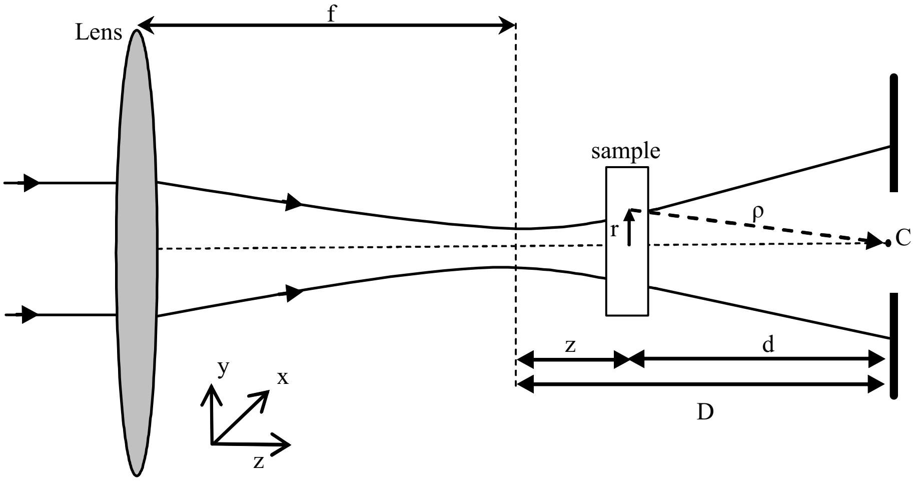

Figure B.1: Scheme of the coordinates utilized in the calculation of the Fresnel integral.

The electric field at front face of the sample ($E_e(r, z)$) is described by equation (A.1). The electric field at the exit face of the material ($E_{out}(r,z)$) is given by equation (A.8), where we set $\Delta\alpha_0 = 0$ to consider pure refractive case. The electric field at point C (see Fig.B.1), i.e. the on-axis point in the far-field aperture plane, can be found by applying Huygens-Fresnel diffraction integral:

$$E_C(z) = i\frac{d}{\lambda}\int_0^{2\pi} d\Theta \int_0^{\infty} E_{out}(r,z)\,\frac{\exp(-i2\pi\rho/\lambda)}{\rho^2} rdr, \tag{B.1}$$

where $\exp(-i2\pi\rho/\lambda)/\rho^2$ is the Huygens propagation term (for spherical wave) with $\rho = \sqrt{r^2+d^2}$, λ representing the wavelength and d is a distance from aperture to sample. To calculate the integral, as $d \gg r$, we can approximate distance ρ by :

$$\rho = \sqrt{r^2+d^2} \approx d + \frac{1}{2}\frac{r^2}{d}. \tag{B.2}$$

This is the standard paraxial approximation, which is applied in the phase term of integral (B.1) and we use $\rho \approx d$ for the amplitude term. Changing the variables according to:

$$\Lambda = i\frac{2\pi E_0}{\lambda d}\frac{w_0}{w(z)}\exp\left(-\frac{\alpha_s L}{2} - i\frac{2\pi d}{\lambda}\right), \tag{B.3}$$

$$\upsilon = \frac{2}{w_0^2}, \tag{B.4}$$

$$\vartheta = \frac{1}{w^2(z)} + i\frac{\pi}{\lambda}\left(\frac{1}{R(z)} + \frac{1}{d}\right), \tag{B.5}$$

we can write the integral to be solved as:

$$E_C = \Lambda\int_0^{\infty} \exp\left(-\vartheta r^2\right)\exp\left[-i\Delta\Phi_0\exp\left(-\upsilon r^2\right)\right] rdr. \tag{B.6}$$

This integral is similar to the integral given in equation (A.13). Hence it can be solved in the same way applying an incomplete gamma function theory. Following the procedure depicted in appendix A we found that electric field at point C is proportional to

$$E_C(z) \propto \sum_{m=0}^{\infty}\frac{(-1)^m}{m!}\frac{(i\Delta\Phi_0)^m}{(\gamma(z)+m)}, \tag{B.7}$$

where

$$\gamma\left(z\right)=\frac{1}{2}\left(\frac{z_0^2+iz_0z}{z_0^2+z^2}+i\frac{z_0}{D-z}\right) \tag{B.8}$$

with $D=d+z$ denoting the distance from the focal plane to the aperture plane. For a small phase shift $|\Delta\Phi_0|\ll 1$ only two terms in the sum of (B.7) can be retained. Then the normalized on-axis transmittance in the far field conditions ($D\gg z_0$) is given by:

$$T(z)=\lim_{D\to\infty}\frac{\left|E_C\left(z,\Delta\Phi_0\right)\right|^2}{\left|E_C\left(z,\Delta\Phi_0=0\right)\right|^2}=\lim_{D\to\infty}\left|1-\frac{i\Delta\Phi_0}{1+1/\gamma\left(z\right)}\right|^2. \tag{B.9}$$

The limit ($D\to\infty$) of this expression, after disregarding terms of second order, is given by

$$T(z)=1+\frac{4\Delta\Phi_0x}{4x^2+9}, \tag{B.10}$$

where $x=z/z_0$. This result is exactly the same as the one (equation (A.25)) calculated by Gaussian Decomposition Method.

Appendix C

Focal on-axis intensity for Gaussian beam

In this appendix we derive an expression for on-axis intensity (I_0) of focused Gaussian beam. Consider a situation shown in Fig.C.1. The Gaussian beam with radius w_e falls on converging lens (of focal length f) and is focused to a focal spot of waist w_0. We assume that the spatial and temporal distributions of laser light intensity in the focal plane are Gaussians:

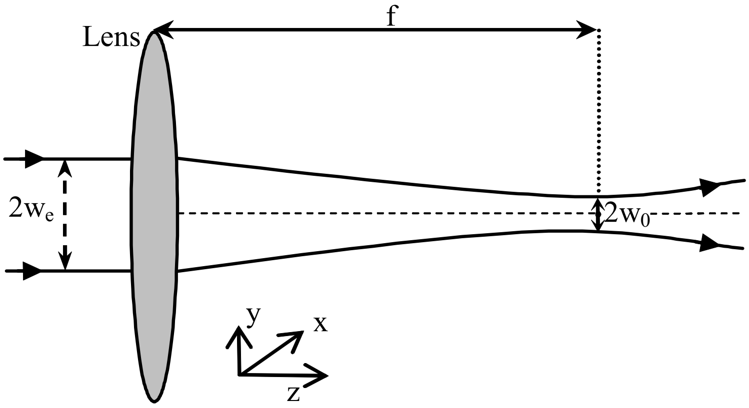

Figure C.1: Gaussian beam with waist w_e focused to a focal spot of radius w_0.

$$I\left(r,t\right)=I_0\exp\left(-\frac{2r^2}{w_0^2}\right)\exp\left(-\frac{2t^2}{t_0^2}\right), \qquad \text{(C.1)}$$

where I_0 is the peak (on-axis) intensity and t_0 is the pulse width defined by the half width at $1/e^2$ maximum. However, usually it is τ, the full width at half maximum (FWHM) which is measured rather than t_0. In a case of Gaussian pulse defined in (C.1) the relation between t_0 and τ is given by $\tau = t_0\sqrt{2\ln(2)}$. The spatial and temporal integration of intensity in (C.1) gives a total energy inside the system:

$$\varepsilon = 2\pi I_0 \int\limits_0^\infty \exp\left(-\frac{2r^2}{w_0^2}\right) r dr \int\limits_{-\infty}^\infty \exp\left(-\frac{2t^2}{t_0^2}\right) dt. \tag{C.2}$$

These two integrals can be solved analytically giving:

$$\varepsilon = \frac{1}{4} I_0 \pi w_0^2 \tau \sqrt{\frac{\pi}{\ln(2)}}. \tag{C.3}$$

If $f \gg w_e$ then the focal spot size (w_0) can be related directly to beam waist at the entry (w_e) of the system by $w_0 = \lambda f/\pi w_e$ [66]. After few simple transformations we get a final expression for focal peak intensity:

$$I_0 = 4\sqrt{\pi \ln(2)} \left(\frac{w_e}{\lambda f}\right)^2 \frac{\varepsilon}{\tau}. \tag{C.4}$$

Appendix D

Publications

Papers in Refereed Journals

1. G. Boudebs, K. Fedus, C. Cassagne, H. Leblond, "Degenerate multi-wave mixing using Z-scan technique", Appl. Phys. Lett. **93**, 021118 (2008)

2. K. Fedus, G. Boudebs, "Sensitivity of the $4f$ coherent imaging system used in degenerate multi-wave mixing experiments," J. Opt. Soc. Am. B, **26**, 244-248 (2009)

3. G. Boudebs, K. Fedus, "Absolute measurement of the nonlinear refractive indices of reference materials," J. Appl. Phys. **105**, 103106 (2009)

4. K. Fedus, G. Boudebs, Cid B. de Araújo, M. Cathelinaud, F. Charpentier, and V. Nazabal, "Photo-induced effects in thin films of $Te_{20}As_{30}Se_{50}$ glass with nonlinear characterization," Appl. Phys. Lett. **94**, 061122 (2009)

5. G. Boudebs, K. Fedus, "Linear optical characterization of transparent thin films by Z-scan technique," Appl. Opt. **48**, 4124-4129 (2009)

6. K. Fedus, G. Boudebs, " Determination of photo-induced changes in linear optical coefficients by Z-scan technique," J. Opt. Soc. Am. B **26**, 2171-2175 (2009)

7. F. E. P. dos Santos, Cid B. de Araújo, A. S. L. Gomes, K. Fedus and G. Boudebs, D. Manzani and Y. Messaddeq, "Nonresonant third – order nonlinear properties of $NaPO_3$-WO_3-Bi_2O_3 glasses in the near infrared," J. Appl. Phys. **106**, 063507 (2009)

8. K. Fedus, G. Boudebs, Q. Coulombier, J. Troles, X.H.Zhang, "Nonlinear characterization of GeS_2–Sb_2S_3–CsI glass system," J. Appl. Phys. **107**, 023108 (2010)
9. Q. Coulombier, M. Sergent, K. Fedus, G. Boudebs, J. Troles, G. Canat, O. Vasseur, M. P. Bourdon, Cathelinaud and X.H Zhang, "Sulfide-halide glasses with high nonlinear refractive index and low nonlinear absorption," Opt. Mat. (2010)
10. K. Fedus, G. Boudebs, H. Leblond, "Degenerate multi-wave mixing inside a $4f$ imaging system in presence of nonlinear absorption," Appl. Phys. B, (2010)
11. P. Nemec,S. Zhang, V. Nazabal, K. Fedus, G. Boudebs, A. Moreac, M. Cathelinaud, X.-H. Zhang, "Photo-stability of pulsed laser deposited $Ge_xAs_ySe_{100-x-y}$ amorphous thin films," Opt. Express **18,** 22944 (2010)
12. K. Fedus, G. Boudebs, "Sensitivity of Z-scan using diffraction efficiency," Opt. Commun. accepted to publication (October 2010)
13. T. R. Oliveira, K. Fedus, D. Manzani, E. L. Falcão–Filho, G. Boudebs, Cid B. de Araújo, Y. Messaddeq, "Near - infrared Kerr nonlinearity of $Pb(PO_3)_2$ - WO_3 glasses," J. Appl. Phys. accepted to publication (October 2010)

Conference papers

1. G. Boudebs, K. Fedus, "Comparison of different nonlinear optical characterization techniques", Invited talk, Proceedings of 2008 10th Anniversary International Conference on Transparent Optical Networks, ICTON, art. no. 4598414, Athens, Greece (2008)
2. G. Boudebs, K. Fedus, "Sensitivities of different nonlinear optical characterization techniques", Invited talk, 11th International Conference on Transparent Optical Network, ICTON:, art. no. 5185051, Island of São Miguel, Azores (2009)
3. G. Boudebs, K. Fedus, "Nonlinear optical characterization in a degenerate multi-wave mixing configuration", Invited talk, Proceedings of SPIE - The International Society for Optical Engineering 7403, art. no. 74030N, San Diego, USA (2009)
4. K. Fedus, G. Boudebs, "Degenerate multi-wave mixing inside the 4f coherent imaging system,", CLEO/Europe - EQEC 2009 - European Conference on Lasers and Electro-

Optics and the European Quantum Electronics Conference, art. no. 5196566, Munich, Germany (2009)

5. G. Boudebs, K. Fedus, “Nonlinear Characterization Techniques inside a $4f$ system”, Invited talk, Latin America Optics and Photonics Conference, September 27-30, Recife, Brazil (2010)

References

[1] P. A. Franken, A. E. Hill, C. W. Peters, G. Weinreich, Phys. Rev. Lett. **7**, 118 (1961)

[2] R. Sutherland, *Handbook of nonlinear optics*, second ed., (Marcel Dekker Inc., New York 2003)

[3] R. W. Boyd, *Nonlinear Optics*, third ed., (Academic Press, New York 2007)

[4] G. S. He and S. H. Liu, *Physics of Nonlinear Optics* (World Scientific, London 1999)

[5] R. W. Hellwarth, J. Cherlow, and T. T. Yang, Phys. Rev. B **11**, 964 (1975)

[6] I. Kang, S. Smolorz, T. Krauss, F. Wise, B. G. Aitken, N. F. Borrelli, Phys. Rev. B **54**, R12641 (1996)

[7] M. Falconieri, J. Opt. A: Pure Appl. Opt. **1**, 662 (1999)

[8] R. de Nalda, R. del Coso, J. Requejo-Isidro, J. Olivares, A. Suarez-Garcia, J. Solis, and C. N. Afonso, J. Opt. Soc. Am. B **19**, 289 (2002)

[9] A. A. Said, M. Sheik-Bahae, D. J. Hagan, T. H. Wei, J. Wang, J. Young, E. W Van Stryland, J. Opt. Soc. Am. B **9**, 405 (1992)

[10] K. Ogusu, K. Shinkawa, Opt. Exp. **16**, 14780 (2008)

[11] P. D. Maker, R. W. Terhune, C. M. Savage, Phys. Rev. Lett. **12**, 507 (1964)

[12] Z.-B. Liu, X.-Q. Yan, J.-G. Tian, W.-Y. Zhou, W.-P. Zang , Opt. Exp. **15**, 13353 (2007)

[13] M. Göppert-Mayer, Ann. Physik **9**, 273 (1931)

[14] W. Kaiser, C.G.B Garrett,. Phys. Rev. Lett. **7**, 229 (1961)

[15] R.C. Miller, Appl. Phys. Lett. **5**, 17 (1964)

[16] J.J. Wynne, Phys. Rev. **178**, 1295 (1969)

[17] C.C. Wang, Phys. Rev. **B2**, 2045 (1970)

[18] N.L. Boling, A.J. Glass, A. Owyoung, IEEE J. Quantum Electronics **QE-14**, 601 (1978)

[19] M. Sheik-Bahae, D.J. Hagan, E.W. Van Stryland, Phys. Rev. Lett. **65**, 96 (1990)

[20] M. Sheik-Bahae, D.C. Hutchings, D.J. Hagan, E.W. Van Stryland, IEEE J. Quantum Electron. **27**, 1296 (1991)

[21] E.W. Van Stryland, M. A. Woodall, H. Vanherzeele, and M. J. Soileau, Opt. Lett. **10**, 490 (1985)

[22] M. Sheik-Bahae, E.W. Van Stryland, *Optical nonlinearities in the transparency region of bulk semiconductors*, Eds. E. Garmire and A. Kost, Chap. 4, 257 Nonlinear Optics in Semiconductors I, (Academic Press,1999)

[23] R. DeSalvo, A. A. Said, D. J. Hagan, E. W. Van Stryland, and M. Shiek-Bahae, IEEE J. Quantum Electron. **32**, 1324 (1996)

[24] R. Adair, L. L. Chase, and S. A. Payne, Opt. Mater. (Amsterdam, Neth.) **1**, 185 (1992)

[25] S.H. Wemple, M. DiDomenico, Phys. Rev. B **3 (4)**, 1338 (1971)

[26] S.H. Wemple, Phys. Rev. B **7 (8)**, 3767 (1973)

[27] K. Petkov and P. J. S. Ewen, J. Non-Cryst. Solid. **249**, 150 (1999).

[28] M. E. Lines, J. Appl. Phys. **69**, 6876 (1991).

[29] G. Lenz, J. Zimmermann, T. Katsufuji, M. E. Lines, H. Y. Hwang, S. Spalter, R. E. Slusher, S.-W. Cheong, J. S. Sanghera, and I. D. Aggrawal, Opt. Lett. **25**, 254 (2000).

[30] J.S. Sanghera, C.M. Florea, L.B. Shaw, P. Pureza, V.Q. Nguyen, M. Bashkansky, Z. Dutton, I.D. Aggarwal, J. Non-Cryst. Solids **354**, 462 (2008)

[31] P. D. McWane, D. A. Sealer, Appl. Phys. Lett. **8**, 278 (1966).

[32] R. W. Hellwarth, A. Owyoung, N. George, Phys. Rev. A **4**, 2342 (1971)

[33] A. Owyoung, IEEE J. of Quantum Electron. **QE-9**, 1064 (1973)

[34] G. K. L. Wong, Y. R. Shen, Phys. Rev. A **10**, 1277 (1974)

[35] P. P. Ho and R. R. Alfano, Phys. Rev. A **20**, 2170 (1979)

[36] Y. R. Shen, *The Principles of Nonlinear Optics* (Wiley, New York, 1984)

[37] H. Kanbara, H. Kobayashi, T. Kaino, T. Kurihara, N. Ooba, K. Kubodera, J. Opt. Soc. Am. B **11**, 2216 (1994)

[38] M. Paciaroni, M. Linne, Appl. Opt. **43**, 5100 (2004)

[39] L. Yan, J. Yue, J. Si, X. Hou, Opt. Expr. **16**, 12069 (2008)

[40] M.A. Dugay, *The ultrafast optical kerr shutter*, E. Wolf, Progress in Optics XIV, North-Holland, (1976)

[41] E. L. Falcao-Filho, C. A. C. Bosco, G. S. Maciel, L. H. Acioli, Cid B. de Araujo, A. A. Lipovskii, D. K. Tagantsev, Phys. Rev. B **69**, 134204 (2004)

[42] H. S. Albrecht, P. Heist, J. Kleinschmidt, D. V. Lap, and T. Schroder, Appl. Phys. B **55**, 362-364(1992)

[43] M. E. Orczyk, M. Samoc, J. Swiatkiewicz, M. Tomoaia-Cotisel, P. N. Prasad, Appl. Phys. Lett. **60**, 2837 (1992)

[44] P. D. Maker and R. W. Terhune, Phys. Rev. **137**, A801 (1965)

[45] M. D. Levenson, IEEE J. of Quantum Electron. **QE-10**, 110 (1974)

[46] R. Adair, L. L. Chase, and S. A. Payne, J. Opt. Soc. Anler. B, **4**, 875 (1987)

[47] R. W. Hellwarth, J. Opt. Soc. Am. **67**, 1 (1977)

[48] A. Yariv and D. M. Pepper, Opt. Lett. **1**, 16 (1977)

[49] P. W. Smith, W. J. Tomlinson, D. J. Eilenberger, P. J. Maloney, Opt. Lett. **6**, 581 (1981)

[50] Z. Wu, W.G. Tong, Anal. Chem. **65**, 112 (1993)

[51] M. Samoc, A. Samoc, B. Luther-Davies, Z. Bao, L. Yu, B. Hsieh, U. Scherf, J. Opt. Soc. Am. B **15**, 817 (1998)

[52] E. Yousef, M. Hotzel, C. Russel, J. Non-Cryst. Solids **342**, 82 (2004)

[53] P. A. Fleitz, R. L. Sutherland, L. V. Natarajan, T. Pottenger, and N. C. Fernelius, Opt. Lett. **17**, 716 (1992)

[54] M. Zhao, Y. Cui, M. Samoc, P. N. Prasad, M. R. Unroe, and B. A. Reinhardt, J. Chem. Phys. **95**, 3991 (1991)

[55] E. J. Canto-Said, D. J. Hagan, and E. W. Van Stryland, IEEE J. Quant. Electron. **27**, 2274 (1991)

[56] R. L. Sutherland, E. Rea, L. V. Natarajan, T. Pottenger, P. A. Fleitz, J. Chem. Phys. **98**, 2593 (1993)

[57] X. Zhang, X. Ye, and K. Chen, Opt. Commun. **113**, 519 (1995)

[58] A. Khyzniak, V. Kondilenko, Y. Kucherov, S. Lesnik, S. Odoulov, M. Soskin, J. Opt. Soc. Am. A **1**, 169 (1984)

[59] F. P. Strohkendl, L. R. Dalton, R. W. Hellwarth, H. W. Sarkas, Z. H. Kafafi, J. Opt. Soc. Am. B, **14**, 92 (1997)

[60] S.-Y. Tseng, W.Cao, Y.-H. Peng, J. M. Hales, S.-H. Chi, J. W. Perry, S. R. Marder, C. H. Lee, W. N. Herman, J. Goldhar, Opt. Exp. **14**, 8737 (2006)

[61] R.L Carman, R.Y. Chiao, P.L. Kelley, Phys. Rev. Lett. **17**, 1281 (1966)

[62] M. Sheik-Bahae, A.A. Said, E.W. Van Stryland, Opt. Lett. **14**, 955 (1989)

[63] M. Sheik-Bahae, A. A. Said, T. H. Wei, D. Hagan, E. W. Stryland, IEEE J. Quant. Elect. **26**, 760 (1990)

[64] J. W. Goodman, *Introduction to Fourier optics*, 2d edition, (Mc Graw Hill, 1996)

[65] D. Wearie, B. S. Wherett, D. A. B. Miller, and S. D. Smith, Opt. Lett. **9**, 331 (1984)

[66] H. Kogelnik and T. Li, Appl. Opt. **5**, 1550-1567 (1966)

[67] E. W. Van Stryland and M. Sheik-Bahae,in *Characterization Techniques and Tabulations for Organic Nonlinear Materials*, M. G. Kuzyk and C. W. Dirk, Eds., page 655-692, Marcel Dekker, Inc., (1998)

[68] T. Xia, D. J. Hagan, M. Sheik-Bahae, E.W. Van Stryland, Opt. Let. **19**, 317 (1994)

[69] W. Zhao and P. Palffy-Muhoray, Appl. Phys. Lett. **63**, 1613 (1993)

[70] B. Gu, X.-C. Peng, T. Jia, J.-P. Ding, J.-L. He, H.-T. Wang, J. Opt. Soc. Am. B **22**, 446 (2005)

[71] B. Taheri, H. Liu, B. Jassemnejad, D. Appling, R.C. Powell, , J.J. Song, Appl. Phys. Lett. **68**, 1317 (1996)

[72] Q. Yang, J. T. Seo, S. Creekmore, D. Temple, A. Mott, N. Min, K. Yoo, S. Young Kim, S. Jung, Appl. Phys. Lett. **82**, 19 (2003)

[73] Q. Yang, J. T. Seo, S. J. Creekmore, D. A. Temple, K. P. Yoo, S. Y. Kim, S. S. Jung, and A. Mott, 47th Annual Conference of SPIE, July 2002, Seattle, WA (SPIE, Bellingham, WA, 2002)

[74] B.K. Rhee, J.S. Byun, E.W. Van Stryland, J. Opt. Soc. Am. B **13**, 2720 (1996)

[75] S.M. Mian, B. Taheri, J.P. Wicksted, J. Opt. Soc. Am. B **13**, 856 (1996)

[76] S. Hughes, J.M. Burzler, Phys. Rev. A **56**, R1103 (1997)

[77] B. Gu, J. Yan, Q. Wang, J.L. He, H.T. Wang, J. Opt. Soc. Am. B **21**, 968 (2004)

[78] P.B. Chapple, J. Staromlynska, R.G. McDuff, J. Opt. Soc. Am. B **11**, 975 (1994)

[79] M. Sheik-Bahae, A. A. Said, D. J. Hagan, M. J. Soileau, E. W. Stryland, Opt. Eng **30**, 1228 (1991)

[80] R. DeSalvo, M. Sheik-bahae, A. A. Said, D. J. Hagan, E. W. Van Stryland, Opt. Lett. **18**, 194 (1993)

[81] J.G. Tian, W.P. Zang, G.Y. Zhang, Opt. Commun. **107**, 415 (1994)

[82] G. Tsigaridas, M. Fakis, I. Polyzos, P. Persephonis, V. Giannetas, Appl. Phys. B **76**, 83 (2003)

[83] D. V. Petrov, A. S. L. Gomes, C. B. de Araujo, Appl. Phys. Lett. **65**, 1067 (1995)

[84] D. V. Petrov, J. Opt. Soc. Am. B **13**, 1491 (1996)

[85] X.-Q. Yan, Z.-B. Liu, X.-L. Zhang, W.-Y. Zhou, J.-G. Tian, Opt. Exp. **17**, 6397 (2009)

[86] H. Ma, A. S. Gomez, C. B. de Araujo, Appl. Phys. Lett. **59**, 2666 (1991)

[87] M. Sheik-Bahae, J. Wang, R. DeSalvo, D. J. Hagan, E. W. V. Stryland, Opt. Lett. **17**, 258 (1992)

[88] H. Ma, Cid B. de Araujo, Appl. Phys. Lett. **66**, 27 (1995)

[89] J. Wang, M. Sheik-Bahae, A. A. Said, D. J. Hagan, E. W. Van Stryland, J. Opt. Soc. Am. B, **11**, 1009 (1994)

[90] M. Balu, J. Hales, D. J. Hagan, E. W. V. Stryland, Opt. Exp. **12**, 3820 (2004)

[91] M. Balu, J. Hales, D. J. Hagan, E. W. Van Stryland, Opt. Exp. **13**, 3595 (2005)

[92] M. Balu, L. A. Padilha, D. J. Hagan, E. W. Van Stryland, S. Yao, K. Belfield, S. Zheng, S. Barlow, S. Marder, J. Opt. Soc. Am. B **25**, 159 (2008)

[93] A. Marcano, H. Maillotte, D. Gindre, D. Metin, Opt. Lett. **21**, 101 (1996)

[94] F.E. Hernandez, A. Marcano, H. Maillotte, Opt. Commun. **134**, 529 (1997)

[95] M. Falconieri, G. Salvetti, Appl. Phys. B **69**, 133 (1999)

[96] A. Gnoli, L. Razzari and M. Righini, Opt. Express **13**, 7976 (2005)

[97] A. S. L. Gomes, E. L. Falcao Filho, Cid B. de Araujo, D. Rativa, R. E. de Araujo, Opt.Exp. **15**, 1712 (2007)

[98] B. M. Patterson, W. R. White, T. A. Robbins, R. J. Knize, Appl. Opt. **10**, 1854 (1998)

[99] D. H. Osborne, Jr., R. F. Haglund, Jr., F. Gonella, and F. Garrido, Appl. Phys. B **66**, 517 (1998)

[100] G. Boudebs, M. Chis, J. P. Bourdin, J. Opt. Soc. Am. B **13**, 1450 (1996)

[101] G. Boudebs, M. Chis, A. Monteil, Opt. Commun. **150**, 287 (1998)

[102] J. A. Hermann, J. Opt. Soc. Am. B **1**, 729 (1984)

[103] S. Cherukulappurath, G. Boudebs, A. Monteil, J. Opt. Soc. Am. B, **21**, 273 (2004)

[104] G. Boudebs, S. Cherukulappurath, Phys. Rev. A **69**, 053813 (2004)

[105] G. Boudebs, S. Cherukulappurath, Opt. Commun. **250**, 416, (2005)

[106] G. Boudebs and C. B. de Araújo, Appl. Phys. Lett. **85**, 3740 (2004)

[107] Y. Li, Y. Song, T. Wei, C. He, X. Zhang, Y. Wang, J. Yang, K. Yang, Appl. Phys. B **91** (1), 119 (2008)

[108] Y. B. Li, G. F. Pan, K. Yang, X. R. Zhang, Y. X. Wang, T. H. Wei, Y. L. Song, Opt. Exp. **16**, 6251 (2008)

[109] J. Yang, X. Zhang, Y. Wang, M. Shui, C. Li, X. Jin, Y. Song, Opt. Lett. **34**, 2513 (2009)

[110] J. Yang, Y. Song, Opt. Lett. **34**, 157 (2009)

[111] J. Yang, Y. Song, Y. Wang, C. Li, X. Jin, M. Shui, Opt. Commun. **283**, 209 (2010)

[112] W. H. Steel, Interferometry, 2nd ed. (Cambridge U. Press, Cambridge, U.K., 1983)

[113] G. Boudebs, M. Chis, X. N. Phu, J. Opt. Soc. Am. B **18**, 623 (2001)

[114] G. Boudebs, F. Sanchez, C. Duverger, B. Boulard, Opt. Commun. **199**, 257 (2001)

[115] G. Boudebs, F. Sanchez, J. Troles, F. Smektala, Opt. Commun. **199**, 425 (2001)

[116] J. Troles, *Verres Infrarouges à base de chalcogénures: Nouveaux systèms vitreux, synthèsis, caractérisations et propriétes optiques non linéaires pour applications en télécommunications et limitation optique*, Ph.D. thesis, Université de Rennes I (2002).

[117] *The metrology handbook*, Ed. Jay L. Bucher, Measurements Quality Division (ASQ, 2004)

[118] M. Sypek, C. Prokopowicz, M. Gorecki, Opt. Eng. **42**, 3158 (2003)

[119] G. Boudebs, K. Fedus, C. Cassagne, H. Leblond, Appl. Phys. Lett. **93**, 021118 (2008)

[120] K. Fedus, G. Boudebs, J. Opt. Soc. Am. B, **26**, 244 (2009)

[121] K. Fedus, G. Boudebs, H. Leblond, Appl. Phys. B (2010)

[122] Y. Liu, H. K. Tsang, Appl. Phys. Lett. **90**, 211105 (2007)

[123] K. Fedus, G. Boudebs, Opt. Commun. accepted to publication (October 2010)

[124] T. Godin, M. Fromager, B. Paivanranta, N. Passilly, G. Boudebs, E. Cagniot, K. Ait-Ameur, Appl. Phys. B **95**, 579 (2009)

[125] Y. Li, X. Zhang, Y. Wang, K. Yang, Y. Song, Opt. Commun. **266**, 686 (2006)

[126] Y. Li, K. Yang, X. Zhang, Q. Chang, Y. Wang, Y. Song, Opt. Commun. **281**, 3913 (2008)

[127] A. Zakery S.R. Elliott, *Optical Nonlinearities in Chalcogenide Glasses and their Applications* (Springer 2007)

[128] V. G. Taeed, N. J. Baker, L. Fu, K. Finsterbusch, M. R.E. Lamont, D. J. Moss, H. C. Nguyen, B. J. Eggleton, D. Y. Choi, S. Madden, and B. Luther-Davies, Opt. Express **15**, 9205 (2007)

[129] A.V. Belykh, O.M. Efimov, L.B. Glebov, Yu.A. Matveev, A.M. Mekryukov, M.D. Mikhailov, K. Richardson, J. Non-Cryst. Solids **213 & 214**, 330 (1997)

[130] K. Tanaka, J. Non-Crystal. Solids **352**, 2580 (2006)

[131] G. Chen, H. Jain, M. Vlcek, and A. Ganjoo, Phys. Rev. B **74**, 174203 (2006).

[132] P. Nemec,S. Zhang, V. Nazabal, K. Fedus, G. Boudebs, A. Moreac, M. Cathelinaud, X.-H. Zhang, Opt. Express **18,** 22944 (2010)

[133] R. A. Jarvis, R. P. Wang, A. V. Rode, C. Zha, B. Luther-Davies, J. Non-Cryst. Solids **353**, 947 (2007)

[134] K. Fedus, G. Boudebs, Cid B. de Araujo, M. Cathelinaud, F. Charpentier, and V. Nazabal, Appl. Phys. Lett. **94**, 061122 (2009)

[135] V. Nazabal, M. Cathelinaud, W. Shen, P. Nemec, F. Charpentier, H. Lhermite, M.-L. Anne, J. Capoulade, F. Grasset, A. Moreac, S. Inoue, M. Frumar, J.-L. Adam, M. Lequime, C. Amra, Appl. Opt. **47**, C114 (2008)

[136] W. Shen, M. Cathelinaud, M. Lequime, V. Nazabal, X. Liu, Opt. Comm. **281**, 3726 (2008)

[137] J.-L. Godet, H. Derbal, S. Cherukulappurath, G. Boudebs, Eur. Phys. J. D. **39**, 307 (2006)

[138] K. Fedus, G. Boudebs, J. Opt. Soc. Am. B **26**, 2171 (2009)

[139] K. Tanaka, N. Toyosawa, and H. Hisakuni, Opt. Lett. **20**, 1976 (1995)

[140] C. Meneghini, A. Villeneuve, J. Opt. Soc. Am. B **15**, 2946 (1998)

[141] J.-F. Viens, C. Meneghini, A.Villeneuve, T. V. Galstian, E. J. Knystautas, M. A. Duguay, K. A. Richardson, T. Cardinal, J. Lightwave Technol. **17**, 1184 (1999)

[142] T. M. Monro, D. Moss, M. Bazylenko, C. M. de Sterke, L. Poladian, Phys. Rev. Lett. **80**, 4072 (1998)

[143] A. M. Ljungstrom, T. M. Monro, J. Lightwave Technol. **20**, 78 (2002)

[144] N. Hô, J. M. Laniel, R. Vallée, A. Villeneuve, Opt. Lett. **28**, 965 (2003)

[145] D.A. Turnbull, J.S. Sanghera, V.Q. Nguyen, I.D. Aggarwal, Mat. Lett. **58**, 51 (2003)

[146] A. Zoubir, M. Richardson, C. Rivero, A. Schulte, C. Lopez, K. Richardson, N. Hô, R.Vallée, Opt. Lett. **29**, 748 (2004)

[147] H. Ebendorff-Heidepriem, Opt. Mat. 25, 109 (2004)

[148] K. M. Davis, K. Miura, N. Sugimoto, and K. Hirao, Opt. Lett. **21**, 1729 (1996)

[149] O.M. Efimov, L.B. Glebov, K.A. Richardson, E.Van Stryland, T. Cardinal, S.H. Park, M. Couzi, J.L. Brunéel, Opt. Mat. **17**, 379 (2001)

[150] A. C. van Popta, R. G. DeCorby, C. J. Haugen, T. Robinson, and J. N. McMullin, D. Tonchev, S. O. Kasap, Opt.Exp. **15**, 639 (2002)

[151] A.M. Ljungstrom, T.M. Monro, Opt. Express **10**, 230 (2002)

[152] R.E Samad,.N.D. Vieira Jr., J. Opt. Soc. Am. B **15**, 2742 (1998)

[153] G. Boudebs, K. Fedus, Appl. Opt. **48**, 4124 (2009)

[154] J. Cardin, D. Leduc, Appl. Opt. **47**, 894 (2008)

[155] R.M.A. Azzam, N.M. Bashara, *Ellipsometry and polarized light* (Elsevier, Amsterdam, 1987)

[156] A.-H. Liu, P. C. Wayner, Jr., and J. L. Plawsky, Appl. Opt. **33**, 1223 (1994)

[157] G. Jin, R. Jansson, H. Arwin, Rev. Sci. Instrums. **67,** 2930 (1996)

[158] A. Albersdorfer, G. Elender, G. Mathe, K. R. Neumaier , P. Paduschek, E. Sackmann, Appl. Phys. Lett. **72**, 2930 (1998)

[159] S. Otsuki, K. Tamada, and S. Wakida, Appl. Opt. **44**, 1410 (2005)

[160] C. Wang, J. Lin, H. Jian, and C. Lee, Appl. Opt. **46**, 7460 (2007)

[161] H.M. Zidan, M. Abu-Elnader, Physica B **355**, 308 (2005)

[162] G. Boudebs, K. Fedus, J. Appl. Phys. **105**, 103106 (2009)

[163] A. Major, F. Yoshino, J. S. Aitchison, P. W. E. Smith, Opt. Let. **29**, 16 (2004)

[164] A. Major, F. Yoshino, J. S. Aitchison, P. W. E. Smith, Opt. Let. **30**, 19 (2005)

[165] S. L. Shapiro, H. P. Broida, Phys. Rev. **154**, 129 (1967)

[166] D. McMorrow, W. T. Lotshaw, G. A. Kenney-Wallace, IEEE J. Quantum Electron. **24**, 443 (1988)

[167] A. G. Bezerra, Jr. A. S. L. Gomes, D. A. da Silva-Filho, L. H. Acioli, Cid B. de Araujo, C. P. de Melo, J. Chem. Phys; **111**, 5102, (1999)

[168] M.E. Orczyk,M. Samoc, J. Swiatkiewicz,P. Prasad, J. Chem. Phys. **98**, 2524 (1993)

[169] D. Mc Morrow, Opt. Commun. **86**, 236 (1991)

[170] H.-S. Albrecht,P. Heist,J. Kleinschmidt, D.V. Lap,Appl. Phys. B **57**, 193 (1993)

[171] T. Kawazoe,H. Kawaguchi, J. Inoue, O. Haba, M. Ueda, Opt. Commun. **160**, 125 (1999)

[172] K. Minoshima,M. Taiji, T. Kobayashi,Opt. Lett. **16**, 1683 (1991)

[173] S. Couris, M. Renard, O. Faucher, B. Lavorel, R. Chaux, E. Koudoumas, X. Michaut, Chem. Phys. Lett. **369**, 318 (2003)

[174] R. A. Ganeev, A . I., Ryasnyansky, M. Baba, M. Suzuki, N. Ishizawa, M. Turu, S. Sakakibara, H. Kuroda, Appl. Phys. B **78**, 433 (2004)

[175] S. Couris,E. Koudoumas, F. Dong,S. Leach, J. Phys. B **29**, 5033 (1996)

[176] M. J. Moran, C.-Y. She, R. L. Carman, IEEE J. Quant. Electron. **QE-11**, 259 (1975)

[177] N. P. Xuan, J.-L. Ferrier, J. Gazengel, G. Rivoire, Opt. Commun. **51**, 433 (1984)

[178] M. J. Soileau, W. F. Williams, E. W. Van Stryland, IEEE J. Quant. Electron. **QE-19**, 731 (1983)

[179] I. Golub, Y. Beaudoin, S. L. Chin, Opt. Lett. **13**, 488 (1988)

[180] G. R. Meredith, B. Buchalter, C. Hanzlik, J. Chem. Phys. **78**, 1533 (1983)

[181] D.Milam, Appl.Opt. **37**, 546 (1998)

[182] F. Billard, *Metrology of the nonlinear refractive index of glasses in nanoseconde, picoseconde and sub-picoseconde regime*, Ph.D. thesis, Universite Paul Cezzanne Aix-Marseille III

[183] I. N. Ross, W. T. Toner, C. J. Hooker, J. R. M. Barr, I. Correy, J. Mod. Opt. **37**, 555 (1990)

[184] Y. P. Kim, M. H. R. Hutchinson, Appl. Phys. B **49**, 69 (1989)

[185] W. L. Smith, J. H. Bechtel, and N. Bloembergen, Phys. Rev. B **12**, 706 (1975)

[186] W. T. White, W. L. Smith, D. Milam, Opt. Lett. **9**, 10 (1984)

[187] T. Shimada, N. A. Kurnit, M. Shiek-Bahae, in *Laser-Induced Damage in Optical Materials*, H. E. Bennett, A. H. Gunther, M. R. Kozlowski, B. E. Newman, M. J. Soileau, eds., Proc. SPIE 2714, 52 (1995)

[188] S. Santran, L. Canioni, L. Sarger, T. Cardinal, E. Fargin, J. Opt. Soc. Am. B **21**, 2180 (2004)

[189] A. J. Taylor, G. Rodriguez, and T. S. Clement, *Measurement of* n_2 *for KDP and fused silica at 400 nm and 800 nm* Attachment 1 in Effort in Support of Core Science and Technology Plan for Indirect-Drive Inertial Confinement (ICF) Fusion, LA-UR-96-2689 (Los Alamos National Laboratory, Livermore, Calif., 1996)

[190] R. H. Stolen, A. Ashkin, Appl. Phys. Lett. **22**, 294 (1973)

[191] W. E. Williams, M. J. Soileau, E. W. Van Stryland, in *Laser-Induced Damage in Optical Materials*, H. E. Bennett, A. H. Gunther, D. Milam, B. E. Newman, eds., Natl. Bur. Stand. (U.S.) Spec. Publ. 688 (U.S GAO, Washington, D.C., 1985), pp. 522–531

[192] A. P. Veduta , B. P. Kirsanov, Sov. Phys. JETP **27**, 736 (1968)

[193] M. A. Vasileva, Yu. Vischakas, V. Gulbinas, Sov. J. Quantum Electron. **15**, 656 (1985)

[194] D. Milam, M. J. Weber, J. Appl. Phys. **47**, 2497 (1976)

[195] G. B. Altshuler, A. I. Barbashev, V. B. Karasev, K. I. Krylov, V. M. Ovchinnkov, S. F. Sharlai, Sov. Tech. Phys. Lett. **3**, 213 (1977)

[196] F. Kajzar, J. Messier, Phys. Rev. A **32**, 2352 (1985)

[197] U. Gubbler, C. Bosshard, Phys. Rev. B **61**, 10702 (2000)

[198] K. S. Kim, R. H. Stolen, W. A. Reed, K. W. Quoi, Opt. Lett. **19**, 257 (1994)

[199] T. Kato, Y. Suetsugu, M. Takagi, E. Sasaoka, M. Nishimura, Opt. Lett. **20**, 988 (1995)

[200] E. L. Falcão-Filho, Cid B. de Araújo, C. A. C. Bosco, G. S. Maciel, and L. H. Acioli, M. Nalin, Y. Messaddeq, J. Appl. Phys. **97**, 013505 (2005)

[201] A. J. Taylor, G. Rodriguez, T . S Clement, Opt. Lett. **21**, 1812 (1996)

[202] I. Rau, F. Kajzar, A. Humeau, J. Luc, B. Sahraoui, G. Boudebs, J. Opt. Soc. Am. B. **25**, 1738 (2008)

[203] A. Zakery, S.R. Elliott, J. Non-Cryst. Solids **330**, 1 (2003)

[204] G. I. Stegeman, E. M. Wright, N. Finlayson, R. Zanoni, C. T. Seaton, IEEE J. Lightwave Technol. **6**, 953 (1988)

[205] G.I. Stegeman, in *Contemporary Nonlinear Optics* (Academic, New York, 1992)

[206] V. Mizrahi, K. W. DeLong, G. I. Stegeman, M. A. Saifi, M. J. Andrejco, Opt. Lett. **14**, 1140 (1989)

[207] H. Garcia, H. Krishna, R. Kalyanaraman, App. Phys. Lett. **89**, 141109 (2006)

[208] M. Yamane and Y. Asahara, *Glasses for Photonics* (Cambridge University Press, Cambridge, UK, 2000)

[209] D. Monoz-Martin, H. Fernandez, J. M. Fernandez-Navarro, J. Gonzalo, J. Solis, J. L. G. Fierro, C. Domingo, J. V. Garcia-Ramos, J. Appl. Phys. **104**, 113510 (2008), and references therein.

[210] S. Cherukulappurath, M. Guignard, C. Marchand, F. Smektala, G. Boudebs, Opt. Comm. **242**, 313 (2004)

[211] L. Petit, N. Carlie, H. Chen, S. Gaylord, J. Massera, G. Boudebs, J. Huc, A. Agarwal, L. Kimerling, K. Richardson, J. Solid State Chem. **182**, 2756 (2009)

[212] L. A. Gómez, C. B. de Araújo, D. N. Messias, L. Misoguti, S. C. Zílio, M. Nalin, Y. Messaddeq, J. Appl. Phys. **100**, 116105 (2006)

[213] L. A. Gómez, C. B. de Araújo, R. Putvinskis Jr., S. H. Messaddeq, Y. Ledemi, Y. Messaddeq, Appl. Phys. B **94**, 499 (2009)

[214] E. L. Falcão - Filho, C. B. de Araújo, C. A. C. Bosco, L. H. Acioli, G. Poirier, Y. Messaddeq, G. Boudebs, M. Poulain, J. Appl. Phys. **96**, 2525 (2004)

[215] G. Poirier, M. Poulain, Y. Messaddeq, S. J. L. Ribeiro, J. Non - Cryst. Solids **351**, 293 (2005)

[216] K. Fedus, G. Boudebs, Q. Coulombier, J. Troles, X.H.Zhang, J. Appl. Phys. **107**, 023108 (2010)

[217] L. Calvez, H.-L. Ma, J. Lucas, X.-H. Zhang, Adv. Mat. **19**, 129 (2007)

[218] L. Petit, N. Carlie, F. Adamietz, M. Couzi, V. Rodriguez, K. C. Richardson, Mat. Chem. Phys. **97**, 64 (2006)

[219] L. Petit, N. Carlie, K. Richardson, A. Humeau, S. Cherukulappurath, G. Boudebs, Opt. Lett. **31**, 1495 (2006)

[220] M. Guignard, V. Nazabal, A. Moreac, S. Cherukulappurath, G. Boudebs, H. Zeghlache, G. Martinelli, Y. Quiquempois, F. Smektala, J.-L. Adam, J. Non-Cryst. Solids **354**, 1322 (2008)

[221] C. Quemard, F. Smektala, V. Couderc, A. Barthelemy, and J. Lucas, J. Phys. Chem. Solids **62**, 1435 (2001)

[222] J.M. Harbold, F.O. Ilday, F.W. Wise, B.G. Aitken, IEEE Photon. Technol. Lett. **14** (6), 822 (2002)

[223] J.M. Harbold, F.O. Ilday, F.W. Wise, J.S. Sanghera, V.Q. Nguyen, L.B. Shaw, I.D. Aggarwal, Opt. Lett. **27**, 119 (2002)

[224] N. K. Sahoo, S. Thakur, R. B. Tokas, J. Phys. D: Appl. Phys. **39**, 2571 (2006)

[225] N. F. Nott and E. A. Davis, *Electronic Processes in Non-Crystalline Materials*, 2nd ed. (Oxford U. Press, Oxford, 1979)

[226] K. Morigaki, *Physics of Amorphous Semiconductor* (Imperial College Press, London, 1999)

[227] K. Tanaka, S. Nakayama, J. Opt. Adv. Mater. **2**, 5 (2000)

[228] G. A. Khan, C. A. Hogarth, J. Mat. Sci. **25**, 3002 (1990)

Année 2011
N° d'ordre : 1120

Développement des méthodes de mesures des non linéarités optiques du troisième ordre.

VERSION FRANÇAISE ABRÉGÉE

Spécialité : Physique

ÉCOLE DOCTORALE 3MPL (ED 500)

Matière, Molécules et Matériaux en Pays de Loire

Présentée et soutenue publiquement
Le 13 janvier 2011
à l'Université d'Angers

par **Kamil FEDUS**

Devant le jury ci-dessous:

Dominique BOSC, Rapporteur, *Ingénieur de Recherche (HDR), Université de Rennes 1*

Philippe GRELU, Rapporteur, *Professeur, Université de Bourgogne*

Cid B. de ARAUJO, Examinateur, *Professeur, Universidade Federal de Pernambuco*

Mathieu CHAUVET, Examinateur, *Professeur, Université de Franche-Comté*

Georges BOUDEBS, Directeur de thèse, *Maître de Conférences (HDR), Université d'Angers*

Laboratoire des Photonique d'Angers, EA4464, Université d'Angers, UFR Sciences,
2 Boulevard Lavoisier, 49045 ANGERS Cedex 01

Introduction Générale

Avec l'invention du laser en 1960 un domaine nouveau et fascinant de la recherche a été introduit dans la communauté scientifique : « l’optique non linéaire ». Historiquement, l'optique non linéaire a commencé avec les travaux expérimentaux de P.A. Franken *et al.* [1] qui en 1961 ont découvert le phénomène de la génération de la seconde harmonique. Après cette date, l'interaction de la lumière laser intense et cohérente avec la matière est devenue un sujet de recherche de pointe en raison de ses applications potentielles dans des domaines variés. Beaucoup de phénomènes nouveaux ont été découverts. En particulier, il a été constaté que dans la gamme des intensités lumineuses utilisées pour générer des effets optiques non linéaires, les paramètres optiques habituels des matériaux ne peuvent pas être considérés comme constants, mais sont eux-mêmes des fonctions de l'intensité lumineuse. Une grande partie des effets non linéaires peut être expliquée en se référant à des changements d'intensité dépendant de la réfraction et de l'absorption habituellement décrites par l'indice de réfraction non linéaire (n_2) et le coefficient d'absorption non linéaire (β), respectivement. Les effets non linéaires ont été utilisés pour de nombreuses applications pratiques, en particulier dans les dispositifs tout-optiques et électro-optiques utilisés dans les télécommunications, le stockage optique de l’information, les commutateurs optiques, la limitation optique, etc. La double dépendance à n_2 et β a une influence significative sur la performance des applications de certains appareils optiques. Par exemple, le coefficient n_2 est responsable des effets tels que l'auto-modulation de phase et l'auto-focalisation du faisceau laser. Ces deux phénomènes permettent de compenser la tendance naturelle de l'impulsion à la dispersion et à la diffraction créant en définitive des solitons spatio-temporels. C'est un grand pas vers la communication tout-optique. Cependant l'absorption non linéaire caractérisée par β peut réduire considérablement la puissance transmise par la fibre optique ou le guide d'onde. Une situation semblable a lieu pour toutes les applications en commutation optique où un grand n_2 et un petit β sont nécessaires pour la conception de commutateurs tout-optiques ultra-rapides qui peuvent remplacer leurs homologues électroniques relativement plus lents. Par ailleurs, dans le domaine de la limitation optique, les matériaux caractérisés par une forte absorption non linéaire sont souhaitables afin de construire des limiteurs optiques pour réduire la puissance lumineuse à l’entrée d’un système. Ainsi la connaissance de l'indice de réfraction non linéaire, n_2, et du coefficient d'absorption non linéaire, β, des matériaux est d'un grand intérêt en raison de leurs applications potentielles dans la conception de dispositifs optiques ultra-rapides.

En conséquence, diverses techniques pour déterminer les coefficients non linéaires ont été développées. Il s'agit notamment de la génération de la troisième harmonique, de l'interférométrie non linéaire (par exemple Michelson [2] ou Mach-Zender [3]), et l'ellipsométrie [4] [5], les techniques de mélange d'ondes (par exemple, mélange à trois ondes [6], mélange à quatre ondes [7]) et diverses méthodes utilisant la distorsion d'un faisceau (par exemple Z-scan [8], I-scan [9]). Toutes ces méthodes présentent des avantages et des inconvénients. En particulier, il s'agit de caractériser et de comparer la sensibilité de chaque méthode en tenant compte d'un rapport signal/bruit maximal. La question de la sensibilité est particulièrement importante dans le contexte de la caractérisation des couches minces. La nouvelle génération des circuits optoélectroniques intégrés, de plus en plus petits avec une vitesse de commutation de plus en plus élevée, s'oriente vers le développement de films minces. Les films minces considérés comme un système à deux dimensions sont d'une grande importance pour de nombreux problèmes pratiques. Le coût du matériau est relativement plus faible et ils remplissent la même fonction quand il s'agit de processus de surface. Ainsi, la détermination des propriétés des couches minces est-il un enjeu important car la connaissance précise de leurs caractéristiques peut être utile pour de futures applications. Dans le domaine de la caractérisation de couches minces en optique non linéaire, la tâche est difficile. La longueur d'interaction avec la lumière est très courte lorsque l'épaisseur du matériau est de l'ordre de plusieurs couches atomiques et, par conséquent, les effets optiques non linéaires générés sont très faibles. On pourrait accroître l'intensité lumineuse afin de renforcer le signal issu de la non-linéarité, mais un tel accroissement est limité par le seuil d'endommagement du matériau. Ce seuil est particulièrement faible pour les matériaux photosensibles. Il est donc nécessaire de disposer de méthodes de caractérisation très sensibles permettant de convertir une petite réponse non linéaire du matériau en une grande quantité mesurable sans pour autant détruire l'échantillon. Parmi les diverses techniques de caractérisation, la méthode Z-scan a été jugée particulièrement efficace dans la transformation des petits changements au niveau de la réfraction et l'absorption non linéaires en signaux détectables. Cette technique est devenue populaire et a été acceptée par la communauté scientifique pour réaliser les mesures de n_2 et β. Elle offre à la fois, la simplicité de la configuration optique et la possibilité de la détermination simultanée du signe et du type de la non-linéarité (réfraction ou absorption). En outre de nombreuses améliorations de la méthode Z-scan ont été proposées afin d'améliorer la sensibilité [10, 11, 12, 13, 14, 15, 16, 17, 18]. En particulier la méthode 'Z-scan éclipsé' (EZ-scan pour Eclipsed Z-scan) [19] a été introduite ; elle offre une sensibilité supérieure d'un ordre de grandeur par rapport à la méthode originale. Toutefois, une telle amélioration, impressionnante, se fait au détriment d'une réduction de la précision parce que le rapport signal sur bruit est sensiblement plus petit en éclipsant les mesures. En général, dans les expériences Z-scan, un équilibre doit être trouvé entre le signal non linéaire et l'amélioration de la sensibilité afin d'obtenir une précision satisfaisante [20].

G. Boudebs *et al.* [21, 22] ont introduit une technique d'imagerie non-linéaire (NIT) qui exploite les propriétés de filtrage d'un système d'imagerie 4*f* cohérent. Il a été démontré qu'il est possible de caractériser les non-linéarités en analysant le profil d'intensité de l'image acquise par une caméra CCD, après filtrage non linéaire à travers le matériau placé dans le plan de Fourier de la configuration. La comparaison de l'image expérimentale avec sa simulation numérique conduit aux coefficients non linéaires de l'échantillon étudié. Différents objets comme les fentes d'Young [21], le profil gaussien, l'objet rectangulaire [23] et l'objet de phase [24] ont été proposés à l'entrée du système 4*f* afin d'optimiser la caractérisation non linéaire. En particulier l'utilisation des objets de phase (PO) permet d'obtenir une sensibilité comparable à Z-scan. Dans cette thèse, les techniques d'imagerie non linéaires sont généralisées par l'introduction du mélange multi-ondes à l'intérieur de la configuration 4*f*. En outre, nous montrons qu'en choisissant un objet approprié à l'entrée et un filtre spatial correspondant dans le plan image il est possible d'effectuer diverses expériences connues, comme le mélange quatre ondes (DFWM), Z-scan, EZ-scan et I-scan. Un seul dispositif expérimental pour toutes ces techniques nous permettra de comparer leur sensibilité optique. En outre, nous montrons qu'en définissant le signal mesuré d'une manière appropriée, l'optimisation de la sensibilité peut être accompagnée d'une augmentation du rapport signal sur bruit. Par suite, les conditions optimales pour les mesures seront établies pour chaque méthode afin de tenter et faciliter la caractérisation de couches minces.

La deuxième partie de notre étude porte sur la caractérisation des échantillons minces. En particulier, nous étudions la photosensibilité des films dans le cadre de la caractérisation non linéaire. Les effets photo-induits (PIE) tels que l'ablation ou le photo-noircissement peuvent être compris comme une destruction de l'échantillon ayant entraîné une modification permanente de la réfraction et de l'absorption au niveau de la matière. Ces modifications se produisent lorsque l'échantillon est irradié par des intensités au-dessus du seuil de dommage. Cependant, les fortes intensités sont parfois indispensables afin d'induire une réponse (y compris parfois une diffraction linéaire sur la zone d'impact après ablation), en particulier dans les couches minces. Comme nous le montrons dans cette thèse, les PIE affectent non seulement la caractérisation non linéaire, mais peuvent aussi imiter le signal non linéaire issu de la méthode Z-scan avec ses caractéristiques typiques faisant apparaître un maximum et un minimum dans le profil. Cela peut conduire à des résultats erronés pour la mesure de n_2 et β par cette méthode. Néanmoins, nous montrons qu'il est aussi possible d'exploiter cet effet dans un sens positif. Nous introduisons Z-scan comme une nouvelle technique à mettre en place pour caractériser les effets photo-induits dans les changements permanents au niveau de la réfraction et de l'absorption. Cela pourrait être particulièrement utile pour quantifier le processus d'écriture des guides ondes optiques. Ce dernier est largement étudié en tant que mécanisme potentiel permettant la réduction des coûts de fabrication des guides d'ondes [25]. Le guide pouvant être créé par les changements permanents de l'indice de réfraction linéaire induit localement le long du faisceau laser. La description quantitative d'un tel phénomène serait utile. Nous utilisons également la méthode Z-scan pour mesurer les propriétés optiques linéaires des couches minces transparentes. L'utilité de cette technique va bien au-delà domaine de l'optique non linéaire puisqu'il a été possible de mesurer l'épaisseur (ou l'indice de réfraction linéaire) d'un échantillon mince de profil rectangulaire.

La dernière partie de notre thèse est consacrée à la caractérisation optique non linéaire d'échantillons massifs. Tout d'abord nous procédons à des mesures absolues de réfraction non linéaire dans le disulfure de carbone (CS_2) et la silice fondue (SiO_2) pour trois longueurs d'ondes : 355 nm, 532 nm et 1064 nm. Ces deux matériaux sont souvent utilisés comme références pour calibrer les montages expérimentaux lors de la caractérisation non linéaire. Pour obtenir des valeurs de n_2 plus précises que celles utilisées depuis quelques dizaines d'années, nous combinons Z-scan à l'intérieur du système $4f$ avec la méthode d'obturation Kerr (Kerr shutter) afin d'analyser avec précision le profil spatio-temporel du faisceau pompe. Les valeurs absolues ainsi obtenues pour n_2 sont comparées à ceux déjà rapportés dans la littérature. Une discussion à la lumière des théories de dispersion de l'indice de réfraction non linéaire en fonction de la longueur d'onde sera réalisée. Enfin, nous présentons les caractérisations optiques linéaires et non linéaires de nouvelles familles de verres en chalcogénures (GeS_2-Sb_3S_2-CSI) et des verres d'oxydes à base de métaux lourds ($Pb(PO_3)$ 2-WO_3). Les verres en chalcogénures sont des matériaux vitreux inorganiques qui contiennent toujours un ou plusieurs éléments chalcogènes: S, Se ou Te, mais pas d'oxygène (contrairement à des verres d'oxydes). Les verres chalcogénures sont bien connus pour posséder une grande réfraction linéaire et non linéaire associée à une transparence dans l'infrarouge. Les verres d'oxydes à base des métaux lourds sont intéressants en raison d'une absorption non linéaire relativement faible, en particulier dans le domaine infrarouge. Avec un indice n_2 dix fois plus élevé que celui de la silice fondue, ces verres sont des candidats potentiels pour des applications dans les télécommunications. Les résultats obtenus pour les deux familles de verres sont comparés dans le contexte des applications en commutation et traitement tout-optique du signal. En outre, un modèle théorique introduit par Boling et. al. [26] (que l'on appelle BGO) est adopté afin de prédire le coefficient non linéaire à partir des données expérimentales caractéristiques en optique linéaire. Il est très important d'avoir des expressions théoriques permettant de prédire l’importance des non-linéarités et donc, facilitant le choix de la composition du verre en fonction des propriétés optiques souhaitées. Comme nous le montrons dans cette thèse, le modèle BGO peut fournir des prédictions correctes pour les deux familles des verres que nous avons examinés.

1. Sensibilité des techniques de caractérisation non linéaire à l'intérieur du système d'imagerie 4*f*

Dans ce chapitre, nous montrons qu'il est possible de combiner le processus du mélange quatre ondes avec la technique Z-scan à l'intérieur du système 4*f*. De plus nous démontrons qu'en changeant l'objet à l'entrée et le diaphragme de champ dans le plan image (filtre spatial) (voir Fig. 1), il est possible d'effectuer différentes expériences bien connues telles que le mélange multi ondes dégénérées (DFWM [7]), Z-scan [8], Z-scan éclipsé (EZ-scan [19]), I-scan ou la technique d'imagerie non linéaire avec un objet de phase (NIT-PO [24]). Nous établissons que toutes ces techniques peuvent être considérées comme des cas particuliers d'un même processus d'imagerie non linéaire. Une telle unification des méthodes de caractérisation non linéaire nous permet de comparer leur sensibilité optique. L'optimisation des mesures dans chaque cas est proposée en maximisant le rapport signal/bruit. Les résultats expérimentaux sont soutenus par un modèle numérique simple basé sur l'optique de Fourier qui est décrit en détails dans [27, 28, 29].

1.1 Le mélange quatre ondes dégénéré utilisant Z-scan [27]

Cette section est basée sur nos résultats publiés Ref. [27]. Nous introduisons le mélange multi-ondes dans l'expérience Z-scan. Nous montrons qu'il est possible de simplifier le dispositif expérimental complexe du mélange quatre ondes (DFWM) en vue de caractériser les milieux non linéaires. Un objet composé de trois ouvertures circulaires est utilisé à l'entrée dans le système d'imagerie 4*f* comme le montre la Fig. 1. Dans la région du plan focal de la lentille L_1, le phénomène d'interférence crée une combinaison de réseaux de diffraction circulaire et sinusoïdale à l'intérieur du milieu non linéaire. En supposant une réponse instantanée du milieu, l'auto-diffraction du spectre sur ce réseau induit génère d'autres faisceaux à la sortie de l'échantillon. Par conséquent, dans le plan image, nous obtenons une multitude d'ordres diffractés comme on peut le voir sur la Fig. 2. Dans la figure 2 (a) nous pouvons voir l'image expérimentale acquise par la caméra CCD (en présence de CS_2) tandis que la figure 2 (b) montre la simulation numérique dans les mêmes conditions expérimentales (pour plus de détails, voir Réf.[27]). Deux filtres spatiaux sont utilisés alternativement dans le plan de l'image comme cela est montré dans la figure 1. Le premier filtre arrête tous les faisceaux, sauf la quatrième onde diffractée et le second filtre bloque seulement l'image géométrique de l'objet en vue d'acquérir l'ensemble des faisceaux diffractés.

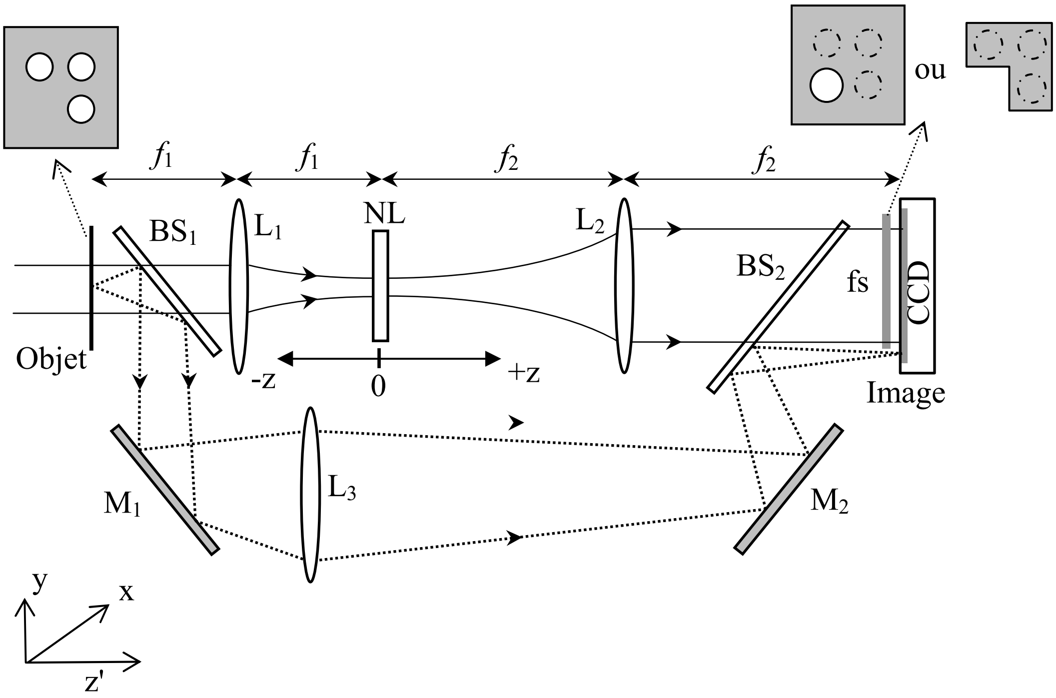

Fig. 1 Schéma du système imageur 4f utilisé pour le mélange multi-ondes. L'échantillon est situé dans la région focale : lentilles convergentes (L_1-L_3); miroirs (M_1, M_2); lames semi transparentes (BS_1, BS_2); milieu non linéaire (NL), filtre spatial (fs).

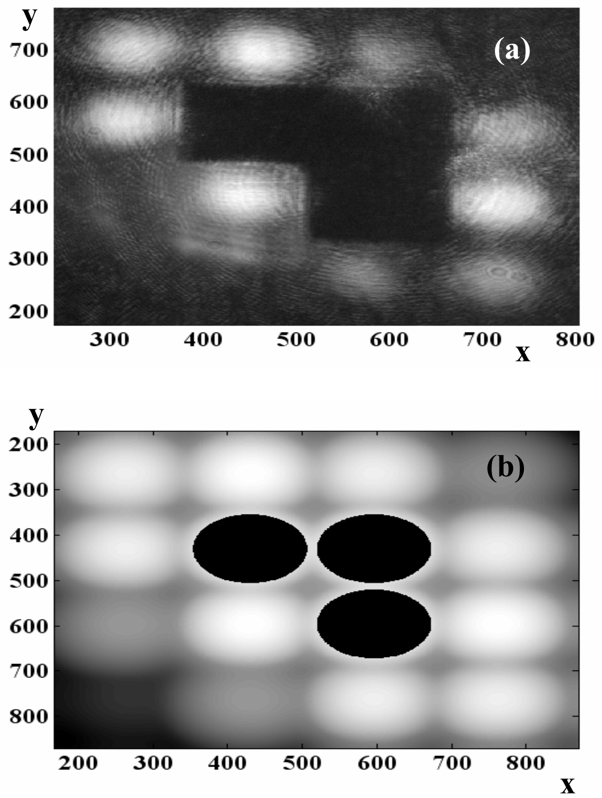

Fig. 2 Comparaison entre les images de l'acquisition expérimentale (a) et celle calculée numériquement (b). Le motif en forme de "L" apparaissant dans (a) est le filtre spatial (fs) dans la figure 1. Les coordonnées x et y sont exprimées en nombre de pixels et le logarithme népérien est utilisé pour accentuer les faibles intensités.

Pour décrire quantitativement l'énergie diffractée en régime non linéaire dans le plan image, nous définissons le rendement de diffraction comme étant la quantité à mesurer:

$$\eta = \frac{\left(E_{\mathrm{DNL}} - E_{\mathrm{DL}}\right)}{E_{\mathrm{TOT}}} , \tag{1}$$

où E_{DNL} est l'énergie diffractée en régime non linéaire (avec une forte intensité laser), E_{DL} est l'énergie diffractée en régime linéaire (avec une faible intensité laser) et E_{TOT} est l'énergie totale détectée dans le régime non linéaire sans filtre spatial à la sortie. Lorsque le matériau non linéaire est déplacé autour du foyer (en fonction de z) nous observons les variations de l'énergie de la quatrième onde à la sortie ainsi que cette variation pour toutes les autres ondes diffractées. Les acquisitions expérimentales et les simulations numériques correspondantes représentant le rendement de diffraction en fonction de z, sont présentées dans la figure. 3.

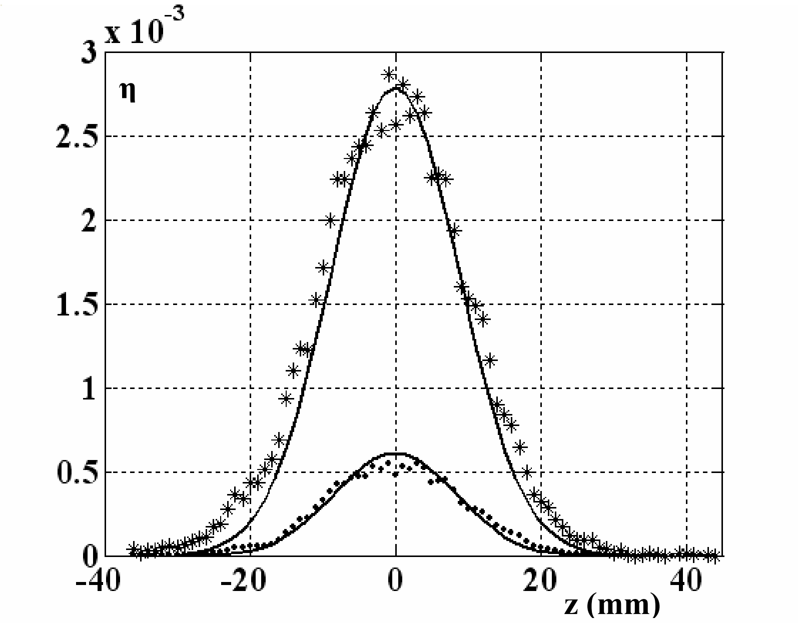

Fig. 3 Acquisitions expérimentales (points en étoiles: pour toutes les ondes diffractées et points circulaires: pour un seul faisceau diffracté) et simulations numériques (trait plein) représentant le rendement de diffraction en fonction de z, la position de l'échantillon dans le plan focal du système.

En nous basant sur la simulation numérique, nous avons pu constater que l'efficacité de diffraction est indépendante des paramètres géométriques de l'objet. En outre dans le régime faiblement non linéaire ($\Delta\Phi_0 < 1$) et pour un milieu non absorbant (*i.e.* $\beta = 0$), nous avons trouvé une expression quadratique simple reliant le rendement de diffraction au maximum du déphasage non linéaire:

$$\eta = 2.41 \times |\Delta\Phi_0|^2 \times 10^{-2} \tag{2}$$

où $\Delta\Phi_0 = 2\pi n_2 I_0/\lambda$ est le déphasage non linéaire sur l'axe optique avec λ désignant la longueur d'onde et I_0 est l'intensité pic dans le plan focal ($z = 0$). Pour un faisceau diffracté $\eta = 5.13 \times |\Delta\Phi_0|^2 \times 10^{-3}$. La sensibilité de la méthode est définie comme la pente de la courbe donnant le signal (η) en fonction de $\Delta\Phi_0$ [8]: i.e. $d\eta/d\Delta\Phi_0$. Il est facile de constater qu'en utilisant tous les faisceaux diffractés la sensibilité est accrue d'un facteur $2.41/0.513 \approx 5$.

1.2 La sensibilité des techniques en mélange multi-ondes dans une configuration I-scan [28]

Cette section se rapporte aux résultats publiés dans la Réf. [28]. Nous analysons l'influence de différents objets sur la sensibilité du système 4*f* en l'absence d'absorption (i.e. $\beta = 0$). L'échantillon est placé au foyer ($z = 0$) où le maximum du signal non linéaire est obtenu. Nous considérons des objets composés d'une deux, trois et quatre ouvertures circulaires (toutes les ouvertures ayant le même rayon R). Dans la figure 4 (a) on peut voir les images simulées pour tous les objets. On peut distinguer la diffraction d'ordre zéro autour des images géométriques des ouvertures où les filtre spatial éclipsant les images géométriques est placé. En outre, nous pouvons remarquer que, pour un nombre croissant d'ondes incidentes, les faisceaux diffractés sont plus intenses (ordres de diffraction supérieur). Dans la figure 4 (b), nous pouvons voir la variation du rendement de diffraction par rapport à *a*, le rayon des disques opaques en sortie (filtre spatial). Il est évident que, quel que soit l'objet, le signal maximal est obtenu pour $a = R$, quand le filtre spatial bloque exactement l'image géométrique de l'objet. Par ailleurs, le signal le plus élevé est obtenu pour un objet avec ouverture circulaire unique.

Pour chaque objet, nous avons obtenu la relation quadratique entre le signal (η) et l'entrée $\Delta\Phi_0$ dans deux cas pour $a = R$ et $a = 2R$. Dans le premier cas pour nous obtenons:

i) Ouverture circulaire unique (top-hat beam): $\eta_1(R) = 9.8 \times |\Delta\Phi_0|^2 \times 10^{-2}$

ii) 2 ouvertures circulaires: $\eta_2(R) = 7.5 \times |\Delta\Phi_0|^2 \times 10^{-2}$

iii) 3 ouvertures circulaires: $\eta_3(R) = 5.4 \times |\Delta\Phi_0|^2 \times 10^{-2}$

iv) 4 ouvertures circulaires: $\eta_4(R) = 5.3 \times |\Delta\Phi_0|^2 \times 10^{-2}$

Ces résultats indiquent que la plus haute sensibilité $(d\eta / d\Delta\Phi_0)$ est obtenue pour un objet composé d'une ouverture circulaire unique lorsque le rapport signal sur bruit est maximum.

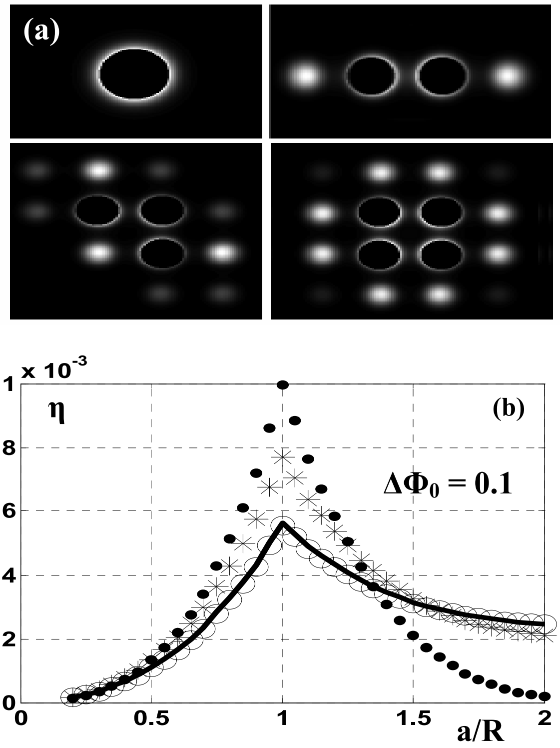

Fig. 4 (a) Simulation numérique montrant les images des faisceaux diffractés avec des objets composés d'une deux, trois et quatre ouvertures circulaires. Les filtres spatiaux adaptés apparaissent en noir dans le plan de l'image. Le rendement de diffraction (b) en fonction du rayon normalisé du disque opaque; les points en cercles pleins, en étoiles, en cercles vides et en trait plein sont pour une, deux, trois et quatre ouvertures, respectivement.

L'alignement optique du filtre spatial est plus facile lorsque le rayon des disques éclipsant est plus élevé que le rayon des ouvertures à l'entrée. La simulation numérique pour $a = 2R$ a donné les résultats suivants:

i) Ouverture circulaire unique (top-hat beam): $\eta_1(2R) = 0.2 \times |\Delta\Phi_0|^2 \times 10^{-2}$

ii) 2 ouvertures circulaires: $\eta_2(2R) = 2.1 \times |\Delta\Phi_0|^2 \times 10^{-2}$

iii) 3 ouvertures circulaires: $\eta_3(2R) = 2.4 \times |\Delta\Phi_0|^2 \times 10^{-2}$

iv) 4 ouvertures circulaires: $\eta_4(2R) = 2.4 \times |\Delta\Phi_0|^2 \times 10^{-2}$

Dans ce cas, les résultats indiquent que la sensibilité augmente avec le nombre des ondes (ouvertures circulaires) et atteint une valeur asymptotique lorsqu'il y a plus de trois ouvertures circulaires. Enfin, afin de valider nos simulations numériques, nous avons également effectué des acquisitions expérimentales. Dans la figure. 5, nous pouvons voir la variation du rendement de la diffraction mesuré expérimentalement en fonction du déphasage non linéaire obtenue avec le CS_2 et objet composé de trois ouvertures circulaires (de rayon R) où l'image est éclipsée par trois disques ayant des rayons $a = 2R$. Le fit numérique des points expérimentaux donne exactement la même relation quadratique ($\eta_3(2R) = 2.4\times|\Delta\Phi_0|^2\times10^{-2}$) que celle obtenue dans notre simulation, validant ainsi l'ensemble de notre étude numérique.

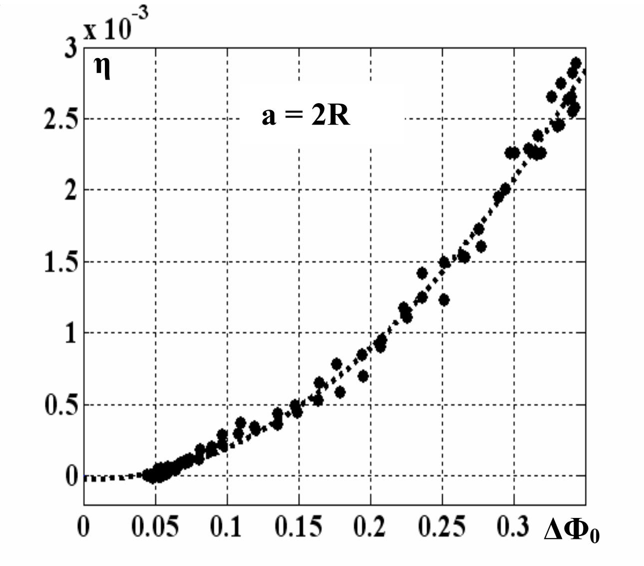

Fig. 5 Rendement de diffraction expérimentale (η) en fonction du déphasage non linéaire ($\Delta\Phi_0$) obtenu avec un objet composé de trois ouvertures circulaires et un filtre spatial de rayon $a = 2R$. La courbe en pointillé est la simulation numérique.

1.3 Mélange multi-ondes en présence de l'absorption non linéaire [29]

Cette section est basée sur les résultats publiés dans la réf. [29]. Nous analysons l'influence de l’absorption linéaire et non linéaire sur le processus du mélange multi-ondes à l'intérieur du système $4f$ comme cela a été décrit dans les deux paragraphes précédents. Nous présentons les calculs analytiques montrant que les effets de réfraction et d'absorption non linéaire peuvent contribuer au signal des faisceaux diffractés. En outre les calculs numériques sont effectués afin de comparer la sensibilité de la technique I-scan en mélange multi-ondes en l'absence et en présence d'absorption (pour plus de détails, voir la thèse en anglais ou Réf. [29]).

Grâce aux calculs numériques, nous avons constaté que les faibles effets non linéaires d'absorption ($i.e. \gamma = \beta\lambda / 4\pi n_2 < 1$) peuvent être inclus dans la description du mélange des ondes en remplaçant $\Delta\Phi_0$ dans toutes les relations quadratiques fournies dans la section précédente par un déphasage non linéaire effectif généralisé défini de la façon suivante :

$$\Omega = \left(1 + \gamma^2\right)^{1/2} \Delta\Phi_0^{\mathrm{eff}} \tag{3}$$

où $\Delta\Phi_0^{\mathrm{eff}}$ peut être considéré comme le déphasage non linéaire effectif dans le plan focal:

$$\Delta\Phi_0^{\mathrm{eff}} = \frac{2\pi}{\lambda} n_2 L_{\mathrm{eff}} I_{\mathrm{eff}} \left(z = 0\right). \tag{4}$$

Dans cette expression, $L_{\mathrm{eff}} = \left(1 - e^{-\alpha L}\right) / \alpha$ représente l'épaisseur effective de l'échantillon et tient compte de l'absorption linéaire défini par le coefficient $\alpha(\mathrm{m}^{-1})$, tandis que $I_{\mathrm{eff}}\left(z = 0\right) = I_0 \ln\left(1 + q_0\right) / q_0$ représente l'intensité efficace compte tenu de l'absorption linéaire et non linéaire. Ici $q_0 = \beta L_{\mathrm{eff}} I_0$ avec I_0 désignant l'intensité sur l'axe et dans le plan focal. Toutes les relations quadratiques qui devraient être utilisées pour caractériser n_2 en présence de l'absorption sont résumées dans le tableau 1. La colonne 2 indique les expressions valables lorsque le rayon des disques opaques composant le filtre spatial (placé à la sortie du système) est égal au rayon R des ouvertures circulaires composant l'objet. Dans la colonne 3, nous pouvons trouver les relations valables lorsque $r = 2R$ (avantageux pour faciliter l'alignement optique).

Objet	$r = R$	$r = 2R$
Une ouverture circulaire	$\eta = 9.8 \times \Omega^2 \times 10^{-2}$	-
2 ouvertures circulaires	$\eta = 7.5 \times \Omega^2 \times 10^{-2}$	$\eta = 2.1 \times \Omega^2 \times 10^{-2}$
3 ouvertures circulaires	$\eta = 5.4 \times \Omega^2 \times 10^{-2}$	$\eta = 2.4 \times \Omega^2 \times 10^{-2}$
4 ouvertures circulaires	$\eta = 5.3 \times \Omega^2 \times 10^{-2}$	$\eta = 2.4 \times \Omega^2 \times 10^{-2}$

Tab.1 Relations quadratiques reliant η, le rendement de diffraction à Ω ,le déphasage non linéaire effectif généralisé avec différent objets à l'entrée (composés d'un, deux, trois ou quatre ouvertures circulaires).

Ces relations quadratiques simples ont une conséquence intéressante pour l'évaluation de la sensibilité des techniques de mélange multi-ondes. Pour la réfraction non linéaire pure la sensibilité est définie par $d\eta / d\Delta\Phi_0$. Dans un cas plus général, lorsque l'absorption est présente et parce que la contribution au signal est due à la fois aux effets produits par l'absorption et la réfraction non linéaires, nous devrions utiliser comme entrée Ω. Aussi la généralisation de la sensibilité est-elle : $d\eta/d\Omega$. De par cette définition et compte tenu des relations dans le tableau 1, on peut facilement constater que l'absorption non linéaire n'affecte pas la sensibilité des techniques du mélange multi-ondes par rapport aux cas équivalents avec de la réfraction non linéaire pure.

1.4 Faisceau gaussien en utilisant la configuration I-scan [28]

Cette section est fondée sur les résultats publiés dans la réf. [28]. Nous y considérons un faisceau gaussien à l'entrée du système de 4*f* et un échantillon placé dans le plan focal (voir Fig. 6). Dans ce cas, l'objet est défini par $E_0 \exp\left[-\left(x^2+y^2\right)/w_e^2\right]$, où E_0 désigne l'amplitude sur l'axe optique du champ électrique et w_e (le 'beam-waist') est la taille du faisceau à l'entrée de l'installation (dans le plan de l'objet). La question ici est de savoir quel est le filtre spatial optimisé dans ce cas. La symétrie circulaire du faisceau à l'entrée impose un filtre spatial circulaire à la sortie. L'extension spatiale du champ supposé gaussien étant théoriquement infinie, la question revient à trouver le rayon de cette ouverture ou du disque circulaires afin d'augmenter le signal optique pour un bruit donné dans le système.

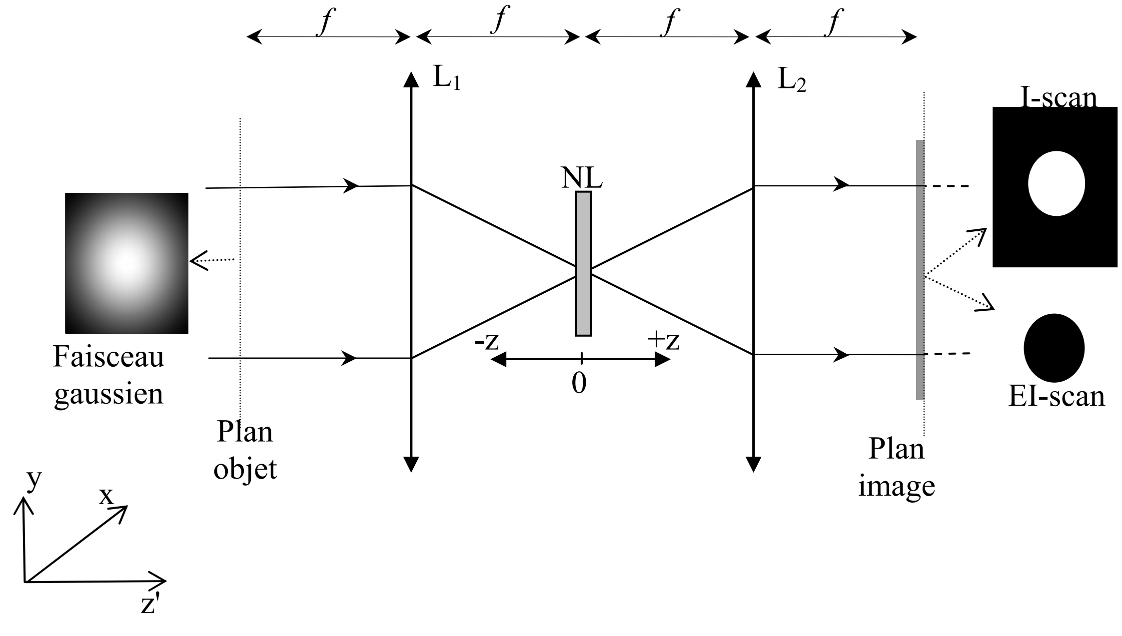

Fig. 6 Faisceau gaussien à l'entrée du système 4f. Une ouverture circulaire ou un disque opaque est placé dans le plan de l'image pour obtenir la configuration en I-scan ou EI-scan, respectivement.

La fraction de la lumière transmise par l'ouverture ou bloquée par le disque est définie dans [8]: $S = 1 - \exp(-2r_a^2 / \omega_a^2)$, où r_a est le rayon de l'ouverture ou du disque et ω_a est le *beam-waist* à la sortie dans le plan de l'ouverture ou du disque et mesuré dans le régime linéaire. Ce *beam-waist* à la sortie est physiquement égal à celui à l'entrée, $\omega_a = \omega_e$, car le grossissement du système imageur considéré est l'unité. Grâce à des calculs numériques (pour plus de détails, voir Ref. [28]) nous avons montré que le maximum de l'efficacité de diffraction peut être obtenu en plaçant dans le plan image une ouverture circulaire ou un disque ayant un rayon $r_a \approx w_a$. La transmission linéaire en intensité d'une telle ouverture (ou la quantité de lumière bloquée par le disque) est égale à $S_{\max} \approx 0.89$. Pour ce filtre spatial optimisé, nous avons obtenu la relation suivante qui peut être utilisée pour déterminer la valeur de n_2:

$$\eta_{(S_{\max} = 0.89)} = 7.0 \times |\Delta\Phi_0|^2 \times 10^{-2} \tag{5}$$

1.5 Z-scan et EZ-scan utilisant le rendement de diffraction [30]

Cette section repose sur les résultats publiés dans la Réf. [30]. Nous considérons le système 4*f* avec un faisceau gaussien à l'entrée et une ouverture circulaire ou un disque opaque à la sortie comme dans le paragraphe précédent (voir Fig. 6), mais cette fois, l'échantillon n'est plus fixe dans le plan focal ; sa position est définie dans la région focale en fonction de z. Cette configuration du système 4*f* correspond au Z-scan classique [8] avec une ouverture circulaire et EZ-scan [19] avec un disque d'obscurcissement. Dans ce cas particulier, nous avons défini le rendement de diffraction par :

$$\eta' = \frac{\varepsilon_{\mathrm{DNL}}}{\varepsilon_{\mathrm{TNL}}} - \frac{\varepsilon_{\mathrm{DL}}}{\varepsilon_{\mathrm{TL}}}, \tag{6}$$

où $\varepsilon_{\mathrm{DNL}}$ et $\varepsilon_{\mathrm{DL}}$ sont les énergies à l'intérieur de l'ouverture ou à l'extérieur du disque opaque dans les régimes non linéaire et linéaire, respectivement. Tandis que $\varepsilon_{\mathrm{TNL}}$ et $\varepsilon_{\mathrm{TL}}$ représentent l'énergie totale dans le plan de l'image dans les régimes non linéaire et linéaire, respectivement. L'Eq. (6) peut être utilisée à la place de l'Eq. (1) dans tous les cas étudiés dans les paragraphes précédents. Ici la soustraction des acquisitions en régime linéaire ($\varepsilon_{\mathrm{DL}}/\varepsilon_{\mathrm{TL}}$) de celles obtenues en régime non linéaire ($\varepsilon_{\mathrm{DNL}}/\varepsilon_{\mathrm{TNL}}$) est appliquée pour réduire le bruit dû aux imperfections de l'objet comme cela a été proposé dans la méthode originale de Z-scan.

Les résultats expérimentaux et numériques montrent que l'allure classique du profil Z-scan, avec une caractéristique pic-vallée du signal mesuré, est préservée. Mais $\Delta\eta_{\mathrm{pv}}$, la différence entre le maximum (pic) et le minimum (la vallée) du signal est exactement la même pour Z-scan et EZ-scan. La sensibilité des deux méthodes se trouve être la même pour la même taille de l'ouverture ou du disque si l'on considère le rendement de diffraction défini dans l'Eq. (6) comme le signal à mesurer. Par ailleurs on obtient le $\Delta\eta_{pv}$ le plus important (et donc le rapport signal/bruit le plus grand) pour S = 0,7.

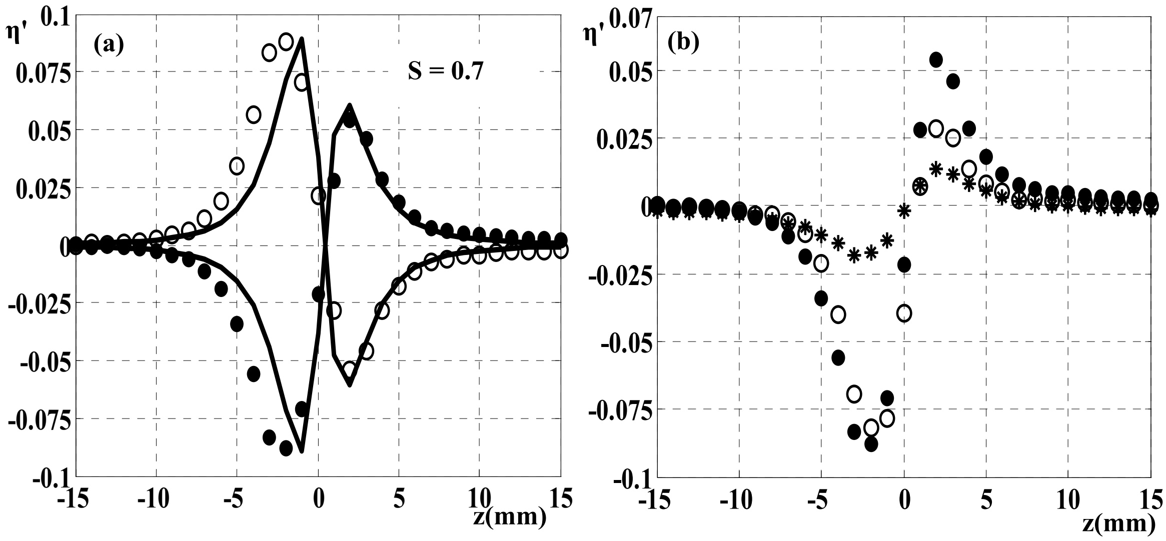

Fig. 7 (a) Comparaison expérimentale de Z-scan (cercles pleins) et EZ-scan (cercles vides) en présence de CS_2 dans les mêmes conditions expérimentales utilisant le rendement de diffraction pour S = 0,7. Les lignes continues sont les simulations numériques correspondantes. (b) Comparaison des acquisitions expérimentales Z-scan obtenues à partir de l'Eq. (6) avec $S = 0.1$ (étoiles), $S = 0.7$ (cercles pleins) et $S = 0.86$ (cercles vides).

Nous avons calculé numériquement que, $\Delta\eta_{pv}$ dépend linéairement de $|\Delta\Phi_0| \leq \pi$ pour $S \leq 0.7$ par l'intermédiaire de l'équation suivante (avec une précision de 5%):

$$\Delta\eta_{pv} = 0.44S\left[\cosh(1-S)-1\right]^{0.14}|\Delta\Phi_0|, \quad (7)$$

En outre, nous montrons que le signal obtenu caractérisant la réfraction non linéaire lorsqu'on utilise le rendement de diffraction est moins sensible à la présence de l'absorption non linéaire. La figure 8 compare l'aspect du profil utilisant le rendement de diffraction (cercles noirs) avec la transmission normalisée du Z-scan classique (étoiles), pour un échantillon en chalcogénures présentant de l'absorption non linéaire. Le profil du Z-scan classique $\varepsilon_{DNL}/\varepsilon_{DL}$ présente une forme typique en présence d'absorption à deux photons: une vallée renforcée et un pic supprimé [8]. Tandis que la trace obtenue avec le rendement de diffraction conserve très bien la configuration symétrique du 'pic-vallée'.

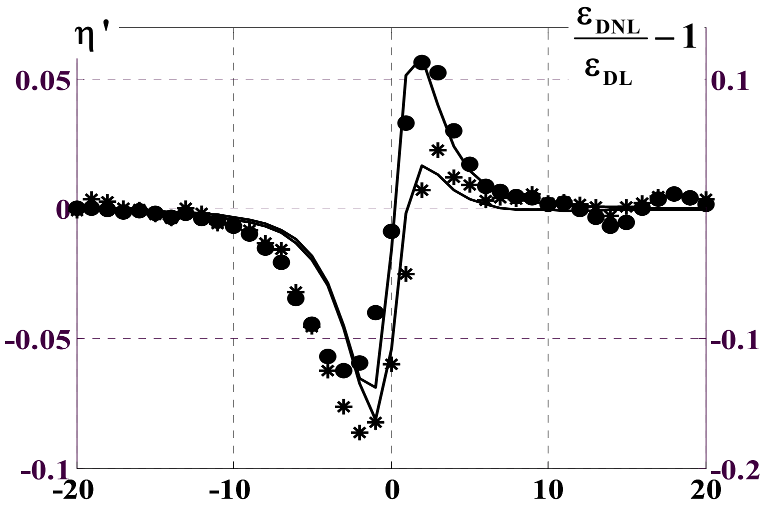

Fig. 8 Transmission normalisée d'un profil expérimental de Z-scan classique (étoiles) et tenant compte du rendement de diffraction (cercle pleins) pour un échantillon ayant une absorption non linéaire non négligeable. Les lignes continues sont les simulations numériques correspondantes.

1.6 Sensibilité de la NIT-PO avec le rendement de diffraction

Dans cette section, nous considérons l'expérience NIT-PO décrite dans la Réf. [24]. L'objet de phase (représenté sur la figure 9.) est placé à l'entrée du système 4*f* et il n'y a pas de filtre spatial dans le plan image.

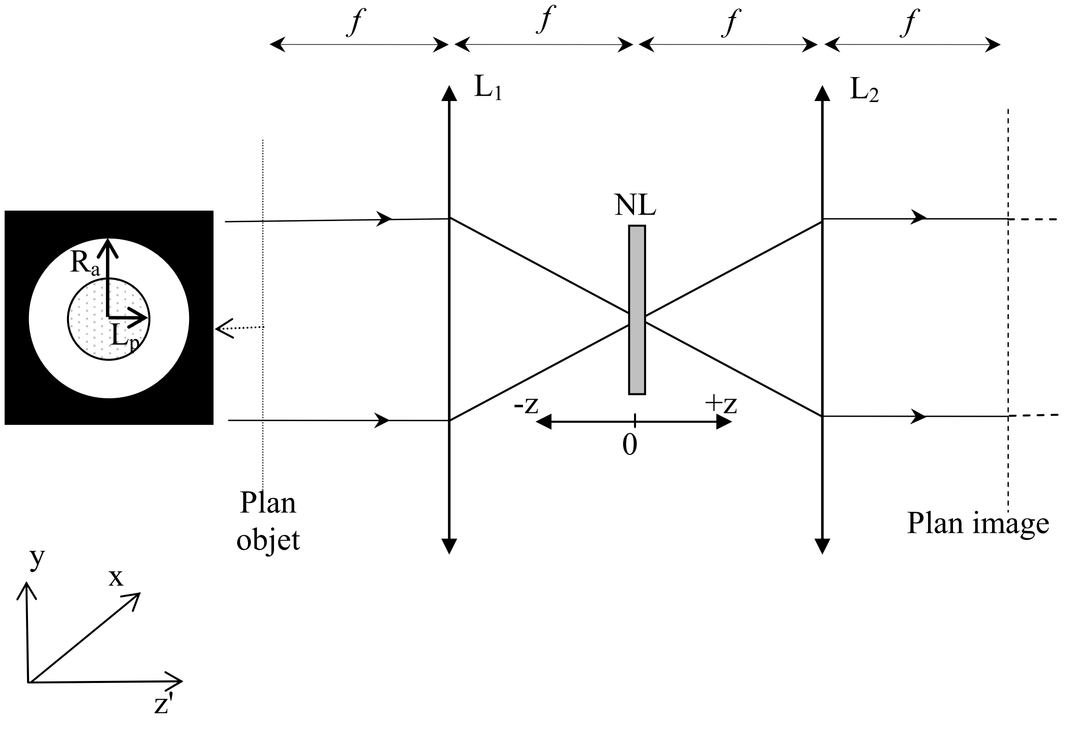

Fig. 9 Objet de phase à l'entrée du système 4f.

L'objet est composé d'une plaque de verre circulaire de rayon R_a sur laquelle un disque diélectrique transparent (de rayon $\mathrm{L_p}$) a été déposé. Le disque a une épaisseur et un indice de réfraction retardant la phase de la lumière incidente de $\Delta\phi_L$ par rapport à celle en dehors du disque. Le rendement de la diffraction est défini comme le rapport entre l'énergie à l'intérieur de la plaque de phase et de l'énergie totale dans le plan de l'image. Les calculs numériques (pour plus de détails, voir la thèse en anglais) montrent que l'efficacité de diffraction est optimisée pour $L_p/R_a \approx 0{,}75$ et $\Delta\phi_L = 0.5\pi$ pour une non-linéarité négative ($\Delta\Phi_0 < 0$) alors que $\Delta\phi_L = 1.5\pi$ pour non-linéarité positive ($\Delta\Phi_0 > 0$). Dans ces conditions la relation suivante est satisfaite pour $|\Delta\Phi_0| < 1$:

$$\eta' \ = \ 0.22 \times |\Delta\Phi_0| \tag{8}$$

Cette relation est quasiment indépendante de l'absorption non linéaire.

1.7 Conclusions

En considérant des faibles non linéarités, parmi toutes les configurations considérées dans le système 4*f*, nous montrons que la sensibilité la plus élevée ($d\eta/d\Delta\Phi_0$ ou $d\Delta\eta_{pv}/d\Delta\Phi_0$), tout en maximisant le rapport signal sur bruit, est obtenue avec Z-scan (EZ-scan) et les techniques d'imagerie introduisant un objet de phase à l'entrée (NIT-PO). Par conséquent nous retiendrons ces deux méthodes en tant que les plus appropriées pour la caractérisation des échantillons sous forme de film mince, où la longueur d'interaction optique est très faible.

2. Les effets photo-induits lors de la caractérisation en optique non linéaire

Ce chapitre est principalement consacré à la caractérisation optique des couches minces par Z-scan et la technique NIT-PO. En particulier, nous discutons l'influence des effets photo-induits (PIE) sur les mesures d'indices de réfraction non linéaires et des coefficients d'absorption non linéaire. Nous entendons par PIE la modification de la structure physico-chimique de l'échantillon conduisant à des modifications permanentes de la réfraction et l'absorption. Nous employons la technique Z-scan pour analyser ces changements permanents de l'indice de réfraction (Δn_0) et du coefficient d'absorption ($\Delta\alpha_0$). En outre, nous appliquons Z-scan pour la caractérisation des paramètres optiques linéaires tels que l'épaisseur (L) et l'indice de réfraction (n_0) des films minces.

2.1 Les PIE avec objet de phase [31]

Cette section est basée sur les résultats publiés dans la Réf. [31]. Nous étudions la photosensibilité de verres amorphes en couches minces en chalcogénures de différentes compositions : $Ge_xAs_ySe_{1-x-y}$. Les paramètres linéaires optiques des échantillons étudiés sont résumés dans le tableau 2, dans les quatre premières colonnes.

Composition	**n_0 (à 1064 nm)**	**ε_g (eV), Tauc**	**L(nm)**	**I_{0T} (GW/cm^2)**	**ε_{pulse} (µJ)**
$Ge_{10}As_{40}Se_{50}$	2.79	1.65	1083	3.1	8.8
$Ge_{10}As_{35}Se_{55}$	2.77	1.70	1040	3.9	10.8
$Ge_{15}As_{30}Se_{55}$	2.71	1.71	941	2.9	8.3
$Ge_{10}As_{30}Se_{60}$	2.70	1.77	994	2.5	7
$Ge_{20}As_{20}Se_{60}$	2.62	1.81	820	4.7	13

Tab.2 Paramètres optiques des films minces en chalcogénures: n_0 indice de réfraction, E_g énergie du band gap, L épaisseur, I_{0T} intensité seuil des PIE, ε_{pulse} énergie correspondante.

Nous avons utilisé l'objet de phase à l'entrée du système 4*f* afin de trouver l'intensité à partir de laquelle la réponse non linéaire de l'échantillon devient détectable. Lorsque l'éclairement sur l'axe focal atteint la valeur seuil d'intensité (I_{0T}; donnée dans la colonne 5 du tableau 2), le contraste de phase semble montrer une image similaire à l'image non linéaire que l'on obtiendrait avec un effet Kerr optique. Cependant, en diminuant l'intensité à un niveau plus bas (pour se retrouver dans le régime linéaire), le contraste de phase reste marqué dans l'image. Ces observations expérimentales nous conduisent à la conclusion que les images modifiées devraient être liées à une détérioration du matériau qui a été mémorisée à l'intérieur de l'échantillon (voir Fig.10).

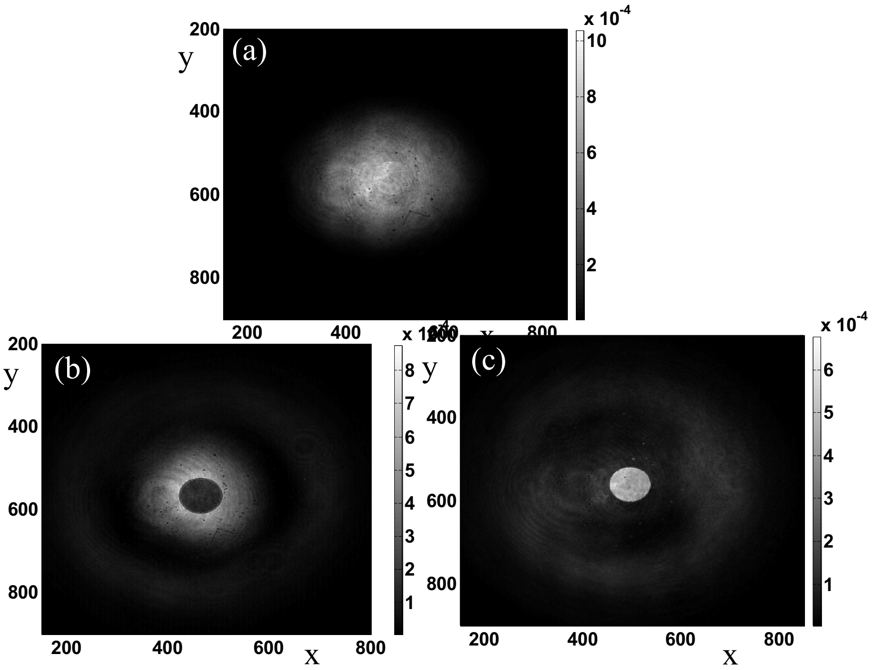

Fig. 10 Images expérimentales de l'objet de phase: (a) avant et après les PIE indiqués par un contraste négatif (b) et un contraste positif (c). La forme circulaire apparaissant au centre de l'image est l'objet de phase. Les coordonnées x et y sont exprimés en nombre de pixels.

Nous avons utilisé cet effet de contraste en étudiant sa dynamique en fonction du temps (nombre des tirs lasers dans l'échantillon) (pour plus de détails, voir Réf. [31]). Nous avons montré que la caractérisation non linéaire des échantillons étudiés est impossible dans notre système expérimental, car la longueur d'interaction non linéaire des couches minces est trop faible pour induire des signaux non linéaires mesurables avant de dépasser le seuil de l'intensité d'endommagement.

2.2 Les PIE avec Z-scan [32]

Cette section est fondée sur les résultats publiés dans la Réf. [32]. Nous avons étudié un verre chalcogénure en film mince de 4,8 µm d'épaisseur : Te20As30Se50. Ce film possède une non-linéarité suffisamment élevée pour induire un signal mesurable avec Z-scan. Cette exaltation des non linéarités de l'échantillon est probablement liée à l'effet de porteur libres au niveau de l'absorption ('free carrier absorption') [33, 34]. L'utilisation de l'objet de phase à l'entrée du système 4*f* (comme dans le paragraphe précédent), nous a permis d'estimer le seuil de dommage à une intensité devant se situer entre 1,2 GW/cm^2 et 2,0 GW/cm^2. Par ailleurs nous avons effectué des mesures Z-scan au-dessus de l'intensité de la valeur seuil (à $I_0 = 3.3\,\mathrm{GW/cm^2}$) afin de montrer l'influence des PIE sur les profils Z-scan. Trois différents balayages (scan) ont été fait dans trois régimes d'intensité différents: le premier en régime linéaire, le second en régime non linéaire et le dernier de nouveau en régime à faible intensité, en faisant attention à chaque fois d'éclairer l'échantillon dans la même zone d'impact.

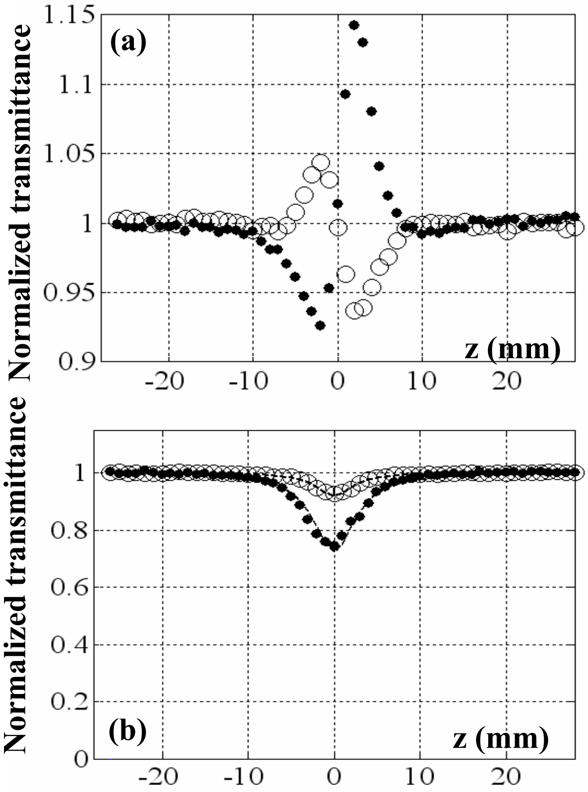

Fig. 11 Acquisitions expérimentales de profils Z-scan (a) diaphragme fermé et (b) diaphragme ouvert dans le régime non linéaire (points gras) obtenus avec une intensité $I_0 = 3.3$ GW/cm^2 plus élevée que le seuil d'endommagement du matériau. Les acquisitions dans le régime linéaire (cercles vides) révèlent les dégâts induits dans le film.

Les acquisitions dans le régime non linéaire révèlent une forme typique genre pic-vallée et masquent totalement la contribution des PIE (voir Fig. 11 (points en gras)). La comparaison des scans effectués en régime linéaire révèle les changements permanents dans la réfraction et l'absorption 'écrits' à l'intérieur de l'échantillon dans le régime non linéaire (voir figure. 11, cercles vides). Le tracé Z-scan sur la Fig. 11 (a) (cercles vides) indique que l'échantillon se comporte comme une lentille divergente agissant comme un matériau ayant un n_2 négatif [35]. Ce profil Z-scan peut être expliqué par la présence d'un trou dû à l'ablation de matière [(confirmé par les images AFM) lors du passage du film autour du point focal en régime non linéaire. Tandis que la diminution de la transmission autour du point (z = 0) comme le montre la figure. 11 (b) (cercles vides) peut être attribuée à l'effet photo-noircissement induit par la forte intensité.

2.3 Détermination des PIEs dans les coefficients optiques linéaires par Z-scan [36]

Cette section se rapporte aux résultats publiés dans la Réf. [36]. Nous y introduisons la technique Z-scan comme un outil pour caractériser les effets photo-induits à l'intérieur de matériaux photosensibles dans les cas de faibles déphasage (<1 rad) et photo-noircissement. Nous obtenons analytiquement et numériquement les relations permettant de faire des mesures directes dans le cas d'un profil gaussien permanent au niveau de l'indice de réfraction et du coefficient d'absorption. Tout d'abord, nous donnons les relations analytiques permettant de quantifier l'effet de photo-noircissement dans le profil Z-scan avec un diaphragme ouvert:

$$T_o(z) = \sum_{m=0}^{\infty} \frac{(-1)^m}{m!} \frac{(\Delta\alpha_0 L)^m}{\left(1+\mathrm{m}\left(1+\mathrm{z}^2/\mathrm{z}_0^2\right)\right)}, \tag{9}$$

où $\Delta\alpha_0$ est la photo-absorption induite sur l'axe optique et z_0 est la distance de Rayleigh du faisceau gaussien. Ensuite nous calculons numériquement et analytiquement la relation entre, la différence entre le maximum et minimum du profil Z-scan de la transmission normalisée et le changement permanent (relativement faible) de la réfraction au niveau de la phase sur l'axe optique $\Delta\Phi_0 = 2\pi\Delta n_0 L/\lambda < 1$ (pour une transmission linéaire du diaphragme en champ lointain vérifiant $S \le 0.5$):

$$\Delta T_{pv} = \frac{2}{3}(1-S)^{0.56}\Delta\Phi_0, \tag{10}$$

où Δn_0 est la variation de l'indice de réfraction sur l'axe optique. Cette relation simple peut être utilisée pour estimer Δn_0 en l'absence de changement d'absorption, directement à partir de tracés Z-scan. En présence de modifications faibles de l'absorption (photo-noircissement avec $\Delta\alpha_0 L \le \Phi_0$), nous avons vérifié numériquement que l'Eq. (10) peut être utilisée en divisant le tracé Z-scan à ouverture fermée par celui obtenu sans ouverture. Comme pour les mesures non linéaires [8], le résultat est un tracé Z-scan où le signal est le même (à moins de 5%) que celui obtenu à partir d'une réfraction pure.

Afin de confirmer l'analyse théorique, nous avons fait des expériences avec le verre massif As_2S_3. Nous avons effectué le processus d'écriture avec des intensités différentes (allant de 2 GW/cm^2 à 10 GW/cm^2) et différentes énergies cumulées (E_c allant de 1 mJ à 20 mJ) dans l'échantillon en plaçant ce dernier dans le plan focal du système 4*f*.

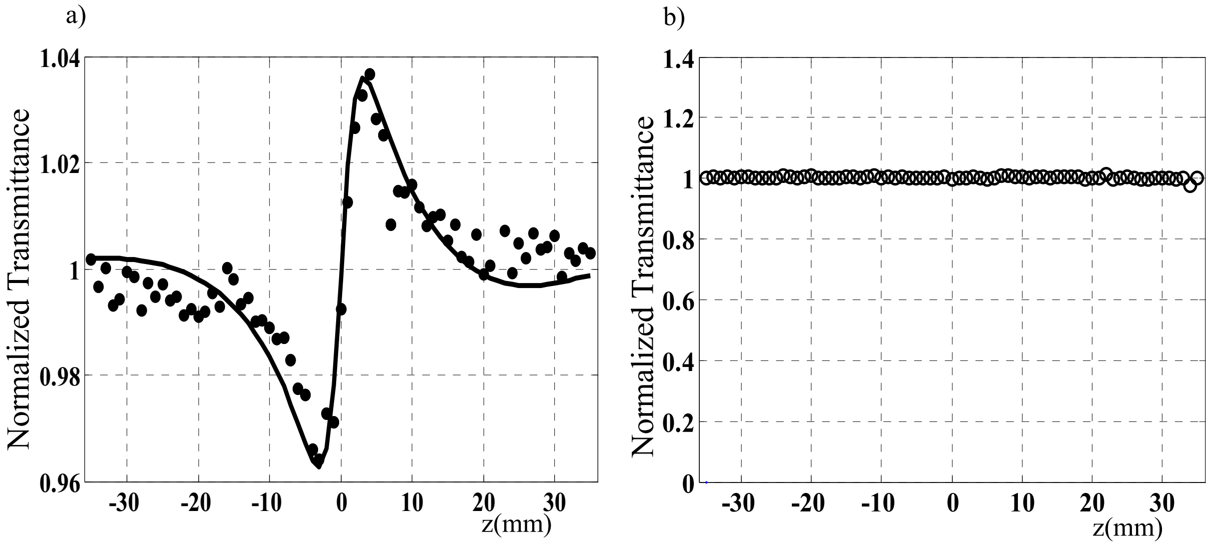

Fig.12 Transmission normalisée de Z-scan révélant le déphasage permanent inscrit à l'intérieur d'un verre As_2S_3 de 1,4 mm d'épaisseur par un faisceau gaussien avec une intensité de 3 GW/cm^2 et $E_c = 18$ mJ : (a) acquisitions expérimentales de profil de réfraction Z-scan (points gras), la ligne continue est le résultat de la simulation numérique avec les mêmes paramètres $S = 0.4$ $\Delta n_0 = 1.7\times10^{-5}$ ($\Delta\Phi_0 = 0.14$), b) acquisitions expérimentales (cercles vides) du profil Z-scan avec un diaphragme ouvert montrant l'absence de photo-noircissement ($\Delta\alpha_0 = 0$).

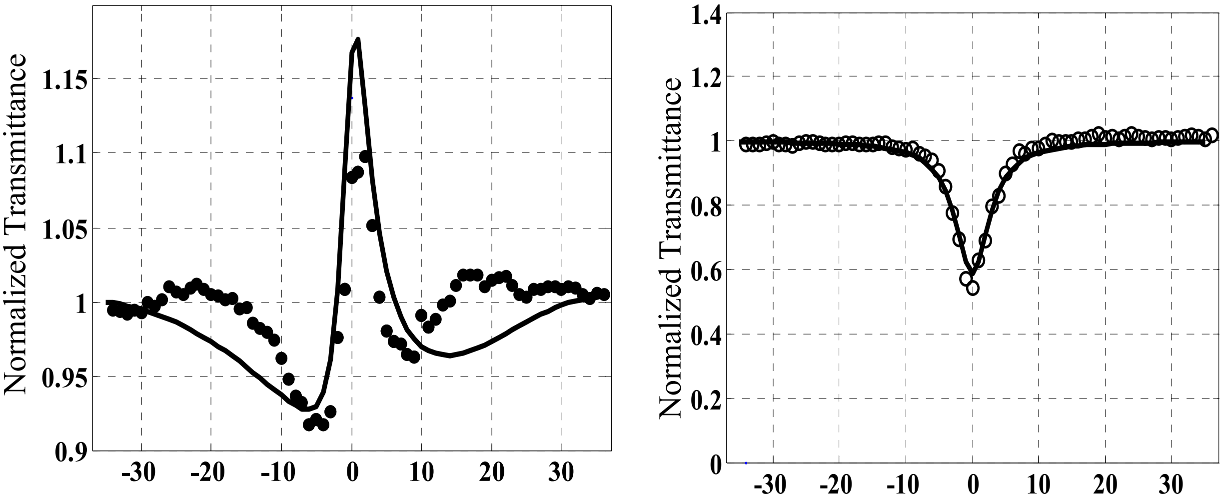

Fig.13 Transmission normalisée de Z-scan révélant le déphasage permanent inscrit à l'intérieur d'un verre As_2S_3 de 1,4 mm d'épaisseur par un faisceau gaussien avec une intensité de 6 GW/cm^2 et $E_c = 5$ mJ : (a) acquisitions expérimentales du profil de réfraction Z-scan (points gras), la ligne continue est le résultat de la simulation numérique avec les mêmes paramètres $S = 0.4$ $\Delta n_0 = 4.3\times10^{-5}$ ($\Delta\Phi_0 = 0.35$), b) acquisitions expérimentales (cercles vides) du profil Z-scan avec un diaphragme ouvert montrant l'effet du photo-noircissement. La courbe en trait plein est calculée pour $\Delta\alpha_0 = 840$ m^{-1}.

Après chaque processus d'écriture nous avons réalisé des acquisitions Z-scan dans le régime linéaire. Pour les PIEs avec des intensités en dessous de 3 GW/cm^2, seuls des changements dans la transmission des tracés Z-scan avec diaphragme fermé (indiquant une pure modification de l'indice de réfraction) ont été détectés pour une durée assez longue d'éclairement (énergie accumulée à l'intérieur du spécimen $E_c > 5$ mJ). Un exemple de tracé est représenté sur la figure 12 (a). Selon l'équation (10), la variation de la transmission ($\Delta T_{pv} = 0.072$) dans la Fig.12 (a) obtenue avec $S = 0.4$ correspond à $\Delta n_0 = 1.7\times 10^{-5}$. Le signe de Δn_0 est sans ambiguïté positif puisque un minimum suivi d'un maximum dans le tracé Z-scan de Fig.10 (a) indique toujours un déphasage inscrit de signe positif. La ligne continue sur cette courbe est la simulation numérique de Z-scan basée sur la méthode de décomposition en gaussienne selon [8]. Un très bon accord est obtenu, validant notre approche théorique. Dans la Fig.13, on peut voir un exemple de tracés Z-scan en régime linéaire caractérisant les modifications permanentes lorsque l'intensité de l'écriture est de 6 GW/cm^2 ($E_c = 5$ mJ). La Fig. 13 (b) montre un effet de photo-noircissement à l'intérieur de l'échantillon et l'ajustement de cette courbe en utilisant l'Eq. (9) donne $\Delta\alpha_0 = 840$ m^{-1}.

2.4 Caractérisation optique linéaire des couches minces transparentes par Z-scan [37]

Cette section repose sur les résultats publiés dans la réf. [37]. Nous analysons l'influence d'une ligne de phase de profil rectangulaire intégrée dans une couche mince sur la transmission normalisée dans le champ lointain grâce à la méthode Z-scan. La ligne de phase de forme rectangulaire a été faite en rayant attentivement une couche mince de polyméthacrylate de méthyle transparent (PMMA) sur une distance $\mathrm{l_x}$ assez longue (2 cm) par rapport à la taille du faisceau gaussien focalisé (w_0) pour pouvoir négliger les effets de diffraction selon la direction x. Le profil de la rayure (représenté sur la figure. 14 (a)) a été mesurée par un profilomètre mécanique donnant une profondeur $\mathrm{L} = 120 \pm 10$ nm et une largeur de $\mathrm{l_y} = 55 \pm 5$ μm. Nous montrons que lorsque $w_0 \approx l_y$ nous pouvons obtenir une transmission normalisée avec une forme de pic - vallée (comme dans la mesure non linéaire). Un exemple d'acquisition expérimental est représenté sur la figure 14 (b). Grâce à des calculs numériques (pour plus de détails, voir Réf. [37]), nous avons montré que la différence entre le maximum (pic) et le minimum (la vallée) dans le tracé Z-scan ($\Delta\mathrm{T_{pv}}$) peut être reliée de façon linéaire au changement de phase lorsqu'il est faible $|\Delta\Phi_0| \le 1$ avec moins de 10% d'erreur:

$$\Delta T_{pv} = a\left|\Delta\Phi_0\right|, \tag{11}$$

où a est un facteur de proportionnalité. Cette formule simple peut être utilisée pour caractériser les paramètres optiques linéaires des couches minces tel que, n_0, l'indice de réfraction linéaire ou L, l'épaisseur. Généralement, le facteur de proportionnalité (a) dépend de la taille de l'ouverture dans le champ lointain (S), la taille du 'beam-waist' (w_0), et les dimensions latérales (l_x et l_y) de l'objet phase rectangulaire. Le problème est assez complexe et possède de nombreux paramètres. Il nous a conduit à fixer S = 0,4 et $w_0 \approx l_y \ll l_x$. Dans ces conditions, le facteur de proportionnalité est égal à 0,9 permettant d'avoir une résolution optique de la mesure aussi petite que λ/550.

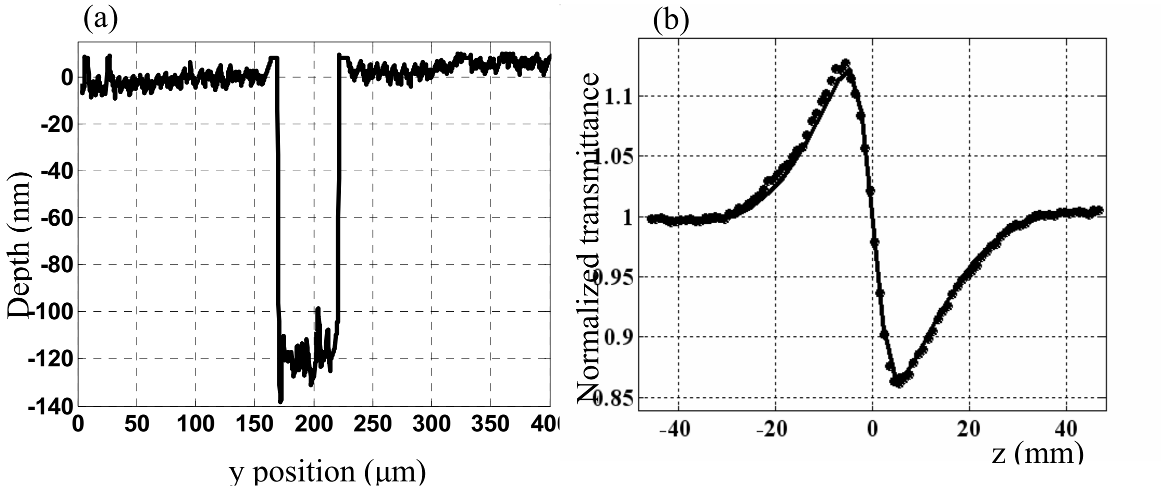

Fig. 14 (a) Scan réalisé par un profilomètre mécanique montrant les paramètres géométriques de la rayure rectangulaire (largeur et profondeur) (b) acquisitions expérimentales (points) montrant le profil Z-scan de la correspondant à la réfraction et la simulation théorique correspondante (trait plein).

2.5 Conclusions

Dans ce chapitre, nous avons montré que de très faibles épaisseurs combinées avec des non-linéarités relativement faibles rendent la caractérisation non linéaire de films minces impossible. Lorsque la longueur d'interaction optique est trop courte, il n'est pas possible dans certains cas d'induire un signal non linéaire avant de dépasser le seuil d'intensité induisant des dommages. Même la grande sensibilité des méthodes NIT-PO ou Z-scan n'est pas suffisante pour caractériser les échantillons minces si la résolution en transmission du signal mesuré donnée par le photo-détecteur n'est pas suffisamment élevée. De plus nous avons montré que les effets photo-induits (PIE) peuvent contribuer au signal non linéaire donné par les méthodes NIT-PO et Z-scan et conduisant à des résultats erronés de n_2 et β. En outre des nouvelles applications de la technique Z-scan ont été introduites. Nous avons montré que cette méthode peut être utilisée pour caractériser les changements permanents dans la réfraction et l'absorption induits dans l'échantillon en régime non linéaire, ainsi que de caractériser les propriétés optiques linéaires des couches minces telles que l'épaisseur et l'indice de réfraction.

3. Caractérisation non linéaire des matériaux massifs

Dans ce chapitre, nous présentons des mesures absolues à partir de Z-scan sur les indices de réfraction non linéaire du disulfure de carbone (CS_2) et la silice fondue (SiO_2) pour trois longueurs d'onde (1064 nm, 532 nm et 355 nm) dans le régime picoseconde. Les deux matériaux sont couramment utilisés comme références dans les expériences en optique non linéaire afin de calibrer l'intensité dans le plan focal.

Nous présentons également les résultats des mesures Z-scan (1064 nm, 17 ps) des indices de réfractions non-linéaires et des coefficients d'absorptions non linéaires pour différentes compositions de verres en chalcogénures GeS_2-Sb_2S_3-CsI et des verres d'oxydes à base de métaux lourds dans le système $Pb(PO_3)_2$-WO_3. Nous montrons que le modèle simple développé par Boling et al. [26] (dit BGO) basé sur la théorie de l'oscillateur harmonique semi-classique peut être un outil très utile pour les prédictions théoriques de l'indice de réfraction non linéaire dans l'infrarouge. Le facteur de mérite (FOM) $2\beta\lambda/n_2$ de ces matériaux est étudié et leur utilisation potentielle pour des applications en commutation est discutée.

3.1 Mesures absolues du n_2 du CS_2 et de la silice fondue [38]

Les résultats présentés dans cette section ont été publiés dans la référence [38]. Nous présentons des mesures absolues du n_2 du disulfure de carbone et de la silice fondue, deux matériaux de références utilisés en optique non linéaire. Ces deux milieux Kerr ont une absorption non linéaire négligeable. CS_2 est généralement utilisé pour étalonner les intensités incidentes dans le montage expérimental pour la caractérisation des matériaux ayant relativement un indice de réfraction non linéaire élevé (n_2 autour de 10^{-18} m^2/W). En revanche, la silice fondue est utilisée pour les matériaux non-linéaires ayant un n_2 deux ordres de grandeur plus petits. Pour obtenir des valeurs plus précises que celles déjà publiées dans la littérature, nous avons combiné la méthode Z-scan dans un système d'imagerie 4*f* (afin d'analyser la distorsion spatiale du faisceau diffracté) avec l'expérience du «Kerr Shutter» [39, 40] (pour évaluer la durée temporelle de la largeur d'impulsion pour trois longueurs d'onde différentes 1064 nm, 532 nm et 355 nm). Nous avons obtenu des valeurs de n_2 un ordre de grandeur inférieures à celles habituellement considérées dans le régime picoseconde [8, 41], et une dispersion plus importante de l'indice de réfraction non linéaire. Les résultats des mesures sont résumés dans le tableau 3.

Matériaux	λ (nm)	L (mm)	**n_2 x 10^{-20} m^2/W**	**β x 10^{-3} (cm/GW)**	**I_0(GW/cm^2)**
SiO_2	355	3.76	**2.0 ± 0.4**	< 2	37
SiO_2	532	3.76	**0.9 ± 0.3**	< 0.2	76
SiO_2	1064	3.76	**0.4 ± 0.07**	< 0.2	221
CS_2	532	1.0	**80 ± 17**	< 17	5.5
CS_2	1064	1.0	**40 ± 6**	< 7	23

Tab.3 Valeurs des coefficients non linéaires (n_2 et β) mesurés par Z-scan correspondant aux matériaux de références étudiés pour différentes longueurs d'onde.

3.2 Caractérisation non linéaire des verres chalcogénures dans le système GeS_2-Sb_2S_3-CsI [42]

Les résultats présentés dans cette section ont été publiés dans la référence [42]. Nous présentons les résultats des mesures Z-scan (à 1064 nm, 17 ps) des indices de réfraction et des coefficients d'absorption non linéaires pour différentes compositions de verres de chalcogénures dans le système GeS_2-Sb_2S_3-CsI. En outre, nous montrons que le modèle simple bien connu BGO basé sur la théorie de l'oscillateur harmonique semi-classique peut être un outil utile pour les prédictions théoriques de l'indice de réfraction non linéaire dans ces verres infrarouges. Un comportement quasi-linéaire est observé entre l'indice non linéaire et l'indice linéaire. Certaines de ces compositions mettent en évidence des propriétés potentiellement utiles pour les applications de commutation tout-optique ($2\beta\lambda/n_2 < 1$) [43].

Les mesures d'absorption réalisées avec un spectromètre UV-visible-NIR (CARY500) montrent une absorption linéaire négligeable dans l'infrarouge pour toutes les compositions et plus particulièrement à 1064 nm. La bande d'énergie interdite (ε_g) a été déterminée à partir des spectres d'absorption comme étant la longueur d'onde pour laquelle le coefficient d'absorption linéaire est égal à 10 cm^{-1}. Les indices de réfraction linéaire ont été mesurés à deux longueurs d'onde, 1331 nm et 1551 nm, en utilisant un laser polarisé avec une incidence TE dans un système Metricon. Les compositions ainsi que les coefficients linéaires et non linéaires de verres étudiés sont résumées dans le tableau 4.

	Composition			**Caractéristiques optiques**					
No	**GeS_2**	**Sb_2S_3**	**CsI**	**n_2 (10^{-19} m^2/W)**	**β (10^{-2} cm/GW)**	**$2\beta\lambda/n_2$**	**$h\nu/E_g$**[1]	**n_0 (1331 nm)**	**n_0 (1551 nm)**
A	90%	10%	0	2.0 ± 0.4 (50)	< 0.2	<0.22	0.470	2.146	2.140
B	75%	10%	15%	3.6 ± 0.9 (90)	1.0 ± 0.4	0.6	0.560	2.154	2.146
C	51.25%	26.25%	22.5%	3.9 ± 0.6 (97.5)	2.0 ± 0.4	1.08	0.571	2.274	2.265
D	66.25%	26.25%	7.5%	3.9 ± 0.6 (97.5)	1.0 ± 0.3	0.54	0.556	2.303	2.293
E	35%	35%	30%	4.7 ± 0.7 (117.5)	3.0 ± 0.7	1.36	0.584	2.309	2.299
F	42.5%	42.5%	15%	5.6 ± 1.8 (140)	3.0 ± 1.0	1.14	0.590	2.420	2.408
G	26.25%	51.25%	22.5%	7.5 ± 2.2 (187.5)	10 ± 1	2.84	0.622	2.457	2.444
H	10%	60%	30%	9.0 ± 2.0 (225)	19 ± 2	4.50	0.629	2.484	2.469
I	26.25%	66.25%	7.5%	9.7 ± 1.9 (242.5)	20 ± 2	4.38	0.660	2.619	2.602
J	10%	75%	15%	10.8 ± 3.0 (270)	16 ± 5	3.16	0.652	2.646	2.629

Tab.4 Compositions des verres étudiés (GeS_2+Sb_2S_3+CsI) et leurs coefficients optiques linéaires et non linéaires. La colonne 5 donne les valeurs de n_2 (dans la parenthèse le rapport de n_2 à celui de la silice fondue $n_2 = 4\times10^{-21}$ m^2/W), tandis que la colonne 6 montre les valeurs β.

En utilisant un modèle simple basé sur un oscillateur non linéaire classique (Boiling, Glass, et Owyoung – modèle BGO [24]), il a été possible d'estimer les valeurs de n_2 qui sont en accord avec les données expérimentales. Ce modèle suppose que l'hyper-polarisabilité du troisième ordre est proportionnelle au carré de la polarisabilité linéaire. Cela suppose également que la dispersion optique linéaire du milieu est déterminée par une seule fréquence de résonance ω_0 et que la fréquence de la lumière est loin de la résonance ($\omega << \omega_0$). En outre, la réponse diélectrique doit avoir une nature électronique pure. L'indice de réfraction non linéaire dans le modèle BGO, est donnée en unités SI par

$$n_2(\mathrm{m}^2/\mathrm{W}) = \frac{(gs)(n_0{}^2+2)^2(n_0{}^2-1)^2}{12n_0^2c\hbar\omega_0(Ns)} \tag{12}$$

où g est un paramètre anharmonique sans dimension, s est la force efficace de l'oscillateur, N est la densité d'ions dépendant de la composition et c est la vitesse de la lumière. L'indice linéaire de réfraction pour une longueur d'onde λ satisfait l'expression suivante:

---

[1] E_g est définie comme l'énergie pour laquelle le coefficient d'absorption linéaire est égal à 10 cm^{-1}

$$\frac{1}{3}\frac{(n_0^2+2)}{(n_0^2-1)}=\frac{\omega_0^2-\omega^2}{(e_c^2/m_e\varepsilon_0)(NS)} \tag{13}$$

où ε_0 est la permittivité du vide, e_c et m_e sont la charge et la masse de l'électron, respectivement. Les paramètres Ns et ω_0 sont obtenus à partir des valeurs $n_0(\lambda=1331\text{ nm})$ et $n_0(\lambda=1551\text{ nm})$ mesurés pour chaque échantillon. Ensuite, les valeurs de Ns et ω_0 sont introduites dans l'équation. (12) pour déterminer n_2. Le meilleur accord avec les données expérimentales a été obtenu pour un facteur d'échelle $gs=0.59$. Les comparaisons des valeurs théoriques avec les valeurs expérimentales sont présentées dans la figure 15 en fonction de l'indice de réfraction linéaire à 1064 nm. Les valeurs $n_0(\lambda=1064\text{ nm})$ ont été déterminées à l'aide de l'équation. (13) avec les valeurs de Ns et ω_0 obtenus pour chaque échantillon. Un très bon accord est trouvé entre les valeurs expérimentales et théoriques.

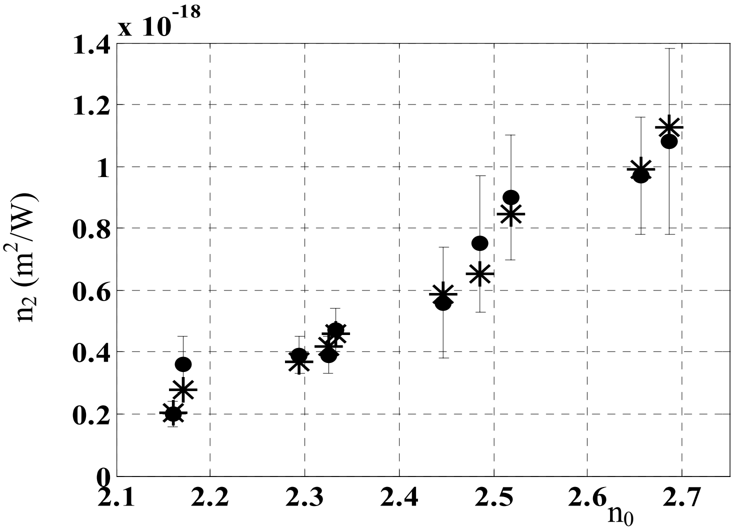

Fig. 15 Comparaison entre les données expérimentales n_2 (points gras) et les valeurs calculées à partir de la formule BGO (Eq. (12)) (étoiles)

3.3 Caractérisation non linéaire des verres $Pb(PO_3)_2$-WO_3 [44]

Nous présentons les résultats de la caractérisation optique linéaire et non linéaire des verres d'oxyde de métaux lourds $Pb(PO_3)_2$–WO_3. Les indices de réfraction linéaire ont été mesurés pour chaque échantillon en utilisant un ellipsomètre Horiba Jobin Yvon. Les coefficients d'absorption linéaire (α) ont été déterminés en utilisant un spectrophotomètre. Tous les résultats sont résumés dans le tableau 5.

Echantillon	Composition	n_0 (800 nm)	α (cm^{-1}) (800 nm)[2]	n_0 (1064 nm)	α (cm^{-1}) (1064 nm)[2]
A	$70Pb(PO_3)_2$-$30WO_3$	1.78	0.13	1.77	0.005
B	$60Pb(PO_3)_2$-$40WO_3$	1.85	0.48	1.84	0.29
C	$50Pb(PO_3)_2$-$50WO_3$	1.87	1.45	1.86	1.18
D	$40Pb(PO_3)_2$-$60WO_3$	1.95	2.94	1.93	1.16

Tab.5 Les coefficients optiques linéaires des verres $Pb(PO_3)_2$–WO_3

La caractérisation non linéaire a été réalisée en effectuant des mesures Z-scan à 1064 nm dans le régime de la picoseconde (17 ps) ainsi que par la technique Kerr-Shutter à 800 nm dans le régime femtoseconde (100 fs). Cette expérience a été calibrée avec le CS_2 compte tenu de la valeur de $n_2 = 3\times10^{-19}$ m^2/W. Cette valeur a été mesurée dans le régime femtoseconde par différents groupes [45, 46, 47, 48]. Les résultats des deux mesures ont été comparés avec les prédictions du modèle BGO. Le meilleur accord avec les données expérimentales a été obtenu pour un facteur d'échelle $gs = 0.37$ (voir Eq. (12)). Les données expérimentales et théoriques sont résumées dans le tableau 6.

Echantillon	$n_2^{EXP}\times10^{-20}$ m^2/W (800 nm)[2]	$n_2^{BGO}\times10^{-20}$ (800 nm) m^2/W	$n_2^{EXP}\times10^{-20}$ (1064 nm) m^2/W	$n_2^{BGO}\times10^{-20}$ (1064 nm) m^2/W	β (10^{-3} cm/GW)	$2\beta\lambda/n_2$ (1064 nm)
A	4.2 ± 0.4	3.2	4.0 ± 0.6	3.0	<0.7	<0.37
B	5.1 ± 0.5	5.2	4.7 ± 1.0	4.9	<1.5	<0.68
C	5.6 ± 0.6	5.5	4.7 ± 0.8	5.2	<3.0	<1.36
D	6.2 ± 0.6	6.8	6.0 ± 1.1	6.4	3.0 ± 0.7	1.1

Tab.6 Nonlinear optical coefficients and theoretical predictions with basis on the BGO model

Les résultats de n_2 présentés dans le tableau 6 sont importants à la lumière de nos mesures absolues pour les matériaux de références décrit dans le paragraphe précédent. La réponse optique des verres transparents dans le picoseconde et le régime femtoseconde devrait être à peu près égale dans l'infrarouge (800 nm et 1064 nm) compte tenu du fait que seulement la non-linéarité électronique est sondée dans ces milieux solides. L'étalonnage de Z-scan basé sur nos résultats (i.e. $n_2 \approx 0.4\times10^{-18}$ m^2/W pour le CS_2) donne des valeurs cohérentes entre deux expérimentateurs dans deux laboratoires différents. Si en revanche on tenait compte de l'ancienne valeur (i.e. $n_2 \approx 3\times10^{-18}$ m^2/W pour le CS_2 d'après [8]) on obtiendrait des résultats

---

[2] Les mesures ont été faites dans le groupe du Prof. C. B. de Araújo, *Departamento de Fìsica*, *Universidade Federal de Pernambuco*, (50670-901 Recife, PE, Brazil)

environ un ordre de grandeur plus grand dans le régime picoseconde pour les mêmes verres. Aucune explication physique ne pourrait justifier un tel écart important entre les valeurs de n_2 dans les régimes picoseconde et femtoseconde pour ces matériaux solides.

3.4 Conclusions

Nous avons effectué des mesures absolues de l'indice de réfraction non linéaire pour deux matériaux de référence (CS_2 et SiO_2). L'expérience Kerr-Shutter a été combinée avec la technique Z-scan afin de déterminer avec précision les profils spatio-temporels du faisceau de la pompe. Les n_2 obtenus dans le régime picoseconde ont été trouvés un ordre de grandeur inférieurs à ceux publiés dans la littérature et en outre une dispersion plus importante en fonction de la longueur d'onde a été trouvée. Nous avons également caractérisé les indices de réfraction non linéaire (n_2) et les coefficients d'absorption non linéaire (β) pour différentes compositions de verres de chalcogénures en massif GeS_2-Sb_2S_3-CsI et des verres d'oxydes de métaux lourds $Pb(PO_2)_3$—WO_3. Nous avons montré que le modèle simple dénommé BGO peut être utile pour prédire les indices non linéaires à partir des indices linéaires de ces verres infrarouges.

CONCLUSIONS GENERALES

Cette étude traite des caractérisations optiques non-linéaires du troisième ordre des couches minces et des matériaux massifs. Nous avons combiné différentes techniques de caractérisation bien connues à l'intérieur du système d'imagerie $4f$ afin d'optimiser la sensibilité avec un rapport signal sur bruit maximum pour les mesures des indices de réfraction non linéaire (n_2) et les coefficients d'absorption non linéaire (β). Nous avons montré que, dans le régime de faible excitation non linéaire, à l'aide de divers objets à l'entrée et des filtres spatiaux adaptés en sortie du système imageur, il est possible de réaliser diverses expériences telles que le mélange à quatre ondes dégénérées (DFWM), I-scan , Z-scan, Z-scan éclipsant (EZ-scan) et la technique d'imagerie non linéaire avec l'objet de phase (NIT-PO). Nous avons montré que toutes ces techniques peuvent être considérées comme des cas particuliers du même processus d'imagerie où la modification de la répartition de l'intensité dans le plan de l'image, après filtrage non linéaire à travers le matériau testé, placé à proximité du plan de Fourier, conduit à une information sur les coefficients non linéaires. En outre, nous avons unifié leur description théorique en utilisant un modèle simple basé sur l'optique de Fourier. Pour analyser quantitativement les distorsions non linéaires des images acquises par la caméra CCD, nous avons défini le rendement de diffraction comme le signal à mesurer. Nous en avons tiré des relations entre cette quantité et le déphasage non linéaire pour chacune des techniques de caractérisations considérées. L'influence de l'absorption non linéaire a été également traitée. Nous avons établi que Z-scan/EZ-scan ainsi que la technique NIT-PO possèdent les sensibilités les plus élevées tout en gardant les meilleurs rapports signal/bruit. Ces techniques permettent de mesurer des signaux correspondant à $\sim \lambda / 500$ au niveau de la distorsion du front de phase.

Suivant ces conclusions, nous avons montré que la sensibilité optique de Z-scan et NIT-PO ne garantissent pas la caractérisation précise des couches minces en optique non linéaire. Nous avons montré que, même dans les conditions optimisées, il est impossible d'induire un signal non linéaire si la longueur d'interaction optique est trop faible. L'amélioration de la réponse non linéaire des échantillons minces en augmentant l'intensité incidente est finalement limitée par le seuil des dommages. Grace à une caméra CCD, nous avons pu voir les changements dans le faisceau diffracté à l’infini à cause des effets photo-induits (PIE). Ce qui ne peut être fait lorsque l'on utilise des photodiodes ou des photomultiplicateurs. Par ailleurs, nous avons utilisé la technique NIT-PO pour caractériser les PIE. Nous avons montré que l'analyse par le contraste de phase en fonction du temps et de l'intensité incidente permet d'estimer le seuil des dommages ainsi que d'étudier la cinétique des PIEs. En particulier, nous avons étudié la photosensibilité des films minces chalcogénures $Ge_xAs_ySe_{1-x-y}$ et $Te_{20}As_{30}Se_{50}$. En outre, nous avons montré que les modifications permanentes de la réfraction et l'absorption induite par les PIEs peuvent contribuer à la réponse non linéaire mesurée avec Z-scan. Pour vérifier la présence de PIE au cours de Z-scan, il est nécessaire d'effectuer trois scans: en régime linéaire, puis en régime non linéaire et de nouveau en linéaire. La comparaison des scans en régime linéaires avant et après la mesure permet de révéler les changements permanents dans la réfraction et l'absorption inscrit à l'intérieur de l'échantillon. Il a été montré qu'une ablation d'une dizaine de nanomètres peut être détectée par Z-scan et ceci aboutit à des résultats erronés dans les valeurs de n_2 et β.

De plus nous avons démontré expérimentalement que la technique Z-scan peut être un outil très utile pour étudier le profil gaussien des modifications permanentes photo-induites au niveau des coefficients optiques à l'intérieur des matériaux photosensibles. Une théorie semi-analytique pour Z-scan donnant les mesures en régime linéaire a été développée. Il a été montré que le signe de la réfraction et de l'absorption peuvent être déterminé sans aucune ambigüité. En particulier, nous avons étudié les PIEs dans les paramètres optiques linéaires d'un verre chalcogénure massif As_2S_3 causés par une irradiation infrarouge. Une autre application a été trouvée pour la mesure de l'épaisseur ou l'indice des couches minces. Il a été démontré qu'en présence d'objets de phase rectangulaire (rainure rectangulaire sur film d'épaisseur très faible devant λ) il est possible d'obtenir une configuration pic-vallée avec la technique Z-scan. La différence entre le pic et la vallée de la transmission normalisée est liée linéairement au déphasage dû à la réfraction permanente.

Nous avons également réalisé des mesures absolues de n_2 dans le disulfure de carbone (CS_2) et la silice fondue (SiO_2), deux matériaux standards utilisés dans les expériences d'optique non linéaire. La méthode Z-scan à l'intérieur du système d'imagerie 4*f* a été combinée avec l'expérience 'Kerr-Shutter' afin d'analyser précisément le profil spatio-temporel des faisceaux de pompe à 355 nm, 532 nm et 1064 nm dans le régime de picoseconde. Les valeurs absolues obtenues de n_2 ont été trouvées 7,5 fois plus petites que celles couramment utilisées jusqu'à présent et mesurées il y a quelques décennies. En outre une dispersion plus importante de n_2 en fonction de la longueur d'onde a été trouvée.

Nous avons également caractérisé les indices de réfraction non linéaire (n_2) et les coefficients d'absorption non linéaire (β) pour différentes compositions de verres massifs en chalcogénures GeS_2-Sb_2S_3-CsI et en oxyde de métaux lourds $Pb(PO_2)_3$—WO_3 dans le cadre de leur aptitude à des applications de commutation tout optique (AOS). Nous avons constaté que seulement trois compositions parmi les dix étudiés en verres chalcogénures ont un facteur de mérite $2\beta\lambda/n_2$ (FOM) <1, les rendant aptes à l'AOS. Au contraire, tous les verres d'oxydes étudiés remplissent le critère retenu. En outre, nous avons confirmé que l'indice de réfraction non linéaire a un comportement étroitement liée à l'indice linéaire dans les deux familles de verres. De plus, nous avons montré que le modèle BGO pourrait être un outil très utile pour estimer les valeurs n_2 dans les deux groupes de matériaux en tenant compte de nos mesures absolues. Par ailleurs, on constate que les prédictions du modèle BGO ne sont pas influencées par la présence d'une faible absorption non linéaire.

En résumé, notre étude a porté sur le large éventail des questions concernant la caractérisation optique non linéaire de la susceptibilité du troisième ordre : à partir de l'optimisation de la sensibilité et le rapport signal / bruit dans les techniques de mesures, en passant par le problème de la photosensibilité et les effets photo-induits dans les films minces et pour finir sur la mesure absolue des matériaux massifs. Il y a quelques points qui valent la peine d'être envisager pour les perspectives d'avenir. Des fluctuations d'énergie moindres à la sortie du laser combiné avec un seuil de bruit plus faible au niveau du capteur sont indispensables pour réaliser des mesures de coefficients non linéaires dans des bonnes conditions. Nous sommes convaincus que la précision de la mesure absolue de l'intensité dans le plan focal d'une lentille reste la clé conduisant à des résultats plus reproductibles et cohérents pour toutes les expériences menées en optique non linéaire.

Références

[1] P. A. Franken, A. E. Hill, C. W. Peters, G. Weinreich, Phys. Rev. Lett. **7**, 118 (1961)

[2] W. H. Steel, *Interferometry,* 2nd ed. (Cambridge U. Press, Cambridge, U.K., 1983)

[3] G. Boudebs, M. Chis, X. N. Phu, J. Opt. Soc. Am. B **18**, 623 (2001)

[4] Y. R. Shen, *The Principles of Nonlinear Optics* (Wiley, New York, 1984)

[5] E. L. Falcao-Filho, C. A. C. Bosco, G. S. Maciel, L. H. Acioli, Cid B. de Araujo, A. A. Lipovskii, D. K. Tagantsev, Phys. Rev. B **69**, 134204 (2004)

[6] R. Adair, L. L. Chase, and S. A. Payne, J. Opt. Soc. Anler. B, **4**, 875 (1987)

[7] F. P. Strohkendl, L. R. Dalton, R. W. Hellwarth, H. W. Sarkas, Z. H. Kafafi, J. Opt. Soc. Am. B, **14**, 92 (1997)

[8] M. Sheik-Bahae, A. A. Said, T. H. Wei, D. Hagan, E. W. Stryland, IEEE J. Quant. Elect. **26**, 760 (1990)

[9] B. Taheri, H. Liu, B. Jassemnejad, D. Appling, R.C. Powell, , J.J. Song, Appl. Phys. Lett. **68**, 1317 (1996)

[10] W. Zhao and P. Palffy-Muhoray, Appl. Phys. Lett. **63**, 1613 (1993)

[11] B.K. Rhee, J.S. Byun, E.W. Van Stryland, J. Opt. Soc. Am. B **13**, 2720 (1996)

[12] B. Gu, J. Yan, Q. Wang, J.L. He, H.T. Wang, J. Opt. Soc. Am. B **21**, 968 (2004)

[13] J.G. Tian, W.P. Zang, G.Y. Zhang, Opt. Commun. **107**, 415 (1994)

[14] H. Ma, A. S. Gomez, C. B. de Araujo, Appl. Phys. Lett. **59**, 2666 (1991)

[15] M. Sheik-Bahae, J. Wang, R. DeSalvo, D. J. Hagan, E. W. V. Stryland, Opt. Lett. **17**, 258 (1992)

[16] H. Ma, Cid B. de Araujo, Appl. Phys. Lett. **66**, 27 (1995)

[17] A. Marcano, H. Maillotte, D. Gindre, D. Metin, Opt. Lett. **21**, 101 (1996)

[18] F.E. Hernandez, A. Marcano, H. Maillotte, Opt. Commun. **134**, 529 (1997)

[19] T. Xia, D. J. Hagan, M. Sheik-Bahae, E.W. Van Stryland, Opt. Let. **19**, 317 (1994)

[20] T. Godin, M. Fromager, B. Paivanranta, N. Passilly, G. Boudebs, E. Cagniot, K. Ait-Ameur, Appl. Phys. B **95**, 579 (2009)

[21] G. Boudebs, M. Chis, J. P. Bourdin, J. Opt. Soc. Am. B **13**, 1450 (1996)

[22] G. Boudebs, M. Chis, A. Monteil, Opt. Commun. **150**, 287 (1998)

[23] S. Cherukulappurath, G. Boudebs, A. Monteil, J. Opt. Soc. Am. B, **21**, 273 (2004)

[24] G. Boudebs, S. Cherukulappurath, Phys. Rev. A **69**,053813 (2004)

[25] H. Ebendor¤-Heidepriem, Opt. Mat. **25**, 109 (2004)

[26] N.L. Boling, A.J. Glass, A. Owyoung, IEEE J. Quantum Electronics **QE-14**, 601 (1978)

[27] G. Boudebs, K. Fedus, C. Cassagne, H. Leblond, Appl. Phys. Lett. **93**, 021118 (2008)

[28] K. Fedus, G. Boudebs, J. Opt. Soc. Am. B, **26**, 244 (2009)

[29] K. Fedus, G. Boudebs, H. Leblond, Appl. Phys. B (2010)

[30] K. Fedus, G. Boudebs, Opt. Commun. accepted to publication (October 2010)

[31] P. Nemec,S. Zhang, V. Nazabal, K. Fedus, G. Boudebs, A. Moreac, M. Cathelinaud, X.-H. Zhang, Opt. Express **18**, 22944 (2010)

[32] K. Fedus, G. Boudebs, Cid B. de Araujo, M. Cathelinaud, F. Charpentier, and V. Nazabal, Appl. Phys. Lett. 94, 061122 (2009)

[33] A. A. Said, M. Sheik-Bahae, D. J. Hagan, T. H. Wei, J. Wang, J. Young, E. W Van Stryland, J. Opt. Soc. Am. B **9**, 405 (1992)

[34] K. Ogusu, K. Shinkawa, Opt. Exp. **16**, (2008)

[35] B. M. Patterson, W. R. White, T. A. Robbins, R. J. Knize, Appl. Opt. **10**, 1854 (1998)

[36] K. Fedus, G. Boudebs, J. Opt. Soc. Am. B **26**, 2171-2175 (2009)

[37] G. Boudebs, K. Fedus, Appl. Opt. **48**, 4124 (2009)

[38] G. Boudebs, K. Fedus, J. Appl. Phys. **105**, 103106 (2009)

[39] A. Major, F. Yoshino, J. S. Aitchison, P. W. E. Smith, Opt. Let. **29,** 16 (2004)

[40] A. Major, F. Yoshino, J. S. Aitchison, P. W. E. Smith, Opt. Let. **30**, 19 (2005)

[41] D.Milam, Appl.Opt. **37**, 546 (1998)

[42] K. Fedus, G. Boudebs, Q. Coulombier, J. Troles, X.H.Zhang, J. Appl. Phys. **107**, 023108 (2010)

[43] V. Mizrahi, K. W. DeLong, G. I. Stegeman, M. A. Saifi, M. J. Andrejco, Opt. Lett. **14**, 1140 (1989)

[44] T. R. Oliveira, K. Fedus, D. Manzani, E. L. Falcão-Filho, G. Boudebs, Cid B. de Araújo, Y. Messaddeq, submitted to publication in J. Appl. Phys. (October 2010)

[45] M. Falconieri, G. Salvetti, Appl. Phys. B **69**, 133 (1999)

[46] A. Gnoli, L. Razzari and M. Righini, Opt. Express **13**, 7976 (2005)

[47] S. Couris, M. Renard, O. Faucher, B. Lavorel, R. Chaux, E. Koudoumas, X. Michaut, Chem. Phys. Lett. **369**, 318 (2003)

[48] R. A. Ganeev, A . I., Ryasnyansky, M. Baba, M. Suzuki, N. Ishizawa, M. Turu, S. Sakakibara, H. Kuroda, Appl. Phys. B **78**, 433 (2004)